

6G Wireless Communication Links Operating at Frequencies beyond 200 GHz: an Analysis of their Performance and Main Limitations



BERGISCHE
UNIVERSITÄT
WUPPERTAL

Dissertation

Submitted in partial fulfillment of the requirements for the degree of
Doktor der Ingenieurwissenschaften

at the

University of Wuppertal, Germany

School of Electrical, Information and Media Engineering

by

Pedro Rodríguez Vázquez

from Málaga, Spain

February 2021

The PhD thesis can be quoted as follows:

urn:nbn:de:hbz:468-urn:nbn:de:hbz:468-20220127-110702-8

[<http://nbn-resolving.de/urn/resolver.pl?urn=urn%3Anbn%3Ade%3A468-20220127-110702-8>]

DOI: 10.25926/tvmc-z778

[<https://doi.org/10.25926/tvmc-z778>]

Acknowledgements

To my family.

Abstract

Wireless mobile communication is one of the fastest-growing fields of technology. Currently, society is immersed in the deployment of 5G mobile networks. However, this technology will not be enough to meet society's wireless connectivity demand in the near-to mid-term future. A new generation of wireless mobile networks has to be developed to address this demand. With the spectrum below 100 GHz already congested, the future 6G networks will have to be operated in the high mmWave band above 200 GHz. Due to the recent advancements in semiconductor process technology, these bands have become accessible using silicon technologies. These technologies allow for the co-integration of high-frequency radios and digital baseband processors, present a highly reliable fabrication process, and offer low production cost for high production volumes. All these characteristics make this technology the key enabler for 6G radios.

This thesis investigates the system design considerations that need to be addressed to develop the radio-frequency front-ends for the future 6G wireless links.

As part of this thesis scope, multiple wireless communication links established with different radio-frequency front-ends have been characterized. After the discovery that the links were performing below the limit set by Shannon's theorem, a deep analysis was carried out to investigate which is the source of this limitation. During this analysis, it was found that five different system impairments limit the wireless link. These impairments are the error introduced by the measurement setup, the signal to noise ratio at the receiver output, the phase error generated by the broadband noise floor of the LO generation path, the interference created by the harmonics spurs, and the IQ cross-talk induced by a non-perfect symmetry between the upper side-band and the lower side-band. The phase noise and the IQ cross-talk are the dominant among these errors. The phase error sets a practical boundary to the modulation order employed in the wireless link, limiting its spectral efficiency. The IQ cross-talk influences the maximum signal bandwidth that can be used in the wireless link.

This thesis also presents techniques to overcome these limitations. To reduce the influence of the IQ cross-talk, an ultra-wideband Rx was designed. Using this Rx, the first silicon-based 100 Gb/s wireless link was established over a 1-meter distance. Moreover, this thesis presents the first MIMO wireless link operating at frequencies beyond 200 GHz. Using this system, data-rates of 110 Gb/s and 80 Gb/s were achieved over a 1-meter and 2-meter link distances, respectively.

In conclusion, this thesis presents an analysis of the system impairments that limit the wireless link performance at frequencies beyond 200 GHz. These impairments need to be considered by anyone designing radio-frequency front-ends for the future 6G networks. Moreover, it advances over the current state of the art. It presents the first 100 Gb/s

wireless link based on silicon technologies and the first MIMO wireless link at frequencies beyond 200 GHz, achieving an aggregated data-rate of 110 Gb/s over a 1-meter distance.

Zusammenfassung

Die drahtlose mobile Kommunikation ist eines der am schnellsten wachsenden Technologiefelder. Zurzeit werden die Mobilfunknetze mit Systemen der 5. Generation 5G erweitert. Diese Technologie wird jedoch nicht ausreichen, um den Bedarf der Gesellschaft an drahtloser Konnektivität in naher bis mittelfristiger Zukunft zu decken. Es muss eine neue Generation von drahtlosen Mobilfunknetzen entwickelt werden, um diesen Bedarf zu decken. Da das Spektrum unter 100 GHz bereits überlastet ist, müssen die zukünftigen 6G-Netzwerke im hohen mm-Wellenlängenbereich über 200 GHz betrieben werden. Aufgrund der jüngsten Fortschritte in der Halbleiterprozesstechnologie sind diese Bänder mit Siliziumtechnologien zugänglich geworden. Diese Technologien ermöglichen die Kointegration von Hochfrequenz-Funkgeräten und digitalen Basisband-Prozessoren, einen äußerst zuverlässigen Herstellungsprozess und haben niedrige Produktionskosten für hohe Produktionsmengen. All diese Eigenschaften machen diese Technologie zur Schlüsseltechnologie für 6G-Funkgeräte.

In dieser Arbeit werden die Überlegungen zum Systemdesign untersucht, die bei der Entwicklung der Hochfrequenz-Frontends für die zukünftigen 6G-Funkverbindungen berücksichtigt werden müssen.

Im Rahmen dieser Arbeit wurden mehrere drahtlose Kommunikationsverbindungen, die mit verschiedenen Hochfrequenz-Frontends aufgebaut wurden, charakterisiert. Nachdem festgestellt wurde, dass die Verbindungen unterhalb der durch das Shannon'sche Theorem gesetzten Grenze arbeiten, wurde eine tiefgehende Analyse durchgeführt, um herauszufinden, was die Ursache für diese Einschränkung ist. Während dieser Analyse wurde festgestellt, dass fünf verschiedene Systembeeinträchtigungen die drahtlose Verbindung begrenzen. Bei diesen Beeinträchtigungen handelt es sich um Fehler, die durch den Messaufbau verursacht werden, den Signal-Rausch-Abstand am Empfängerausgang, den Phasenfehler, der durch das breitbandige Grundrauschen des LO-Pfades erzeugt wird, die Interferenzen, die durch die Oberschwingungen entstehen, und das IQ-Übersprechen, das durch eine nicht perfekte Symmetrie zwischen dem oberen Seitenband und dem unteren Seitenband verursacht wird. Das Phasenrauschen und das IQ-Übersprechen sind die dominierenden Fehler im System. Der Phasenfehler setzt eine praktische Grenze für die in der drahtlosen Verbindung verwendete Modulationsordnung und reduziert die spektrale Effizienz. Das IQ-Übersprechen beeinflusst die maximale Signalbandbreite, die in der drahtlosen Verbindung genutzt werden kann.

In dieser Arbeit werden auch Techniken zur Überwindung dieser Einschränkungen vorgestellt. Um den Einfluss des IQ-Übersprechens zu reduzieren, wurde ein Ultrabreitband-Rx entwickelt. Mit diesem Rx wurde die erste Silizium-basierte drahtlose 100 Gb/s-Verbindung über eine Entfernung von einem Meter aufgebaut. Darüber hinaus wird in

dieser Arbeit die erste drahtlose MIMO-Verbindung vorgestellt, die bei Frequenzen jenseits von 200 GHz arbeitet. Mit diesem System wurden Datenraten von 110 Gb/s und 80 Gb/s über eine 1-Meter- bzw. 2-Meter-Strecke erreicht.

Zusammenfassend wird in dieser Arbeit eine Analyse der Systembeeinträchtigungen vorgestellt, die die Leistung der drahtlosen Verbindung bei Frequenzen jenseits von 200 GHz einschränken. Diese Beeinträchtigungen müssen von jedem berücksichtigt werden, der Hochfrequenz-Frontends für die zukünftigen 6G-Netzwerke entwickelt. Außerdem stellt es einen Fortschritt gegenüber dem aktuellen Stand der Technik dar. In dieser Arbeit werden unter anderem die erste drahtlose 100 Gb/s-Verbindung auf der Basis von Siliziumtechnologien vorgestellt und es wird die erste drahtlose MIMO-Verbindung für Frequenzen oberhalb von 200 GHz beschrieben, die eine aggregierte Datenrate von 110 Gb/s über eine Entfernung von 1 Meter ermöglicht.

Contents

Abstract	iii
Zusammenfassung	v
I. Context	1
1. Introduction	2
1.1. Current status of mobile communication networks	2
1.2. The high mm-Wave and THz bands	5
1.2.1. Technologies for high mm-Wave and THz communications	5
1.3. SoA of fully-electronic wireless communication links for frequencies beyond 200 GHz	6
1.3.1. Limitations of the SoA	7
1.4. Central Research Question and Contributions	9
1.5. Thesis Structure	10
2. Digital Communications	11
2.1. Introduction to Digital Communications	12
2.2. Bit Error Rate, Error Vector Magnitude, and Signal to Noise Ratio	20
2.2.1. EVM/BER relation	20
2.2.2. SNR/EVM relation	23
II. RF Front-ends for Wireless Communications	27
3. Tx and Amplifier-first Rx RF-front-end modules	28
3.1. Transmitter and Amplifier-first Receiver Architecture	29
3.1.1. $\times 16$ IQ LO generation path	31
3.1.2. Tx up-conversion path	33
3.1.3. Rx down-conversion path	34
3.1.4. On-Chip antenna and BB packaging scheme	35
3.2. RF Characterization	37
3.2.1. Single-tone RF measurements of the Tx and Rx	37

3.2.2.	Tx and Rx back-to-back results	44
3.3.	Wireless Communication Link	48
3.3.1.	Set-up description	48
3.3.2.	Measured Link results	49
3.3.3.	EVM analysis	51
3.4.	Conclusions	63
4.	Mixer-First Receiver RF front-end	64
4.1.	Introduction	64
4.2.	Mixer-First Rx Architecture	65
4.2.1.	Down-Conversion Stage Design and Simulated Results	66
4.3.	RF characterization	70
4.3.1.	Single-tone RF measurements of the Rx	70
4.3.2.	Tx and Rx back-to-back results	72
4.4.	Wireless Communication Link	74
4.4.1.	Measured link results	74
4.4.2.	EVM analysis	75
4.4.3.	Tx and Rx operated with independent external drive	79
4.5.	Conclusions	82
5.	IQ-polarized Tx and Rx RF front-ends	83
5.1.	Introduction	83
5.2.	Tx and Rx Architecture	85
5.2.1.	Operation principle	86
5.2.2.	$\times 8$ Lo generation path	88
5.2.3.	Tx up-conversion path	90
5.2.4.	Rx down-conversion path	90
5.2.5.	Linear Dual-Polarization antenna	91
5.2.6.	Packaging	92
5.3.	RF characterization	93
5.3.1.	Single-tone RF measurements of the Tx and the Rx	93
5.3.2.	Tx and Rx back-to-back results	97
5.4.	Wireless Link Results	100
5.4.1.	Measured link results	100
5.4.2.	EVM analysis	102
5.4.3.	Wireless link performance for different Tx/Rx azimuthal rotations	103
5.5.	Conclusions	106
6.	MIMO RF front-end	107
6.1.	Introduction	107
6.2.	DP Tx and Rx RF Front-end Architecture	108
6.2.1.	Tx and Rx circuit building blocks	111

6.2.2. Packaging	111
6.2.3. Circular Dual-Polarization antenna	114
6.3. RF characterization	117
6.3.1. Single-tone RF measurements of the Tx and Rx	118
6.3.2. Tx and Rx back-to-back results	124
6.4. Wireless Communication link	127
6.4.1. EVM results and analysis	129
6.5. Conclusions	134
III. Conclusion and future outlook	135
7. Thesis Summary	136
7.1. Thesis Summary	136
7.2. Future Directions	138
Bibliography	141

Declaration

I, Pedro Rodríguez Vázquez, herewith declare that I have produced this thesis without the prohibited assistance of third parties and without making use of aids other than those specified; notions taken over directly or indirectly from other sources have been identified as such. This work has not previously been presented in identical or similar form to any other German or foreign examination board.

The thesis work was conducted from 2014 to 2020 under the supervision of Prof. Dr. rer. nat. Ullrich R. Pfeiffer at the University of Wuppertal. This work was partially funded by the German Research Foundation (DFG) as part of the SPP 1655 *Drahtlose Ultra-hochgeschwindigkeitskommunikation für den mobilen Internetzugang* (*Wireless 100 Gb/s and beyond*), and as part of the European Commission EU 316755 *Towards 0.7 Terahertz Silicon Germanium Heterojunction Bipolar Technology* (*DOTSEVEN*).

Wuppertal, February 2021

Publications

Journal Publications

1. **P. Rodríguez-Vázquez**, J. Grzyb, B. Heinemann and U. R. Pfeiffer, "A QPSK 110-Gb/s Polarization-Diversity MIMO Wireless Link With a 220-255 GHz Tunable LO in a SiGe HBT Technology," *IEEE Transactions on Microwave Theory and Techniques*, Early access.
2. **P. Rodríguez-Vázquez**, J. Grzyb, B. Heinemann and U. R. Pfeiffer, "A 16-QAM 100-Gb/s 1-M Wireless Link With an EVM of 17% at 230 GHz in an SiGe Technology," *IEEE Microwave and Wireless Components Letters*, vol. 29, no. 4, pp. 297-299, Apr. 2019.
3. I. Aziz, D. Dancila, S. Dittmeier, A. Siligaris, C. Dehos, P. M. De Lurgio, Z. Djurcic, G. Drake, J. L. González Jiménez, L. Gustaffson, D. W. Kim, E. Locci, U. R. Pfeiffer, **P. Rodríguez-Vázquez**, D. Röhrich, A. Schöning, H. K. Soltveit, K. Ullaland, P. Vincent, S. Yang, R. Brenner, "Effects of proton irradiation on 60 GHz CMOS transceiver chip for multi-Gbps communication in high-energy physics experiments", *The Journal of Engineering*, vol. 8, p. 5391-5396, Apr. 2019.
4. **P. Rodríguez-Vázquez**, J. Grzyb, N. Sarmah, B. Heinemann and U. R. Pfeiffer, (2018). "A 219–266 GHz LO-tunable direct-conversion IQ receiver module in a SiGe HBT technology". *International Journal of Microwave and Wireless Technologies*, vol. 10, no. 5-6, pp. 587-595, June 2018.
5. S. Malz, B. Goettel, J. Eisenbeis, F. Boes, J. Grzyb, **P. Rodríguez-Vázquez**, T. Zwick, and U. R. Pfeiffer (2017). "Real100G.RF: A Fully Packaged 240 GHz Transmitter with In-Antenna Power Combining in 0.13 μm SiGe Technology", *Frequenz*, vol. 71 no. 9-10, pp. 415-425, Aug. 2017.
6. N. Sarmah, J. Grzyb, K. Statnikov, S. Malz, **P. Rodríguez-Vázquez**, W. Förster, B. Heinemann, and U. R. Pfeiffer "A Fully Integrated 240-GHz Direct-Conversion Quadrature Transmitter and Receiver Chipset in SiGe Technology," *IEEE Transactions on Microwave Theory and Techniques*, vol. 64, no. 2, pp. 562-574, Feb. 2016.

Conference Publications

1. **P. Rodríguez-Vázquez**, M. E. Leinonen, J. Grzyb, N. Tervo, A. Parssinen, and U. R. Pfeiffer, "Signal-processing Challenges in Leveraging 100 Gb/s Wireless THz," *2020 2nd 6G Wireless Summit (6G SUMMIT)*, Levi, Finland, 2020, pp. 1-5.
2. J. Grzyb, **P. Rodríguez-Vázquez**, B. Heinemann, and U. R. Pfeiffer, "The Influence of RF Front-End Imperfections on Performance of a 220-260 GHz Tunable M-QAM Wireless Link in SiGe HBT Technology," *2019 44th International Conference on Infrared, Millimeter, and Terahertz Waves (IRMMW-THz)*, Paris, France, 2019, pp. 1-2.
3. **P. Rodríguez-Vázquez**, J. Grzyb, and U. R. Pfeiffer, "RF Front-End Impairments for Ultra-Broadband Wireless Communication above 200 GHz," *2019 16th International Symposium on Wireless Communication Systems (ISWCS)*, Oulu, Finland, 2019, pp. 335-339.
4. **P. Rodríguez-Vázquez**, J. Grzyb, B. Heineman, and U. R. Pfeiffer, "Optimization and Performance Limits of a 64-QAM Wireless Communication Link at 220-260 GHz in a SiGe HBT Technology," *2019 IEEE Radio and Wireless Symposium (RWS)*, Orlando, FL, USA, 2019, pp. 1-3.
5. **P. Rodríguez-Vázquez**, J. Grzyb, B. Heinemann, and U. R. Pfeiffer, "Performance Evaluation of a 32-QAM 1-Meter Wireless Link Operating at 220–260 GHz with a Data-Rate of 90 Gbps," *2018 Asia-Pacific Microwave Conference (APMC)*, Kyoto, 2018, pp. 723-725.
6. K. KrishneGowda, **P. Rodríguez-Vázquez**, A. C. Wolf, J. Grzyb, U. R. Pfeiffer, and R. Kraemer, "100 Gbps and beyond: Hardware in the Loop experiments with PSSS modulation using 230 GHz RF frontend," *2018 15th Workshop on Positioning, Navigation and Communications (WPNC)*, Bremen, 2018, pp. 1-5.
7. U. R. Pfeiffer, R. Jain, J. Grzyb, S. Malz, P. Hillger, and **P. Rodríguez-Vázquez**, "Current Status of Terahertz Integrated Circuits - From Components to Systems," *2018 IEEE BiCMOS and Compound Semiconductor Integrated Circuits and Technology Symposium (BCICTS)*, San Diego, CA, 2018, pp. 1-7.
8. J. Grzyb, **P. Rodríguez-Vázquez**, N. Sarmah, B. Heinemann, and U. R. Pfeiffer, "Performance Evaluation of a 220–260 GHz LO Tunable BPSK/QPSK Wireless Link in SiGe HBT Technology," *2018 48th European Microwave Conference (EuMC)*, Madrid, 2018, pp. 1397-1400.
9. **P. Rodríguez-Vázquez**, J. Grzyb, N. Sarmah, B. Heinemann, and U. R. Pfeiffer, "Towards 100 Gbps: A Fully Electronic 90 Gbps One Meter Wireless Link at 230

-
- GHz," *2018 48th European Microwave Conference (EuMC)*, Madrid, 2018, pp. 1389-1392.
10. J. Grzyb, **P. Rodríguez-Vázquez**, B. Heinemann, and U. R. Pfeiffer, "A High-Speed QPSK/16-QAM 1-m Wireless Link with a Tunable 220–260 GHz LO Carrier in SiGe HBT Technology," *2018 43rd International Conference on Infrared, Millimeter, and Terahertz Waves (IRMMW-THz)*, Nagoya, 2018, pp. 1-2.
 11. **P. Rodríguez-Vázquez**, J. Grzyb, N. Sarmah, B. Heinemann, and U. R. Pfeiffer, "A 65 Gbps QPSK one meter wireless link operating at a 225–255 GHz tunable carrier in a SiGe HBT technology," *2018 IEEE Radio and Wireless Symposium (RWS)*, Anaheim, CA, 2018, pp. 146-149.
 12. **P. Rodríguez-Vázquez**, J. Grzyb, N. Sarmah, B. Heinemann, and U. R. Pfeiffer, "A 219–266 GHz fully-integrated direct-conversion IQ receiver module in a SiGe HBT technology," *2017 12th European Microwave Integrated Circuits Conference (EuMIC)*, Nuremberg, 2017, pp. 261-264.
 13. **P. Rodríguez-Vázquez**, J. Grzyb, N. Sarmah, U. R. Pfeiffer, and B. Heinemann, "Towards THz High Data-Rate Communication: a 50 Gbps All-Electronic Wireless Link at 240 GHz. *2017 Proceedings of the 4th ACM International Conference on Nanoscale Computing and Communication (NanoCom '17)*, New York, 2017, article 25, pp. 1–2.
 14. J. Grzyb, **P. Rodríguez-Vázquez**, N. Sarmah, B. Heinemann, and U. R. Pfeiffer, "A 240 GHz high-speed transmission link with highly-integrated transmitter and receiver modules in SiGe HBT technology," *2017 42nd International Conference on Infrared, Millimeter, and Terahertz Waves (IRMMW-THz)*, Cancun, 2017, pp. 1-2.
 15. S. Dittmeier, R. Brenner, D. Dancila, C. Dehos, P. De Lurgio, Z. Djurcic, G. Drake, J. L. González Giménez, L. Gustafsson, D. W. Kim, E. Locci, U. Pfeiffer, D. Röhrich, A. Rydberg, A. Schöning, A. Siligaris, H. K. Soltveit, K. Ullaland, P. Vincent, **P. Rodríguez-Vázquez**, D. Wiedner, and S. Yang, "Wireless data transmission for high energy physics applications", *2017 EPJ Web Conf.* vol. 150, pp. 2.
 16. N. Sarmah, **P. Rodríguez-Vázquez**, J. Grzyb, W. Förster, B. Heinemann and U. R. Pfeiffer, "A wideband fully integrated SiGe chipset for high data rate communication at 240 GHz," *2016 11th European Microwave Integrated Circuits Conference (EuMIC)*, London, 2016, pp. 181-184.
 17. **P. Rodríguez-Vázquez**, N. Sarmah, K. Aufinger, and U. R. Pfeiffer, "An OOK-modulator at 240 GHz with 20 GHz bandwidth," *2016 German Microwave Conference (GeMiC)*, Bochum, 2016, pp. 345-348.

Book Chapters

1. S. Malz, **P. Rodríguez-Vázquez**, J. Grzyb, and U. Pfeiffer, "Real100G.RF: A Fully Integrated, Multi-Purpose Radio Front-End for Wireless 100 Gbps", in *Wireless 100 Gbps and Beyond*, R. Kraemer, S. Scholz, Ed. Gistrup, Germany: IHP Publisher Service, 2020, ch. 9, pp. 295–358.

Contributions of Others

This work would clearly not have been possible without the contributions from group members and project partners. Most of the circuit blocks utilized in this work were designed by group members of the Institute for High-Frequency and Communication Technology (IHCT) at the University of Wuppertal, led by Prof. Dr. rer. nat. Ullrich R. Pfeiffer. The central part of this work, addressing the analysis of RF front-end for beyond 200 GHz/6G wireless communications was funded by the German Research Foundation within the Priority Program SPP 655/0 - Wireless Ultra High Data Rate Communication for Mobile Internet Access "Wireless 100 Gb/s and beyond" and under the EU 316755 DOTSEVEN: "Towards 0.7 Terahertz Silicon Germanium Heterojunction Bipolar Technology" projects. All contributions are detailed below.

Chapter 1 introduces the motivation and the scientific context of this thesis. It presents the current state of mobile wireless networks and provides an estimation on the data-rates that the future 6G wireless networks will support. It also presents the frequency bands beyond 200 GHz, where 6G is expected to operate. Finally, it presents a State-of-the-Art review for fully-electronic wireless communication links operating at frequencies beyond 200 GHz.

Chapter 2 gives a short theoretical introduction. It explains the concept of digital modulations and its basic performance metrics, relating them with the typical wireless transceiver figures of merit. It also provides an estimation on how a wireless communication link at frequencies beyond 200 GHz will operate.

Chapter 3 presents the first generation of RF front-ends for frequencies beyond 200 GHz. The active circuits composing the Tx and the Rx front-end were designed by Neelanjan Sarmah, while the 90° hybrid and the antenna were developed by Janusz Grzyb. I arranged both Tx and Rx top-level layout, designed the PCB, and constructed the RF measurement set-up. I also developed the wireless communication link set-up, performed the wireless link measurements, analyzed the data, and develop the theory for estimating the impact of the different error sources in the wireless link performance for frequencies beyond 200 GHz.

Chapter 4 presents the mixer-first Rx. I designed the mixer, arranged the top level layout, performed the system level simulations, measured the RF performance, characterized the wireless communication link, and analyzed the resulting EVM.

Chapter 5 presents a Tx and a Rx whose I and Q channels are separated by polarization. I developed the architectural concept to answer the question whether the IQ cross-talk is the main limiting factor for the wireless communication link in terms of achievable data-rate. The circuits that are included in these RF front-end modules were developed by Stefan Malz, who also did the top-level layout and Tx and Rx simulations. The PCB baseband filter was designed by Marcel André . The dual-polarization antenna was designed by Janusz Grzyb. I performed the RF and wireless communication measurements and analyzed the EVM.

Chapter 6 presents a MIMO wireless communication link operating at frequencies beyond 200 GHz. Based on the existing building blocks that were previously designed, I developed the conceptual idea and arranged the top-level layout. Furthermore, I performed all RF simulations and measurements required to fully understand the system, including the wireless communication link measurements and EVM analysis.

Part I.
Context

Chapter 1

Introduction

This chapter introduces the motivation and the scientific context of this thesis. It is organized as follows. Section 1.1 introduces the current deployment status of the fifth-generation (5G) of mobile networks and its limitations, as well as the steps that have been recently taken to define the future sixth-generation (6G) of mobile communication networks. Section 1.2 introduces briefly the high mmWave and THz frequency bands, including a review of the most common applications and the technology advancements that enabled wireless communication links at these bands. Section 1.3 presents the state of the art (SoA) for wireless communication links operating at frequencies beyond 200 GHz. Section 1.4 presents the main research question that this work aims to answer, and Section 1.5 provides an outline for the rest of the thesis.

1.1. Current status of mobile communication networks

While the 5G of mobile communication systems are being deployed, it becomes clear that this technology will not be enough to meet all society's wireless connectivity demands in the near- to mid-term future. Cisco forecasted the global mobile data traffic to seven-fold from 2017 to 77.5 EB/month by 2022 with 28.5 B networked devices [1]. Yole estimates that 5G phones will exhibit 72 % compound annual growth rate between 2019 and 2025 and represent 29 % of the phone market [2], indicating that the data traffic that the future mobile communication networks need to support will grow exponentially. This aligns well with the historical data, which shows an expansion of wireless data capacity of about a factor of 10 per decade, as shown in Fig. 1.1 [3]. In ten years, with links supporting data-rates of 100 Gb/s [4], 5G will not offer enough capacity to attend the demand. The future

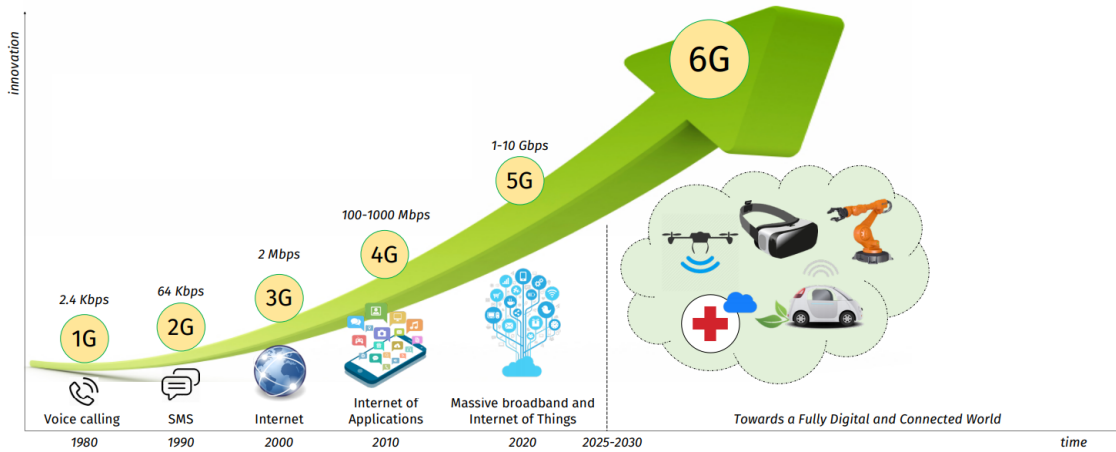


Figure 1.1.: Evolution of the capacity of the wireless networks. Modified after [own1] © 2020 IEEE.

6G of mobile communication systems will have to operate with data-rates of 100 Gb/s. However, these data-rates are challenging to achieve, if not impossible, with the bandwidth available in the congested spectrum under 100 GHz. To sustain this ever-increasing need for capacity, the new 6G mobile communication networks will have to operate at higher spectral bands.

This band migration is a gradual process that has already started. Currently, 5G networks are defined to operate at sub-6 GHz and from 24.25 to 52.6 GHz, with the 57-71 GHz band also reserved for this use. The inclusion of bands up to 114 GHz is currently under study [5]. There are also bands between 95 GHz and 3 THz recently opened by the Federal Communications Commission (FCC) for practical use to support higher bands [6], although it is not clear if they will be employed in 5G or 6G. The future 6G wireless communications will require enhancements over the current 5G spectrum and expand the spectrum into potential new bands, addressing the high mmWave and THz regions. These potential spectrum regions are illustrated in Fig. 1.2. Higher frequency bands allow for wider bandwidths. Wider bandwidths support high data-rates.

In Europe, the wireless industry addressed this need by targeting the high mmWave and THz band to implement future 6G mobile communication networks, as announced during the first and second 6G wireless summit held at the Levi resort in Finnish Lapland [7]. In the US, a center for Converged THz Communication has been established in the University of California under a DARPA project [8].

The future 6G networks will implement extreme capacity backhaul, enhanced hotspots, and ultra-fast device-to-device communication [4] to enable novel applications. Some of these use-cases are in line with the use-cases established on the new IEEE 802.15.3d-

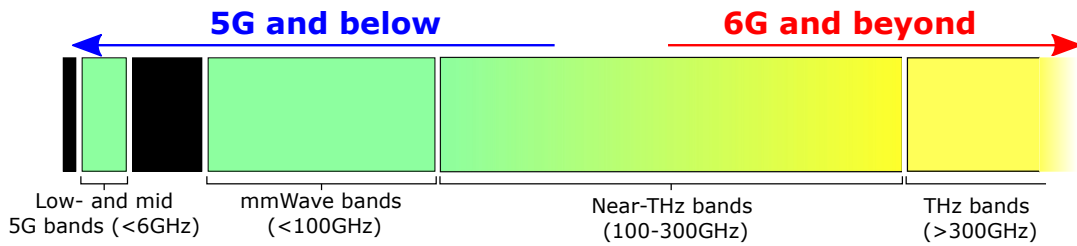


Figure 1.2.: Potential spectrum regions for 6G.

2017 standard. This standard assigns the 252-322 GHz band for point-to-point wireless communication [9]. Some key prospects and applications of 6G wireless communications are described briefly below.

- **Super-smart society.** The 6G wireless connectivity will increase the integration level of our societies. Smart mobile devices, autonomous vehicles, robots, and other devices will create a network managed with artificial intelligence (AI), improving the quality of life in cities and towns [10].
- **Extended reality.** Extended reality (XR) services include augmented reality (AR), mixed reality (MR), and virtual reality (VR). With VR requiring data-rates of +10 Gb/s [11], it is clear that 5G will not support sufficiently high data-rates to ensure its proper deployment. All these features use 3D objects and AI as their key driving elements. Thanks to the high data-rates supported, the low link latency, and the high reliability of the wireless links that 6G will enable and bring together AR, MR, and VR to offer a genuine XR experience [12].
- **Connected robotics and autonomous systems.** 6G systems will help in the deployment of connected robots and autonomous systems. Not only autonomous cars will benefit from higher data-rates. For example, a drone-delivery system based on crewless aerial vehicles (UAV) will require enormous data acquisition from the environment to ensure a safe drive. Moreover, these UAVs can be used as a mobile wireless broadcast hot-spot in areas where cellular base stations cannot be deployed [13].
- **Brain-computer interactions.** The brain-computer interface (BCI) is an approach to control devices through a direct communication path with the brain. This technology is expected to be used in medical processes and as an interface with smart homes [14], [15]. Some private companies, like Neuralink have already started with the development of this interface technology [16].
- **Smart healthcare.** Innovations such as the BCI or the XR will build the proper frame to deploy a smart health care system. A high-data-rate, low latency, and

ultra-reliable 6G network will help quickly and reliably transport huge volumes of medical data from a sensor placed in the body to a medical center, improving both the access and the quality of the care [10].

- **Internet of Everything (IoE)**. IoE is the natural evolution of the current internet of things (IoT). IoE will integrate data, people, processes, and physical devices in one single frame [17]. The future 6G wireless networks will provide IoE support for a very large number of nodes [18].

All these applications require that, in ten years, the technology to support the future 6G wireless communication links must be ready to be deployed.

1.2. The high mm-Wave and THz bands

The THz frequency bands represent the frequency range that lies between the millimeter-wave and the infrared regions, defined from 0.3–3 THz [19]. The frequencies between 100 and 300 GHz are typically called the high mmWave bands. Although these frequencies present unique characteristics for sensing and communication applications, the current status of THz technology for generating, detecting, and analyzing THz radiation is not as advanced as for low mm-Wave electronics or infrared photonics, creating the so-called "Terahertz gap" [20].

THz technology has been employed in the past in various applications due to its unique characteristics. THz radiation penetrates many non-conducting materials, such as paper or clothes, and can achieve higher image resolution than its mm-Wave counterpart [21] thanks to its reduced wavelength. Although in the past THz radiation was almost exclusively used for spectroscopic purposes in the scientific community [22], with the beginning of the new century, the use of THz technology became common in multiple other fields, such as biology [23], chemistry [24], medicine [25], pharma-industry [26], industrial quality and process control [27], security screening [28], radar [29], and many more. However, during the first decade of the 21st century, very few advancements were made in the field of communications.

1.2.1. Technologies for high mm-Wave and THz communications

High output power sources for frequencies beyond 200 GHz were bulky, expensive, and presented a very low integration level. The most common technologies used at these

frequencies were backward-wave oscillators [30] or quantum cascaded lasers [31]. In communications, high-power sources are required both in the Tx and in the Rx to ensure proper drive of the mixers that up-convert and down-convert the signal that carries the information [own2] and to overcome the high propagation loss at these high frequencies. However, these technologies set very stringent mechanical and cooling constraints, making them unfeasible for wireless communication applications.

In the past, the market for mobile communication technologies has been dominated by semiconductor technologies. Due to its high reliability, low cost, and high integration level, it is almost impossible to think that the future 6G systems will employ any other technology for their implementation unless there is a new device breakthrough. In recent years, advancements in process technology have improved the performance of semiconductor devices, enabling their operation at higher frequencies. The highest performance has been achieved in III-V technology, where the first amplifier operating at 1 THz was demonstrated in 2015 [32]. However, III-V technologies exhibit a low integration level, which results in increased module assembly costs. Implementation of circuits in low-cost silicon-based technologies offers the advantage that all necessary system components can be realized on the same chip. The ultra-complex CMOS baseband of modern modems can be developed on a single chip of a few square millimeters [33]. Additionally, CMOS and BiCMOS process technologies provide industry standards of repeatability and reliability at a high yield, which is not the case for III-V. With a cut-off frequency (f_{\max}) approaching 700 GHz [34], silicon-germanium (SiGe) has demonstrated power generation on the level of few milliwatts for frequencies beyond 200 GHz [own3], high enough to support wireless communication links at distances of few meters.

1.3. SoA of fully-electronic wireless communication links for frequencies beyond 200 GHz

The recent improvements in semiconductor process technology allowed the development of multiple wireless communication links operating beyond 200 GHz. Solutions based on RF front-ends fabricated in III-V technology lead the path. In [35], a 120 Gb/s wireless link was established, achieving a maximum distance of 4-meters. In [36], a data-rate of 96 Gb/s was reported over a distance of 40-meters. Although these two publications show impressive performance, the links were established using expensive wave-guide assemblies, and the distance was achieved employing horn-antennas and external lenses to focus the radiated power. This resulted in bulky transmitters (Tx) and receivers (Rx) which can not be integrated into a smartphone, although they might be useful for back-haul imple-

mentations. With a maximum data-rate of 110 Gb/s over 1-meter distance and 80 Gb/s over 2-meter distance [own4]–[own9], [37]–[40], comparable results have been achieved with SiGe-based wireless communication links. With the same off-package optics, the link distance would be comparable to the one achieved with III-V. Additionally, the higher integration capabilities of SiGe-HBT, where the complete RF front-end can be packaged within a single module and co-integrated with the baseband (BB) signal processing circuitry, as well as lower fabrication cost, positions SiGe-HBT as a more attractive solution for the mass-production mobile communications market [41]. Although CMOS solutions would be the preferred option for mass-fabrication due to its lower cost per unit, the reduced frequency performance of these transistors [42], [43] limits the data-rate to a few tens of Gb/s and the link distance to a few centimeters, even if external high-gain horn antennas are employed [44]–[46].

1.3.1. Limitations of the SoA

The main reason to move the wireless communication channel towards frequencies beyond 200 GHz is to achieve higher data-rates in the link. Higher carrier frequencies offer broad bandwidths, and these bandwidths can be directly related to the data-rate that the communication channel can support. According to the Shannon capacity theorem [47], the channel capacity can be related to the averaged received signal power, the average noise power, and the bandwidth as

$$C = BW \cdot \log_2(1 + SNR), \quad (1.1)$$

with C being the channel capacity in bits/s, SNR the signal-to-noise ratio, and BW the bandwidth. Assuming that the SNR is constant, the channel capacity increases linearly with the available bandwidth. It could be assumed that by moving the communication channel towards the frequency band beyond 200 GHz, an increase in the wireless communication link data-rate would be trivial to achieve. However, this hypothesis presents two limitations:

1. It assumes that the SNR will stay constant after migrating into a higher frequency band, which is not the case. Free-space propagation losses are higher than at lower carrier frequencies, and power generation is more challenging, decreasing the SNR and channel capacity. As mentioned before, semiconductor technology is the critical enabler. Advanced technologies and novel circuit designs allow for higher gain and output power, increasing the SNR and the channel capacity.

2. The Shannon theorem does not consider any system impairment apart from arbitrary white gaussian noise (AWGN). Second-order effects, such as phase noise and amplitude imbalance [48] are not included in Eq. 1.1. These impairments will reduce the channel capacity beyond the Shannon limit. The characterization of such impairments and the system analysis of its influence on the wireless link quality is essential to understand how to design the future 6G radio TxS and RxS.

The first point was thoroughly investigated in [49], [50]. The state of the art presented in the previous section also focuses mainly on improving the Tx and the Rx specifications directly related to the SNR. In the previous publications, novel design techniques were presented to maximize the Tx output power and minimize the Rx noise figure. However, little work has been put into understanding the major limitations of wireless links operating at frequencies beyond 200 GHz. With respect to the Tx and Rx specifications, all the publications mentioned above perform below the Shannon limit, without exception. However, no analysis can be found in the literature addressing this issue. Even up to now, most of the publications focus on increasing the Tx output power even more or minimizing the noise figure, leading to minor improvements in the data-rate, if any. This thesis tries to fill this gap, aiming to determine the key limitations that the future 6G radio transceivers will face. To this end, four sets of RF front-ends were developed and tested. These RF front-ends enabled the first 100 Gb/s wireless link operating beyond 200 GHz [own7]. Comparing the measured link performance with the estimated link capacity for a certain SNR, it turned out that the measured results are significantly lower than the Shannon limit. After a detailed analysis of the RF front-end, it was discovered that this performance difference was due to a set of system impairments, such as phase noise, in-band spurs, and IQ cross-talk. This thesis provides a set of measurement techniques for characterizing these impairments and a mathematical model to estimate its influence on the final wireless link performance. Furthermore, to overcome the limitations that these impairments set to the wireless communication link, this thesis introduces a novel approach to enhance data-rate, presenting the first multiple-inputs multiple-outputs (MIMO) system operating beyond 200 GHz with an aggregated data-rate of 110 Gb/s [own9].

1.4. Central Research Question and Contributions

The research questions that are sought to be answered in this thesis are listed below. The related original contributions of this work are also given.

Central Research Question

Which system design considerations need to be addressed to develop RF front-ends for the future 6G wireless links?

Previous research on RF front-ends operating beyond 200 GHz across different technologies has been mostly focused on improving circuit specifications, such as output power (P_{out}), conversion gain (CG), and noise figure (NF). Little work has been done in understanding which of the system parameters is the limiting factor for the data-rate or distance in such links, particularly when the link operates below the Shannon limit. This work aims to provide an understanding of these limitations and to design RF front-ends capable of overcoming them. In this context, the following research sub-questions arise:

- What are the main advantages and disadvantages of wireless communication systems operating at frequencies beyond 200 GHz?
- Are wireless links at frequencies beyond 200 GHz limited by the classical link-budget SNR calculation set by Shannon's theorem?
- Which are the principal impairments that limit the link data-rate at frequencies beyond 200 GHz?
- Are different modulation-techniques affected equally by the same impairment? Or does its influence depend on the modulation order?
- How to correct/minimize these impairments? Can we address these limitations at the circuit-design level to enhance the link data-rate?
- How is the maximum link distance affected by these impairments?
- Traditionally, broader bandwidths and/or higher modulation orders are required to increase the link data-rate. Even if such improvements are not possible, by what means can the data-rate be further enhanced? Is it possible to use channel aggregation in a multiple-inputs multiple-outputs (MIMO) configuration to enhance the link data-throughput beyond its limits?

Original Contribution

This thesis presents the world-wide-first 100 Gb/s wireless link operating at frequencies beyond 200 GHz, established with a fully-package silicon-based RF front-end set. It details the design of a maximum bandwidth receiver used for this link. The thesis provides the guidelines and major challenges to consider when designing an RF front-end for wireless communications beyond 200 GHz. It analyses the influence of the different system impairments in the wireless communication link, providing a specific test-bed where the different errors can be studied independently. It also presents the first polarization MIMO wireless communication link operating at frequencies beyond 200 GHz, achieving an aggregated data-rate of 110 Gb/s.

1.5. Thesis Structure

This thesis is divided into three major parts, comprising a total of seven chapters. The organization is as follows:

Part I: Context. Part I, including Chapter 1 and Chapter 2, gives the motivation and the scientific context for this thesis. Chapter 2 provides a theoretical background in wireless communications.

Part II: RF front-ends for wireless communications. Part II addresses the central research question and is the core of this thesis. Based on the previous RF front-end chipsets designed at the IHCT, Chapter 3 analyses the RF front-end impairments that set the wireless link's data-rate below the limit defined by Shannon's theorem, establishing a hypothesis on the influence of each of the system impairments. A new Rx RF front-end with maximized RF bandwidth is presented in Chapter 4 to enhance the link data-rate. A new test-bed, consisting of a new Tx and a new Rx RF front-end, developed to isolate the wireless link's impairments, is presented in Chapter 5 to validate the hypothesis presented before. Finally, Chapter 6 introduces an alternative way to overcome this limitation by channel aggregation in a MIMO configuration.

Part III: Conclusion. This part summarizes the thesis and gives suggestions for future research.

Chapter 2

Digital Communications

As it was stated by R. Gallager in [51] "Communication has been one of the deepest needs of the human race throughout history. It is essential to form social unions, educate the young, and express a myriad of emotions and needs. Reliable communication is central to a civilized society. From smoke signals and drum rolls of primitive societies to our technology-advanced optical fiber and mobile wireless networks, communications have always been a medium of progress by sharing ideas and experiences".

The first steps into wireless electronic communications were taken by Guglielmo Marconi at the beginning of the 20th century when he performed the first transatlantic radio transmission [52]. Here, an analog signal (voice) was directly modulated on top of the radio local oscillator (LO) frequency. These first analog communications could only transmit a minor fraction of the information that modern digital communications support [53]. Here, the Morse code could be considered as the first step in the direction of digital communications [54]. However, the scientific community agrees that the pioneering work in digital communications was the development of the Information Theory by Claude Shannon in 1949 [47]. Without his contribution, the information age where we currently live would not be possible.

This chapter presents the theory behind digital communications as well as a technique to evaluate the link quality depending on the specifications of the Tx and the Rx that compose the link. The chapter is organized as follows: Section 2.1 presents an introduction to the digital communication theory as well as two of the most common modulation techniques applied, starting with the pulse amplitude modulation (PAM) and continuing with the quadrature amplitude modulation (QAM). The content presented in this section is based

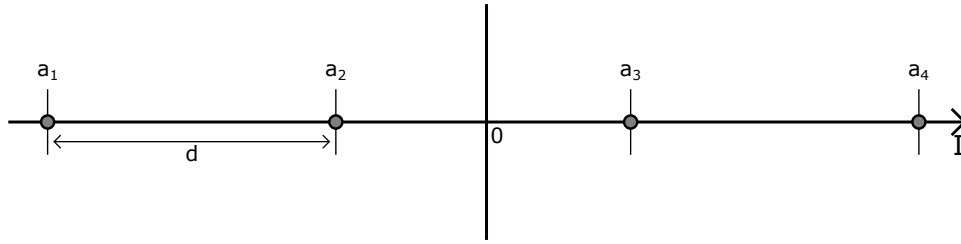


Figure 2.1.: A PAM-4 constellation diagram.

on the theory presented in [51]. Section 2.2 presents a set of metrics and equations used to evaluate the quality of a digital communication link established using a QAM modulation format.

2.1. Introduction to Digital Communications

Digital modulation is the process of converting an input sequence of bits into a waveform suitable for transmission over a communication channel, while digital demodulation is its inverse. From all digital modulations, the most simple to understand is the PAM. Here, the incoming bits are segmented in b -bit blocks. Each of these segments are mapped to a set of $M = 2^b$ possible blocks into a signal constellation $A = \{a_1, a_2, \dots, a_M\}$ of real numbers. Assuming that the incoming bit-rate is R , the symbol-rate for the sequence of b -bit blocks would be $R_s = R/b$. This sequence corresponds to a M -ary signal (u_1, u_2, \dots) . A waveform $u(t)$ maps the sequence of signals by the use of time shifts of a basic pulse waveform $p(t)$ as

$$u(t) = \sum_k u_k \cdot p\left(t - \frac{k}{R_s}\right). \quad (2.1)$$

When $b = 1$, this modulation technique is called binary PAM, while for $b > 1$, this modulation is normally referred to as PAM- M . The constellation A of a standard PAM- M signal consists of $M = 2^b$ real numbers and can be defined as a set of d -spaced points that are the representation of a symmetric-uniform scalar array of M point

$$A = \left(\frac{-d(M-1)}{2}, \dots, \frac{-d}{2}, \frac{d}{2}, \dots, \frac{d(M-1)}{2} \right). \quad (2.2)$$

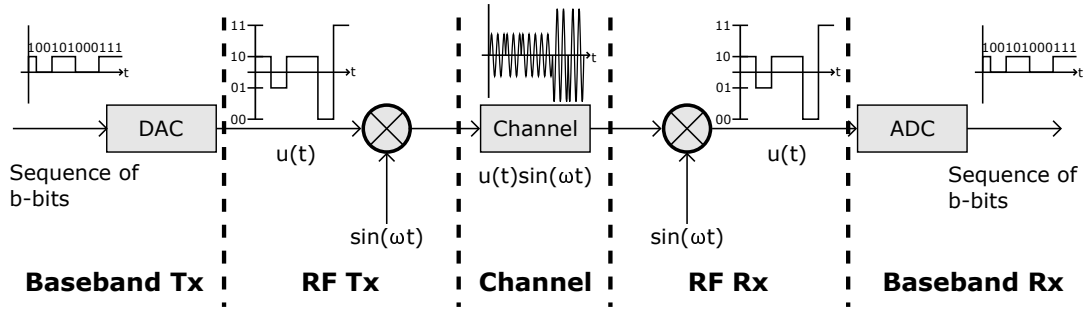


Figure 2.2.: Block diagram of a PAM-4 communication link. In the baseband Tx, the digital signal, a sequence of bits, is converted into a M -ary $u(t)$ analog signal, which is up-converted in the RF Tx. After the channel, the RF Rx down-converts the signal back into a M -ary $u(t)$. This signal is then digitized in the baseband Rx to recover the bit sequence.

An exemplary PAM-4 constellation diagram is shown in Fig. 2.1. A set of elements is required to realize a wireless communication system that implements this digital modulation technique. A digital-to-analog converted (DAC) converts the bit sequence into a multilevel waveform $u(t)$ on the Tx side. Afterward, an up-conversion stage allocates the signal in the RF channel, and then the signal is radiated. The signal is down-converted on the Rx side. An analog-to-digital (ADC) converter digitizes the down-converted $u(t)$ multilevel waveform into the bit sequence. A system representation of this concept for a PAM-4 signal is depicted in Fig. 2.2.

The objective of up-converting the baseband (BB) PAM-4 waveform $u(t)$ to a passband around a LO frequency f_c is to allocate the signal into the correct RF channel [51]. In order to better understand this concept, the signals need to be analyzed in the frequency domain through the Fourier Transformation (FT). The FT of the signal $u(t)$ is $\hat{u}(f)$, which is defined in the frequency-domain. This baseband signal is zero except for the interval $-BW_{bb} < f < BW_{bb}$, with BW_{bb} being the baseband signal bandwidth (BW), which is proportional to the symbol-rate R_s . After FT, the LO-signal $\sin(\omega_c t)$ is transformed into two delta functions $-\delta(f - f_c) + \delta(f + f_c)$. The multiplication in the time-domain corresponds to a convolution in the frequency-domain. Therefore, the transmitted signal can be described in the frequency domain as $\hat{x}(f) = \hat{u}(f - f_c) + \hat{u}(f + f_c)$. The down-conversion process is analog, but the signal allocated at twice the LO frequency is filtered out at the mixer's output. Fig. 2.3 illustrates the process in the frequency-domain.

In communications, the system bandwidth is defined as the range of positive frequencies used in the transmission. All transmitted waveforms must be real. The negative frequency part is a mathematical redundancy that always shows a perfect symmetry with the positive part. As can be observed, the bandwidth requirements in the passband have been

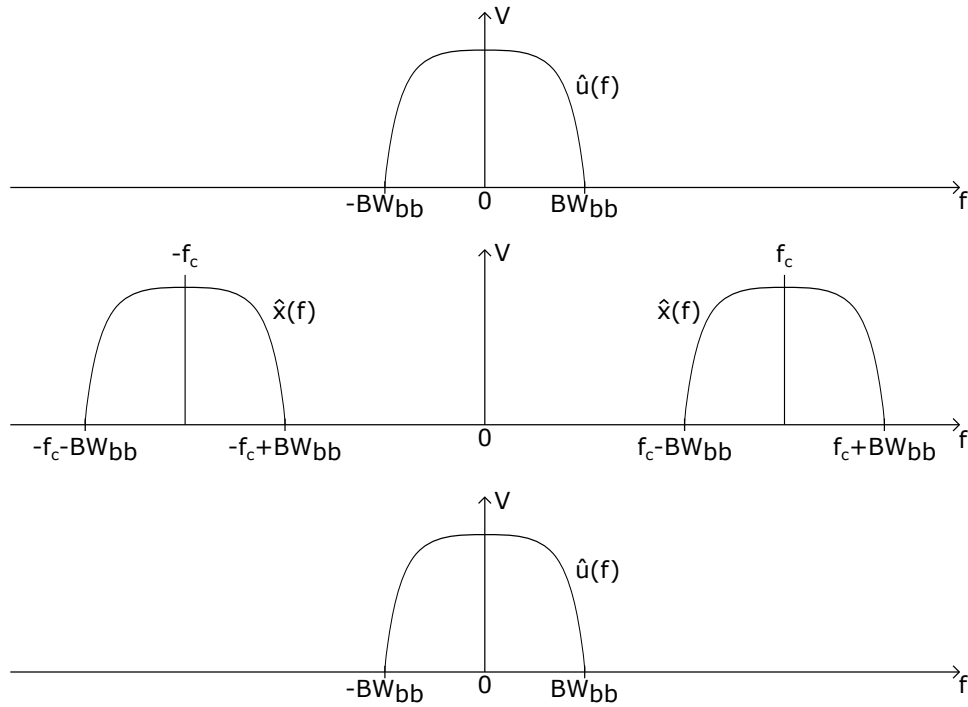


Figure 2.3.: Frequency domain representation of a baseband waveform $u(t)$ shifted up to a passband around the LO f_c . Note that the baseband bandwidth BW_{bb} of $u(t)$ has been doubled after up-converting to the bandpass. The signal is then converted again to the baseband. The signals allocated at twice the LO frequency and the scalars have been removed for simplicity.

doubled without adding new information. The upper-sideband USB ($[f_c, f_c + BW_{BB}]$) and the lower-sideband LSB ($[f_c, f_c - BW_{BB}]$) are symmetric. That is to say, that the same information is transmitted in two bands simultaneously, wasting bandwidth since half of the transmitted band is redundant. The most widely used technique to employ this wasted bandwidth is the quadrature amplitude modulation (QAM). QAM could be easily understood as two PAM signals $u(t)$ and $u'(t)$ transmitted in parallel exploiting the inherent orthogonality of the function sine and cosine. In the time domain, it is possible to define the transmitted signal $x(t)$ as

$$x(t) = u(t) \cdot \sin(\omega_c t) + u'(t) \cdot \cos(\omega_c t). \quad (2.3)$$

The input bit sequence shows a rate of R bits per second. Then sets of b bits are converted into a real 2-tuple $(a'$ and $a'') \in \mathbb{R}^2$. A standard (M) -QAM signal set where $M = (M')^2$ is the Cartesian product of two PAM- M' signals and can be defined in the complex plane as

$$A = \{(a' + ia'') | a' \in A', a'' \in A'\}, \quad (2.4)$$

with A' defined as

$$A' = \left(\frac{-d(M' - 1)}{2}, \dots, \frac{-d}{2}, \frac{d}{2}, \dots, \frac{d(M' - 1)}{2} \right). \quad (2.5)$$

The constellation diagram of A consists of a square array of $M = (M')^2 = 2^b$ points located symmetrically around the origin. As an example, the constellation diagram of a 16-QAM modulation is presented in Fig. 2.4.

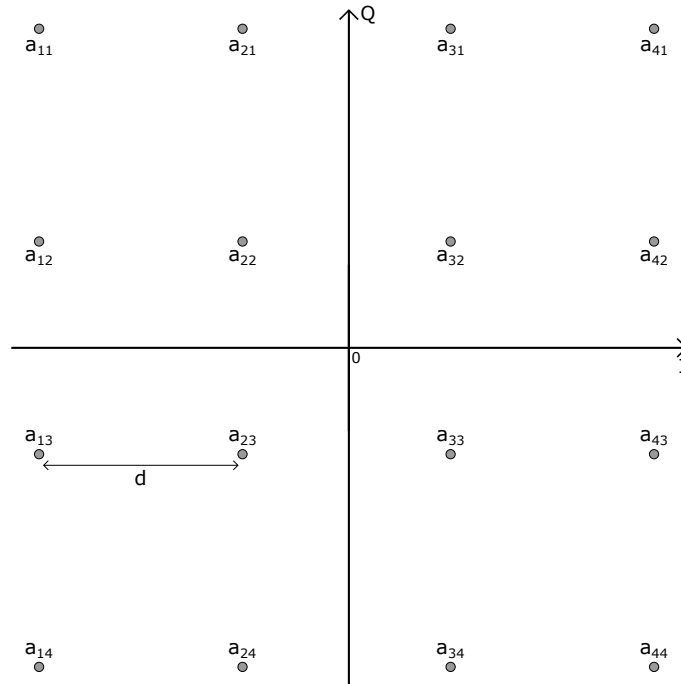


Figure 2.4.: 16-QAM constellation diagram.

Similarly to the PAM-4 case, the block-level representation of a 16-QAM communication system is presented in Fig. 2.5. Here, the baseband Tx converts a b -sequence of bits into two analog waveforms $u(t)$ and $u'(t)$. Each of these signals is then up-converted with sine and cosine signals, respectively. Both up-converted signals are added and sent through the channel. In the receiver, each down-conversion mixer receives a signal containing the full transmitted signal $u(t) \cdot \sin(\omega_c) + u'(t) \cdot \cos(\omega_c)$. Thanks to the inherent orthogonality

between sine and cosine functions, the RF Rx separates in the down-conversion process the two signals back into the M -ary signals $u(t)$ and $u'(t)$. These signals are then digitized in the baseband Rx to recover the original bit sequence.

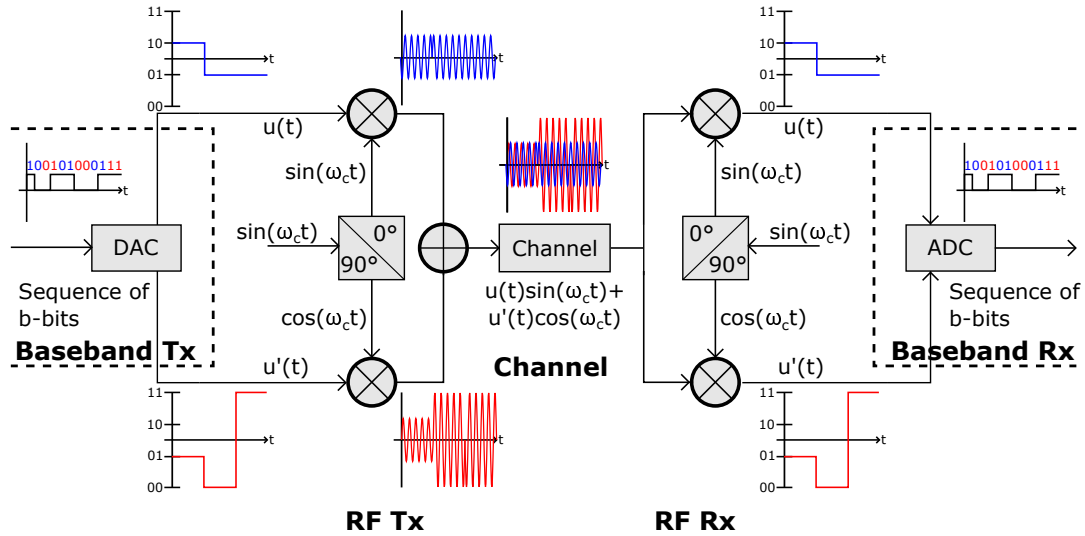


Figure 2.5.: Block diagram of a 16-QAM communication link. In the baseband Tx, the digital signal is converted into a set of two M -ary $u(t)$ analog signals $u(t)$ and $u'(t)$. These two analog signals are up-converted in the RF Tx. Both signals are added together and transmitted through the channel. Thanks to the inherent orthogonality between sine and cosine functions, the RF Rx separates in the down-conversion process the two signals back into M -ary signals $u(t)$ and $u'(t)$. These signals are then digitized in the baseband Rx to recover the original bit sequence.

The 90° phase difference between the two carrier frequencies creates the orthogonality between the sine and the cosine signals. This thesis identifies carrier frequency and local oscillator (LO) as the same terms. Therefore, the two nominations will be used indistinctly. The QAM technique effectively doubles the transmitted data-rate using the same bandwidth. The M^2 -QAM technique doubles the spectral efficiency (defined as bits/Hertz) of a PAM- M signal. The spectral analysis that was applied to the PAM is also valid for the QAM. It can be assumed that both signals $u(t)$ and $u'(t)$ have the following Fourier transform

$$\begin{aligned} u(t) &\xrightarrow{\mathfrak{F}} \hat{u}(f), \\ u'(t) &\xrightarrow{\mathfrak{F}} \hat{u}'(f). \end{aligned} \quad (2.6)$$

In the same way, the frequency-domain representation of the sine and the cosine signal are delta functions

$$\begin{aligned} \sin(\omega_c t) &\xrightarrow{\mathfrak{F}} i \cdot \frac{-\delta(f - f_c) + \delta(f + f_c)}{2}, \\ \cos(\omega_c t) &\xrightarrow{\mathfrak{F}} \frac{\delta(f - f_c) + \delta(f + f_c)}{2}. \end{aligned} \quad (2.7)$$

With Eq. 2.6 and 2.7, the transmitted signal can be defined as

$$\hat{x}(f) = \frac{-i \cdot \hat{u}(f - f_c) + \hat{u}'(f - f_c) + i \cdot \hat{u}(f + f_c) + \hat{u}'(f + f_c)}{2}. \quad (2.8)$$

When this signal arrives at the Rx is down-converted in the mixers. The mixer driven by a sine will be called in-phase component (I), while the mixer driven by a cosine quadrature component (Q). The outputs of the I and the Q mixers are defined as

$$\hat{I}(f) = \hat{x}(f) \otimes i \cdot \frac{(-\delta(f - f_c) + \delta(f + f_c))}{2}. \quad (2.9)$$

The mixer output filters out the components allocated at two times the LO frequency ($2f_c$), and $\hat{u}'(f)$ is canceled out, thus it only remains

$$\hat{I}(f) = \hat{u}(f), \quad (2.10)$$

By analogy, the Q channel output can be defined as

$$\hat{Q}(f) = \hat{u}'(f). \quad (2.11)$$

Fig. 2.6 illustrates the process described above. By applying this technique, two different channels are transmitted using the same bandwidth as was previously employed for PAM.

This analysis raises questions about the limits of this technique and the maximum achievable data-rate that can be obtained. The bandwidth available for wireless communication is determined by regulatory agencies such as FCC or similar, depending on the country. However, according to what has been explained in this section, the data-rate can be

increased theoretically to infinite by increasing M . Unfortunately, this is not possible. Errors in the channel will determine which is the maximum M for a given link. Here, two concepts need to be introduced to evaluate these errors: the bit error rate (BER) and the error vector magnitude (EVM).

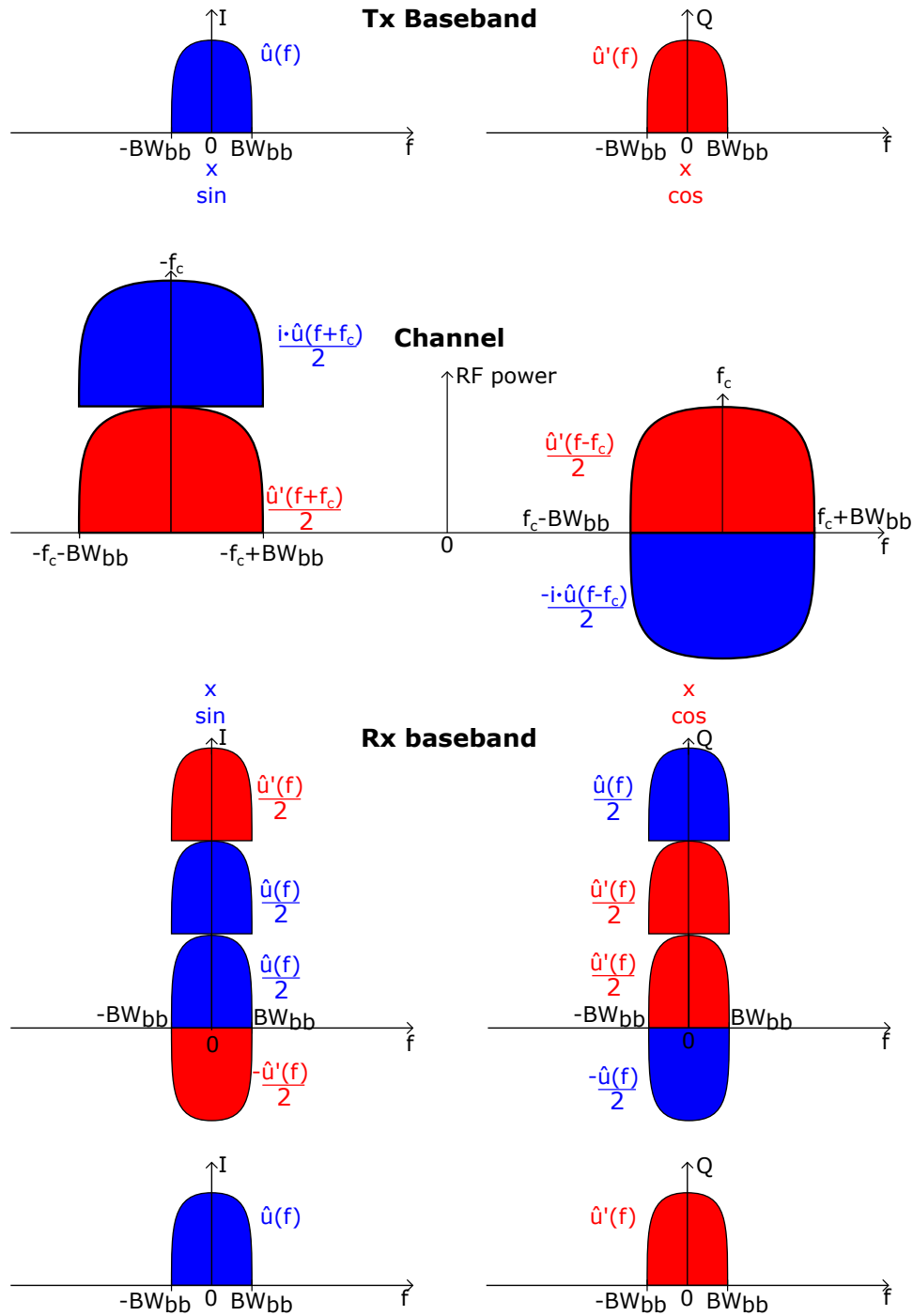


Figure 2.6.: Frequency domain representation of a baseband waveform $u(t)$ and $u(t)'$ shifted up to a passband around the LO f_c using the QAM technique. The signal is then converted to the baseband, where the phase orthogonality of the I and Q signals is used to separate $u(t)$ and $u(t)'$ again. The imaginary factor i and the signals allocated at twice the LO frequency have been removed for simplicity.

2.2. Bit Error Rate, Error Vector Magnitude, and Signal to Noise Ratio

The quality of any communication link is typically measured as the proportion of erroneous bits that are transmitted. This metric is called BER and can be defined as:

$$BER = \frac{\text{Number of erroneous bits}}{\text{Number of transmitted bits}} \quad (2.12)$$

First, the question of the maximum tolerable BER must be answered. According to [55], the maximum BER that can be corrected by applying forward error correction (FEC) codes is 4.5×10^{-3} . Hence, this value denotes the operating threshold, as considered in the course of this work. However, to calculate the BER, the erroneous bits need to be known. In reality, this means that the transmitted bit sequence has to be known at the receiver output beforehand, which might not always be possible. Therefore, the BER cannot always be measured properly. Another parameter has to be employed for the link characterization. This parameter must work in all circumstances and present a clear relation to the BER. The EVM matches all these requisites.

2.2.1. EVM/BER relation

The EVM analysis is based on the constellation diagrams. Any received symbol will be placed in a different position of the I-Q plane. Hence, an error-vector can be defined as the vector between the ideal constellation point and the received symbol's point. The EVM can be defined as the root mean square (RMS) of the error vector, normalized to the ideal signal amplitude reference. This is illustrated in Fig. 2.7. The notation used here follows the one presented in [56]. Here, the dotted lines represent the decision boundaries for each received symbol. Each symbol's energy can be measured as the magnitude of the vector that connects them with the origin. Here, $E_{t,m}$ is the highest energy vector possible in the constellation, $E_{t,i}$ is the vector of a single ideal point, $E_{r,i}$ and $E'_{r,i}$ are the vector of the actually received symbols \hat{a}_{33} and \hat{a}'_{33} and $E_{err,i}$ is the error vector. The symbol \hat{a}_{33} lies in the decision area of a_{33} , which means it will be demodulated without giving an error. On the contrary, \hat{a}'_{33} will be demodulated as a_{23} , producing an erroneous detection. By performing the same analysis over a collection I of symbols, the root-mean-square deviation of the error vector σ_{error} can be calculated as

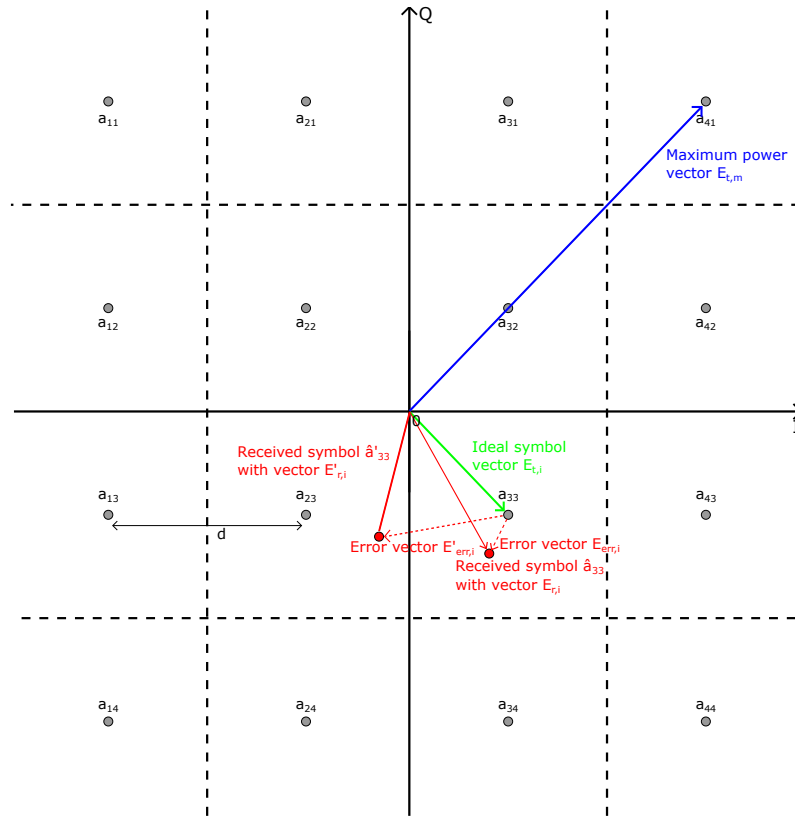


Figure 2.7.: 16-QAM constellation diagram. The decision boundaries are limited by the dotted lines. $E_{t,m}$ is the highest energy vector possible in the constellation. $E_{t,i}$ is the vector of a single ideal point, $E_{r,i}$ and $E'_{r,i}$ are the vector of the actually received symbols \hat{a}_{33} and \hat{a}'_{33} and $E_{err,i}$ is the error vector. The symbol \hat{a}_{33} lies in the decision area of a_{33} , which means it will be demodulated without giving an error. Contrary \hat{a}'_{33} will be demodulated as a_{23} , producing an erroneous detection.

$$\sigma_{error} = \frac{1}{I} \sum_{i=1}^I |E_{err,i}|^2 \quad \text{with } E_{err,i} = E_{r,i} - E_{t,i}. \quad (2.13)$$

Although the literature presents different definitions for the EVM [48], all further work presented in this thesis is referred to the average power of all symbol-vectors M presented in the constellation; therefore, only this definition will be presented here

$$EVM_{rms} = \frac{\sigma_{error}}{|E_{t,a}|} \quad \text{with } |E_{t,a}| = \sqrt{\frac{1}{M} \sum_{i=1}^M |E_{t,i}|^2}. \quad (2.14)$$

The EMV_{rms} will be referred to as EVM in the rest of this thesis. For a M -QAM

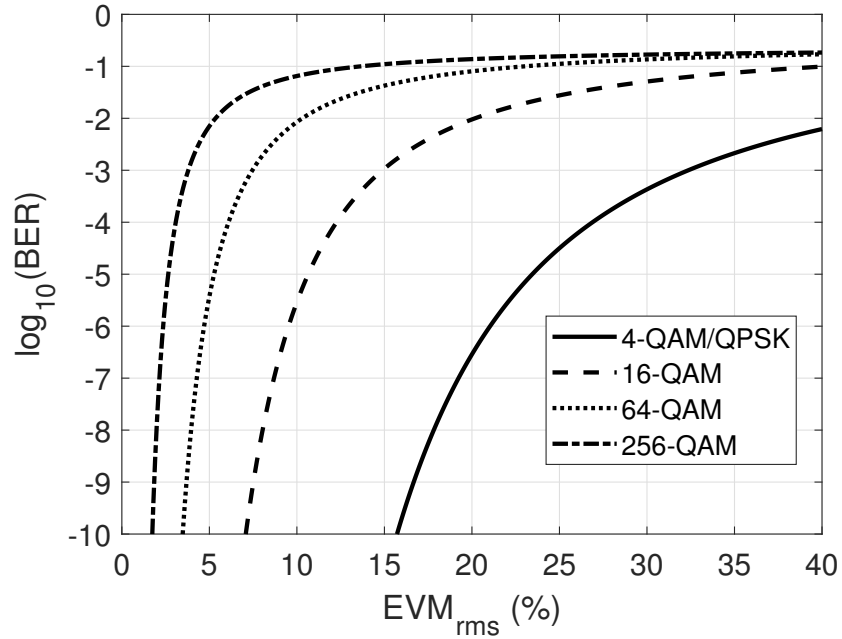


Figure 2.8.: BER vs. EVM for different M-QAM modulation formats.

constellation, the relation between EVM and BER can be modeled according to [57] as

$$BER \approx \frac{1 - L^{-1}}{\log_2(L)} \operatorname{erfc} \left[\sqrt{\frac{3 \cdot \log_2(L)}{(L^2 - 1)} \frac{1}{(EVM)^2 \cdot \log_2(M)}} \right], \quad (2.15)$$

with L being the number of possible levels defined in the vector A' . This equation is evaluated for 4-QAM, or quadrature-phase-shift-keying (QPSK), 16-QAM, 64-QAM and 256-QAM in Fig. 2.8. As can be observed, the impact of the EVM to the BER scales with the modulation order M . That is to say, that higher modulation orders can tolerate much fewer errors affecting the communication link.

2.2.2. SNR/EVM relation

The literature presents a series of system impairments that affect the EVM of the link [48], with the key source of error being the arbitrary white Gaussian noise, which will deteriorate the signal-to-noise ratio at the receiver output. According to [48], [58], the relation between EVM and SNR at the receiver output, denoted as EVM_{SNR} , is given as

$$EVM_{SNR} = \sqrt{\frac{1}{SNR}}. \quad (2.16)$$

By merging Eq. 2.15 and Eq. 2.16 the influence of the SNR at the Rx output to the link quality can be calculated. In order to calculate this SNR, two parameters must be determined. Firstly, the SNR at the input of the Rx is required, which can be calculated by dividing the input signal power by the input noise power. Secondly, the noise figure of the receiver, which is an Rx specification, must be calculated. The signal power at the input of the receiver can be calculated with the Friis formula [59] in dB as

$$P_{Rx \text{ input}} = P_{Tx \text{ output}} + G_{Ant \text{ Tx}} - FSPL + G_{Ant \text{ Rx}}, \quad (2.17)$$

where $P_{Tx \text{ output}}$ is the output power of the transmitter (in dBm), $G_{Ant \text{ Tx}}$ and $G_{Ant \text{ Rx}}$ are the antenna gains of the Tx and the Rx (in dBi), and FSPL is the free-space path loss (in dB), which is defined as

$$FSPL = 20 \cdot \log_{10} \left(\frac{4\pi df}{c} \right), \quad (2.18)$$

where f is the LO frequency, d the link distance, and c the speed of light in the channel. It will be assumed that both transmitter and receiver are equipped with the same antenna, which is the case for all links presented in this thesis. Therefore, it can be assumed that $G_{Ant \text{ Tx}} = G_{Ant \text{ Rx}} = G_{Ant}$. To arrive at the receiver input SNR, the noise power needs to be calculated. This noise power can be modeled as a Johnson-Nyquist noise [60] as

$$Noise_{Rx \text{ input}} = 20 \cdot \log_{10}(KTB), \quad (2.19)$$

where K is the Boltzmann constant, T is the room temperature (25°C), and B is the bandwidth of the received signal. Merging Eq. 2.17, 2.18, and 2.19, the SNR (in dB) at the input of the receiver can be expressed as a function of both link distance d and employed bandwidth B as

$$SNR_{Rx \text{ input}} = P_{Rx \text{ input}} - Noise_{Rx \text{ input}} \quad (2.20)$$

$$SNR_{Rx \text{ output}} = P_{Tx \text{ output}} + 2G_{Ant} - 20 \cdot \log_{10} \left(\frac{4\pi df}{c} \right) - 20 \cdot \log_{10}(KTB), \quad (2.21)$$

Finally, to arrive at the SNR at the output of the Rx, the receiver noise figure NF (in dB) has to be added to the equation as

$$SNR_{Rx \text{ output}} = SNR_{Rx \text{ input}} - NF \quad (2.22)$$

$$SNR_{Rx \text{ input}} = P_{Tx \text{ output}} + 2G_{Ant} - 20 \cdot \log_{10} \left(\frac{4\pi df}{c} \right) - 20 \cdot \log_{10}(KTB) - NF. \quad (2.23)$$

Combining Eq. 2.23 with Eq. 2.15, and 2.16, and assuming a BER threshold of 4.5×10^{-3} [55], the operating boundaries of the link in terms of distance and bandwidth for the different M-QAM modulations can be defined. An exemplary contour plot assuming a $P_{Tx \text{ output}}=4$ dBm, a $G_{Ant}=23$ dBi, a $f=240$ GHz and a $NF=11$ dB, is illustrated in Fig. 2.9. This values have been reported for wireless communication systems operating above 200 GHz [own3], [own8].

According to this estimation, in a channel operated by such Tx and Rx, a maximum bandwidth of 15 GHz can be employed in a 1-meter link using 256-QAM, while a maximum distance of 7.5 meters can be achieved using QPSK with the same bandwidth. The used bandwidth is directly proportional to the data-rate. However, there is no unique relation between both; it heavily depends on the digital pre-conditioning employed in the BB signal fed to the Tx inputs. The most common technique used for BB signal pre-conditioning is the root-raised cosine (RRC) filter [61]–[63]. This filter helps to minimize the inter-symbol interference (ISI) and to reduce the effective bandwidth [64] of the BB signal. The relation between BB signal bandwidth and symbol rate can be expressed as

$$B = \frac{1 + \alpha}{2T}, \quad (2.24)$$

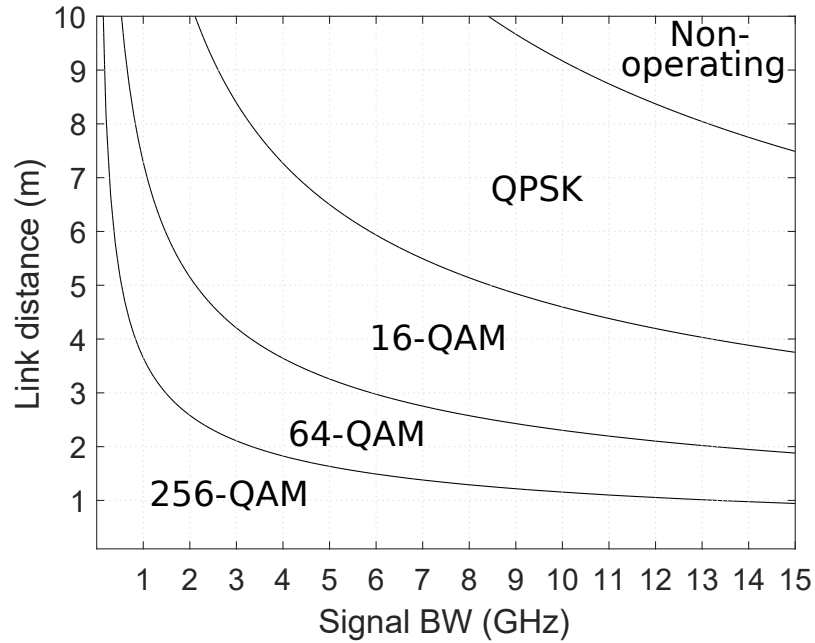


Figure 2.9.: Operating boundaries for each modulation format depending on the used BW and the link distance.

where α is the roll-off factor of the filter ranging from 0 to 1 and T is the symbol period. Assuming a typical RRC roll-off factor of 0.35 [65], a 15 GHz signal can contain 22 Gbaud. The Gbaud is defined as symbol per second, providing a symbol-rate. This symbol-rate delivers a different data-rate for each modulation format (176 Gb/s for 256-QAM, 132 Gb/s for 64-QAM, 88 Gb/s 16-QAM, and 44 Gb/s for QPSK). Lower roll-off factors allow for higher symbol-rates in the same BW, leading to the conclusion that a 1-meter distance link established with a Tx and Rx set with the previously given specifications will be capable of transmitting data-rates close to 200 Gb/s using 256-QAM. Unfortunately, the SNR is not the only parameter influencing the link EVM. Second-order impairments present in the link also influence the EVM. The EVMs generated by each of these impairments are added to the EVM generated by the other impairments as well as the EVM generated by the SNR (EVM_{SNR}) into the total link EVM EVM_{total} as a mean-square addition [48], given as

$$EVM_{total} = \sqrt{(EVM_{SNR})^2 + \sum_{i=1}^k (EVM_i)^2}, \quad (2.25)$$

where each of the EVM_i is the EVM contribution of one of these impairments. In Chapter 3, a detailed analysis of the impairments affecting the near- THz wireless link as

well as its influence on the EVM is presented. The performance analysis of the wireless communication links presented in this thesis will always be based on the EVM. The measured EVM will be compared with the EVM introduced by the SNR and other system impairments introduced by each wireless communication system. By subtracting the influence of these EVMs from the total measured EVM, the relative importance of each of these impairments will be evaluated. The conclusions of this analysis will be employed to improve the RF front-ends performance in future designs, aiming to achieve a wireless communication link at frequencies beyond 200 GHz capable of supporting data-rates of +100 Gb/s.

Part II.

RF Front-ends for Wireless Communications

Chapter 3

Tx and Amplifier-first Rx RF-front-end modules

As discussed in Chapter 1, the future 6G networks operate wireless links supporting data-rates of 100 Gb/s and beyond. The communication channels will move higher in the frequency spectrum towards the frequency band beyond 200 GHz to achieve these speeds, where the absolute available BW is also higher. A new generation of transmitters and receivers has been developed to address this band. This chapter introduces the first Tx and Rx RF front-end set developed at the IHCT for wireless digital communications at frequencies beyond 200 GHz. Both RF front-ends implement a direct-conversion IQ architecture. Thanks to a tunable LO, they can operate at any LO frequency in the 225-255 GHz band. Each of the RF front-ends consists of a single chip manufactured in an experimental 0.13- μm SiGe HBT technology developed in the frame of the DOTSEVEN project [34]. This process was derived from IHP's 0.13- μm BiCMOS technology SG13G2 [66], where an enhanced peak f_t/f_{max} of 350/550 GHz was achieved. The chips are packaged for prototyping following an inexpensive chip-on-board (CoB) scheme. At an LO frequency of 230 GHz, the Tx presents a saturated output power of 8.5 dBm, an IQ imbalance below 1 dB and a 3-dB RF BW of 28 GHz, whereas the Rx shows a conversion gain (CG) of 24.2 dB, a NF of 9 dB an IQ imbalance below 0.5 dB and a 3-dB RF BW of 20 GHz.

With this RF front-end set, a 90 Gb/s 1-meter line-of-sight wireless link was established using a 16-QAM modulation technique. The link was also demonstrated with QPSK and 64-QAM, achieving data-rates of 65 and 81 Gb/s, respectively. However, the measured EVM in the link is higher than the EVM expected from the SNR (see Chapter 2), indicating that second-order impairments are increasing the EVM beyond the limit set by Shannon's

theorem. A detailed analysis of the multiple impairments present in the wireless link is provided in this chapter, explaining the relative importance of each of these impairments in the final link EVM and introducing possible mitigation strategies to minimize their contribution to the link EVM.

This chapter is organized as follows. Section 3.1 presents the architecture and the circuit building blocks of the RF front-end modules. Section 3.2 reports on the RF performance of the RF front-ends. Section 3.3 presents the wireless link results and the EVM analysis, where the contribution of each of the impairments is analyzed and quantified. Finally, Section 3.4 concludes and provides mitigation strategies for future designs to achieve higher data-rates. The presented results and figures have been originally published in [own2]–[own7], [own10] and the copyright has been transferred to IEEE.

3.1. Transmitter and Amplifier-first Receiver Architecture

Due to the large instantaneous BW required for data-rates of 100 Gb/s and beyond, the influence of both the RF band-pass response and the low-pass characteristics of the high-speed BB interface for both transmitter and receiver need to be traded against each other, resulting in some specific choice of transceiver architecture. Both of them set the effective BW of a complete link in a back-to-back configuration ($\text{Tx}_{\text{BB-to-R}_{\text{BB}}}$), and in combination with a suitable packaging solution need to provide both the minimum frequency-dispersion (amplitude distortion and group delay) high-speed BB signaling and high-fidelity, low-loss interface to free-space at LO frequencies beyond 200 GHz. Considering the practical package-level BW limitations, as discussed later in this chapter, a direct-conversion IQ transceiver architecture [67] was favored in comparison to an intermediate heterodyne frequency (IF) [68] topology. In the heterodyne topology, a large modulation BW needs to be accommodated on top of an IF frequency, not only for the analog part but also for the ADC/DAC and digital signal processing (DSP) blocks, increasing the sampling rate and BW requirements for the measurement set-up beyond the currently available lab equipment. A block diagram illustrating the chosen architecture and its composing building blocks of both Tx and Rx is presented in Fig. 3.1. The $\times 16$ LO generation path up-converts a 13.75-16 GHz external reference signal to the desired 225-255 GHz band [69]. A broadband coupled-line hybrid provides the quadrature for the LO signal [70]. On the Tx side, the I and Q signals are up-converted and then amplified before being radiated. In the Rx, the RF signal is pre-amplified and afterward down-converted again to the BB. Both Tx and Rx chips include 50Ω buffers at the input and output ports to facilitate interfacing with the PCB. Both chips are equipped with broadband on-chip ring antennas radiating through the substrate into a high-resistivity hyper-hemispherical

9-mm diameter silicon lens. The chip-on-lens assembly is mounted and wire-bonded on a Rogers 4350B PCB backside with a recess to accommodate the chip. The chip micrographs and a picture of the fully assembled RF module can be found in Fig. 3.2. The circuits presented in this chapter have been previously published in [49] and have been included for completeness.

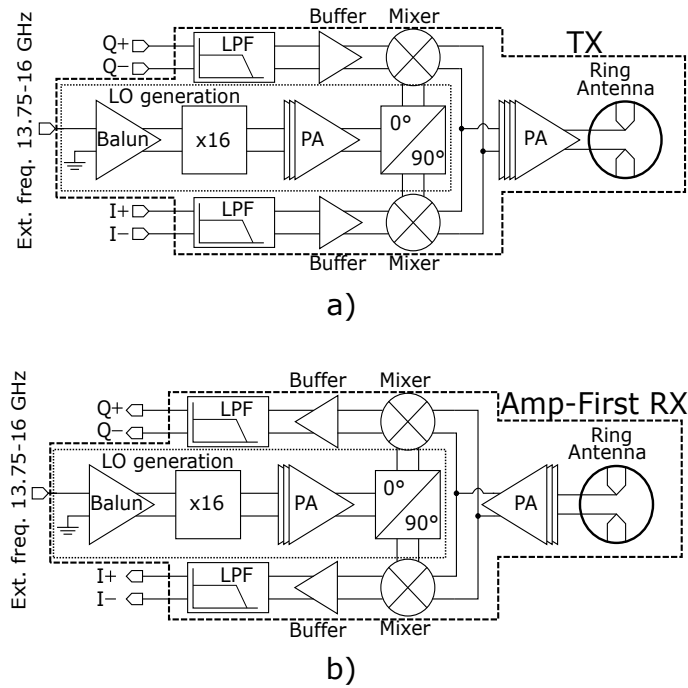


Figure 3.1.: Block diagrams of the a) transmitter and b) amplifier-first receiver. After [own3] © 2016 IEEE.

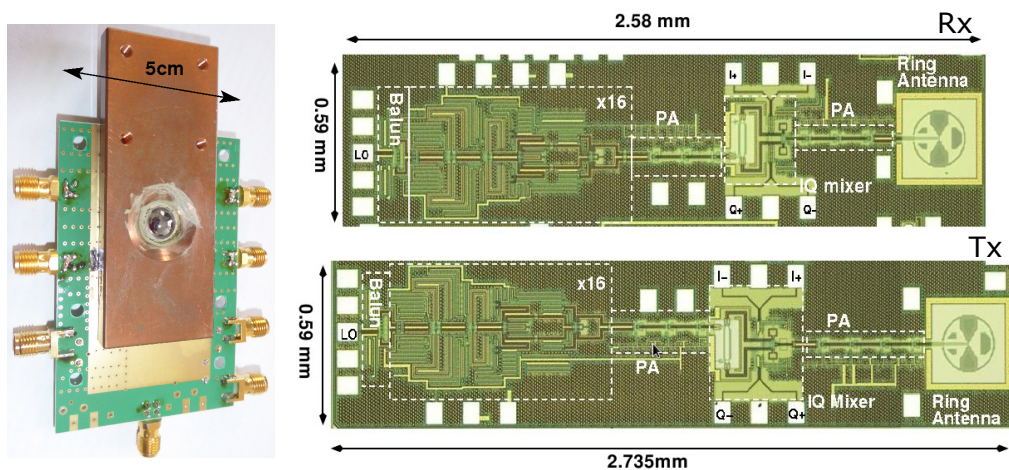


Figure 3.2.: Picture of a fully packaged RF front-end module (left) and chip micrographs (right). After [own3] © 2016 IEEE.

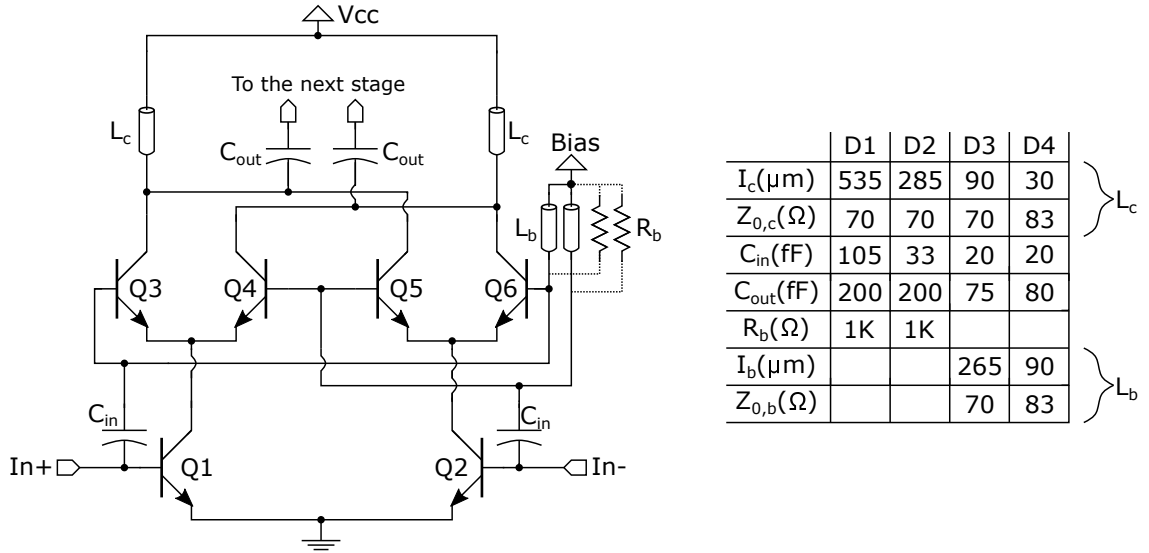


Figure 3.3.: Circuit schematic of the four $\times 2$ frequency doublers stages composing the multiplier chain. The different matching elements for each of the stages are shown in the table. After [own3] © 2016 IEEE.

3.1.1. $\times 16$ IQ LO generation path

The LO signal source consists of a $\times 16$ frequency multiplier (four cascaded doubler stages D1–D4) followed by a three-stage PA. The quadrature is provided by a broadband 90° hybrid coupler placed at the output of the PA. Here, two key parameters have to be considered for the design. First, the output power should be sufficient to drive the up- and down-conversion mixers. Second, the LO generation path should offer enough tunability to account for a possible frequency shift while designing the up-and-down-conversion paths. The constituent elements of the $\times 16$ IQ LO generation path are briefly presented in the following.

$\times 16$ frequency up-conversion chain. It consists of four cascaded Gilbert-cell frequency doublers [69],[own3]. Fig. 3.3 shows the circuit schematic for one of these doublers. The inductance L_b , with a length l_b , and L_c , with a length l_c , are part of the output and the input matching network, respectively. The capacitance C_{in} couples the input signal at the switching quad to the transconductance stage.

For wideband operation, interstage matching is key. If the center frequencies of all four cascaded doubler stages (D1–D4) are aligned (i.e., tuned to the even consecutive harmonics), then the 3-dB BW of the complete multiplier chain is significantly reduced. This configuration would also result in a sharper roll-off beyond the 3-dB BW. This design implements a staggering frequency strategy where the stages are deliberately misaligned in frequency to compensate for this limitation [own3]. The matching structures used for this interstage

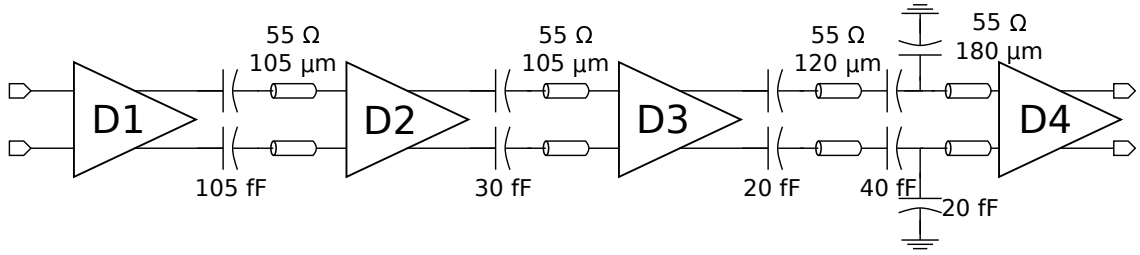


Figure 3.4.: Block diagram of the complete $\times 16$ frequency multiplier chain, consisting of four cascaded Gilbert-cell doublers (D1-D4). After [own3] © 2016 IEEE.

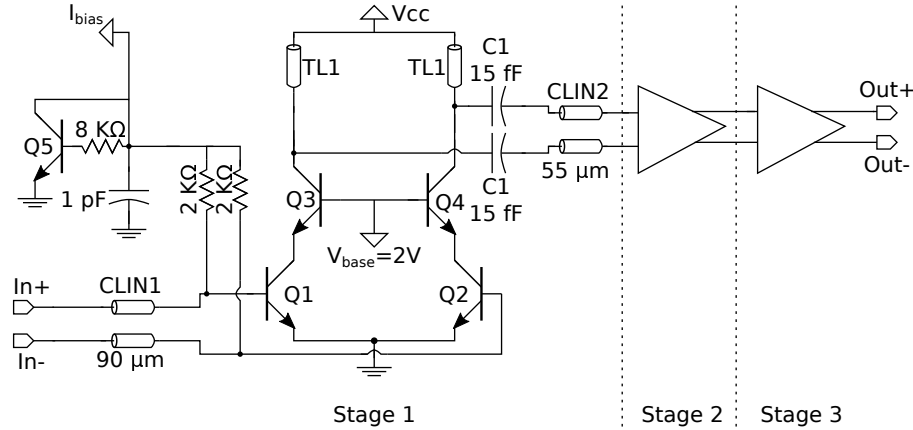


Figure 3.5.: Circuit schematic of the power amplifier. After [own3] © 2016 IEEE.

matching are depicted in Fig. 3.4. The simulations show that the $\times 16$ multiplier chain has an output power exceeding -10 dBm in the 225-265 GHz band. The complete multiplier chain, including the active input balun, consumes 250 mW.

PA. To ensure a proper mixer drive, the $\times 16$ frequency multiplier is cascaded with a three-stage PA. The circuit-level schematic of the 3-stage Class-A PA is shown in Fig. 3.5. The input matching network consists of the coupled microstrip line CLIN1, while the output matching network includes the microstrip-line-based inductor TL1, capacitor C1, and the coupled microstrip line CLIN2. The size of the implemented transistor is $8 \times (0.96 \times 0.1) \mu\text{m}^2$, chosen as a trade-off between maximum saturated output power and impedance profile for matching. The measured small-signal gain for the three-stage PA is 23 dB, with a 3-dB BW of 25 GHz. The simulated P_{sat} for the three-stage PA at 240 GHz is 9 dBm and the input-referred 1-dB compression point $P_{1 \text{ dB}}$ is -10 dB. The 3-stage PA in the LO path draws 200 mW from a power supply.

90° hybrid coupler. The hybrid coupler directly interfaces the $\times 16$ IQ LO generation circuitry with the Tx/Rx up- and down-conversion path [70], providing the IQ drive to the mixer. The hybrid exploits both broadside and edge coupling between 4 buried 110- μm long strip conductors with the ground plane underneath locally removed for appropriate

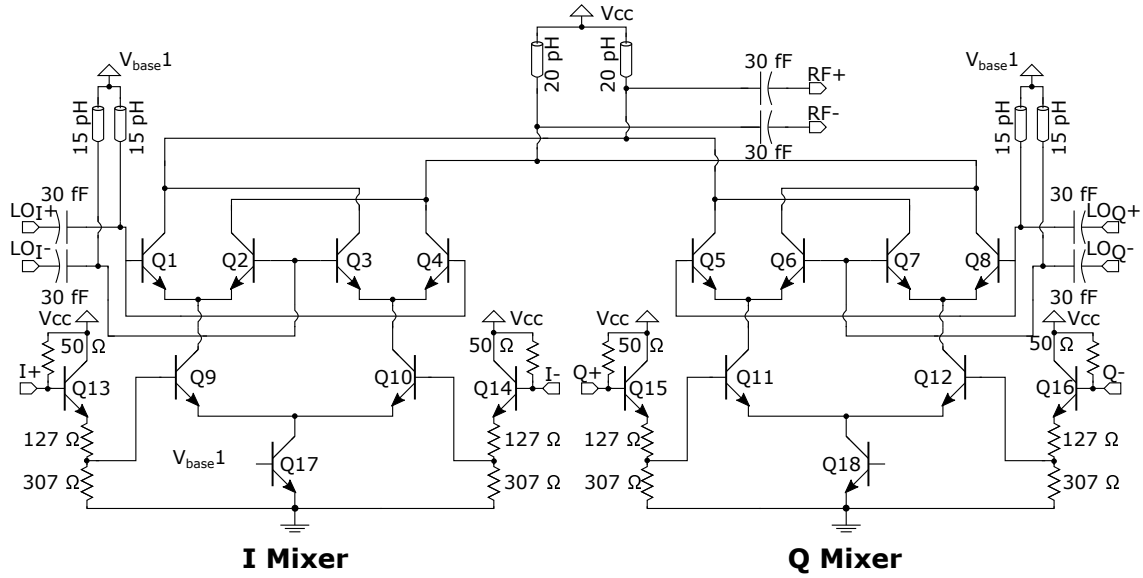


Figure 3.6.: Circuit schematic of the double-balanced IQ Gilbert-cell up-conversion mixer. After [own3] © 2016 IEEE.

control of the even/odd mode impedances to ensure maximum operation BW. In contrast, the feed lines are implemented as 100 Ω grounded coplanar striplines on a thick top metal layer. The isolation port is terminated with on-chip 50 Ω resistors. In the 225-255 GHz band, the hybrid coupler's simulated data shows a loss of 1 dB, an amplitude imbalance below 0.2 dB, and a phase imbalance below 1°.

3.1.2. Tx up-conversion path

The Tx up-conversion path consists of an up-conversion mixer and a PA (Fig 3.1). The PA used here is the same as the one described for the $\times 16$ LO generation path, but with one additional intermediate stage to increase the gain. It is also operated with a higher biasing than in the LO to increase the maximum output power, consuming 400 mW. This section describes only the up-conversion mixer.

Up-Conversion Mixer. Fig. 3.6 shows the schematic for the up-conversion mixer, which is based on the double-balanced Gilbert-cell topology. The transistors Q1–Q4 and Q5–Q8 composing the I and Q mixer's switching quads are driven by quadrature LO signals generated at the outputs of the hybrid coupler. The output collector currents from the two mixer cores are combined and fed to a set of 20 pF load inductors common for both I and Q mixers. Together with a 30 fF capacitor, these inductors constitute the output matching network. The 15 pF biasing inductors connected at the base of the switching quads and another set of 30 fF capacitors compose the LO matching network. The transconductance stage is equipped with emitter-follower buffers to offer a 100 Ω differential impedance over

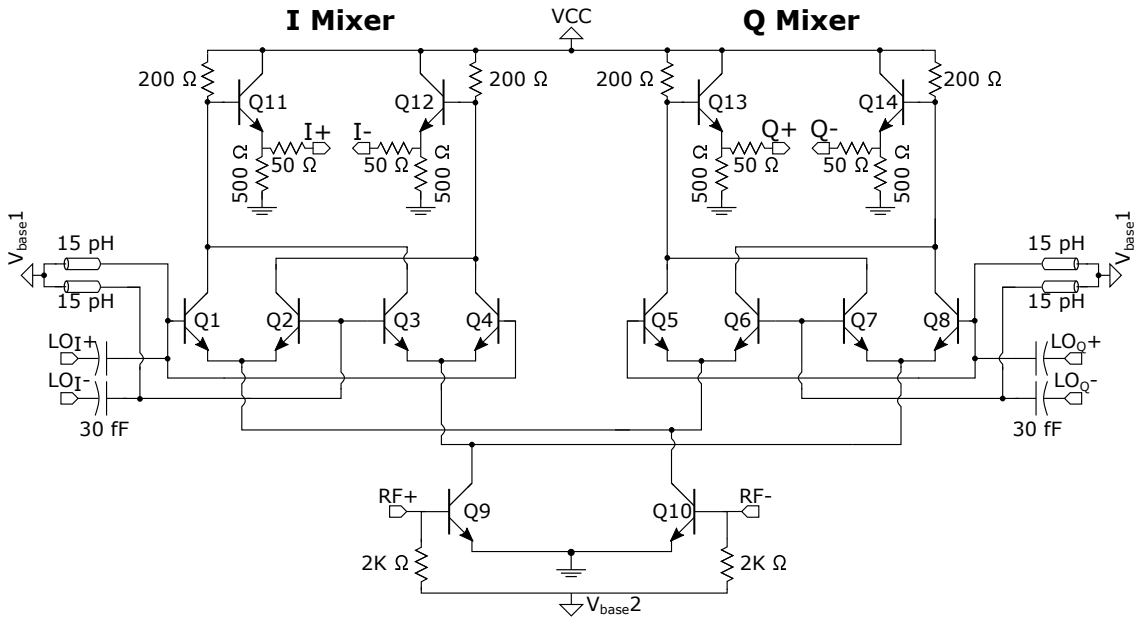


Figure 3.7.: Circuit schematic of the double-balanced IQ Gilbert-cell down-conversion mixer. After [own3] © 2016 IEEE.

a BW that goes from 0 to 30 GHz at the chip BB inputs. The up-conversion mixer, including the BB buffers, consumes 120 mW.

3.1.3. Rx down-conversion path

The Rx down-conversion path implements a PA followed by a down-conversion mixer. Due to the low discrepancy between the gain matching and the noise matching of the device at these high frequencies [71], the three-stage PA presented in Sec. 3.1.1 was used as LNA in the Rx, ensuring RF frequency channel alignment between the Tx and the Rx.

Down-Conversion Mixers. Fig. 3.7 shows the schematic for the down-conversion mixer in the Rx chip, which is based on the double-balanced Gilbert-cell topology. The transconductance stage (Q9–Q10), shared between the I and Q mixers, is fed from the input RF signal through the LNA. The transistors Q1–Q4 and Q5–Q8, which are switching quads for the I and Q mixer, are driven by the quadrature LO signals provided by the hybrid coupler. The LO matching network is similar to the one presented for the up-conversion mixers. The mixers' collector outputs are connected to the common-collector buffer BB amplifiers consisting of the transistors Q11–Q12 for the I-mixer and Q13–Q14 for the Q-mixer through a $200\ \Omega$ load resistance. This value was chosen as a trade-off between conversion gain, noise figure, and BB BW. The buffers have an emitter load resistance of $500\ \Omega$. For wideband BB matching, a $50\ \Omega$ series resistance is connected at the BB outputs

to provide a $100\ \Omega$ differential matching at the board collector level. The down-conversion mixer, including the buffer BB amplifier, consumes 100 mW.

3.1.4. On-Chip antenna and BB packaging scheme

A low-cost COB packaging solution is used to provide all DC, external driving tone for the multiplier chain, and high-speed modulated BB signals on the board level. Here, each of the Tx and Rx chips is mounted on the backside of a 9-mm diameter hyper-hemispherical lens made of high-resistivity silicon with the on-chip antenna aligned with the lens center. The overall chip-on-lens assembly is placed in a recess of a regular two-layer 0.338-mm thick Rogers 4350B board surrounded by a metal plane. To compensate for the inductance generated by the wire-bond that limited the BB BW, a low-pass filter embedding this inductance as one of its components was implemented onboard.

Linearly polarized on-chip ring antenna. The antenna is topologically similar to the differential wire ring topology presented in [72]–[74]. It consists of two wire semi-rings connected along with the center feed. For wideband operation, the feed is non-uniformly tapered using step-wise approximation. It is designed to illuminate a silicon hyper-hemispherical lens through the chip backside. The lens reduces the influence of surface waves on the radiation efficiency and radiation patterns and inherently delivers a high gain to compensate for the high free-space propagation loss. The backside radiation offers significant advantages over the front-side radiation. For example, it allows for an enhanced form factor reduction of 39 % in comparison with a front-side radiator (ϵ_r for silicon is 11, while for silicon oxide is 4). Moreover, the directivity is flexible and can be modified by changing the lens dimensions. In this work, a 9-mm diameter lens was used. The volume of a 9-mm lens provides sufficient thermal control for the chips dissipating up to 2 W. The on-chip heat is further transported through the lens to a heat-sink attached to the printed circuit board (PCB) bottom side. The antenna provides a differential impedance of $100\ \Omega$ over a very wide BW (S_{11} stays below -20 dB in the 180–330 GHz band). The simulated cross-polarization fields stay 20 dB below from the copolar fields when the antenna is operated differentially. Due to its low impedance for the common mode (below $5\ \Omega$ in the whole band), any common-mode radiation is minimized. Moreover, the differential-to-common mode conversion stays below -40 dB in the operating band.

Wire-bond inductance compensation. A manual mm-length wire-bonding process was applied to all on-chip connections, creating a parasitic inductance at the BB port. The low-pass profile of this parasitic inductance is the main limitation for the BB operation BW. To compensate for this inductance, an on-board filter has been implemented on

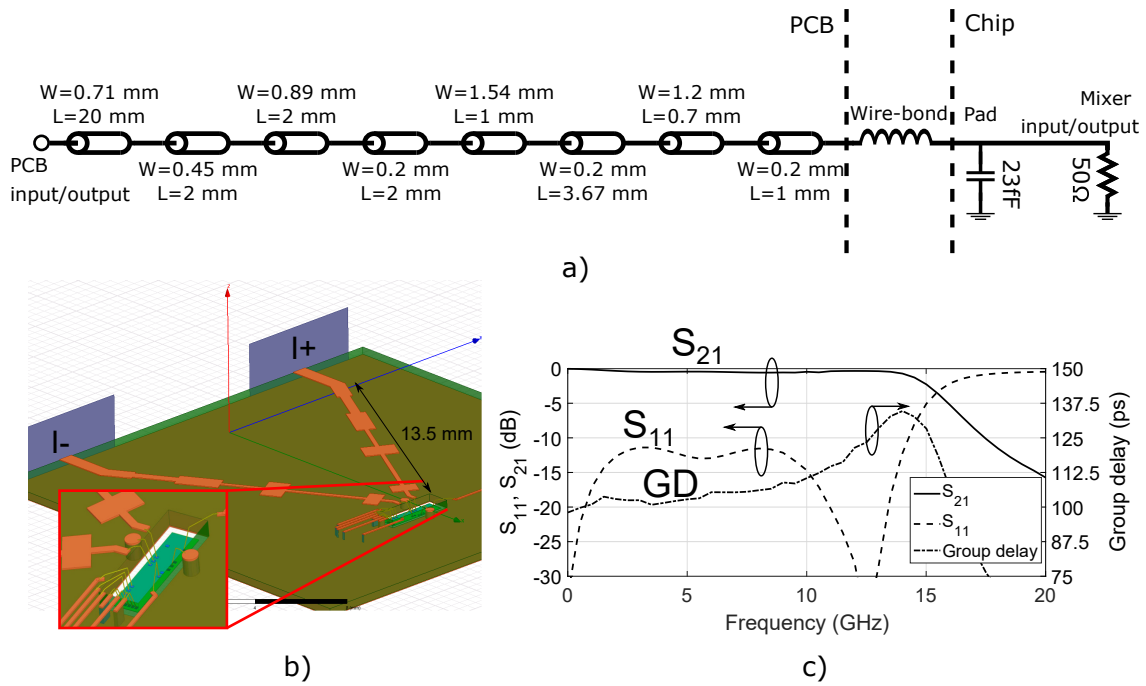


Figure 3.8.: a) Microstrip-line based stepped impedance low-pass filter from the final design iteration including the widths and the lengths of the transmission lines, b) EM model of the on-board filter including the wire-bond connection to the chip, and c) simulated results of the filter. The filter offers a 3-dB BB of 14 GHz with a group delay variation below 37.5 ps in the operating band. After [own2] © 2018 Cambridge University Press.

the PCB. The design goals for this filter are a 3-dB BW of 15 GHz, an input match better than 10 dB up to the 3-dB BW, and minimum group delay variation in-band. The wire-bond will be integrated as the first/last component of the filter. Due to its flat group delay characteristic, a Bessel-based filter would be the topology fitting with these specifications best. However, the inductance introduced by the mm-length wire-bond is on the range of 1 nH, which is an order of magnitude higher than the value extracted from the prototype calculation [75], reducing the 3-dB BW of the filter to 10 GHz. A Butterworth-based topology was chosen instead as a compromise between 3-dB BW and group-delay flatness. The lumped elements from the filter prototype were implemented as step-impedance microstrip-line segments on a low-cost, high-speed 0.338 mm thick Rogers 4350B PCB. Several iterations were required to match the initial values with the filter specification due to the space limitations at the board level. A schematic with the final iteration's values is presented in Fig. 3.8 a), while the full EM model used for this simulation is presented in Fig. 3.8 b). The simulated results are presented in Fig. 3.8 c). The final filter shows a simulated 3-dB BW of 14 GHz with a group delay variation below 37.5 ps in the operating band.

3.2. RF Characterization

Two different groups of RF measurements have been performed. The first encompasses a set of single-tone measurements allowing separate investigation of the frequency-dependent lower- and upper-sideband characteristics for key Tx/Rx performance metrics. In the second, the measurements involve a combined operation of the Tx and Rx modules configured into a free-space back-to-back line-of-sight set-up. Here, both double-sideband quadrature up-conversion and down-conversion are performed between the BB Tx inputs and the Rx outputs, which supports a study of the influence of different hardware imperfections acting simultaneously in the set-up mimicking a real wireless link. All measurements have been taken in free-space and at the board level, including the influence of all on-board and on-chip components cascaded between the on-board high-speed connector and the lens-coupled on-chip antenna. An absorbing material was applied to cover the major reflecting surfaces to minimize the influence of parasitic reflections in the measurement set-up.

3.2.1. Single-tone RF measurements of the Tx and Rx

A WR-03 (220-325 GHz) frequency extension module from OML, equipped with a linearly polarized horn antenna with a directivity of 20 dBi at 270 GHz, operating in the receive and transmit mode was used to characterize the Tx and the Rx. The output power and conversion gain of the OML module were previously calibrated. The characterization set-up for the Tx is depicted in Figs. 3.9. The differential BB inputs I and Q were fed through a broadband balun (BAL0026 Marki). For characterization of the IQ amplitude imbalance, the I and Q ports were driven separately, whereas for the total radiated power measurement in the upper and the lower sideband (USB and LSB), a broadband (0.5–20 GHz) 90° hybrid (QH0226 Marki) was used before the baluns to combine the I and Q signals at the mixer BB ports. A complimentary set-up was used for the Rx [own2], [own11]. All key parameters of the Tx and Rx RF front-end modules were de-embedded from the measurements using the Friis-Formula [59]. The losses of the baluns, hybrids, and interconnection cables were de-embedded from the measured results.

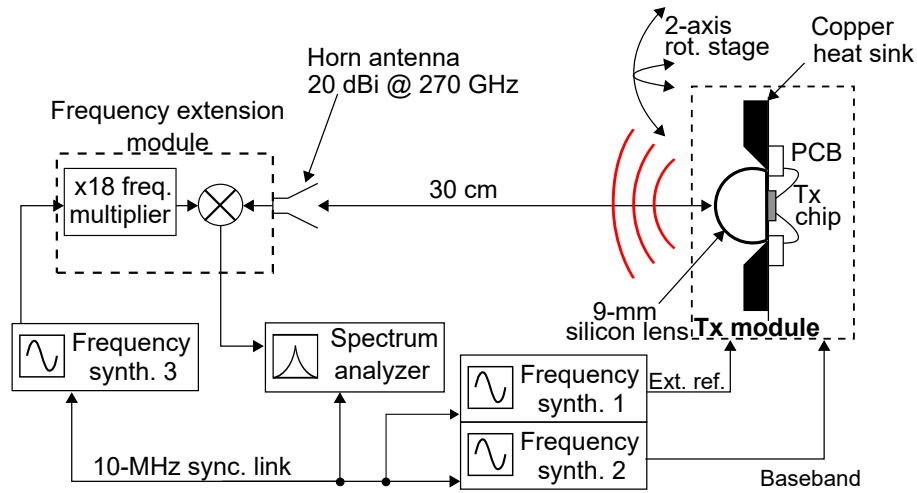


Figure 3.9.: Schematic of the measurement set-up used for the characterization of the Tx. After [own8] © 2019 IEEE.

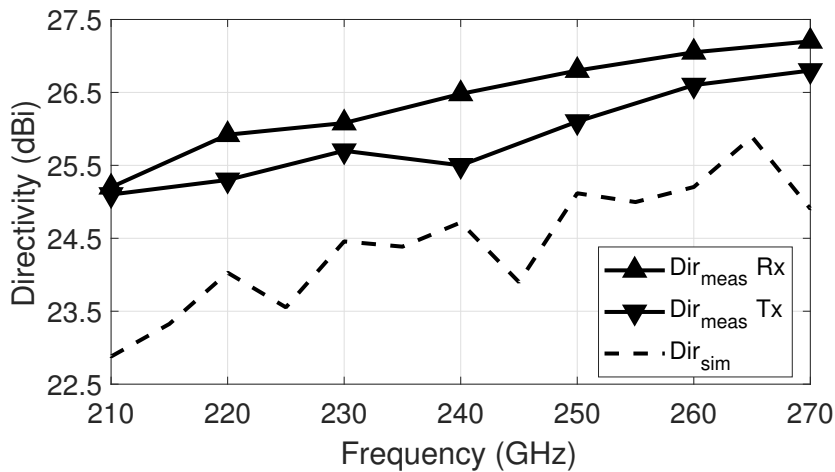


Figure 3.10.: Directivity of the Tx and Rx modules compared with the simulated data.

Antenna measurements: In order to use the Friis-Formula to de-embed the module parameters, the Tx and Rx RF front-end modules' antenna directivity needs to be known. The modules were mounted on a precision alignment 2-D rotational stage controlled by a stepper-motor to measure the directivity. The distance between the OML module and the RF front-end module was set to 30 cm to ensure far-field measurements [76]. The directivity was calculated by integrating the power density values acquired within a hemisphere sector of $\pm 30^\circ \times \pm 30^\circ$. Due to limitations in the measurement setup, the back-side radiation was neglected, increasing the directivity artificially. The measured directivity grows monotonically between 25.2 dBi to 27.1 dBi for the Rx and between 25.1 dBi to 26.8 dBi in the 210-270 GHz band, correlating well with the simulated results. The frequency dependence of the directivity is illustrated in Fig. 3.10. An exemplary radiation pattern of the receiver at 240 GHz is shown in Fig. 3.11.

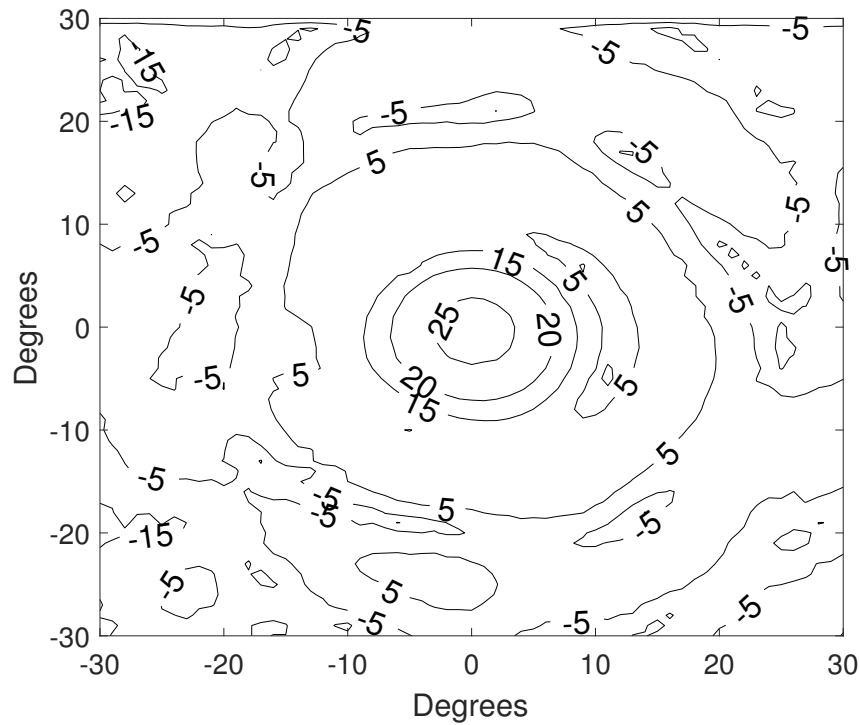


Figure 3.11.: Example of a radiation pattern of the Rx at 240 GHz.

Up-conversion path of the Tx: The Tx RF BW, output power, and IQ imbalance were characterized for three relevant LO frequencies: 230, 240, and 250 GHz. The BB IQ input frequency was swept from 0.5 to 20 GHz with two different input power levels, -5 and -15 dBm. These power levels correspond approximately to the saturated output power and the 1 dB compression point, which were found to be optimum for QPSK and 16-QAM operation, respectively (See Section 3.3.2). The results of these measurements are illustrated in Fig. 3.12. When the Tx is operated with an input power of -15 dBm, the maximum output power is 4.5 dBm. The 3-dB RF BW depends on the chosen LO frequency. At 230 GHz, the RF BW is maximized with a 3-dB BW of 28 GHz. 230 GHz is the LO frequency that holds the symmetry between the USB and the LSB best. Higher LO frequencies deliver lower output power and increase the asymmetry between the USB and the LSB. When the Tx is operated with an input power of -5 dBm, the output power grows to 8.5 dBm. However, the 3-dB RF BW is reduced to 25 GHz at 230 GHz, increasing the USB and LSB's asymmetry. This effect is more pronounced for other LO frequencies. The IQ amplitude imbalance stays below 1 dB for all operation modes.

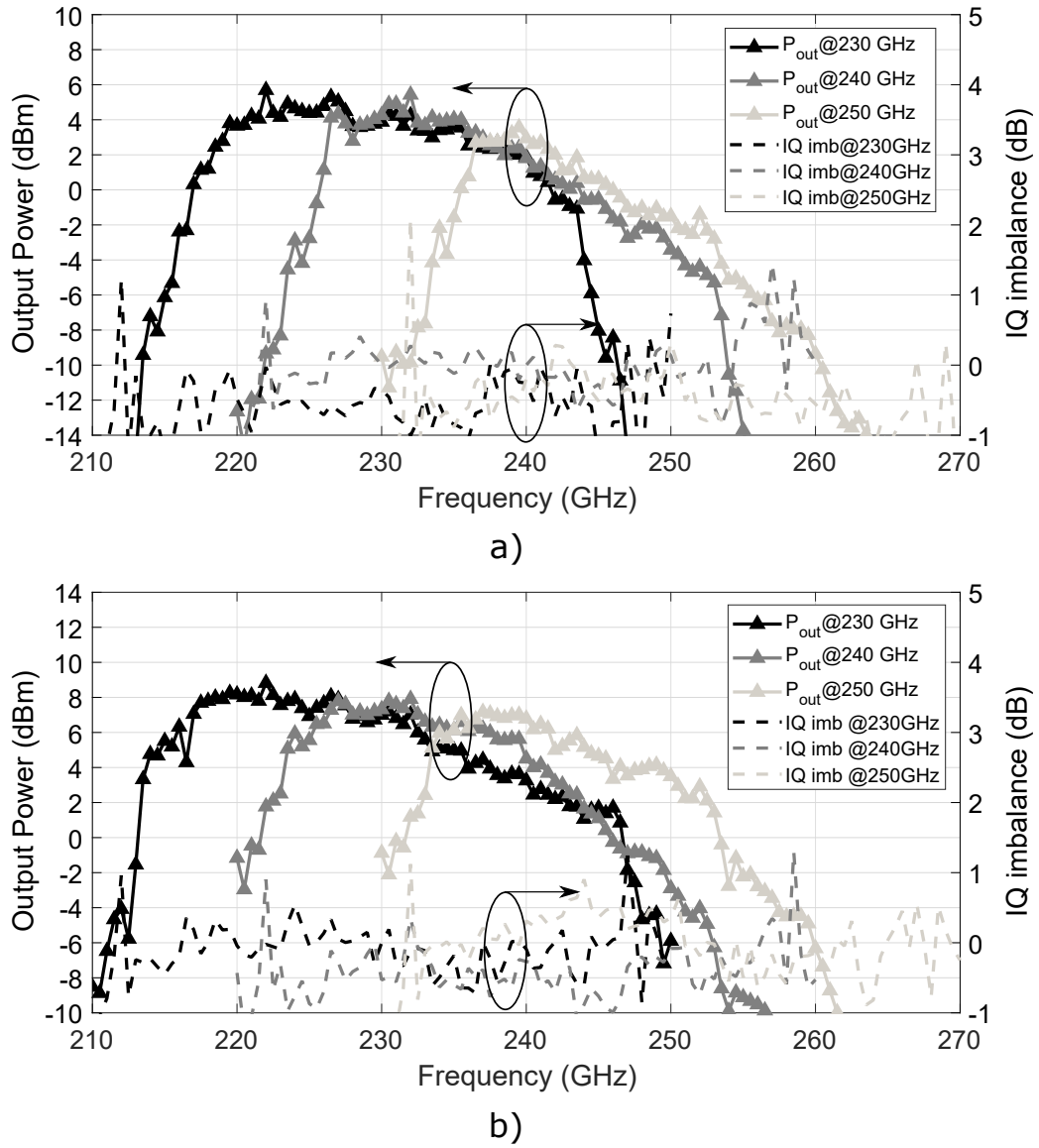


Figure 3.12.: Output power and IQ amplitude imbalance of the Tx when the BB inputs are operated with a input power of a) -15 dBm and b) -5 dBm.

Rx measured results: The Rx conversion gain, BW, IQ imbalance, and noise figure were characterized. These results are presented in Fig. 3.13. Due to the lack of a noise source in our laboratory at this frequency range, the receiver's single-sideband noise figure was calculated from the measured conversion gain and output noise floor (N_{out}). The input noise floor was assumed to be $N_{in} = -174$ dBm/Hz, which is the thermal noise at room temperature [77]. The noise figure can be calculated in dB as

$$NF (dB) = SNR_{in} (dB) - SNR_{out} (dB) = CG (dB) + N_{in} (dBm) - N_{out} (dBm). \quad (3.1)$$

For a LO frequency of 230 GHz, the Rx shows a peak conversion gain of 24.2 dB, a 3-dB RF BW of 20 GHz, a minimum single-sideband noise figure 10 dB, and an IQ amplitude imbalance below 0.5 dB for the operating BW. Higher LO frequencies show narrower RF BW and higher asymmetry between the USB and the LSB. This effect is created by the band-pass characteristic of the power amplifier.

$\times 16$ LO generation path: An inherent drawback of the chosen LO generation method with a high multiplication factor is the potential presence of undesired frequency spurs in the output of the $\times 16$ LO generation path at a spectral distance equal to integer multiples of the external 13.75–16.25 GHz signal drive frequency. Despite the double-balanced operation of the Gilbert-cell doublers used in the $\times 16$ multiplier chain, the presence of both odd ($\times 15$ and $\times 17$) and even ($\times 14$ and $\times 18$) harmonics around the desired $\times 16$ spectral line was identified in the Tx and Rx. To characterize these harmonic spurs, a variation of the set-up presented in Fig. 3.9 was employed. The external signal drive was swept in the 13.75–16.25 GHz band. A fixed 33 MHz intermediate frequency (IF) signal was used to feed the Tx BB inputs. The OML module's frequency was offset from the desired $\times 16$ to acquire the radiated output power of all these harmonics ($\times 14$ – $\times 18$). A complimentary set-up was build for the Rx, where the down-converted signal generated by the LO harmonic spurs was measured. The results of this test are presented in Fig. 3.14 a) and 3.14 b) for the Tx and the Rx, respectively. Additionally, a direct leakage between the externally provided LO driving frequency (LO/16) and the Rx BB outputs was measured at -50 to -55 dB below the power level of the tunable 13.75–16.25 GHz external LO driving signal.

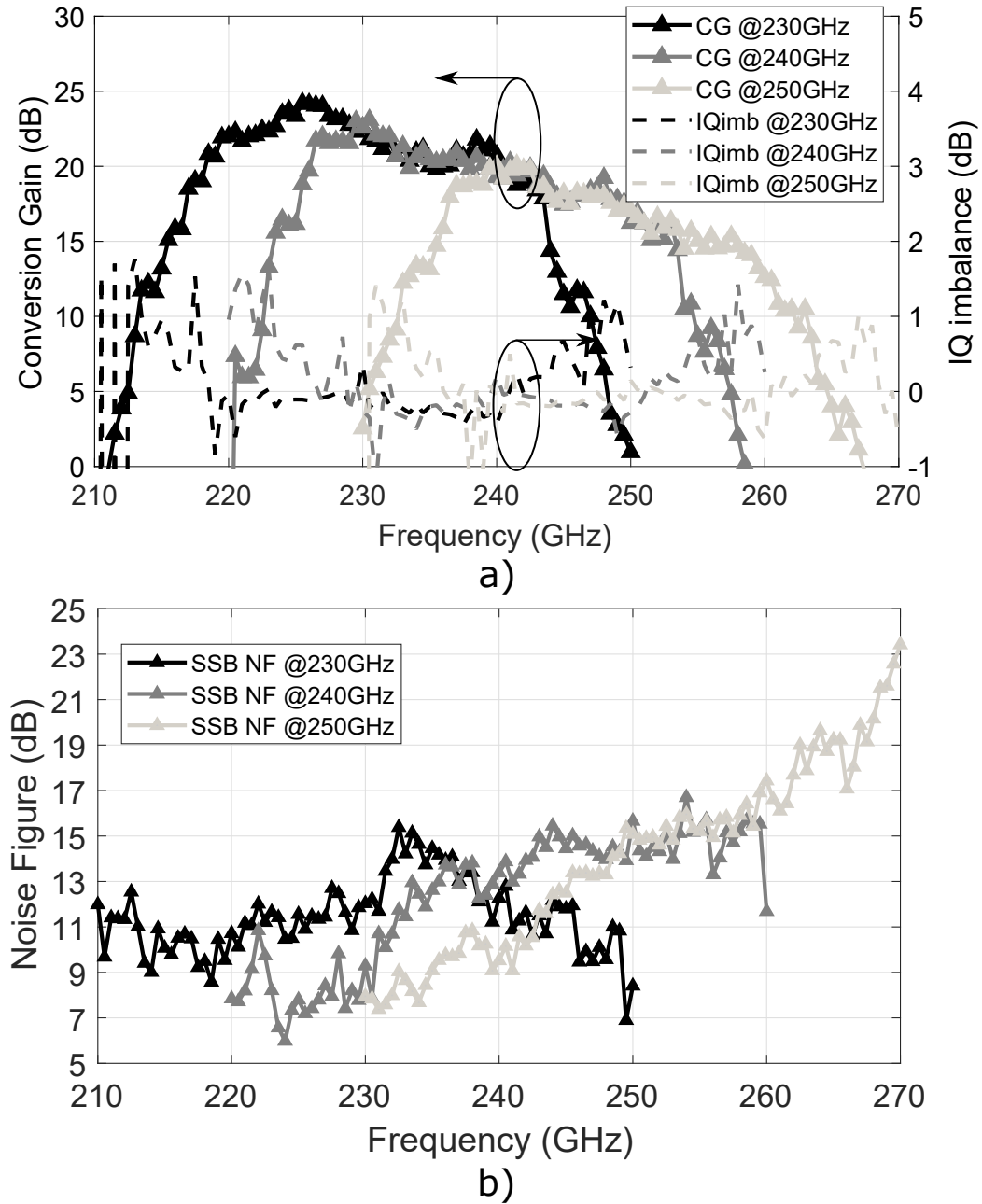


Figure 3.13.: Measured a) conversion gain and IQ amplitude imbalance and b) single side-band noise figure of the amplifier-first Rx at 230, 240 and 250 GHz.

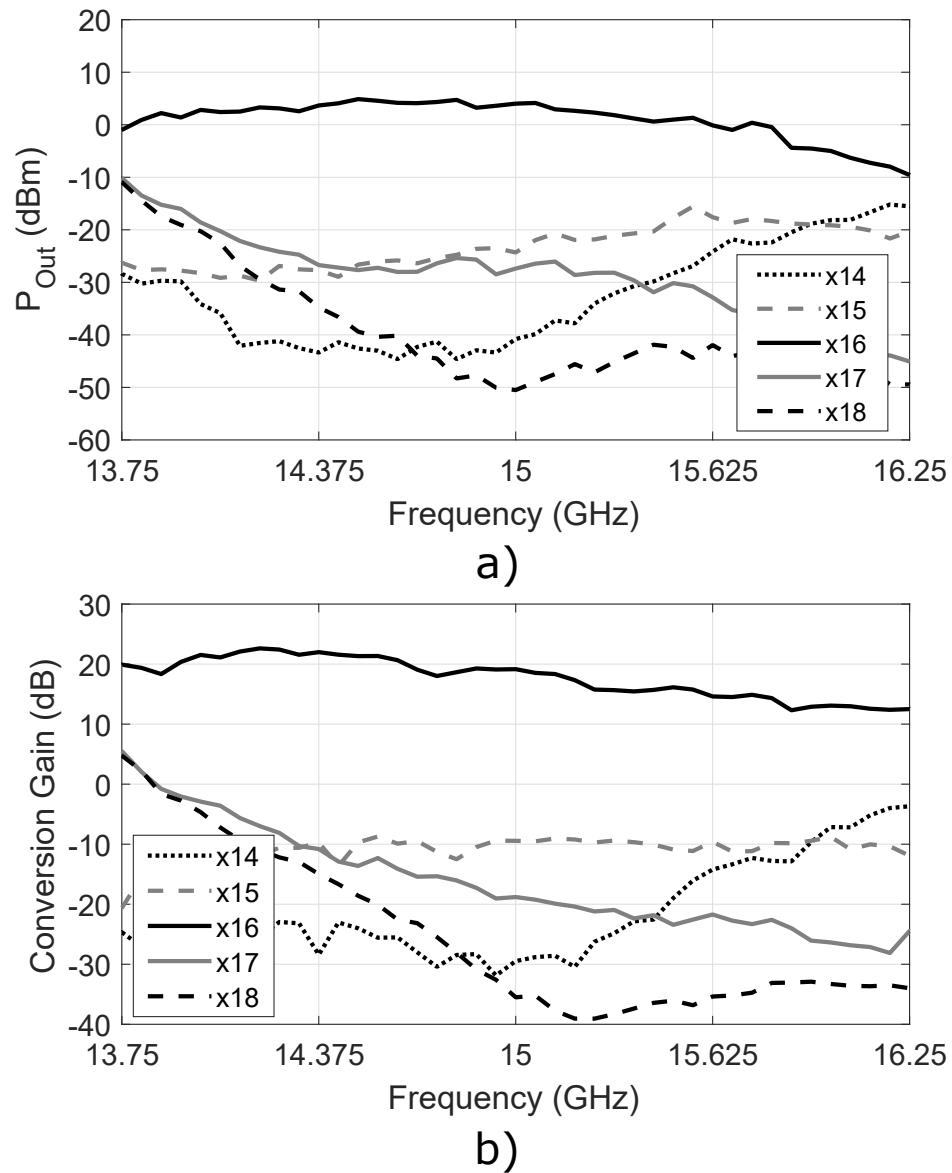


Figure 3.14.: Measured harmonic content vs. external LO drive frequency in the a) Tx and b) Rx.

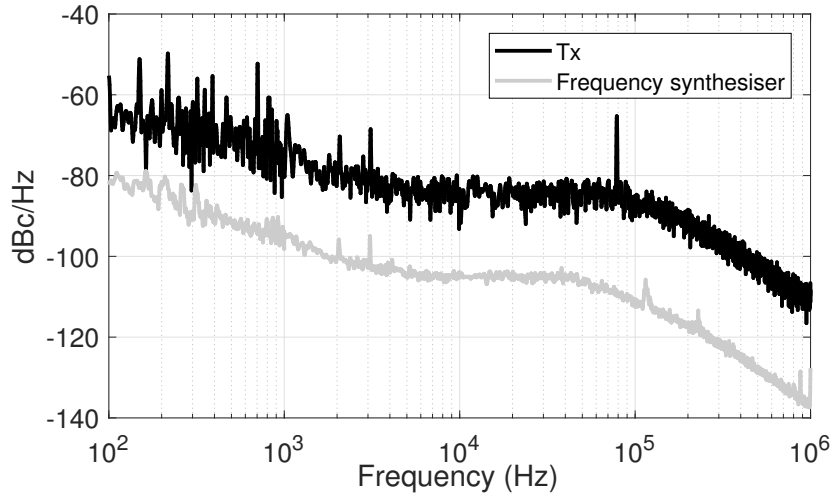


Figure 3.15.: Measured phase noise of the synthesiser at 15 GHz and the Tx at 16×15 GHz (240 GHz). The results for other LO frequencies are similar.

To evaluate the phase noise in the $\times 16$ LO generation path, two measurements were performed. First, the single-sideband phase-noise spectral power density at the output of the frequency synthesizer used to drive the $\times 16$ LO generation path was measured. Second, the RF output of the Tx module was down-converted with the OML extension module used as reference receiver using the set-up presented in Fig 3.9. The single-sideband phase-noise spectral power density of this signal was also measured. These test results are plotted in Fig. 3.15 for a frequency of 15 GHz for the synthesizer and 240 GHz for the Tx. The phase noise scales almost ideally according to $20 \cdot \log_{10}(16) = 24.1$ dB. The phase noise behavior is identical at other LO frequencies in the operation range. The used synthesizer was a Keysight E8257D synthesizer with an excellent single-sideband broadband noise floor of -150 dBc/Hz at 15 GHz.

3.2.2. Tx and Rx back-to-back results

The effective channel BW of the complete transmission path in a back-to-back configuration is set by the RF band-pass and BB low-pass characteristics of both Tx and Rx modules acting together by performing the combined double-sideband up-conversion and down-conversion between the corresponding BB Tx and Rx ports. In particular, double side-band operation involves the asymmetry between LSB and USB of both modules in the transmission process and, therefore, the frequency-dependent characteristics of the complete path are not simple replicas of the Tx and Rx RF properties found from single-tone measurements. In order to measure the Tx/Rx performance in a back-to-back configuration, the set-up shown in Fig. 3.16 was used. Here, the Tx and Rx modules were placed in a LOS at a 1-m distance, and both on-chip LO generation paths were driven from a single

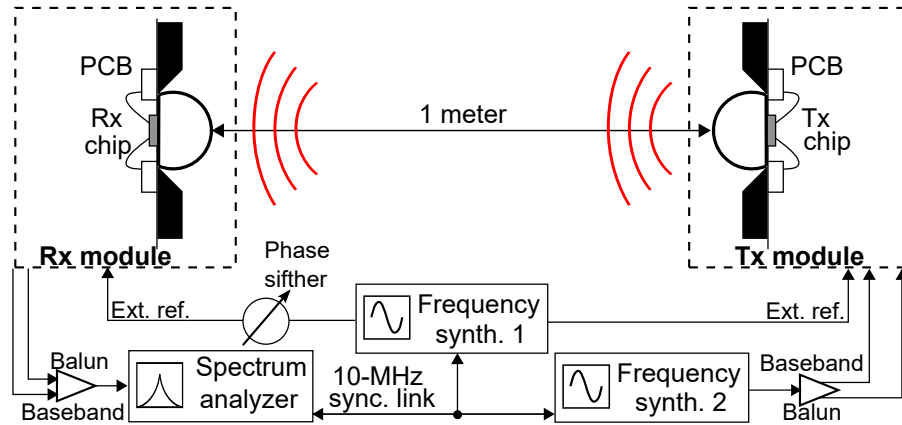


Figure 3.16.: Measurement set-up used for the Tx-Rx back-to-back results. After [own4]
 © 2018 IEEE.

frequency synthesizer. A phase shifter was used to facilitate the channel measurements by maximizing power transfer for the I and Q paths.

Two measurements were taken. First, the I-I and Q-Q transfer values were acquired. Afterwards, the orthogonal channel leak (I-Q and Q-I) was also measured. These measurements were taken for three different LO frequencies (230, 240, and 250 GHz). The results of this test are presented in Fig. 3.17. For a Tx BB input power of -15 dBm, the 6-dB defined BB channel BW at 230 GHz is 11.5 GHz, increasing for higher LO to a maximum of 14 GHz at 250 GHz. For a Tx BB power of -5 dBm, the BB BW extends to 13.5 GHz at 230 GHz and 16 GHz at 250 GHz. The in-band IQ amplitude imbalance was measured to be below 1 dB for all operation modes.

As it can be observed, the best 6-dB RF channel performance is delivered at 250 GHz, where the USB and the LSB asymmetry is maximized for both Tx and Rx. In this configuration, the system operates only using the LSB for transmission. Although this is a possibility when the system does not operate in quadrature, this is not the proper operation mode for a quadrature system. As shown by the results, a non-neglectful frequency-dependent I-Q cross-talk was found by the measurements of the RF channel. This leakage's power is higher for higher LO frequencies, where the USB and LSB asymmetry is more pronounced. Even for the same LO, higher BB frequencies are affected more severely than lower, due to the increased difference between their USB and LSB. The quadrature operation requires a perfect symmetry in the RF band-pass channel to cancel the I channel at the Rx's Q output and vice-versa. The operation of an ideal quadrature system is explained in Chapter 2. Any asymmetry in the band-pass RF channel will result in an insufficient cancellation of the undesired channel at the Rx output. Fig. 3.18 illustrates the quadrature process graphically when an asymmetric RF band-pass channel is included. As it can be observed, the Q signal does not cancel itself at the I output and vice-versa.

Although this representation only illustrates the effect of the amplitude asymmetry, the level of this IQ cross-talk is determined by both amplitude and phase asymmetry in the RF band-pass. At 230 GHz, where the USB and LSB symmetry is optimized, the IQ cross-talk is minimized. For other LO frequencies, this leakage increases due to the more asymmetric band-pass characteristics of the Tx and the Rx. Therefore, although the channel BW is broader at 250 GHz, a higher IQ cross-talk might negatively influence the link performance, reducing the maximum achievable data-rates effectively at these LO frequencies. Higher power at the Tx BB input also increases the asymmetry between the USB and the LSB at the Tx output (see Fig. 3.12), increasing, even more, the Tx_{BB} - Rx_{BB} IQ cross-talk.

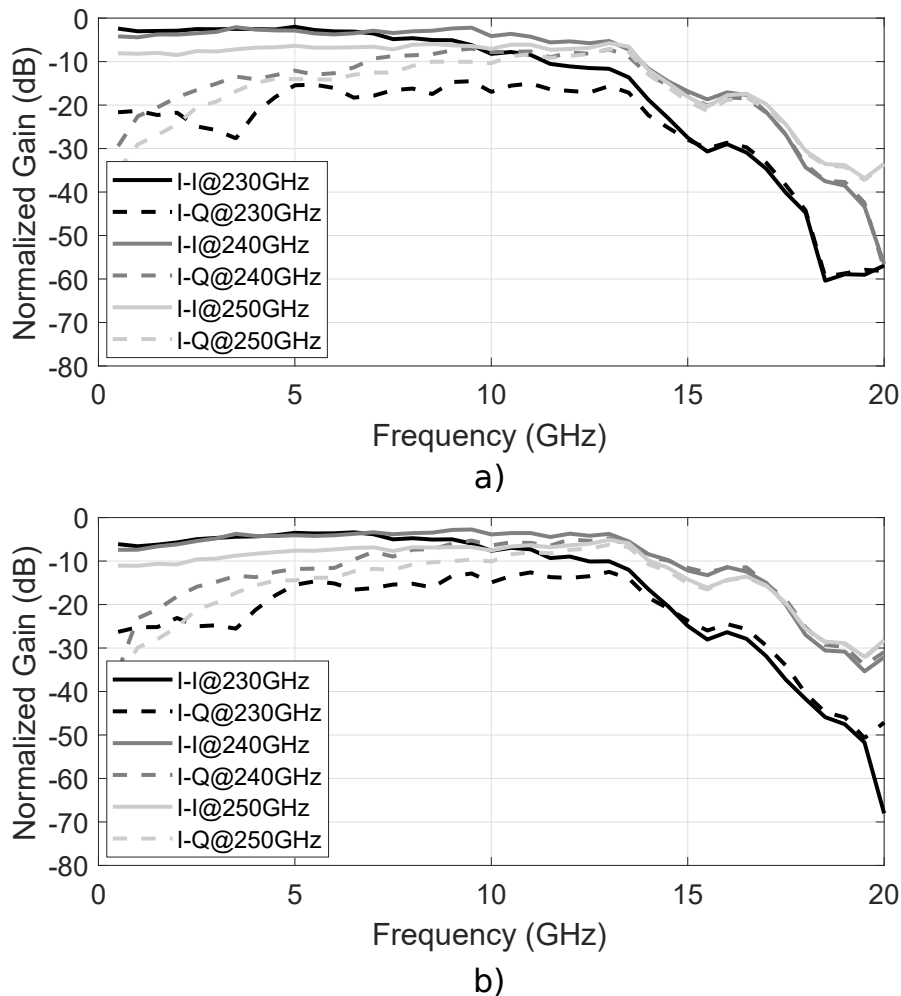


Figure 3.17.: Measured normalized channel gain and IQ cross-talk between the Tx BB input and Rx BB output for a Tx BB input power of a) -15 dBm and b) -5 dBm.

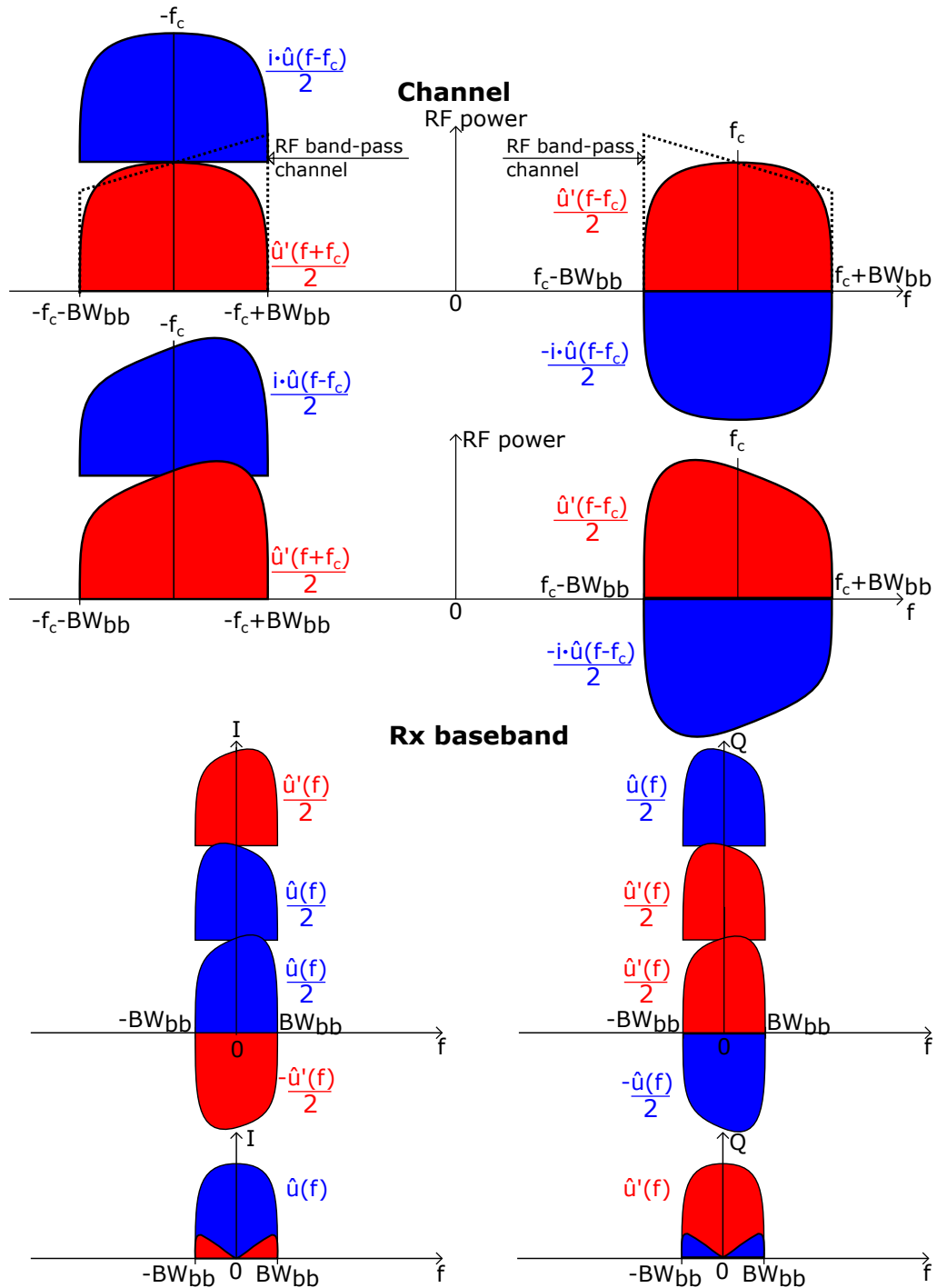


Figure 3.18.: Frequency domain representation of the an IQ transmission system affected by asymmetry between the USB and the LSB in the RF channel. After applying an RF band-pass channel with asymmetry between the USB, the orthogonality between the I and the Q channel does not hold in the receiver output. Higher asymmetry between the LSB and the USB results in higher IQ crosstalk.

3.3. Wireless Communication Link

3.3.1. Set-up description

The Tx and the Rx RF front-end modules were mounted in a 1-meter line-of-sight set-up. A schematic of the measurement set-up can be found in Fig. 3.19. For this measurement, two synchronized Tektronix AWG70001A AWG, each with a 50 Gs/s sampling rate, were used to feed the Tx's differential I and Q inputs. A pseudo-random bit sequence of order nine was digitally modulated as a data source. To reduce the BB signal's spectral density fed to the Tx BB inputs, a root-raised cosine filter with a roll-off factor ranging from 0.7 to 0.2 was applied to the data-stream for pulse shaping. This maximized the symbol rate that can be allocated in the available channel BW (See Fig. 3.17). A set of attenuators of different values (5 and 10 dB) were placed at the output of the AWGs to match the AWG output power with the required Tx input power. At the receiver side, two synchronized differentially-driven DPS77004SX real-time oscilloscopes (100 Gs/s sampling rate per channel) digitized the I and Q outputs of the Rx. This digitized signal was post-processed using a SignalVu vector signal analysis software. This software analyses the EVM, constellation, and eye diagram in real-time, and it also facilitates clock recovery, I/Q imbalance correction and provides an adaptive decision-directed FIR feed-forward equalizer of 41 taps for linear distortion compensation.

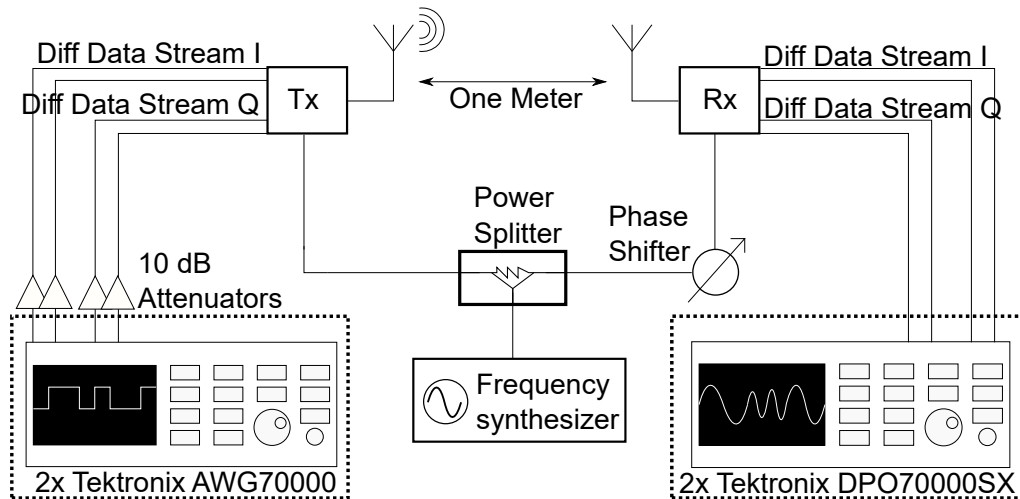


Figure 3.19.: Measurement set-up for the wireless communication link. After [own4]
© 2018 IEEE.

The AWG and the scope were initially connected back to back to find the quality of the used BB signal. The results are shown in Table 3.1, including the measured EVM, the BB signal BW where the signal spectrum has the first zero crossings, and the BW, where

90% of the signal power is contained. After a comparison between the measured channel BW (See Fig. 3.17) and the BW of the BB signal at the output of the AWG, it can be observed that the channel BW for linear operation barely matches the BW required for a link operating at 20 Gbauds, while the saturated channel extends the channel capacity to 25 Gbauds.

Table 3.1.: AWG performance

Symbol rate (Gbauds)	Roll-off factor	EVM (%)	First-zero BW (%)	90% power BW (GHz)
5	0.7	1.1	4.5	2.8
10	0.7	1.3	8.4	5.5
15	0.7	1.7	12.5	8.1
20	0.35	2.2	14.1	9.3
25	0.35	2.8	16.8	11.9
30	0.2	8.4	18.2	13.7
35	0.1	11.4	19.7	15.6
40	0.1	14	21.8	17.3
42.5	0.1	18.4	23.6	19.3

3.3.2. Measured Link results

The link was tested for LO frequencies ranging from 225 to 255 GHz for different modulation formats (QPSK, 16-QAM, and 64-QAM). For each of these LO frequencies and modulation formats, the data-rate was gradually increased until the link showed an EVM beyond the limit set in Chapter 2. In the QPSK experiment, a digital amplitude limiter was set up in the scope to mitigate any amplitude distortion and reduce the effective noise level. This limiter increased the QPSK link's performance but could not be applied to higher modulation orders, like 16- or 64-QAM. The IQ imbalance present in the link was pre-compensated at the AWG by offsetting its output power. The results of this test are gathered in Figs. 3.20, 3.21, and 3.22. Some exemplary constellations have been included in the plots. The constellations did not show any major linearity error (the constellation holds its square form and does not form a circle), neither IQ imbalance (The four sides of the constellation presented the same dimensions).

QPSK results. A maximum data-rate of 65 Gb/s at 230 and 235 GHz was achieved. The digital amplitude limiter increased the link performance for data-rates of 60 Gb/s and below. However, at 65 Gb/s, the digital amplitude limiter did not improve the link performance. The link operates beyond its theoretical BW limitation for QPSK, which according to Fig. 3.17 and Table 3.1 should be around 50 Gb/s. The operation beyond the theoretical BW is allowed by the tolerance of QPSK to errors in the link (Max EVM=32%).

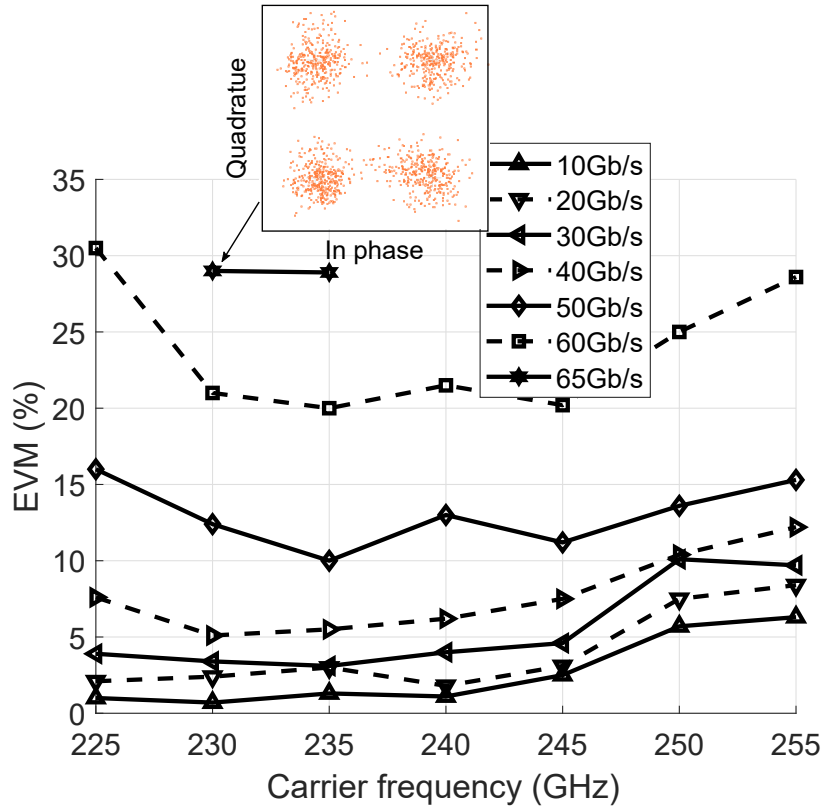


Figure 3.20.: EVM vs. LO frequency and data-rate for a 1-meter link using a QPSK modulation technique.

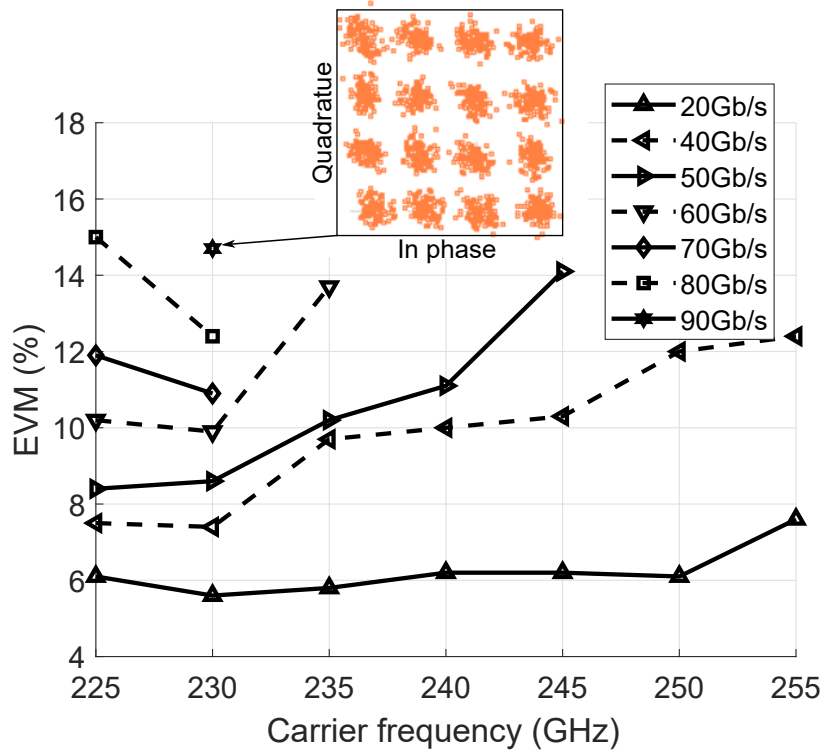


Figure 3.21.: Measured EVM vs. LO frequency and data-rate for a 1-meter link using a 16-QAM modulation technique.

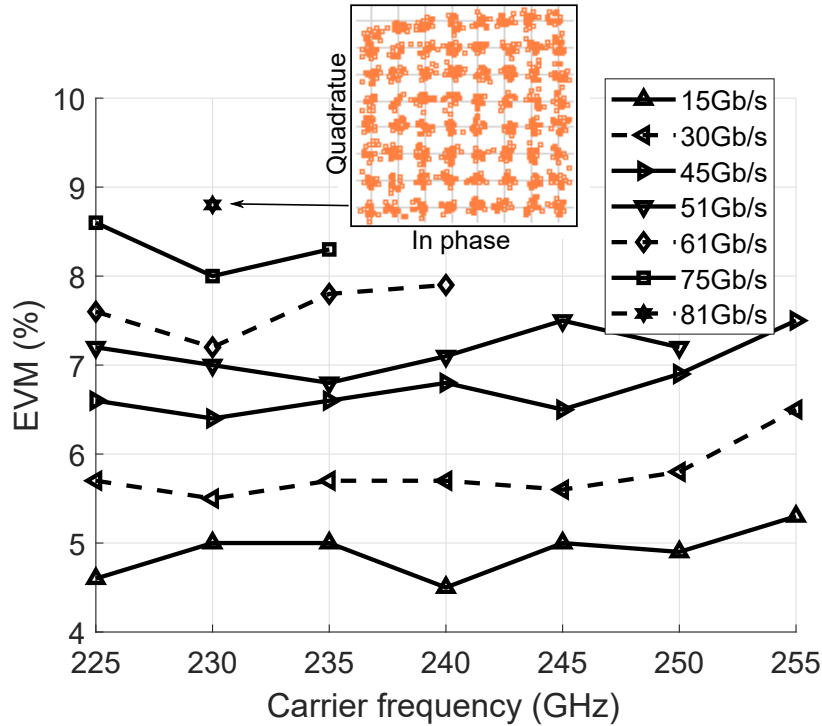


Figure 3.22.: Measured EVM vs. LO frequency and data-rate for a 1-meter link using a 64-QAM modulation technique.

For this modulation format, the amplitude does not carry information, only the phase does.

16- and 64-QAM results. A maximum data-rate of 90 Gb/s and 81 Gb/s was achieved using 16- and 64-QAM, respectively. Both modulation formats show a peak performance at 230 GHz, decreasing faster for other LO frequencies than in the QPSK case. The impossibility of applying a digital amplitude limiter and the lower tolerance to errors of these two formats explain this behavior.

3.3.3. EVM analysis

According to the measured Tx and Rx key parameters presented in Section 3.2, the performance of the wireless link should be very similar to the results depicted in Fig. 2.9. However, the measured performance is inferior to the one estimated from the SNR, meaning that something limits the link performance. This section will analyze all possible errors presented in the wireless communication link and evaluate its impact on the measured EVM. The possible sources of error are the measurement set-up, the SNR, the phase noise, the interference generated by the harmonic spurs, and the IQ cross-talk generated by the USB/LSB asymmetry. The EVM contribution of each of these errors will be cal-

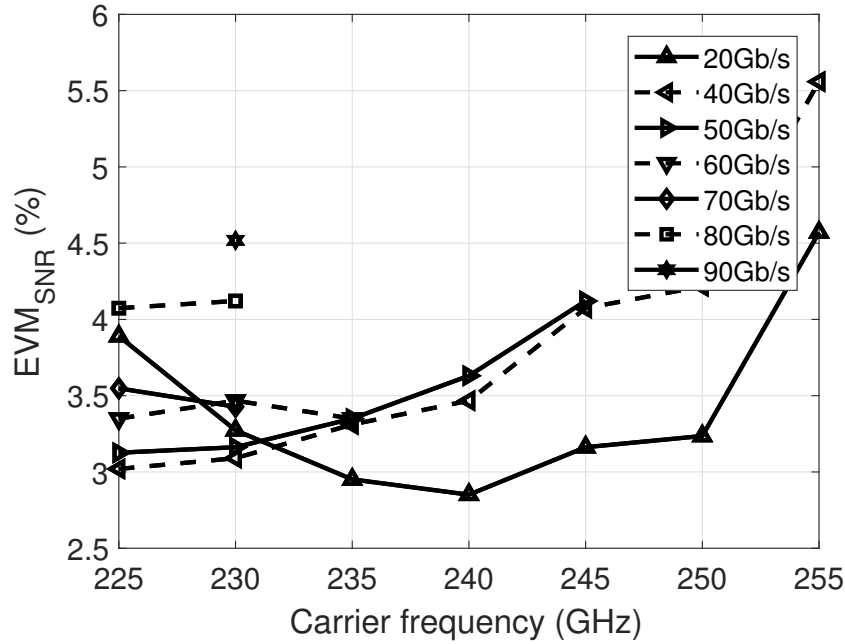


Figure 3.23.: Calculated contribution of the SNR to the EVM in a 1-meter distance link using 16-QAM.

culated and subtracted from the measured EVM to evaluate its influence on the link performance. The analysis presented will refer to 16-QAM due to its better performance, but the conclusions apply to all modulation formats.

SNR. As explained in Chapter 2, the SNR at the receiver output is mostly used as standard metric to estimate the link performance. The link budget calculation predicts an EVM generated by the SNR below 8% for a 1-meter distance, even for a BB signal BW of 15 GHz. However, it is possible that the signal power was lost due to unexpected reasons. The Rx's output signal and its noise level were digitized in the scope and post-processed in MATLAB to calculate the SNR at the Rx's output. Afterward, the SNR contribution to the EVM was calculated following Eq. 2.16. These calculation results are shown in Fig. 3.23 for all used carrier frequencies. Fig. 3.24 provides a comparison at 230 GHz of the EVM associated with the SNR estimated with the EVM expected from link budget calculation.

As it can be seen, the SNR contribution to the measured EVM is minor. A set of conclusions can be extracted from these results:

1. The wireless communication link is not SNR-limited. At 90 Gb/s, the SNR contribution to the final EVM is only 4.5% (SNR of 29.4 dB). With the link EVM threshold set to 17%, the EVM contribution to the SNR could scale up to 8.5% before trespassing this limit. This EVM is associated with an SNR of 21.4 dB. Therefore, the link

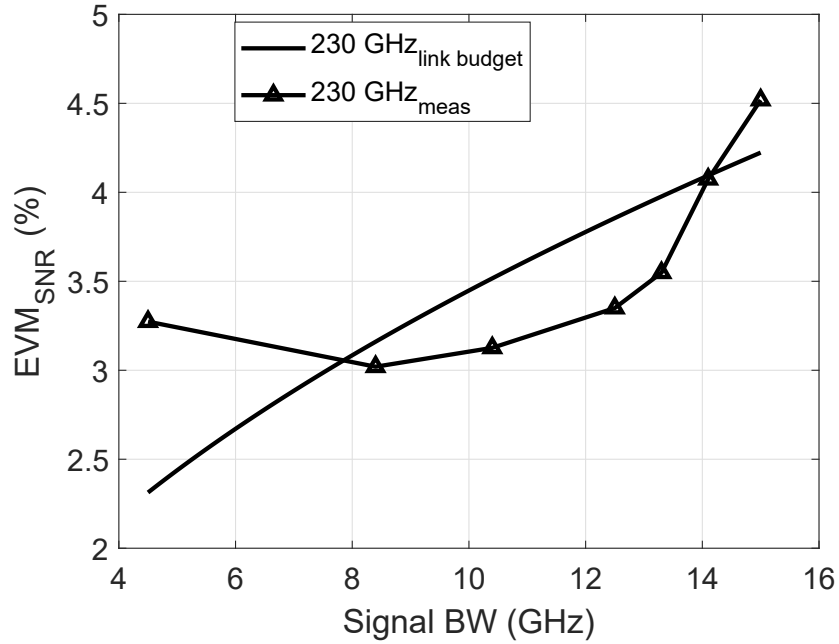


Figure 3.24.: Comparison between estimated and calculated influence of the SNR in the EVM in a 1-meter distance wireless link at 230 GHz.

distance could be extended up to 2.5 meters and will still operate for a data-rate of 90 Gb/s. If only the SNR would affect the link EVM, the distance could be extended to 5 meters for a data-rate of 90 Gb/s.

- As it can be seen in Fig. 3.24, the link budget calculation predicts the influence of the SNR in the EVM of the system at 230 GHz quite accurately. However, it shows a significant discrepancy for lower modulation bandwidths. The noise contribution is not flat along with the complete BW as it was expected from Eq. 2.19 (it does not behave as predicted by the Johnson-Nyquist noise theorem). Due to the Rx's band-pass characteristic, most of the noise power is allocated in the first 5 GHz of the signal bandwidth, with little contribution from the higher BB frequencies.
- The link performance varies drastically over LO frequency, and the EVM generated by the SNR does not explain this behavior. Two of the previously measured system impairments can cause this LO-frequency-dependent behavior: The harmonics spurs present at the output $\times 16$ LO generation path and the IQ cross-talk generated by the asymmetry between the USB and the LSB.

The EVMs generated by the SNR and the measurement set-up (presented in Table 3.1) are already known. These two errors can be subtracted from the measured EVM in the link to arrive at the aggregated EVM excess $EVM_{aggregated}$, given as

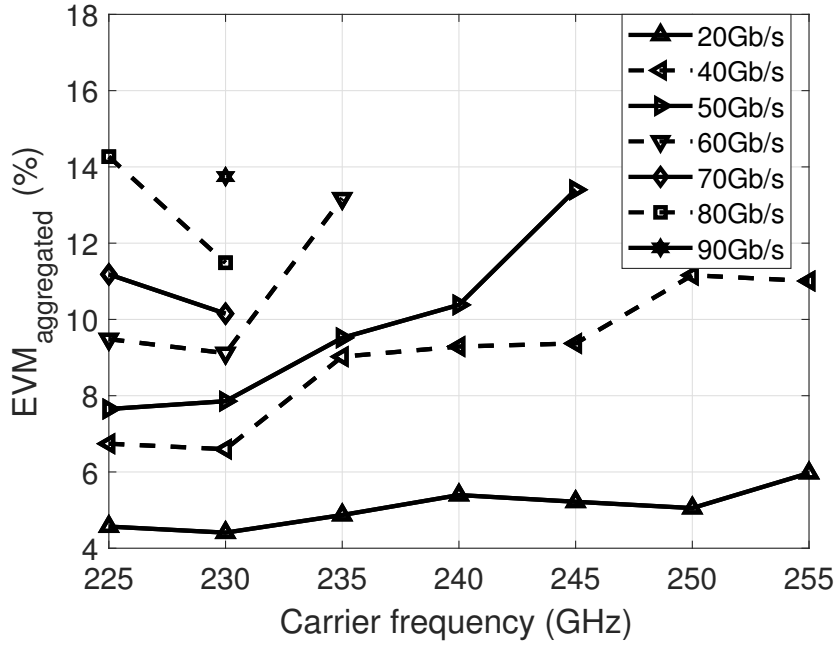


Figure 3.25.: Calculated aggregated EVM excess after subtracting the influence of the measurement set-up and the SNR for a 1-meter distance 16-QAM link.

$$EVM_{aggregated} = \sqrt{(EVM_{meas})^2 - (EVM_{SNR})^2 - (EVM_{AWG})^2}, \quad (3.2)$$

where the EVM_{meas} is the measured EVM in the wireless communication link presented in Fig. 3.21, the EVM_{SNR} is the contribution of the SNR to the final EVM, shown in Fig. 3.23, and EVM_{AWG} the contribution of the measurement set-up to the final EVM. The aggregated EVM illustrates the influence of these impairments in the wireless communication link. An aggregated EVM close to the measured EVM means that there is at least one dominant error in the link that was not considered in the calculation. The results of evaluating Eq. 3.2 are shown in Fig. 3.25. The influence of the SNR and the measurement set-up in the measured EVM are significantly reduced, and its influence decreases with the data-rate. For a carrier frequency of 230 GHz, at 20 Gb/s, the remaining $EVM_{aggregated}$ contributes with a 4.5% of the 5.8% final EVM, while at 90 Gb/s the $EVM_{aggregated}$ represents 13.8% of the total 14.7% link EVM, meaning that the previously mentioned errors contribute little to the EVM present in the wireless link.

Phase noise. The influence of the phase noise in wireless communication is well known [78], [79]. Its influence on the EVM (EVM_{PN}) has been previously quantified in [48] as

$$EVM_{PN} = \sqrt{2 + 2 \cdot \exp\left(-\frac{\sigma}{2}\right)}, \quad (3.3)$$

where σ is the phase noise error in radians. However, due to the relatively small available bandwidth of the wireless links implemented at lower carrier frequencies, most of the studies focus on the influence of the close-carrier phase noise (up to 100 MHz) on the EVM, ignoring the influence of the noise floor. As opposed to these narrow-band channels at low LO frequencies, in this case, the LO phase error deteriorates quickly not only by carrier frequency up-scaling to frequencies beyond 200 GHz but also due to the influence of a broadband noise floor in the LO generation path scaling nearly linear with the modulation bandwidth [80], [81]. Assuming that the noise floor of the synthesizer scales in the same way as the close-carrier phase noise presented in Fig. 3.15, the overall phase noise error σ in radians can be calculated as

$$\sigma = \sqrt{2 \cdot \int_{1\text{Hz}}^B PN(f) df}, \quad (3.4)$$

where $PN(f)$ is the phase noise function and B is the signal bandwidth. This integral can be divided into two different parts: the close-carrier $CC(f)$ phase noise and the broadband noise floor. The result is given as

$$\sigma = 16 \cdot \sqrt{2 \cdot \int_{1\text{Hz}}^{100\text{MHz}} CC(f) df + \int_{100\text{Hz}}^B \text{NoiseFloor} df} = \quad (3.5)$$

$$= 16 \cdot \sqrt{2 \cdot (2.977 \cdot 10^{-7} + 10^{-15} \cdot B)}. \quad (3.6)$$

The $\times 16$ -factor accounts from the multiplication factor of the $\times 16$ LO generation path. Combining Eq. 3.3 and Eq. 3.6, the influence of the phase noise in the EVM can be expressed as a function of the BB signal bandwidth B as

$$EVM_{PN} = \sqrt{2 + 2 \cdot \exp\left(-\frac{16 \cdot \sqrt{2 \cdot (2.977 \cdot 10^{-7} + 10^{-15} \cdot B)}}{2}\right)}. \quad (3.7)$$

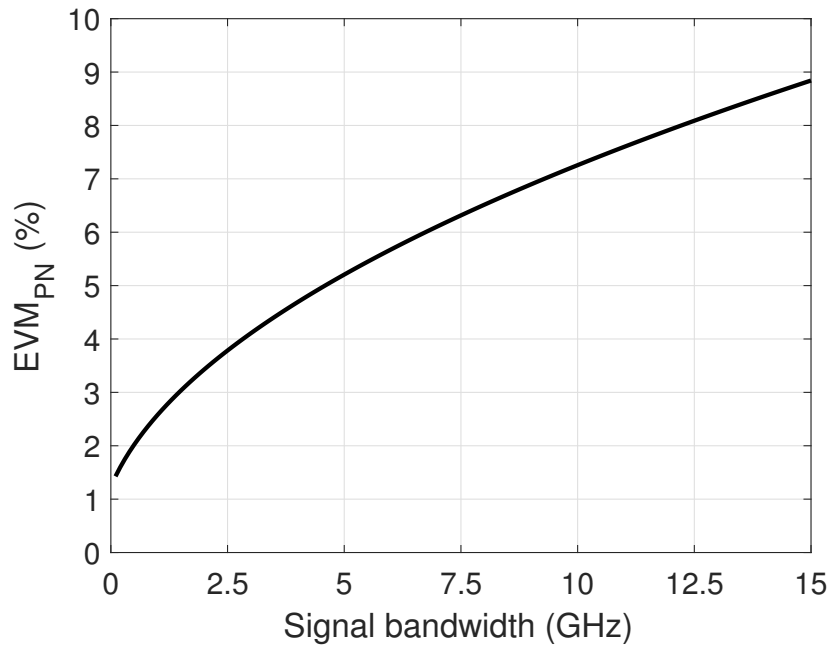


Figure 3.26.: Calculated EVM generated by the phase noise vs. BB signal BW.

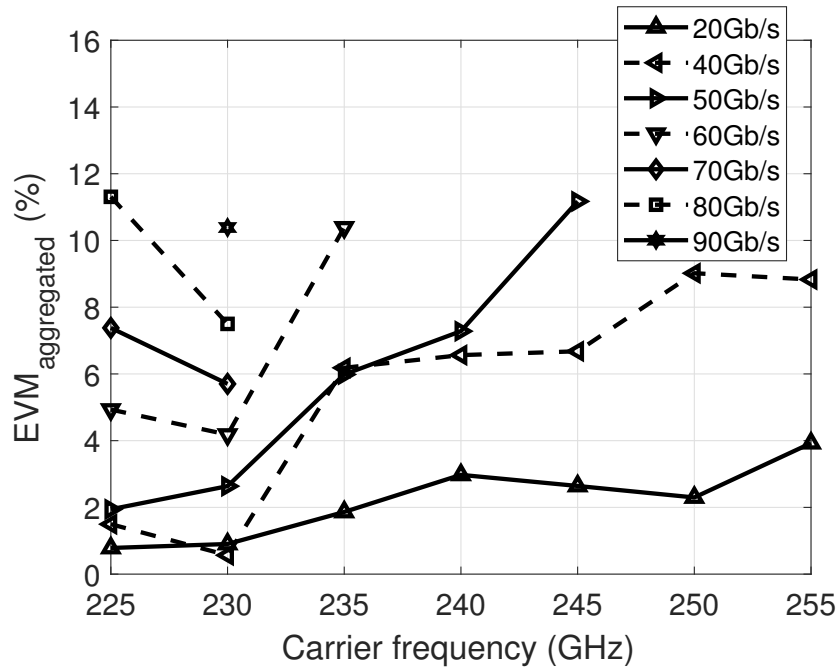


Figure 3.27.: Calculated aggregated EVM excess after subtracting the influence of the measurement set-up, SNR and phase noise for a 1-meter distance 16-QAM link.

The results of evaluating Eq. 3.7 are presented in Fig. 3.26. The first conclusion that can be extracted from this diagram is that the phase noise limits the maximum modulation order. Even for data-rates with a reduced BW of 2.5 GHz, the EVM contribution of the phase noise scales to almost 4%. This EVM level prevents the operation of any modulation with an order beyond 64-QAM. The influence of the EVM generated by the phase noise can now be removed from the measured EVM in the wireless link by applying Eq. 3.8. The results of evaluating this equation are presented in Fig. 3.27.

$$EVM_{aggregated} = \sqrt{(EVM_{meas})^2 - (EVM_{SNR})^2 - (EVM_{AWG})^2 - (EVM_{PN})^2}. \quad (3.8)$$

At 230 GHz, the influence of these three factors (measurement set-up error, SNR, and phase noise) is the only source of error for data-rates below 60 Gb/s. Higher data-rates require more RF BW to operate appropriately. For example, 60 Gb/s requires an RF bandwidth of $2 \times 12.5 \text{ GHz} = 25 \text{ GHz}$, which is not available at the Rx side. For other LO frequencies, the system performance degrades beyond the limit set by these three parameters. Although one possible explanation for this could be the lack of RF bandwidth, which is more pronounced at higher LO frequencies, it makes sense to explore other possibilities, such as the spectral purity of the $\times 16$ LO generation path to discard them as an important source of error.

LO harmonics. As it was explained in Section.3.2, an inherent drawback of the chosen LO generation method with a high multiplication factor is the potential presence of false BB replicas in a spectral distance equal to integer multiples of an external signal drive frequency, which is 13.75–16.25 GHz in the current implementation. When self-mixed, these harmonics will produce interference that will land at the same BB frequency as the desired signal. Moreover, the adjacent mixing products alias with the main modulation spectrum for sufficiently high data-rates with no space for filtering at the Rx output. This second interference occurs only for data-rates with a BW greater than $(13.75\text{--}16.25)/2 \text{ GHz}$, which for 16-QAM means that only data-rates of 60 Gb/s and beyond are affected. The spectral process generating the harmonic interference is illustrated in Fig 3.28. The EVM contribution of these harmonics will be analyzed as if they would set an interference signal. This interference will set a signal-to-interference ratio (SIR). The EVM contribution of this SIR would be evaluated considering that the interference sets a second "noise floor". Therefore, to calculate the EVM, a modified version of the Eq. 2.16 is applied, where instead of the SNR the SIR is employed.

The contribution of the harmonic spurs to the measured EVM can be divided into two

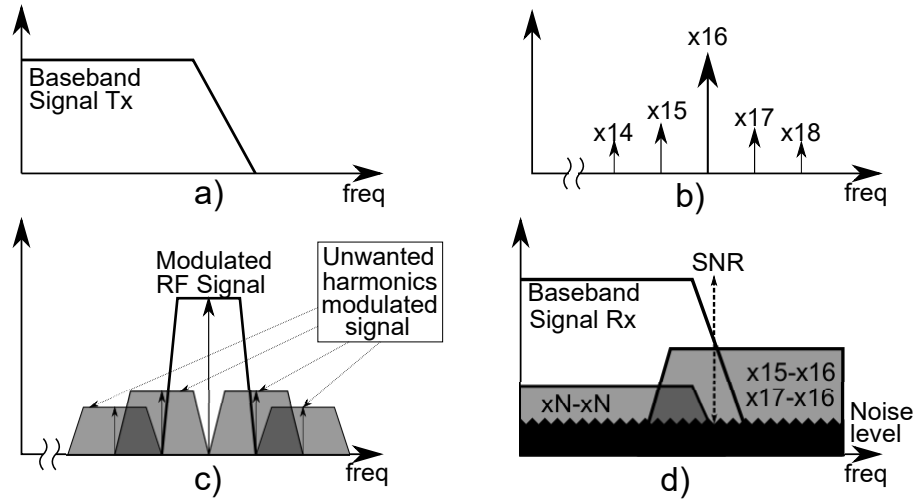


Figure 3.28.: Spectra of the a) baseband signal at the Tx input, b) harmonic spurs generated by the $\times 16$ multiplier chain, c) Modulated signal at the Tx RF output, and d) baseband signal at the Rx output. After [own7] © 2019 IEEE.

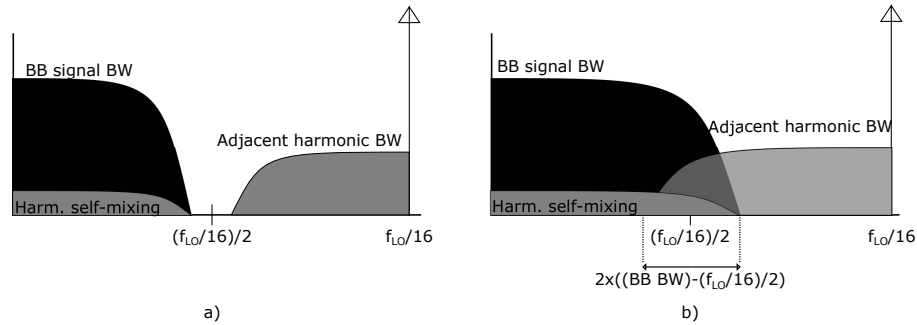


Figure 3.29.: Spectra of the harmonic interference at the output of the Rx for a) data-rate below 60 Gb/s and b) data-rates of 60 Gb/s and beyond.

different components. First, affecting all data-rates, only the self-mixing products will be taken into consideration. For low data-rates (below 60 Gb/s), this is the only source of EVM introduced by the harmonic spurs. Fig. 3.29 a) illustrates how this interference operates in the spectral domain. The SIR can be defined as the difference between the desired harmonic power (16×16) and the combined power of all other harmonics ($(14 \times 14) + (15 \times 15) + (17 \times 17) + (18 \times 18)$). Although these signals are not perfectly correlated, the power contribution of all harmonics will be added into a single interference signal as if they were perfectly correlated, leading to an overestimation of its influence [82]. Assuming that the power of the harmonics behaves as white Gaussian noise, the EVM contribution of this interference signal $EVM_{self\ harm}$ to the final EVM can be defined as

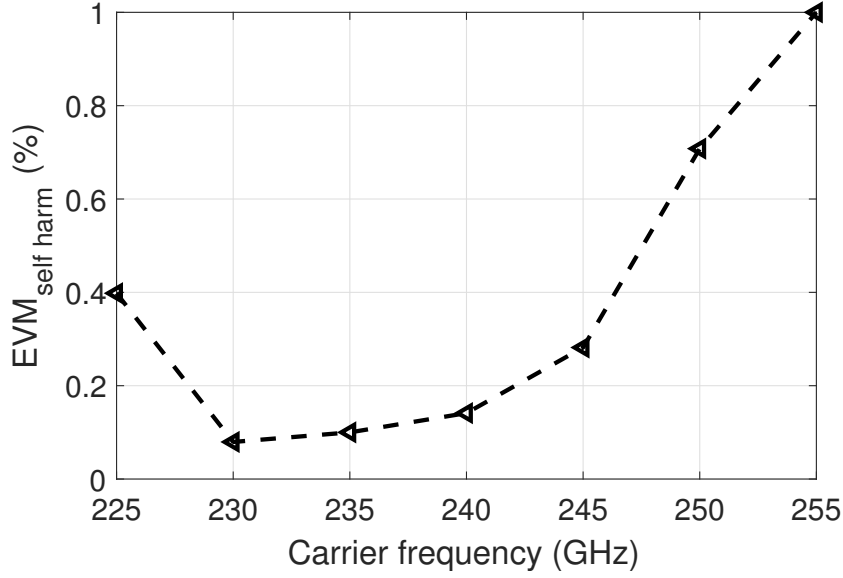


Figure 3.30.: EVM generated in the link by the harmonic self-mixing products.

$$EVM_{self\ harm} = \sqrt{\frac{1}{SIR_{self\ harm}}}, \quad (3.9)$$

where $SIR_{self\ harm}$ is the signal to interference ratio for the self-harmonic mixing products defined as

$$SIR_{self\ harm} = \frac{P_{Tx \times 16} \cdot CG_{Rx \times 16}}{\sum_{i=1}^N (P_{Tx \times N} \cdot CG_{Rx \times N}) - P_{Tx \times 16} \cdot CG_{Rx \times 16}}, \quad (3.10)$$

where $P_{Tx \times N}$ is the harmonic power and $CG_{Rx \times N}$ is the conversion gain depicted in Fig. 3.14 for the harmonic N. The results of evaluating Eq. 3.10 and Eq. 3.9 with the data from Fig. 3.14 are presented in Fig. 3.30. The influence of this error in the system EVM stays below 1% due to the accumulated harmonic rejection between the Tx and the Rx.

The second interference generated by the harmonic spurs is illustrated in Fig. 3.29 b). For data-rates of 60 Gb/s and beyond, the mixing products of the $\times 16$ with the adjacent $\times 15$ and $\times 17$ start aliasing with the BB signal at the Rx output. Assuming that this interference behaves as white Gaussian noise, its EVM contribution can be calculated as

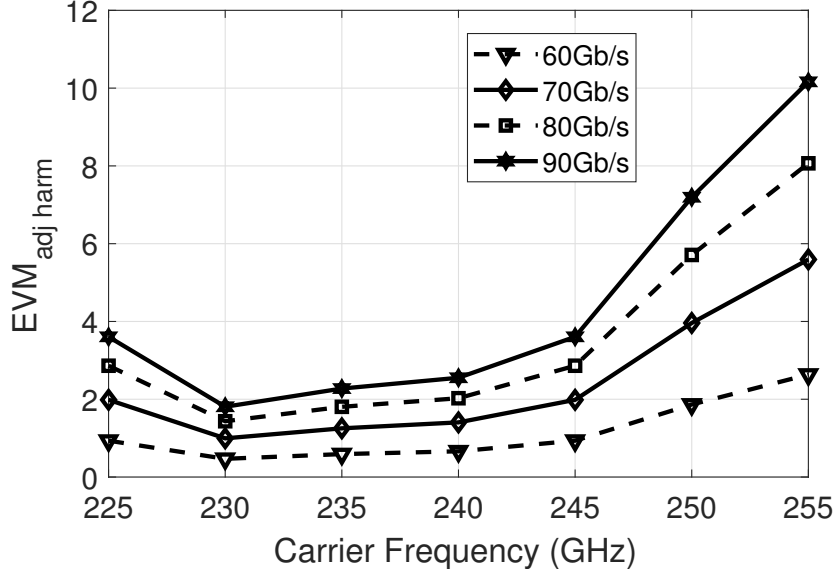


Figure 3.31.: EVM generated in the link by the adjacent harmonic products.

$$EVM_{adj\ harm} = \sqrt{\frac{1}{SIR_{adj\ harm}}}, \quad (3.11)$$

where $SIR_{adj\ harm}$ is the signal to interference ratio generated by the adjacent harmonics. The BW of this interference is dependent on the BB signal BW and the LO frequency. The fraction of signal BB B_{frac} that is affected can be defined as

$$BB_{frac} = \frac{2 \cdot (B - (f_{LO}/16)/2)}{B}, \quad (3.12)$$

where B is the BB signal BW, f_{LO} is the LO frequency. The power difference between the desired harmonic and the interference signal can be extracted from Fig. 3.14 and calculated as

$$SIR_{adj\ harm} = \frac{BB_{frac} \cdot (P_{Tx \times 16} \cdot CG_{Rx \times 16})}{P_{Tx \times 15} \cdot CG_{Rx \times 16} + P_{Tx \times 16} \cdot CG_{Rx \times 15} + P_{Tx \times 16} \cdot CG_{Rx \times 17} + P_{Tx \times 17} \cdot CG_{Rx \times 16}}, \quad (3.13)$$

where $P_{Tx \times M}$ and $CG_{Rx \times N}$ are the harmonic measured power and conversion gain, respectively. The EVM generated by the adjacent harmonic spurs for different LO frequencies and data-rates is illustrated in Fig. 3.31.

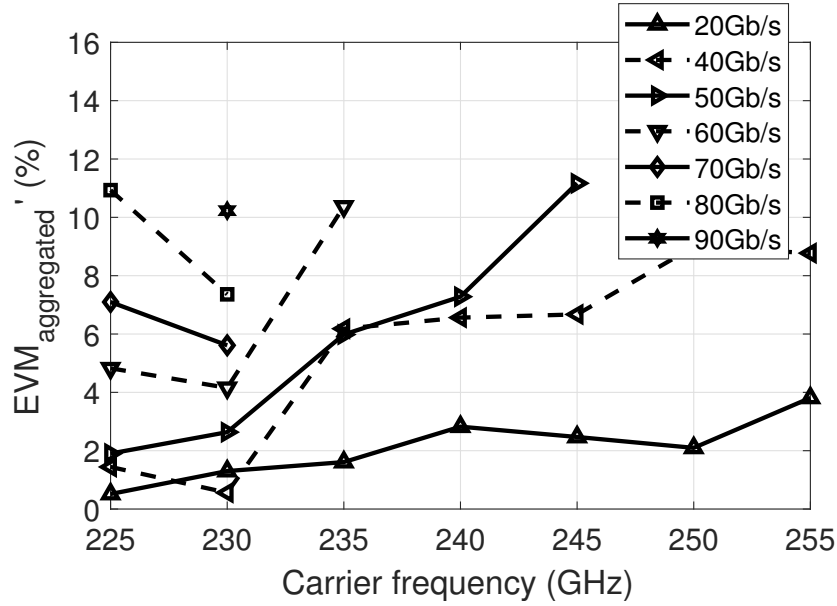


Figure 3.32.: EVM excess after subtracting the influence of the measurement set-up, SNR, phase noise and harmonic interference for a 1-meter distance 16-QAM link.

At 230 GHz, the adjacent harmonic interference creates an EVM below 2% for a data-rate of 90 Gb/s. As it can be observed, the major influence of the adjacent harmonic product happens in the upper edge of the operating band, where the harmonic rejection is reduced. However, the link did not operate at such LO frequencies above 50 Gb/s. The remaining aggregated EVM in the link $EVM'_{aggregated}$ after subtracting the contribution of the interference generated by the harmonic spurs can be calculated from Eq. 3.8, Eq. 3.30 and Eq. 3.31 as

$$EVM'_{aggregated} = \sqrt{(EVM_{aggregated})^2 - (EVM_{self\ harm})^2 - (EVM_{self\ harm})^2}. \quad (3.14)$$

The results of evaluating this equation are presented in Fig. 3.32. The EVM reduction after subtracting the influence of the multiple interferences of the harmonics does not improve substantially from the one presented in Fig. 3.27. In fact, after evaluating the data presented here, it can be concluded that the harmonic spurs generated at the LO chain have a minor contribution. The only remaining impairment to be analyzed is the IQ-cross-talk.

IQ cross-talk The IQ cross-talk is the only remaining source of error in the wireless link. However, its influence is difficult to quantify. If the I-Q leakage were taken as an interference signal, as it was assumed for the harmonic spurs, the EVM generated by this

IQ cross-talk interference would be much higher than the measured EVM (on the level of 30% for a data-rate of 90 Gb/s). This leakage signal can not be considered as simple interference. The I output leakage is directly correlated with the BB signal at the Q output and vice-versa, setting a signal at the output that could be considered as a vector in the complex IQ plane composed of both components, the desired signal and leakage. In the digital domain, the demodulator and the equalizer rotate this vector to deconvolve the I and Q components. However, the effectiveness of this technique is not easily quantifiable. The adaptive decision-directed FIR feed-forward equalizer of 41 taps creates a filter with 41 coefficients following a least mean square algorithm (LSM). This algorithm equalizes a linearly modulated baseband signal through a dispersive channel. However, its performance de-correlating the IQ channels has not been evaluated.

There is no analytic function to evaluate the influence of the I-Q cross-talk in the link performance. However, if the IQ cross-talk is responsible for the remaining aggregated EVM excess, a Tx or an Rx with a broader and flatter 3-dB RF BW could minimize both the leakage power and the frequency dependency of the I-Q cross-talk, potentially improving the link quality and the maximum achievable data-rate.

3.4. Conclusions

A wireless link operating at frequencies beyond 200 GHz capable of achieving a data-rate of 90 Gb/s over a 1-meter distance link was presented. The link was established using Tx and Rx RF front-end modules whose chips were implemented with an advanced SiGe HBT technology and packaged following an inexpensive COB scheme. The link was found not to be limited by the SNR available in the system but by other factors:

1. The SNR contribution to the final EVM of the wireless link is not significant. Even accounting for all the EVM contributions of all impairments, the system could achieve a data-rate of 90 Gb/s over a 2.5 meter distance. If only the SNR would affect the EVM of the link, the distance could be extended to 5 meters for a data-rate of 90 Gb/s.
2. The phase noise error introduced by the noise floor of the frequency synthesizer prevents any modulation order beyond 64-QAM from operating. Any BB signal with a BW of at least 2.5 GHz will immediately show an EVM of 4% due to the phase noise.
3. The EVM associated with the harmonic spurs interference has a minor contribution to the system's final EVM. A harmonic spur rejection of at least 20 dB is enough to minimize the influence of this error.
4. The 3-dB RF BW of the Tx and the Rx is the key parameter to be optimized. A higher 3-dB RF BW will provide enough space to accommodate a higher data-rate with broader BB signal BW. Furthermore, a higher and flatter 3-dB RF BW will reduce the IQ cross-talk, decreasing the EVM associated with this impairment.

Two different paths can be followed to achieve higher data-rates. The first is to increase the modulation order. However, the phase noise error introduced by the noise floor of the frequency synthesizer can not be easily reduced. The used synthesizer offers the best performance in the market. Therefore, this option is discarded. The targeted objective will be to increase the RF BW of the narrowest element, the Rx. In the next chapter, a novel Rx with extended 3-dB RF BW will be presented, achieving a data-rate of 100 Gb/s.

Chapter 4

Mixer-First Receiver RF front-end

4.1. Introduction

From Chapter 3, it can be concluded that the phase noise error introduced by the broadband noise floor limits the maximum modulation order of the wireless communication link if more than 2.5 GHz of BB are used. The frequency synthesizer used to drive the LO generation path sets this error. Therefore it can not be easily addressed from the circuit design perspective. The only remaining approach to achieve higher data-rates is to enhance the 3-dB RF BW of either the Tx or the Rx to increase the symbol rate of low modulation orders, such as QPSK or 16-QAM. The main design challenge to achieve higher data-rates was related to the double-sideband operation principle of the IQ system, particularly the IQ cross-talk generated by the asymmetry between USB and LSB. This challenge is directly linked to the large RF operation BW. In an ideal IQ system with perfect symmetry between the USB and the LSB, the spectrum of the I channel present at the Q channel output of the Rx gets canceled due to destructive interference and vice-versa. If this symmetry is not perfect, the channels will leak into each other (See Fig. 3.18). This symmetry condition is tough to achieve at these frequencies in silicon technologies, specifically for amplification stages with a limited gain-BW product.

This chapter presents a new wireless link operating at frequencies beyond 200 GHz. The wireless communication link presented in this chapter replaces the amplifier-first Rx with a mixer-first Rx. The mixer-first Rx features an improved symmetry between the USB and LSB for the entire LO tuning range of 225-255 GHz, but worse CG and NF. With this mixer-first Rx, the highest data-rate for a single link based on silicon-technologies above 200 GHz was achieved, reaching 100 Gbps in a 1-meter distance wireless link.

Despite a reduced CG from 24 to 8 dB and an increased NF from 10 to 14 dB, the finally achieved data-rate was higher thanks to its superior 3-dB RF BW. The mixer-first Rx was fabricated in an experimental 0.13- μm SiGe HBT technology developed in the frame of the DOTSEVEN project [34].

This chapter is organized as follows. Section 4.2 introduces the mixer-first architecture, including the design details of the down-conversion mixer. The RF performance of the Rx is reported in Section 4.3. The wireless link results are presented in Section 4.4, including an EVM analysis similar to the one presented in Chapter 3. Finally, conclusions are drawn in Section 4.5. The here presented results and figures have been originally published in [own2], [own8], [own12], [own13] and the copyright has been transferred to IEEE and Cambridge University Press.

4.2. Mixer-First Rx Architecture

The proposed architecture for the mixer-first Rx is presented in Fig. 4.1, including a chip-micrograph of the receiver and a picture of the fully-packaged Rx RF module. The 1-meter distance link's main limitation was not the SNR but the USB and LSB asymmetry. The main generator of USB and LSB asymmetry was the RF PA used instead of an LNA in the amplifier-first Rx down-conversion path. At this frequency band, the LNA NF is not good enough to justify the limitation in RF BW that the LNA introduces [own3] [83]–[85]. Furthermore, due to the limited contribution of the SNR to the final EVM, a minor deterioration in the NF of the Rx would not have a significant effect on the final measured EVM in a 1-meter distance link.

The Rx chip includes an on-chip $\times 16$ LO generation path, which allows wide-band 225–255 GHz tuning of the LO carrier with an external on-board reference drive around 13.75–16.25 GHz. The LO path consists of 4 cascaded Gilbert-cell doublers followed by a differential 3-stage PA to ensure enough signal drive at the mixer input. The LO quadrature is provided through a broadband hybrid coupler. The down-conversion path consists of a double-balanced IQ switching-quad mixer followed by a BB amplifier to provide broadband CG characteristics for the entire LO tuning range. The Rx chip also includes an on-chip ring antenna radiating through the substrate into a high-resistivity hyper-hemispherical 9-mm diameter silicon lens. The chip-on-lens assembly is mounted and wire-bonded on a Rogers 4350B PCB backside with a recess to accommodate the chip. An 8-section stepped-impedance low-pass filter is implemented on the PCB to compensate for the wire-bond inductance, limiting the BB BW to 14 GHz.

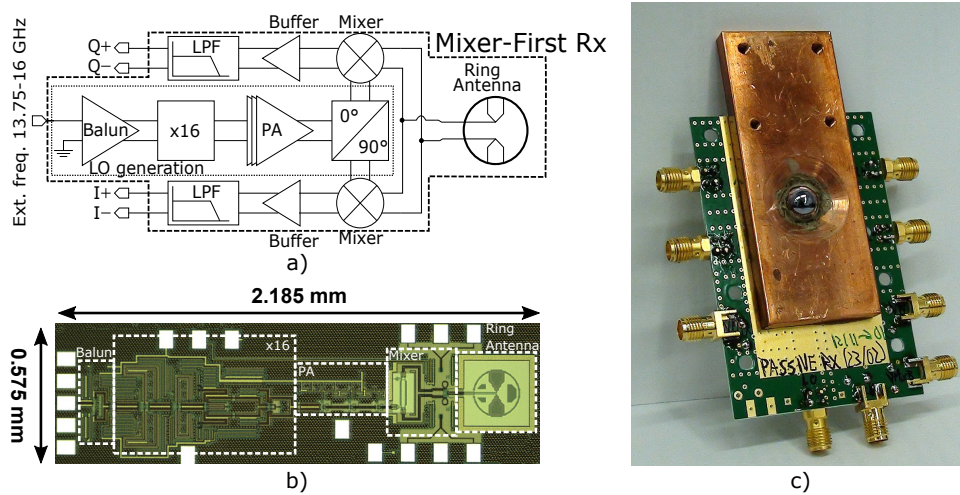


Figure 4.1.: a) Block diagram of the mixer-first Rx, b) Rx chip-micrograph, and c) picture of the fully package Rx RF front-end module. After [own2] © 2018 Cambridge University Press.

The $\times 16$ LO generation path, the antenna, and the packaging concept are described in more detail in Chapter 3. The novelty in this Rx lies in the down-conversion quadrature mixer. The mixer's design goal is to maximize the 3-dB RF BW while keeping the noise figure low and the conversion gain high enough to isolate the noise contribution from the following components in the receiver chain. The down-converted BB signal interfaces a high-speed PCB through a differential BB amplifier that acts as a buffer, providing a broadband 100Ω differential output match.

4.2.1. Down-Conversion Stage Design and Simulated Results

Fig. 4.2 shows the double-balanced fundamentally-operated down-conversion mixer with the BB amplifier used at the outputs of both IQ channels. In comparison to the standard Gilbert-cell mixer topology presented in Chapter 3, the transconductance stage has been removed, eliminating the capacitive internal node between this stage and the switching-quad, leading to an improvement in the RF operating bandwidth of the down-conversion mixer. A comparison between the two different down-conversion mixer topologies can be found in [85]. In order to operate the mixer with the maximum CG and minimum NF, the switching-quad has to be biased around the onset of active forward operation, and the LO drive at the base nodes must be sufficient to minimize the time when both quads differential pairs are on during the LO transition events. This design increases the 3-dB BW of the mixer, although the gain provided by the transconductance stage disappears. Therefore, the receiver conversion gain's realization has to be moved to the baseband. A dc-coupled differential amplifier has been added to increase the receiver's gain and match

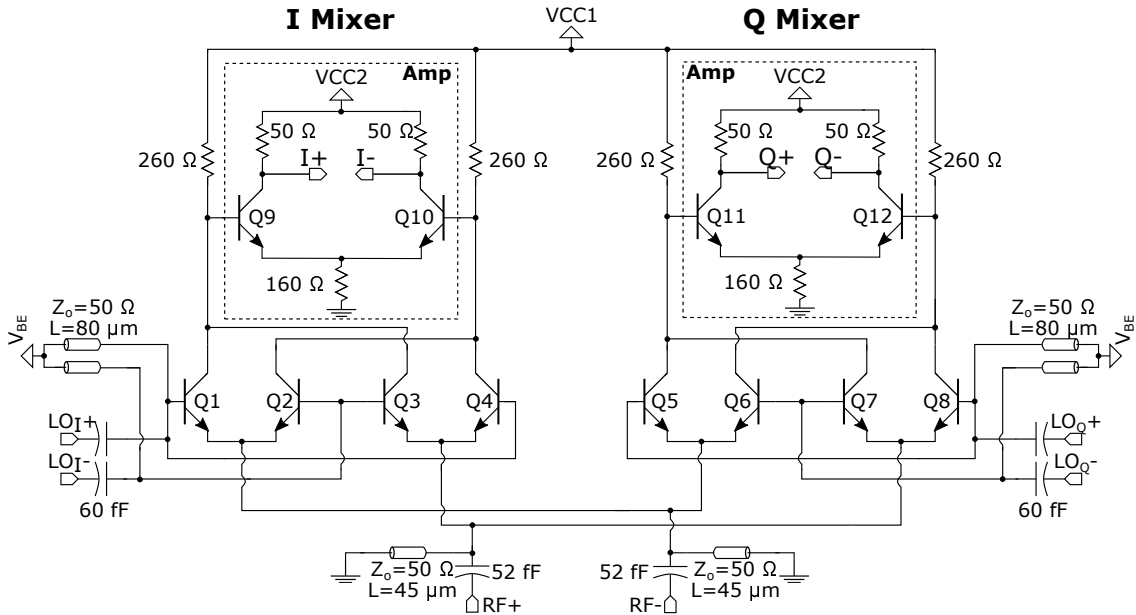


Figure 4.2.: Block diagram of the mixer-first receiver. Modified after [own2] © 2018 Cambridge University Press.

the output impedance to differential 100 Ω.

The size for all transistors included in the mixer and the baseband amplifier are twice the minimum size ($0.96 \times 0.10 \mu\text{m}^2$). The emitter-fed RF input presents an impedance profile constant for the whole operational frequency. The RF matching network consists of a shorted 50 Ω stub of 45 μm, also used as a dc path, and a series MIM-capacitor of 52 fF. The LO matching network includes a 50 Ω transmission line of 80 μm, used for base biasing as well, and a series MIM-capacitor of 60 fF. The resistors at the collectors of the switching quad are used as BB output loads. The value of 260 Ω was chosen as a compromise between CG and BW. The mixer output has been connected (dc-coupled) to the BB amplifier input. This node sets a trade-off between the conversion gain, noise figure, and BB bandwidth. The 160 Ω resistor shifts the dc-level at the emitter of the differential pair for proper biasing. The 50 Ω load resistors at the amplifier collectors set the output impedance to differential 100 Ω for proper interface with the PCB.

To set the optimum operating point of the chip, contour plots of the conversion gain and the noise figure against the mixer V_{BE} and the LO power at the input of the hybrid have been analyzed at 240 GHz (Fig. 4.3). The optimum operating conditions for the minimum noise figure are marked in red. This simulation includes the hybrid, the mixer, and the BB amplifier. The HICUM transistor model [86] has been used for all simulations. For optimum performance in both parameters, the LO power needs to be maximized to provide hard-switching conditions in the quad. The mixer V_{BE} ranges between 0.58-0.65 V, providing a low static bias current to minimize the noise figure. The mixer alone

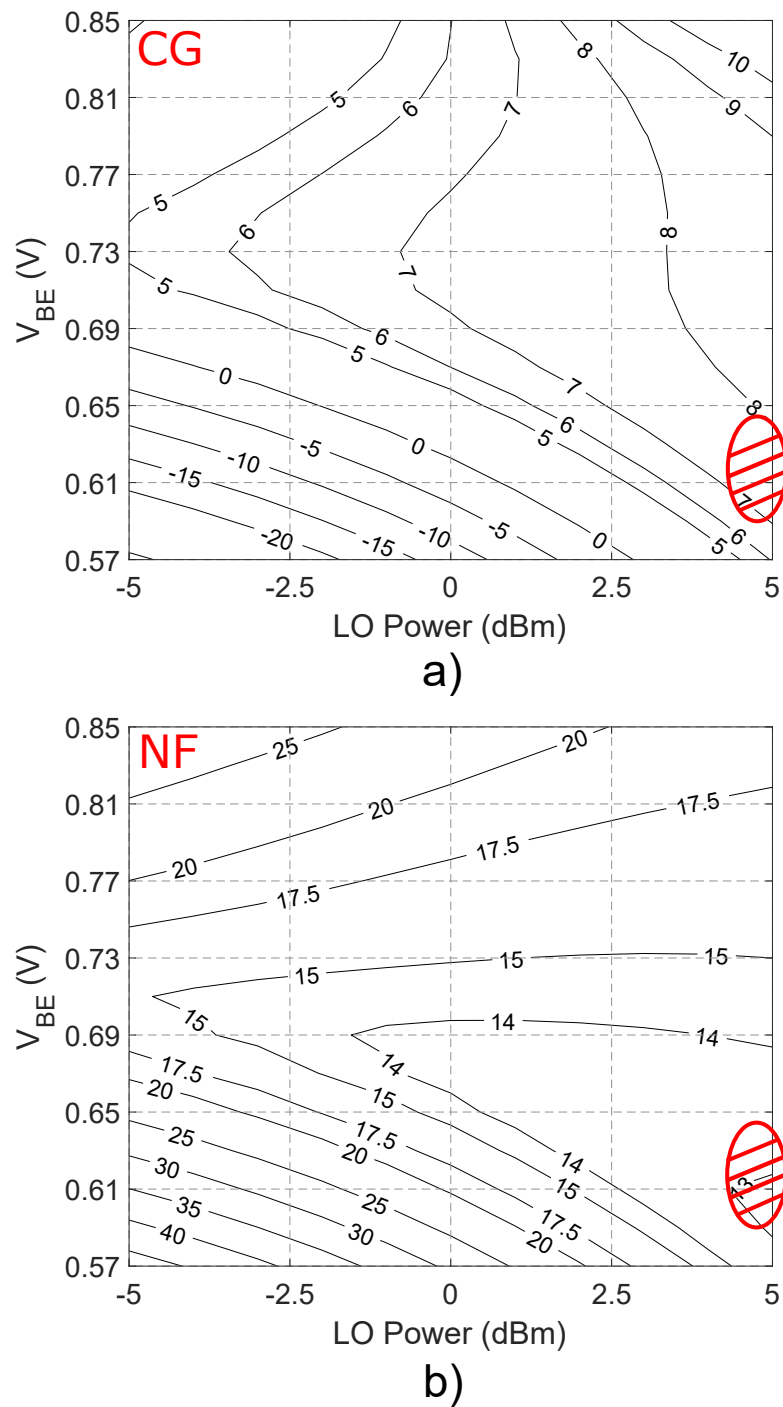


Figure 4.3.: Contour plot of the CG a) and NF b) for both IQ channels combined versus LO power at the input of the hybrid and the mixer V_{BE} . The operating region is marked in red. After [own2] © 2018 Cambridge University Press.

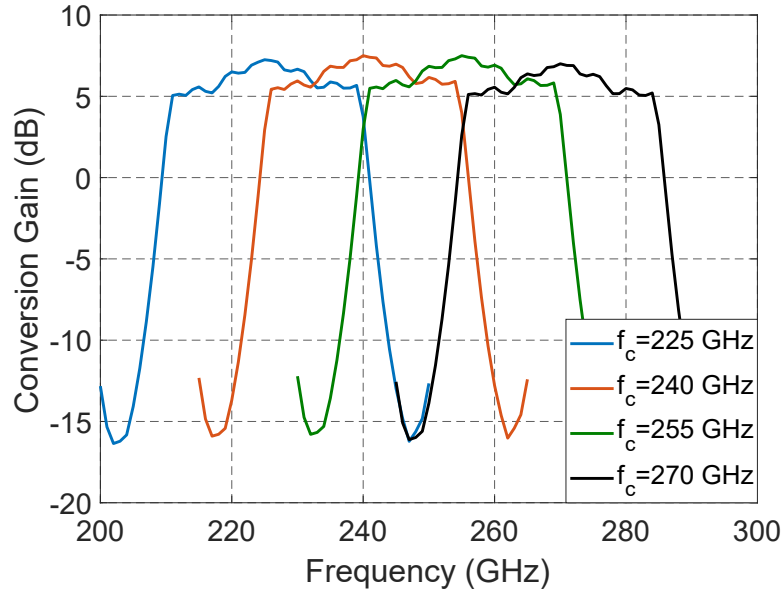


Figure 4.4.: Simulated RF BW for the IQ combined for different LO frequencies. The simulated RF BW is 28 GHz for all carrier frequencies. The simulated CG variation between different LO frequencies stays below 2 dB. The simulation frequency is 240 GHz. After [own2] © 2018 Cambridge University Press.

has a simulated 3-dB RF BW that exceeds 70 GHz with a conversion gain of 0 dB and a noise figure of 11 dB. Together with the BB amplifier, the mixer has a simulated 3-dB RF bandwidth of 36 GHz, which converts to a baseband output bandwidth of 18 GHz. The on-board filter limits the baseband 3-dB bandwidth to 14 GHz (See Chapter 3). Therefore, no more bandwidth on-chip is required. The simulated RF BW and CG of the complete down-conversion path (mixer, BB amplifier, and PCB filter) are presented in Fig. 4.4. The simulated peak CG for the entire chip is 8 dB and the minimum NF 13 dB. The mixer consumes a current of 10.5 mA and the buffer 15.4 mA from a 2.5 V and 3.2 V power supply, respectively.

4.3. RF characterization

Two different groups of RF measurements have been performed. The first encompasses a set of single-tone measurements allowing separate investigation of the frequency-dependent lower- and upper-sideband characteristics for key mixer-first Rx performance metrics. In the second, the measurements involve a combined operation of the Tx and Rx modules configured into a free-space back-to-back line-of-sight set-up. Here, both double-sideband quadrature up-conversion and down-conversion are performed between the BB Tx inputs and the Rx outputs, supporting a study of the influence of the IQ cross-talk leakage. All measurements have been taken in free-space and at the board level, including the influence of all on-board and on-chip components cascaded between the on-board high-speed connector and the lens-coupled on-chip antenna. An absorbing material was applied to cover the major reflecting surfaces to minimize the influence of parasitic reflections in the measurement set-up.

4.3.1. Single-tone RF measurements of the Rx

A WR-03 (220-325 GHz) frequency extension module from OML, equipped with a linearly polarized horn antenna with a directivity of 20 dBi at 270 GHz, operating in the transmit mode was used to characterize the Rx. The output power of the OML module was previously calibrated. The characterization set-up for the Rx is depicted in Figs. 4.5. The differential BB output I and Q were fed through a broadband balun (BAL0026 Marki). For characterization of the IQ amplitude imbalance, the I and Q ports were driven separately, whereas for the total conversion gain and noise figures measurement in the upper and the lower sideband, a broadband (0.5–20 GHz) 90° hybrid (QH0226 Marki) was used after the baluns to combine the I and Q signals at the spectrum analyzer input. All key parameters of the mixer-first Rx RF front-end modules were de-embedded from the measurements using the Friis-Formula [59]. The losses of the baluns, hybrids, and interconnection cables were de-embedded from the measured results. The antenna directivity of the mixer-first RF front-end module was measured and verified to present similar values to the amplifier-first Rx, ranging from 25.2 to 27 dBi in the 220 to 270 GHz band.

The mixer-first Rx CG, BW, IQ imbalance, and NF were characterized. The noise figure was de-embedded using the indirect method (see Chapter 3) conversion gain and output noise assuming an input noise of -174 dBm/Hz. The results of this measurement are gathered in Fig. 4.6. The mixer-first RF shows a 3-dB RF BW of 26 GHz, a peak conversion gain of 8.1 dB, and a minimum SSB NF of 14 dB. Unlike the amplifier Rx or the Tx, the mixer-first Rx holds its performance for all possible LO frequencies in the

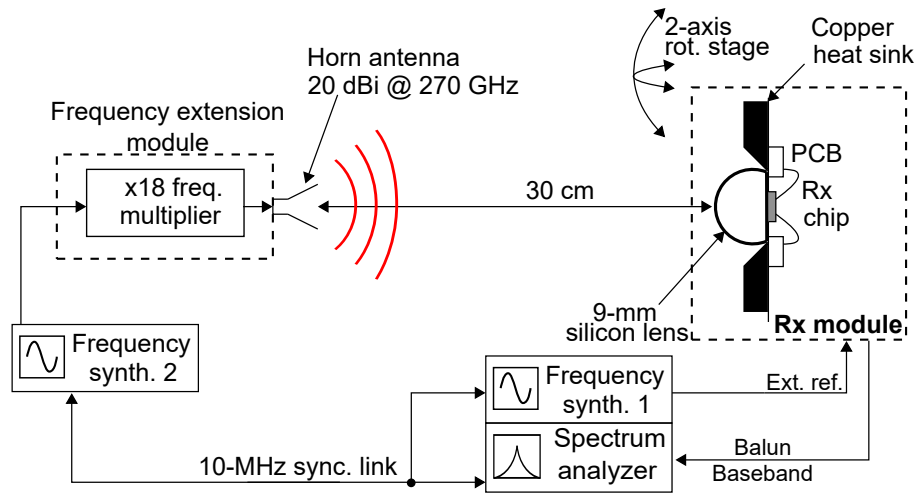


Figure 4.5.: Schematic of the measurement set-up used for the characterization of the Rx. After [own2] © 2018 Cambridge University Press.

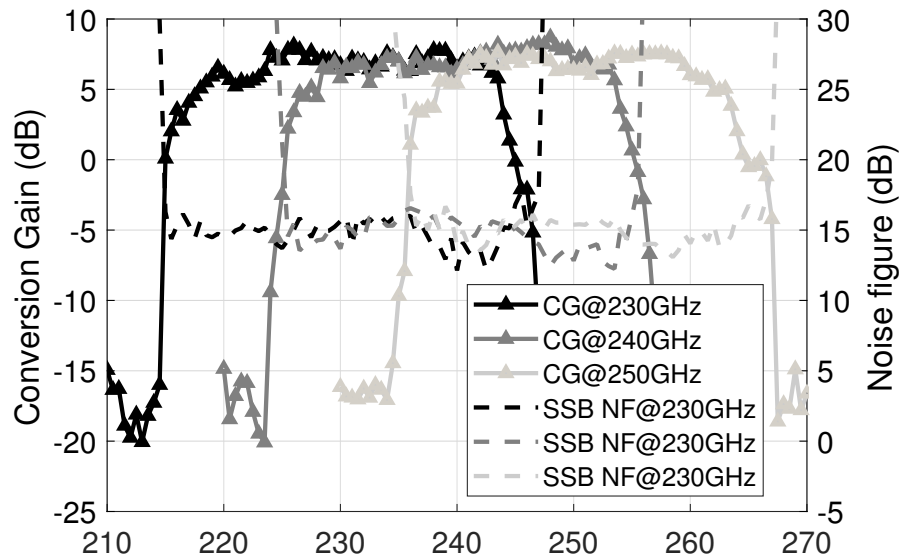


Figure 4.6.: Measured conversion gain and noise figure of the mixer-first Rx at 230, 240 and 250 GHz.

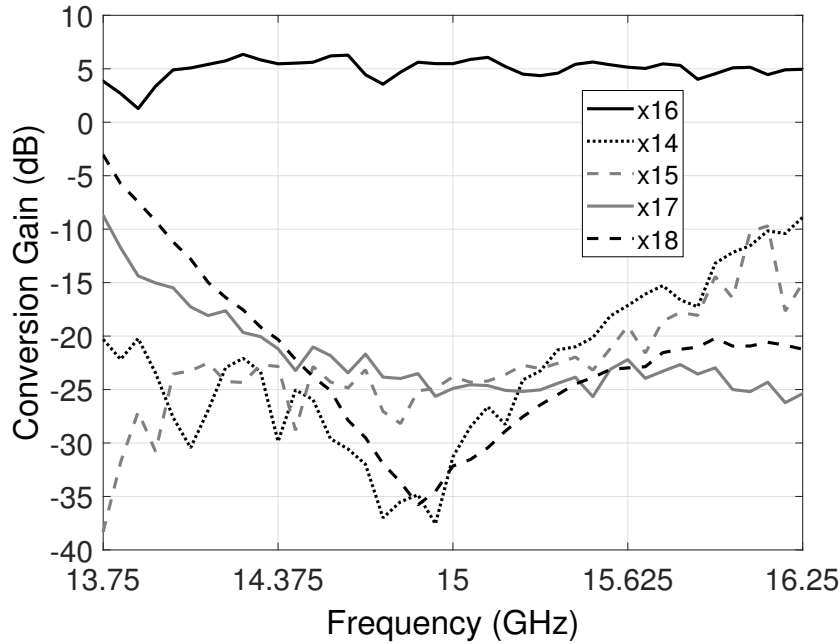


Figure 4.7.: CG of the different harmonics generated in the LO generation path vs. external LO drive frequency.

tuning range. The IQ imbalance was measured to be below 1 dB for all LO frequencies.

Additionally, the harmonic spurs level from the $\times 16$ LO generation path was also characterized. The results of this test are presented in Fig. 4.7. The harmonic rejection is better than 25 dB for the central LO frequencies and stays at a level of -15 dB even at the edges of the LO tuning range.

4.3.2. Tx and Rx back-to-back results

The effective channel BW and IQ cross-talk level of the complete transmission path in a back-to-back configuration are set by the RF band-pass and BB low-pass characteristics of both Tx and Rx modules acting together by performing the combined double-sideband up-conversion and down-conversion between the corresponding BB Tx and Rx ports. The Tx and the mixer-first receiver were placed in a 1-meter LOS set-up. The set-up was previously described in Chapter 3 and it will not be repeated here. Two measurements were taken. First, the I-I and Q-Q transfer values were acquired. Afterward, the orthogonal channel leak (I-Q and Q-I) was also measured. These measurements were taken for three different LO frequencies (230, 240, and 250 GHz). Two different power levels were employed at the Tx input, -5 and -15 dBm, which were found to be the optimum for the QPSK and 16-QAM operation. The results of this test are presented in Fig 4.8.

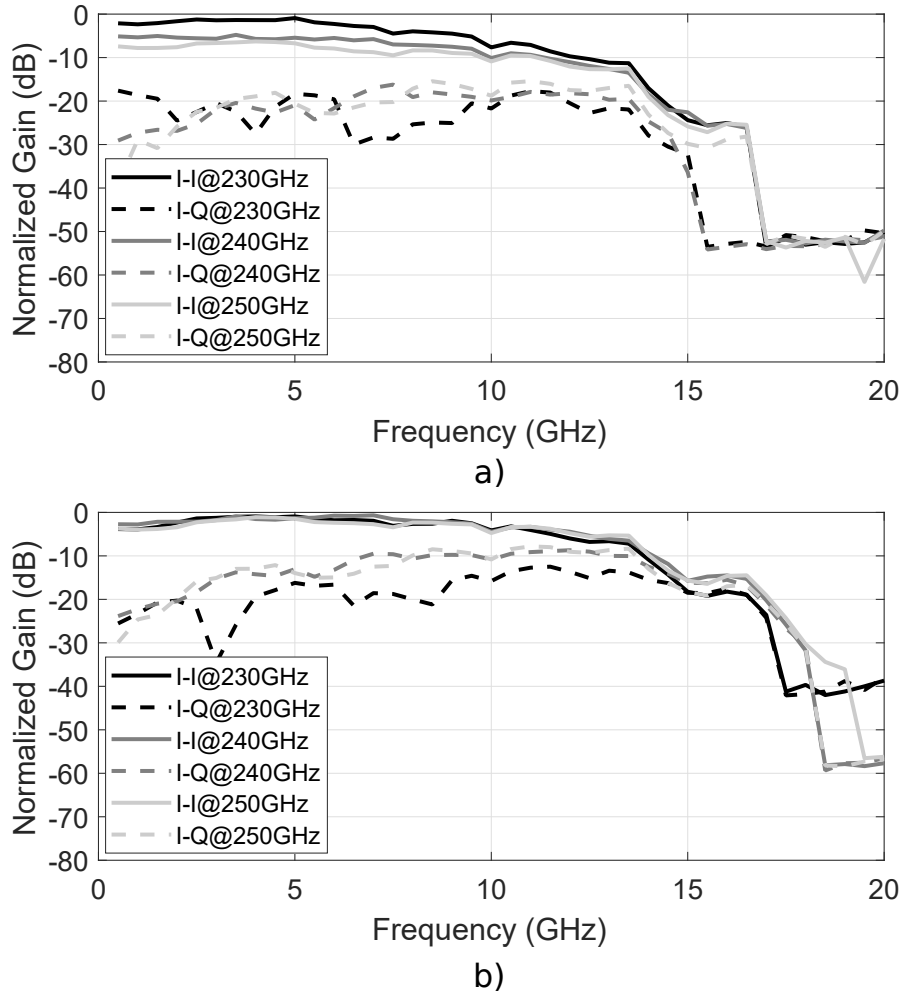


Figure 4.8.: Measured normalized channel gain and IQ cross-talk between the Tx BB input and Rx BB output for a Tx BB input power of a) -15 dBm and b) -5 dBm.

For an input power of -15 dBm, the Tx_{BB} to Rx_{BB} 6-dB channel BW at 230 GHz is 12 GHz, with the BW growing for higher LO frequencies. For an input power of -5 dBm, this BW grows to 14 GHz, independently of the LO frequency. The IQ cross-talk is improved in comparison with the link established with the amplifier first Rx. This improvement is visible when the Tx is operated with an input power of -15 dBm. Under this operation condition, at 230 GHz, the leakage stays below -10 dB for the whole operational BW. Although the leakage is also reduced for other LO frequencies in comparison with the link established with the amplifier first, due to the asymmetry between the USB and the LSB of the Tx RF band-pass characteristic, the leakage level is still high and frequency-dependent. In general, the effect of the enhanced 3-dB RF BW of the mixer-first Rx in the IQ leakage level is marginal.

4.4. Wireless Communication Link

The Tx and the mixer-first Rx were placed in a 1-meter LOS set-up to test the wireless communication link. For more details on the measurement set-up, please refer to the description presented in Chapter 3.3. Due to the low signal power at the mixer-first Rx output, a set of broadband BB amplifiers (PSPSL5882) from Tektronix was placed at the Rx output to raise the output noise spectral density above the noise floor of the oscilloscope. These amplifiers add an EVM of 1% to the wireless link.

4.4.1. Measured link results

The link was tested for LO frequencies ranging from 225 to 255 GHz for QPSK and 16-QAM. For each of these LO frequencies and modulation formats, the data-rate was gradually increased starting from 20 Gb/s.

QPSK. The results of the QPSK test are shown Fig. 4.9. A maximum data-rate of 60 Gb/s was achieved for all LO frequencies except for 225 GHz. These results correspond to a deterioration of 5 Gb/s compared to the link established with the amplifier-first Rx. The external LO drive to BB leakage was found to cause this performance deterioration. This leakage was measured at -50 to -55 dB below the external drive input. In the amplifier-first Rx, the influence of this leakage is less relevant. The amplifier-first Rx conversion gain is realized in the RF, and this gain does not add to the leakage signal. In the mixer-first Rx, the CG happens mainly in the PSPSL5882 external BB amplifier and not on the Rx front-end module. The external LO drive leakage leaks through the PCB to the Rx BB output connector and is amplified afterward by the PSPSL5882 amplifier. This leakage alias with the received BB signal with no space for filtering, decreasing the link performance. A comparison between the amplitude level of this leakage at the BB output of both Rxs is illustrated in Fig. 4.10. The LO leakage power is almost 20 dB higher for the mixer-first Rx than for the amplifier-first Rx.

16-QAM. The results of the 16-QAM test are shown Fig. 4.11. A maximum data-rate of 100 Gbps was achieved at 230 GHz with an EVM of 17%. For a data-rate of 100 Gb/s, the spectrum of the BB signal was aliasing with the LO external drive to BB leakage. The measured spectrum at the Rx BB output of the 100 Gb/s 16-QAM signal is shown in Fig 4.12. The BB signal at the Rx output had to be filtered until the leakage's influence was removed to lock the link. This also filtered out a part of the BB signal BW, potentially increasing the measured EVM at 100 Gb/s. For 100 Gb/s, the measured EVM value corresponds to the maximum tolerable EVM in the link defined in Chapter 2. It is not possible to increase the link distance for this data-rate. Any increase in the SNR

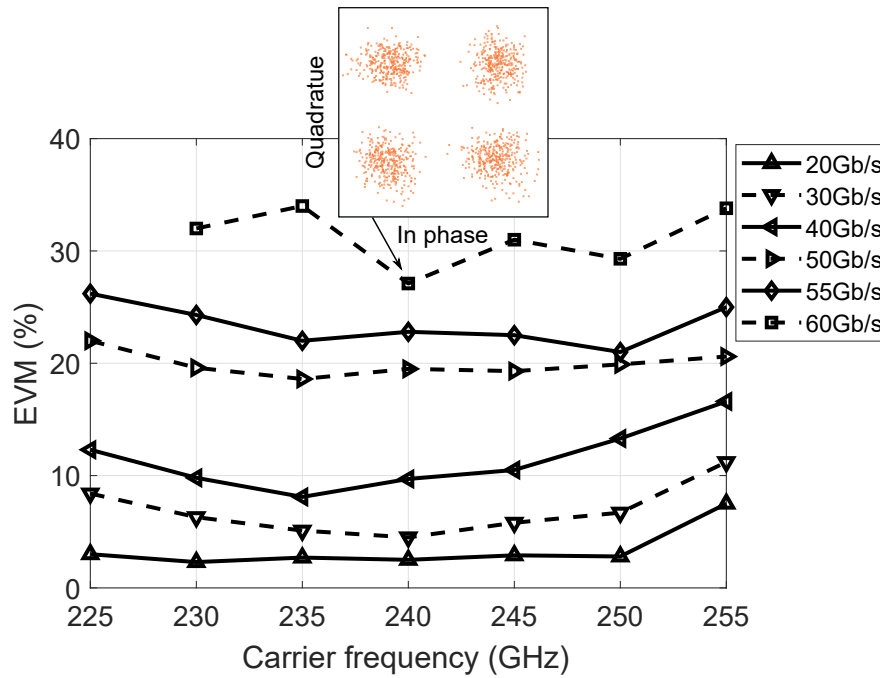


Figure 4.9.: Measured EVM vs. LO frequency and data-rate for a 1-meter link using a QPSK modulation technique.

contribution to the EVM will set a total EVM higher than 17%. The peak data-rate and the range of operating LO frequencies compared to the link established with the amplifier-first RF were enhanced. At 255 GHz, the maximum data-rate increased to 50 Gb/s, 70 Gb/s were achieved at 240 GHz, and the link operates at 90 Gb/s also at 225 GHz. The EVM of 7% for data-rates below 20 Gb/s prevents the link from operating under 64-QAM.

4.4.2. EVM analysis

This section will analyze all possible errors presented in the wireless communication link and evaluate its impact on the measured EVM. The possible error sources are the measurement set-up, the SNR, the phase noise, the interference generated by the harmonic spurs, and IQ cross-talk. The EVM contribution of these errors will be calculated and subtracted from the measured EVM to evaluate its influence on the link performance. The analysis presented will refer to 16-QAM due to its better performance. However, the conclusions apply to all modulation formats.

SNR. The mixer-first Rx's output signal and its noise level were digitized in the oscilloscope and post-processed in MATLAB to calculate the SNR at the Rx's output. Afterwards, the SNR contribution to the EVM was calculated following Eq. 2.16. Fig. 4.13 shows the result of this calculation. The SNR contribution to the measured EVM of the

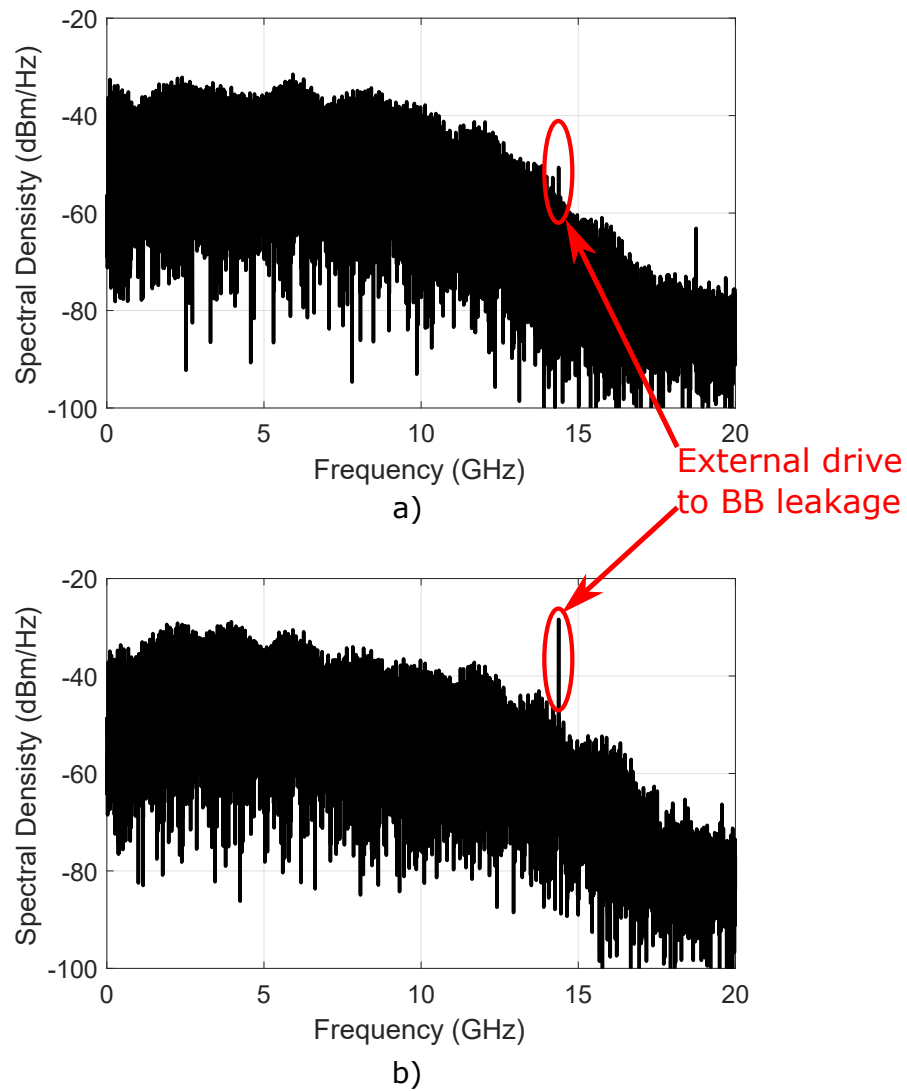


Figure 4.10.: Measured spectrum at the output of the a) amplifier-first Rx, and b) mixer-first Rx, for a 50 Gb/s QPSK signal operated at a LO frequency of 230 GHz. The external drive to BB leakage is 20 dB lower for case a) than for case b).

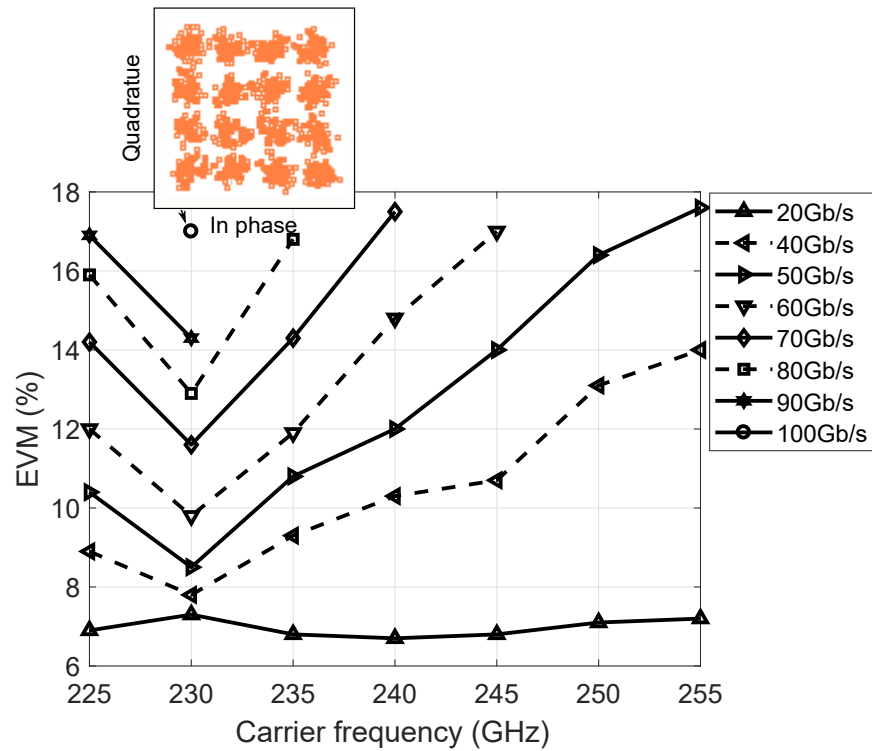


Figure 4.11.: Measured EVM vs. LO frequency and data-rate for a 1-meter link using a 16-QAM modulation technique.

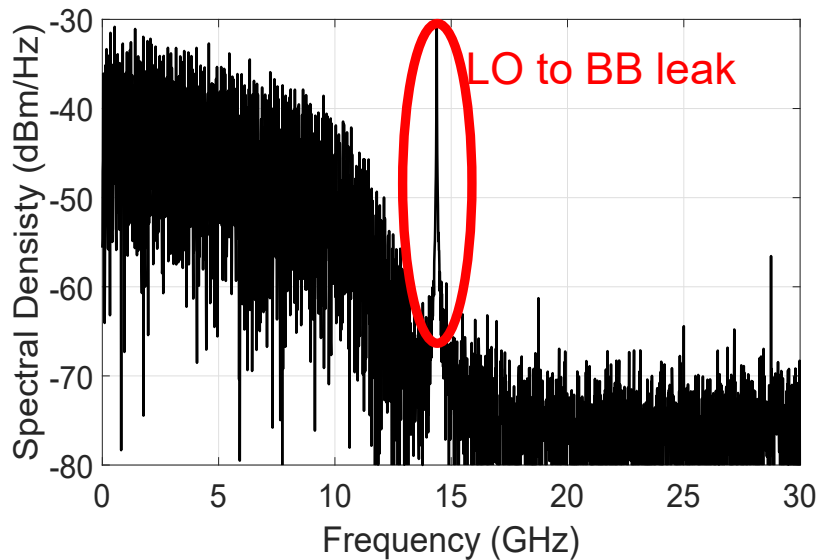


Figure 4.12.: BB signal spectrum at the output of the Rx with the leaking LO external drive to BB spur indicated.

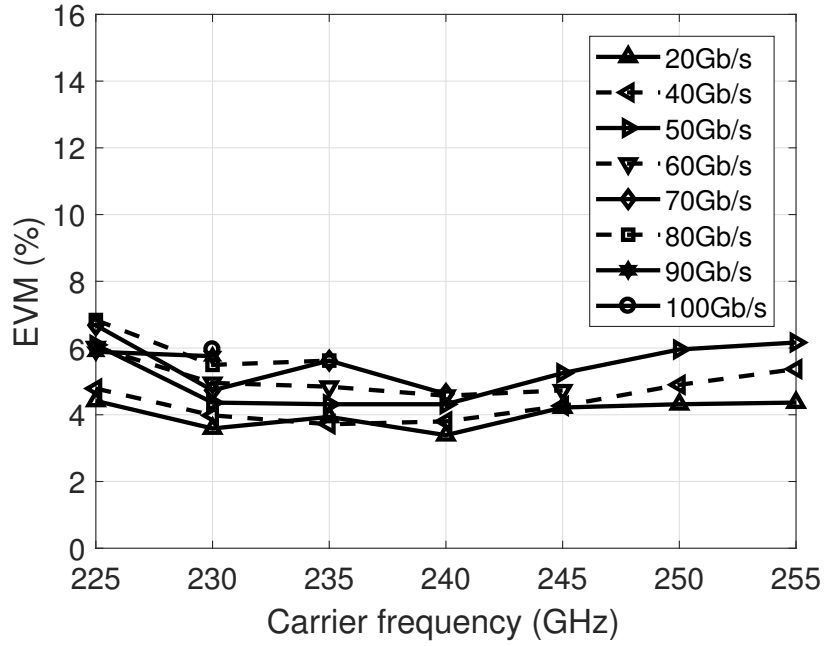


Figure 4.13.: Calculated contribution of the SNR to the EVM in a 1-meter distance link using 16-QAM.

link is minor. The noise power at the output of the mixer-first Rx does not follow the Johnson-Nyquist theorem. 70% of the noise power is allocated in the first 2 GHz BB BW. With a received signal power almost independent of each LO's data-rate, this noise behavior resulted in an SNR-related EVM almost constant for different data-rates. For the maximum data-rate of 100 Gb/s, the SNR contributes to the EVM only 6%, meaning that the other impairments account for the remaining 15.9% EVM. If the link performance would be only limited by the SNR, the maximum achievable distance when operating at 100 Gb/s would be 2.8 meters.

Other impairments. The aggregated EVM excess after de-embedding the EVM introduced by the SNR EVM_{SNR} , the measurement set-up EVM_{AWG} , the PPS5882 BB amplifier $EVM_{BB\ Amp}$, the phase noise EVM_{PN} and the harmonic spurs $EVM_{harm\ self}$ and $EVM_{harm\ adj}$ can be calculated as

$$EVM_{agg} = \sqrt{(EVM_{meas})^2 - (EVM_{AWG})^2 - (EVM_{SNR})^2 - (EVM_{BB\ Amp})^2} \quad (4.1)$$

$$EVM'_{agg} = \sqrt{(EVM_{agg})^2 - (EVM_{PN})^2 - (EVM_{harm\ self})^2 - (EVM_{harm\ adj})^2}, \quad (4.2)$$

The results of evaluating Eq. 4.2 are presented in Fig. 4.14. For data-rates of 20 Gb/s and below, the previously defined EVM contributions account for the total EVM measured

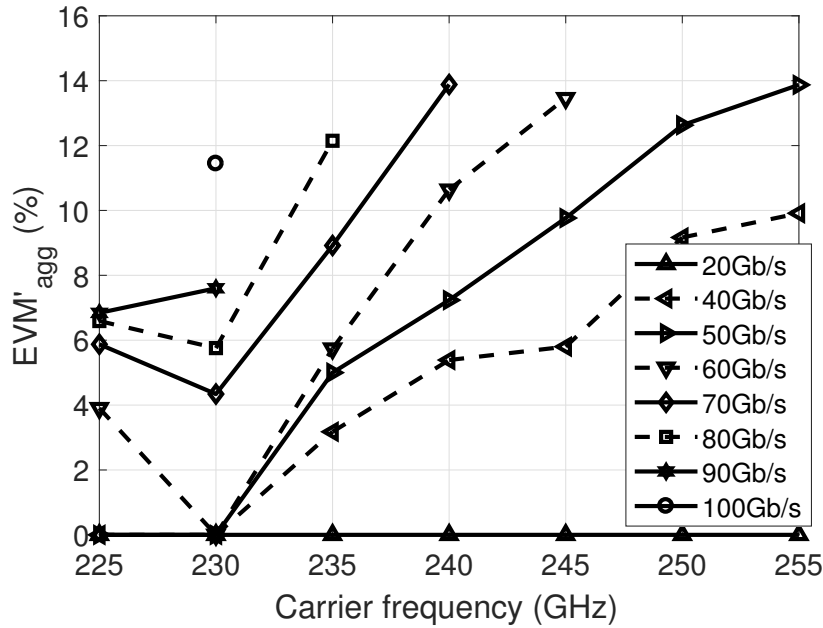


Figure 4.14.: Calculated EVM excess after subtracting the influence of the measurement set-up, BB amplifier, SNR, phase noise and harmonic interference for a 1-meter distance 16-QAM link.

in the link at any carrier frequency. Furthermore, for 225 and 230 GHz, the link is not influenced by any other impairment up to a speed of 50 and 60 Gb/s, respectively. At 90 Gb/s, the mixer-first Rx reduced the remaining aggregated EVM's influence in the link from 10.3% to 7.7% when compared with the link established with the amplifier first Rx. However, for higher LO frequencies, the remaining EVM did not improve. The increase in the data-rate could be attributed to the enhancement in the mixer-first Rx 3-dB RF BW. The hypothesis presented in Chapter 3, that the IQ cross-talk is the main contributor to the final EVM, was not completely verified. Although the system improves at the central LO frequencies, the higher LO frequencies show a remaining EVM equivalent to the EVM showed by the link established with the amplifier first Rx. Unfortunately, the mixer-first Rx did not answer the question if the main limitation for broadband wireless links operating beyond 200 GHz is the IQ leakage or not.

4.4.3. Tx and Rx operated with independent external drive

There is still a test that needs to be applied to demonstrate the feasibility of wireless communications beyond 200 GHz in a real operation scenario. Although using the same external signal drive for the Tx and the Rx module is useful to evaluate the influence of the RF front-ends impairments in the wireless link, in normal operating conditions, the Tx and the Rx would never be operated in such a way. This "not-synchronized" operation

mode is particularly challenging for direct-conversion systems. Any LO leakage through the mixer radiated by the Tx will be down-converted at the Rx side, generating a BB signal with a BW of a few MHz centered at dc that will distort the link. A new test was performed to evaluate how the RF front-end modules behave in a real scenario where they do not share the LO external drive. The link was tested for the Tx and the mixer-first Rx being operated with an independent LO drive. Due to its superior performance, the link was tested at 230 GHz using a 16-QAM modulation technique. It was observed that the radiated Tx LO leakage was down-converted to dc, generating a modulated dc signal with an amplitude 17 dB higher than the BB signal and with a spectral width of a few MHz. Even for a data-rate of 20 Gb/s, this interference prevented the link from operating. To eliminate this effect at the Rx BB signal, a 3rd order high-pass (HP) Butterworth digital filter was implemented inside the oscilloscope DPS chain. The AWG and the oscilloscope were connected in a back-to-back configuration to find the HP filter's appropriate cut-off frequency. This filter's design goal was to effectively suppress the dc-modulated signal with a minimum effect on the link EVM. Several cut-off frequencies were tested for data-rates between 20 Gb/s and 100 Gb/s. The optimum 3 dB cut-off frequency of the HP digital filter was found to be 2.0 MHz. This filter increases the EVM generated by the measurement setup by 2% independently of the data-rate.

The spectral reduction of the interference created by this tone is illustrated in Fig. 4.15. Without the HP filter, the tone centered at dc shows a peak power 17 dB above the signal power distribution preventing the system from locking (Fig 4.15 a). After applying this filter, the tone disappears at the cost of introducing a contribution to the EVM, which stays below 2% (Fig. 4.15 b)). After applying the HP filter, the wireless communication link was tested for a 16-QAM modulation scheme at 230 GHz. The data-rates were increased gradually from 20 Gb/s. The result of this test is gathered in Fig. 4.16. A peak data-rate of 80 Gb/s with an EVM of 12.5% was achieved over a 1-meter distance. For 20 Gb/s, the EVM increases from 7 to 8.1 %, reflecting the EVM contribution caused by the 2 MHz HP filter. This experiment demonstrates the feasibility of wireless communication links above 200 GHz in real operational scenarios.

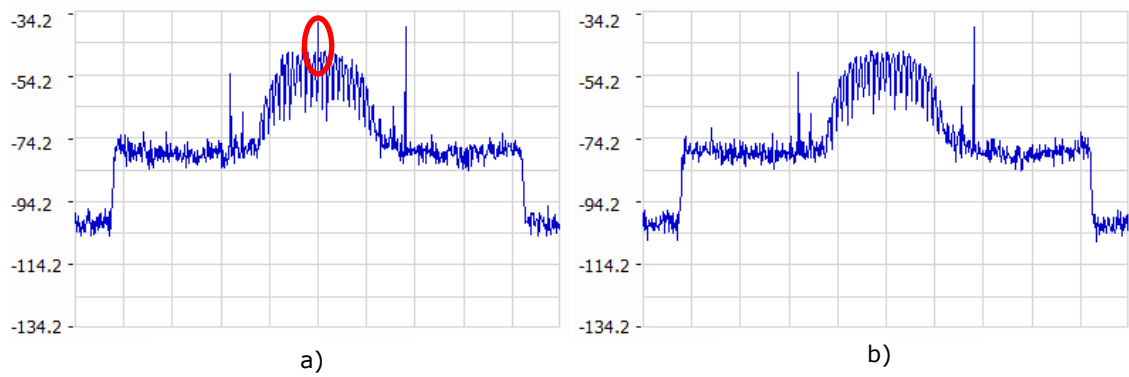


Figure 4.15.: Spectrum of the a) unfiltered received signal and b) after the the 2 MHz digital LP is applied. After [own13] © 2020 IEEE.

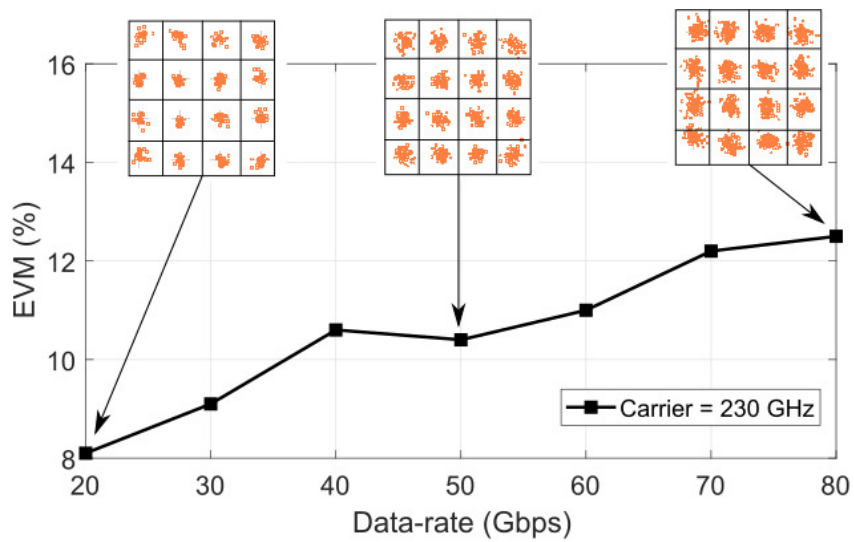


Figure 4.16.: EVM vs. data-rates measured at 230 GHz for independent LO external drive in the Tx and Rx. After [own13] © 2020 IEEE.

4.5. Conclusions

In this chapter, a novel mixer-first Rx front-end for wireless communications beyond 200 GHz has been presented. By removing the LNA in the RF path and using a broadband switching-quad instead of a Gilbert-cell as a down-conversion mixer, the Rx achieved an enhanced 3-dB RF BW of 26 GHz. Combining this Rx with the Tx presented in Chapter 3, the first silicon-based wireless communication link supporting a data-rate of 100 Gb/s beyond 200 GHz was demonstrated. After achieving 60 Gbps at 250 and 255 GHz, this wireless link demonstrates that SiGe-HBT is a valid technology option for the IEEE 802.15.3d standard.

Due to an improvement in the USB and LSB symmetry at the Rx side, the remaining EVM after removing the effect of SNR, measurement set-up, phase noise, and harmonic interference was reduced in comparison with the link presented in Chapter 3 for the central LO frequencies (225-235 GHz). However, this reduction was not enough to appreciate a change in the EVM for LO frequencies allocated in the high edge of the tuning range.

The wireless communication link was tested with an independent LO drive in the Tx and the Rx, achieving a data-rate of 80 Gb/s for a 1-meter distance. A digital HP filter was implemented on the oscilloscope DPS chain to mitigate the influence of the down-converted LO leakage to dc. This experiment demonstrates the feasibility of wireless communication links in real operation scenarios beyond 200 GHz.

The IQ cross-talk hypothesis could not be fully proven in this chapter. The enhanced 3-dB RF BW of the mixer-first Rx was not sufficient to fully eliminate the IQ cross-talk.

Chapter 5

IQ-polarized Tx and Rx RF front-ends

5.1. Introduction

From chapters 3 and 4 it can be concluded that three main impairments influence the wireless communication link performance:

1. The EVM generated by the phase noise prevents any modulation order higher than 16-QAM from operating, exploiting the full RF BW available in the link. This EVM component has different sources. First, the noise floor of the frequency synthesizer. Second, the LO generation path's multiplication factor scales the frequency synthesizer's noise floor by a factor of $20 \cdot \log_{10}(M)$, with M being the frequency multiplication factor of the LO generation path. To minimize this error, either the synthesizer's phase noise or the frequency multiplication factor of the LO path must be reduced.
2. The signal purity of the LO chain limits the operational BW. Although the harmonics' influence in the measured EVM was minor, the LO external drive signal to BB leakage at the Rx outputs limits the usable BW of the system. The external LO drive signal must move higher in frequency to avoid any interference at the Rx output. A higher external LO signal drive will also reduce the LO generation path's multiplication factor, improving the phase noise error.
3. The asymmetry between the USB and the LSB creates a BW-dependent IQ crosstalk. The Tx and the Rx's band-pass RF characteristics must show perfect symmetry between USB and LSB to eliminate this error. However, this is not feasible due to the

gain-BW constraints for the Tx at such high frequencies. Therefore, an alternative strategy must be followed to increase IQ isolation.

A novel Tx and Rx RF front-end module set was developed to address all the design considerations mentioned above. It implements a $\times 8$ LO generation path fed by an external 29-31 GHz drive signal. The lower multiplication factor decreases the multiplier chain contribution to the overall phase noise by 6 dB, while the higher frequency drive signal increases the harmonic spur rejection while keeping the LO external signal drive to BB leakage out of the BB signal BW at the Rx output. The technology-limited gain-BW product sets a practical limit to the achievable USB and LSB symmetry at the Tx side. To further increase the IQ isolation, each of the I and the Q-channel is operated in the link with an orthogonal linear polarization, introducing a new orthogonality level between the I and the Q channels. This functionality is implemented with a lens-integrated dual-polarized antenna, similar to the one presented in [29]. The antenna increases the IQ isolation by a factor relative to the antenna's cross-polar fields. Furthermore, the IQ cross-talk level can be controlled by changing the relative orientation between the Tx and the Rx modules. Testing the wireless communication link for multiple relative orientations between the Tx and the Rx finally proved that the IQ cross-talk is the dominant error in wireless communications operating at frequencies beyond 200 GHz. However, this architecture requires that the Tx and the Rx are connected to the same LO external drive; therefore, it can only be employed as a test-bed for testing the RF front-end influence in the link but will never operate in a real scenario where the Tx and the Rx LO drive must be independent.

This chapter is organized as follows. Section 5.2 presents the architecture that the new chip-set implements and a description of the constituent circuit building blocks used. Section 5.3 presents the RF measured results of the Tx and the Rx front-end modules. Section 5.4 present the measured results of the wireless communication. Finally, conclusions are drawn in Section 5.5.

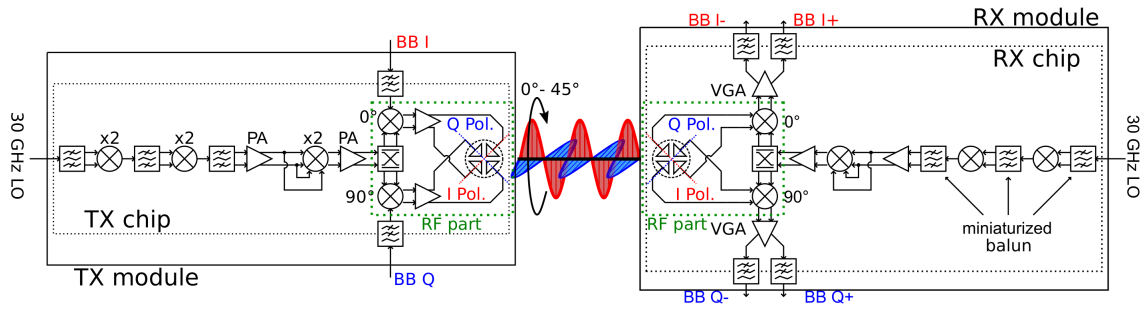


Figure 5.1.: Top level architecture of the IQ polarization orthogonal Tx and Rx. Each of the polarization (red and blue) transmit either I or Q information, increasing the isolation between them.

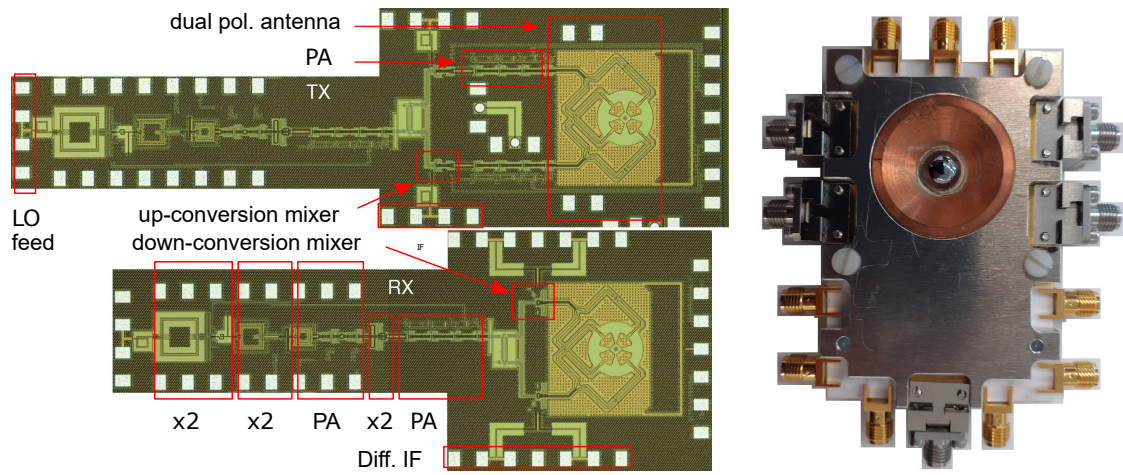


Figure 5.2.: Transmitter and receiver chip micrographs (left) and picture of the fully-assembled RF module. The Tx chip dimensions are 3.745 mm \times 1.13 mm. The Rx chip is 3.205 mm \times 1.27 mm large.

5.2. Tx and Rx Architecture

Fig. 5.1 presents the block level diagram of the Tx and Rx RF front-end modules while the chip micrographs are displayed in Fig. 5.2. The chips were fabricated in IHP 0.13- μm SiGe BiCMOS technology SG13G2 [87] with a $f_T / f_{\text{max}} = 300/450$ GHz.

The 215-240 GHz LO is generated by an externally-fed $\times 8$ multiplier chain in both modules. The $\times 8$ multiplier chain consist of 3 cascaded frequency doublers. The first two doublers are implemented using a Class-B doubler topology. These doublers transform a differential fundamental input signal to a single-ended second harmonic output signal. For proper mode conversion between the inputs and the outputs of these doublers, three baluns are required to cascade such stages. A 2-stage PA is used to drive the final frequency doublers, which is implemented in a Gilbert-cell topology to allow for a differential drive of the mixer without an additional balun. A 4-stage PA follows this last doubler. This PA

is topologically similar to the one presented in Chapter 3. The LO signal's quadrature is provided by a 90° coupled-line hybrid [88] placed after the PA.

The quadrature LO signal drives two separated micro-mixers in the Tx, which independently up-convert the I and the Q BB signals. Each of the I and Q up-converted signals is amplified by a 4-stage PA. These amplified up-converted signals are radiated at a dual-polarization on-chip antenna operating two independent linear polarizations. This antenna introduces a new orthogonality level between the I and the Q channels, increasing the IQ isolation by a factor relative to the antenna's cross-polar fields. Furthermore, it allows for the investigation of the influence of different IQ cross-talk levels. The IQ isolation level can be controlled by changing the relative azimuthal orientation between the Tx and the Rx modules from 0° (maximum IQ separation by polarization) to 45° (no IQ separation by polarization).

A complementary antenna receives the RF signals in the Rx, with each polarization receiving either the I or the Q channel. No LNA was implemented to maximize the RF bandwidth [own2]. Each of the antenna outputs feeds an independent mixer-first down-conversion stage with a similar topology as the one presented in Chapter 4. After down-conversion, the I and Q signals are amplified by a differential variable gain transimpedance amplifier (VGA). The circuit building blocks composing the Tx and the Rx chip have been previously published in [50] as the main part of a PhD thesis. A brief description has been added for completeness.

5.2.1. Operation principle

Although by separating the I and the Q channels by polarization the IQ cross-talk can be minimized, this additional orthogonality level prevents the operation of this system under normal operating conditions. To understand the limitations of a direct-conversion IQ wireless communication system where the I and Q channels have been separated by polarization and not by phase difference in the Tx, the time domain operation mode of a direct-conversion IQ wireless system is used as a reference. Assuming that $I(t)$ is the BB signal fed to the in-phase mixer, and $Q(t)$ is the BB signal fed to the quadrature mixer, the radiated signal at the output of a standard direct-conversion IQ Tx can be expressed as

$$I(t) \cdot \sin(\omega t) + Q(t) \cdot \cos(\omega t), \quad (5.1)$$

where ω is the angular LO frequency, defined as $2\pi f$, f is the LO frequency, and t is the time. At the receiver, this signal is mixed again using the Rx LO frequency. The output of the in-phase I_{out} and quadrature Q_{out} down-conversion mixers can be expressed as

$$I_{out} = I(t) \cdot \sin(\omega t) \cdot \sin(\omega t + \Delta\phi) + Q(t) \cdot \sin(\omega t) \cdot \sin(\omega t + \Delta\phi) \quad (5.2)$$

$$Q_{out} = I(t) \cdot \sin(\omega t) \cdot \cos(\omega t + \Delta\phi) + Q(t) \cdot \sin(\omega t) \cdot \cos(\omega t + \Delta\phi), \quad (5.3)$$

where $\Delta\phi$ is the phase difference between the LO frequency in the Tx and the LO in the Rx. These equations generate two components, centered at dc and two times the LO frequency. The highest frequency component will be filtered out by the output matching of the down-conversion mixer. Therefore it will be ignored in this analysis. The output of the Rx can then be expressed as

$$I_{out} = I(t) \frac{\cos(-\Delta\phi)}{2} + Q(t) \frac{\sin(\Delta\phi)}{2} \quad (5.4)$$

$$Q_{out} = I(t) \frac{\sin(-\Delta\phi)}{2} + Q(t) \frac{\cos(\Delta\phi)}{2}. \quad (5.5)$$

The signal at the Rx output is dependent on $\Delta\phi$. In the case where $\Delta\phi$ is equal to 0° or 180° , both outputs will be perfectly separated, with $I_{out} = \pm I(t)$ and $Q_{out} = \pm Q(t)$. In the case where $\Delta\phi$ is equal to 90° or 270° , the outputs will be reversed, with $I_{out} = \pm Q(t)$ and $Q_{out} = \pm I(t)$. For any other value, each of the receiver outputs will contain a mixture of $I(t)$ and $Q(t)$. However, the total signal power at the outputs will always be constant, and the signal information will not be lost. $I(t)$ and $Q(t)$ can be separated afterward in the receiver's DSP chain. However, a system whose I and Q channel have been separated by polarization operates differently. In this case, each of the different polarization of the Tx will radiate a separate signal P_I and P_Q . These signals can be defined as

$$P_I = I(t) \cdot \sin(\omega t) \quad (5.6)$$

$$P_Q = Q(t) \cdot \cos(\omega t). \quad (5.7)$$

These signals will be down-converted at the receiver side using only either the in-phase or quadrature signal. The signal at the Rx BB output can be expressed as

$$I_{out} = I(t) \frac{\cos(-\Delta\phi)}{2} \quad (5.8)$$

$$Q_{out} = I(t) \frac{\sin(-\Delta\phi)}{2}. \quad (5.9)$$

The limitation of this system is visible after this derivation. The Rx BB output signal shows a dependency on the phase difference between the Tx and Rx LOs. Only in the case where $\Delta\phi$ is equal to 0° or 180° the signal power will be maximized. For any other value of $\Delta\phi$, this power will be reduced, reaching zero when $\Delta\phi$ is equal to 90° or 180° . This system requires that the Tx and the Rx are locked to the same LO reference while a phase shifter controls the relative phase difference. Although impractical in a real scenario, this system allows for the analysis of the IQ cross-talk influence in the wireless link. Furthermore, by controlling the relative orientation between the Tx and the Rx, the IQ cross-talk level can be modified with a minor influence on the SNR. This RF front-end set must be treated like a test-bed that allows for the IQ cross-talk influence analysis instead of a fully operative wireless communication system.

5.2.2. $\times 8$ Lo generation path

Figure. 5.3 presents the schematic of the first two Class-B doublers of the LO generation path. Three miniaturized baluns are used to match their single-ended output with the differential input. These baluns define the operational bandwidth of the system. The first doubler is biased for maximum conversion gain. For sufficient output power a $8 \times (0.12 \times 0.96 \mu\text{m}^2)$ device size was selected. The second doubler was designed trading-off output bandwidth and output power, employing a device with a size of $4 \times (0.12 \times 0.96 \mu\text{m}^2)$. Each doubler has a dc power consumption of 10 mW.

A 2-stage PA is placed after the second doubler to ensure sufficient power to drive the last doubler. The amplifier core implements a pseudo-differential cascode topology (Fig. 5.4 a)). A device size of $8 \times (0.12 \times 0.96 \mu\text{m}^2)$ was chosen for maximizing the output power. The 2-stage PA has a power consumption of 140 mW.

The last doubler implements a Gilbert-cell topology, as illustrated in Fig. 5.4 b). The transconductance pair (Q1–Q2, device size $3 \times (0.12 \times 0.96 \mu\text{m}^2)$) and the switching quad

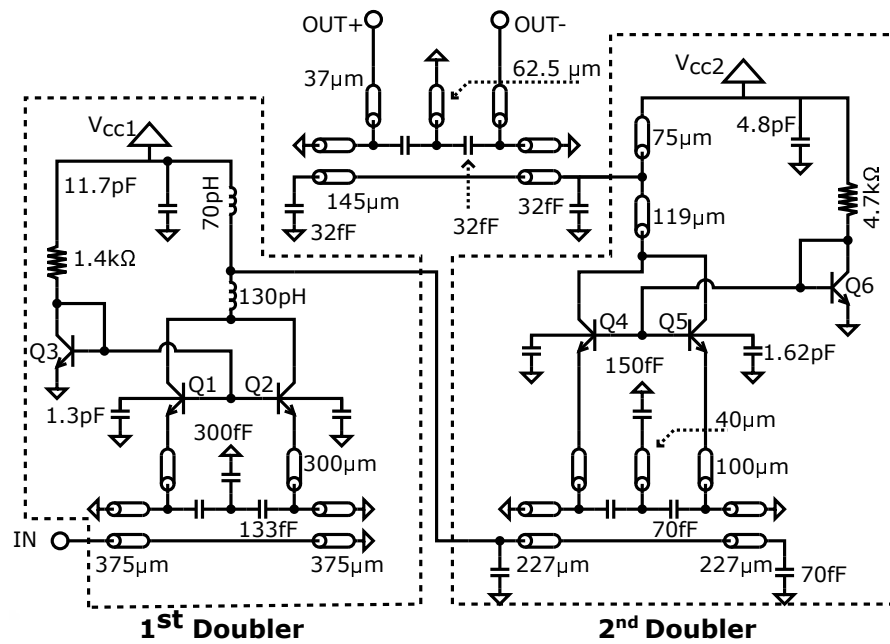


Figure 5.3.: 1st and 2nd frequency doubler stages from 30 GHz to 60 GHz and from 60 GHz to 120 GHz. The lines in the baluns show a Z_o of 30 Ω , while the lines at the output of the doublers show a Z_o of 50 Ω .

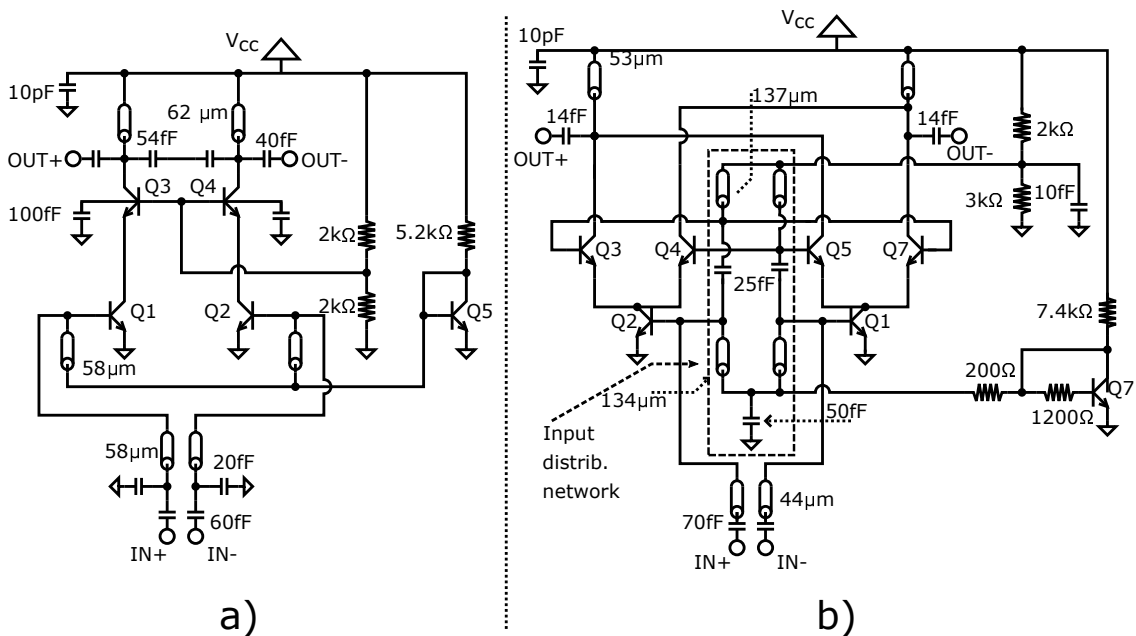


Figure 5.4.: Schematic of a) one stage of the 2-stage PA and b) last doubler. Both amplification stages are identical. The transmission lines presented here exhibit a $Z_o=100 \Omega$ for the differential mode and $Z_o=50 \Omega$ for the single-ended mode.

(Q3–Q6, device size $2 \times (0.12 \times 0.96 \mu\text{m}^2)$) are driven in quadrature to maximize the conversion gain [89]. The input distribution network ensures the 90° phase shift between both stages while keeping a wide input BW. The circuit consumes 30 mW.

The $\times 8$ multiplication path is followed by a 4-stage PA and a hybrid quadrature coupler, similar to the one presented in Chapter 3. The PA delivers an output power in the 215–240 GHz band of 5 dBm, ensuring enough drive to operate the mixers properly. The hybrid coupler generates the IQ functionality.

5.2.3. Tx up-conversion path

The Tx up-conversion path consists of an up-conversion micro-mixer followed by a 3-stage PA. The implemented up-conversion mixer follows a T-padded micromixer topology [90] depicted in Fig 5.5. The transistors Q1–Q2 (device size $2 \times (0.12 \times 0.96 \mu\text{m}^2)$) operate as a broadband balun, transforming the single-ended BB input signal into a differential signal. The rest of the circuit operates as a typical Gilbert-cell mixer. The transconductance stage is implemented with transistor Q3–Q4 (device size $2 \times (0.12 \times 0.96 \mu\text{m}^2)$) and the switching-quad with Q5–Q9 (device size $1 \times (0.12 \times 0.96 \mu\text{m}^2)$). Transistor Q9–Q10 are used for biasing (device size $1 \times (0.12 \times 0.96 \mu\text{m}^2)$). Two key parameters were optimized in the design of this circuit, conversion gain and BB bandwidth. The first one is achieved by biasing the switching quad for maximum switching speed while ensuring enough LO drive. For the second, the transistor sizes in the input BB stage were chosen in conjunction with appropriate emitter degeneration and series resistance to present a wide 50Ω interface. Each up-conversion mixer consumes 55 mW.

5.2.4. Rx down-conversion path

The circuit-level schematic of the down-conversion stage is illustrated in Fig. 5.6, including the down-conversion mixer and the baseband VGA. The different devices' size has been indicated in the figure as a multiple of the minimum device size of $1 \times (0.12 \times 0.96 \mu\text{m}^2)$. To maximize the down-conversion mixer's RF bandwidth, a switching-quad topology, with no transconductance stage, was implemented [own2]. The mixer output currents are fed directly to a Cherry-Hooper transimpedance amplifier for baseband gain. The down-conversion mixer is biased for minimum noise-figure. In the BB amplifier, the first stage is biased for low-noise operation but providing sufficient gain to isolate the down-conversion stage's noise figure from the rest of the receive path. The gain variability is provided by applying a control current (I_{ctrl}) of up to $500 \mu\text{A}$ to the "linear-in-dB" [91] current mirror

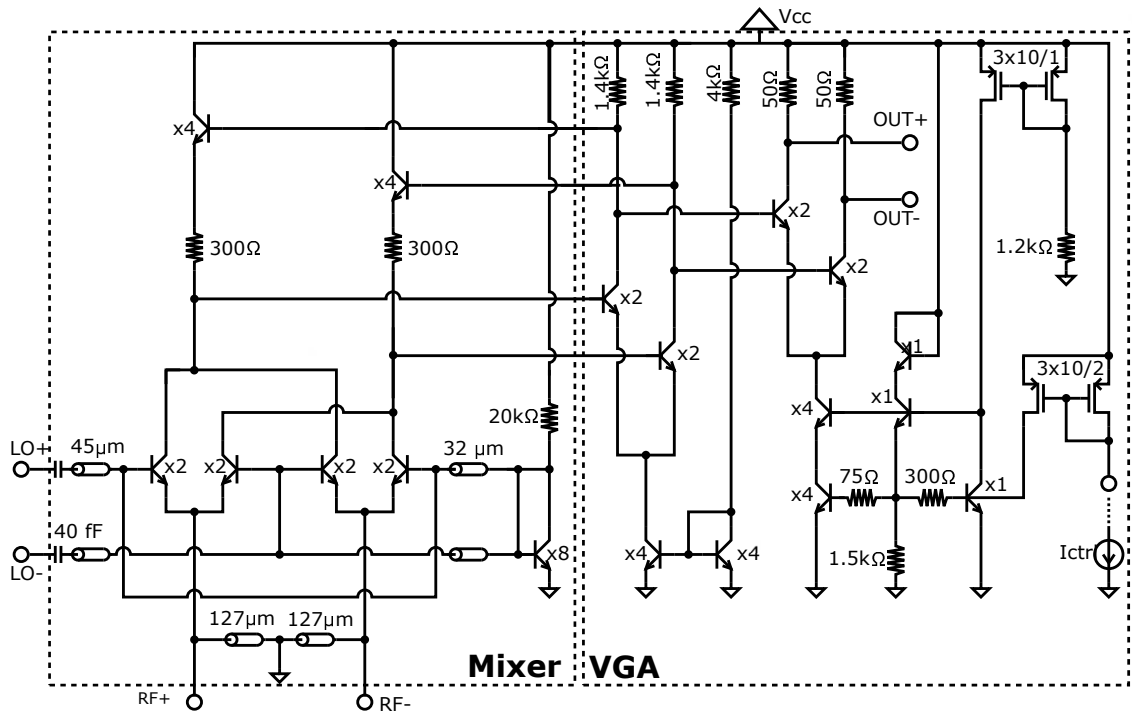


Figure 5.6.: Schematic of the down-conversion mixer and the VGA. The transmission lines used for LO and RF input matching exhibit a $Z_o=100\ \Omega$ for the differential mode.

5.2.6. Packaging

The transmitter and receiver chips are glued to the backside of a hyper-hemispheric high resistivity silicon lens. This chip-on-lens assembly is then mounted and wire-bonded on the backside of a 0.254 mm thick laminated Rogers 4350B PCB with a recess to accommodate the chip. To facilitate the transmission of the wideband BB signals and the high-frequency LO feed, a 6-section low-pass filter with minimum group delay dispersion was implemented to compensate for the wire-bonds' inductance. The filter components are illustrated in Fig. 5.7. Two pads were used to wire-bond the BB signals to minimize the wire-bond inductance.

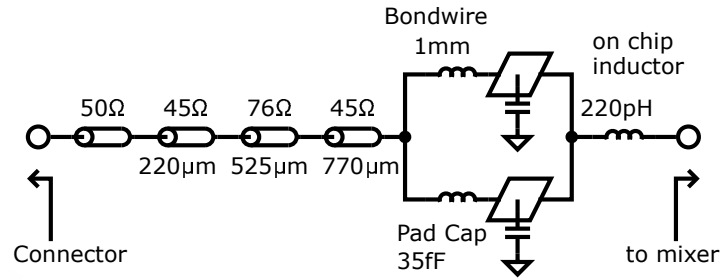


Figure 5.7.: BB low pass filter schematic. The wire-bonds and on-chip pad capacitances are absorbed into a 6th order filter. One inductor is placed on chip to move the bond-wire inductance to a place in the filter, whose prototype value resembles the wire-bond inductance.

5.3. RF characterization

Two different groups of RF measurements have been performed. The first encompasses a set of single-tone measurements allowing separate investigation of the frequency dependent LSB and USB characteristics for key Tx/Rx performance metrics. In the second, the measurements involve a combined operation of the Tx and Rx modules configured into a free-space back-to-back line-of-sight set-up. Here, both double-sideband quadrature up-conversion and down-conversion are performed between the BB Tx inputs and the Rx outputs, which supports a study of the influence of the Tx/Rx relative orientation in the IQ cross-talk. All measurements have been taken in free-space and at the board level, including the influence of all on-board and on-chip components cascaded between the on-board high-speed connector and the lens-coupled on-chip antenna. An absorbing material was applied to cover the major reflecting surfaces to minimize the influence of parasitic reflections in the measurement set-up.

5.3.1. Single-tone RF measurements of the Tx and the Rx

The set-up used for these measurements is similar to the one presented Chapter 3. Each polarization path (corresponding to the I and Q channel) for both Tx and Rx modules was characterized independently by rotating the RF module around its azimuthal axis.

Antenna measurements. The co-polar and the cross-polar far-field radiation patterns of both Tx and Rx modules have been characterized for each polarization. Selected cross-section cuts of the far field radiation patterns are provided in Fig. 5.8 for the Tx and the Rx at an LO frequency of 225 GHz. The E and H planes correspond to the co-polar radiation of the Q channel, while the x-E and the x-H planes correspond to the cross-polar

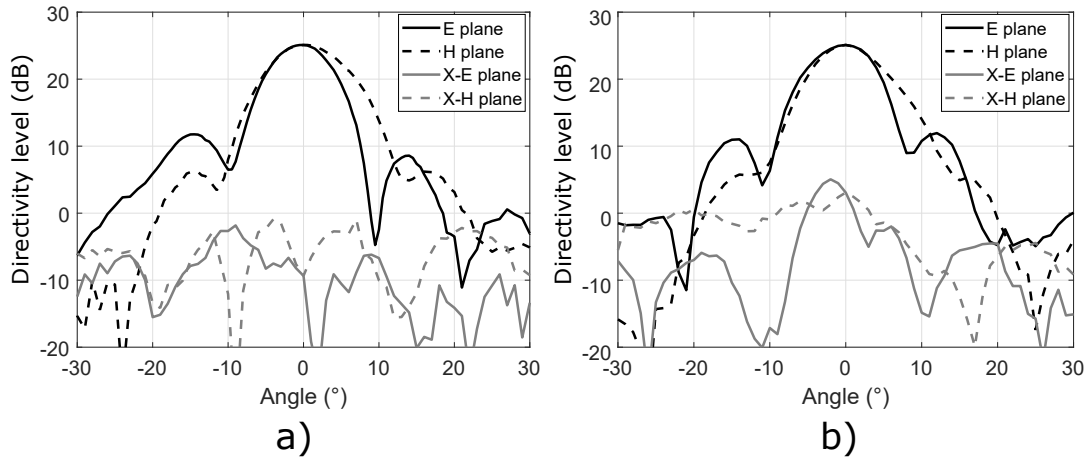


Figure 5.8.: Measured a) Tx and b) Rx antenna patterns at 225 GHz.

radiation patterns of the same channel. The non-infinite suppression of these cross-polar fields generates a parasitic leakage, setting a maximum IQ isolation. At the antenna bore-sight, the cross-polar radiated power stays 31.9 dB and 24 dB below the co-polar for the Tx and the Rx. The cross-polar suppression was similar for other LO frequencies and for the I channel polarization. For both Tx and Rx modules, the directivity was measured to grow monotonically from 24.9 to 25.4 dBi in the 215 to 240 GHz band.

Tx up-conversion path. The Tx output power and IQ imbalance were measured for multiple LO frequencies. Two different power levels were tested, -10 and -5 dBm, which were found to be optimum for 16-QAM and QPSK operation in the wireless communication experiment. The I and the Q channel were characterized independently. The results of these measurements are gathered in Fig. 5.9. A maximum 3-dB RF BW of 21 GHz and 26 GHz was achieved at a LO frequency of 225 GHz for an input power of -10 and -5 dBm, respectively. For other LO frequencies, the 3-dB RF BW was reduced and the asymmetry between the USB and the LSB increased. Each channel shows a saturated P_{out} of 5.5 dBm. The IQ amplitude imbalance stays below 0.8 dB for the whole operation BW.

Rx down-conversion path The Rx CG, NF, and IQ imbalance were characterized for multiple LO frequencies. The differential BB outputs were combined using a broadband balun (BAL0026 Marki) and then measured upto 20 GHz using a spectrum analyzer. The results of this test for the I channel are displayed in Fig. 5.10. The 3-dB BW exceeds 40 GHz for all carrier frequencies. Contrary to the Tx, the Rx shows good in-band symmetry for all LO frequencies thanks to the implemented mixer-first topology. The single side-band noise figure is better than 19 dB for the complete operating BW. The IQ imbalance stays below 0.5 dB for the whole BW.

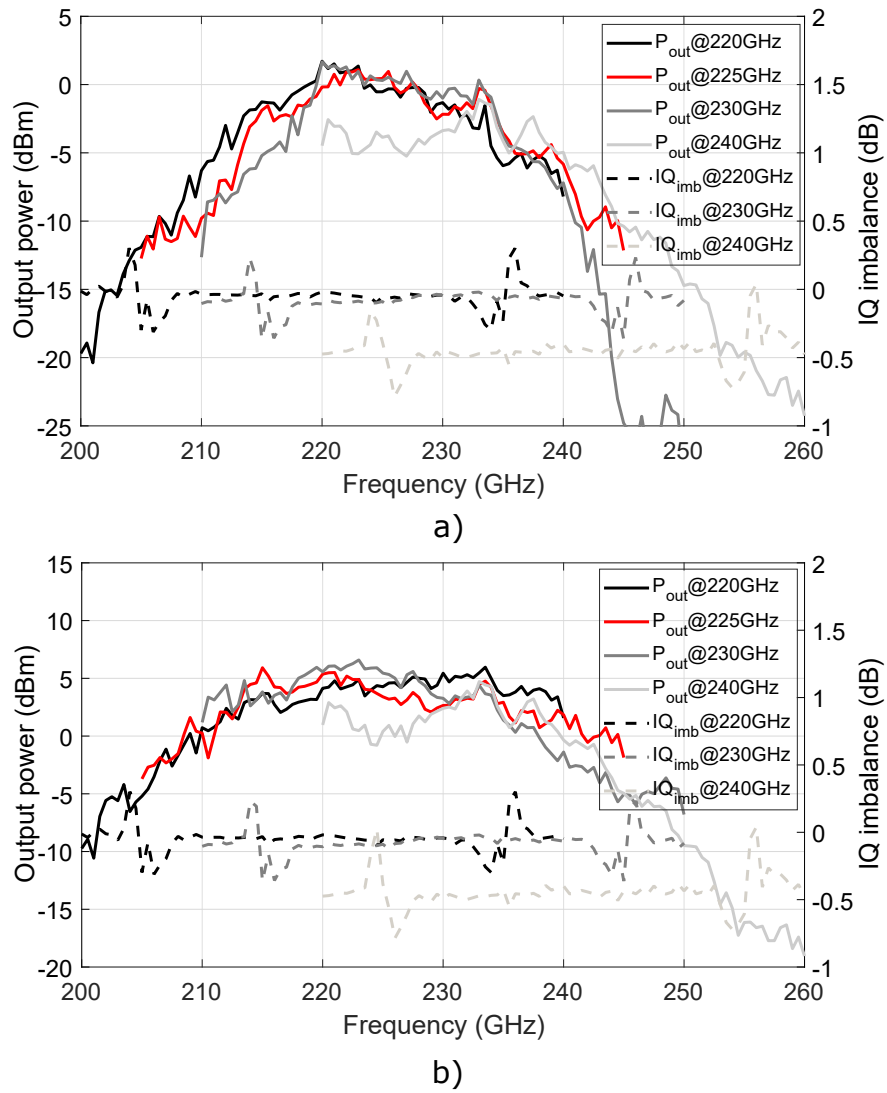


Figure 5.9.: Measured I channel radiated power and IQ amplitude imbalance for a BB input power of a) -10 dBm and b) -5 dBm.

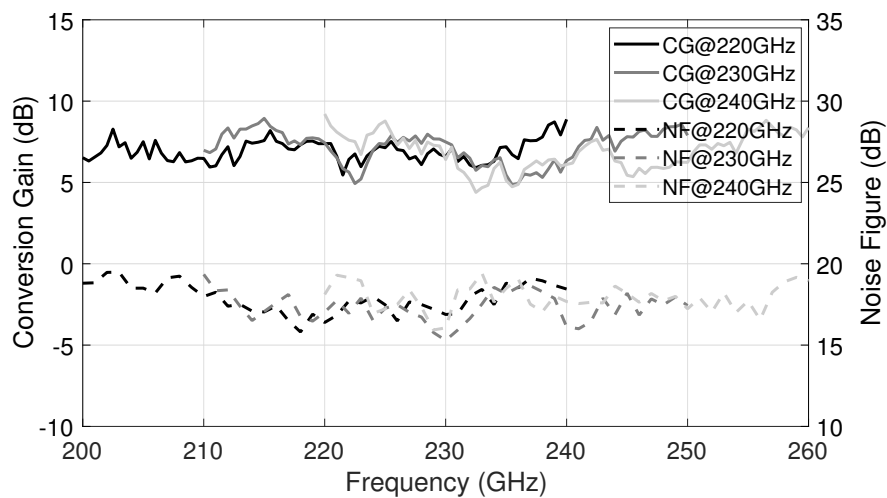


Figure 5.10.: Measured I channel conversion gain and single side-band noise figure.

×8 LO path. A breakout of the ×8 multiplier chain was characterized on-wafer to measure the harmonic spurs level (in this case ×7, ×9). A harmonic spur rejection better than 30 dB was confirmed for the full LO tuning range [50]. This high rejection level ensures that the harmonic contribution to the final measured EVM stays below 1%.

5.3.2. Tx and Rx back-to-back results

The effective channel BW of the complete transmission path in a back-to-back configuration is set by the RF band-pass and BB low-pass characteristics of both Tx and Rx modules acting together by performing the combined double-sideband up-conversion and down-conversion between the corresponding BB Tx and Rx ports. In particular, double side-band operation involves the asymmetry between LSB and USB of both modules in the transmission process and, therefore, the frequency-dependent characteristics of the complete path are not simple replicas of the Tx and Rx RF properties found from single-tone measurements. The Tx and the Rx were mounted in a 1-meter LOS set-up, similar to the one presented in Chapter 3. The effective channel BW of the complete transmission path in a back-to-back configuration was measured between corresponding BB Tx and Rx ports LO frequencies between 220 GHz and 240 GHz and Tx BB input power of -10 dBm and -5 dBm. The relative azimuthal orientation between the Tx and the Rx was also changed between 0° and 45° in steps of 15° . The results of this test are gathered in Fig. 5.11. The 6-dB channel BW is better than 15 GHz for all LO frequencies. At 240 GHz, the channel shows a BW larger than 20 GHz. As it can be observed in Fig. 5.9, at 240 GHz, the Tx operates almost exclusively in single side-band operation. The signal power allocated in the USB is substantially reduced in comparison with the LSB. The relative rotation between the Tx and the Rx affects the total signal power transferred in the link but does not influence the 6-dB channel BW.

The IQ cross-talk level was additionally measured. The isolation level, measured as the difference between the measured I to I signal level and the I to Q leakage level, is presented in Fig. 5.12 and Fig. 5.13 for an input power of -10 dBm and -5 dBm. When both polarizations are perfectly aligned, the IQ isolation is better than 20 dB in the complete operating BW, regardless of the chosen LO frequency. The IQ cross-talk level can be controlled by changing the relative rotation between the Tx and the Rx. For other relative azimuthal orientations between the Tx and the Rx, the IQ isolation level decreases. The decrease in the IQ isolation level is less accused at 225 GHz. At this carrier frequency, the asymmetry between the USB and LSB is less pronounced (See Fig.5.9). For other carrier frequencies the USB/LSB asymmetry increases and the drop in the IQ cross-talk level is more accused. For 225 GHz, an isolation level of at least 10 dB is achieved up to 12.5 GHz. However, at 240 GHz, this isolation level only holds up to 5 GHz. This rotational control on the IQ isolation level will be used in the following section to investigate the effect of different IQ cross-talk levels in the wireless communication experiment.

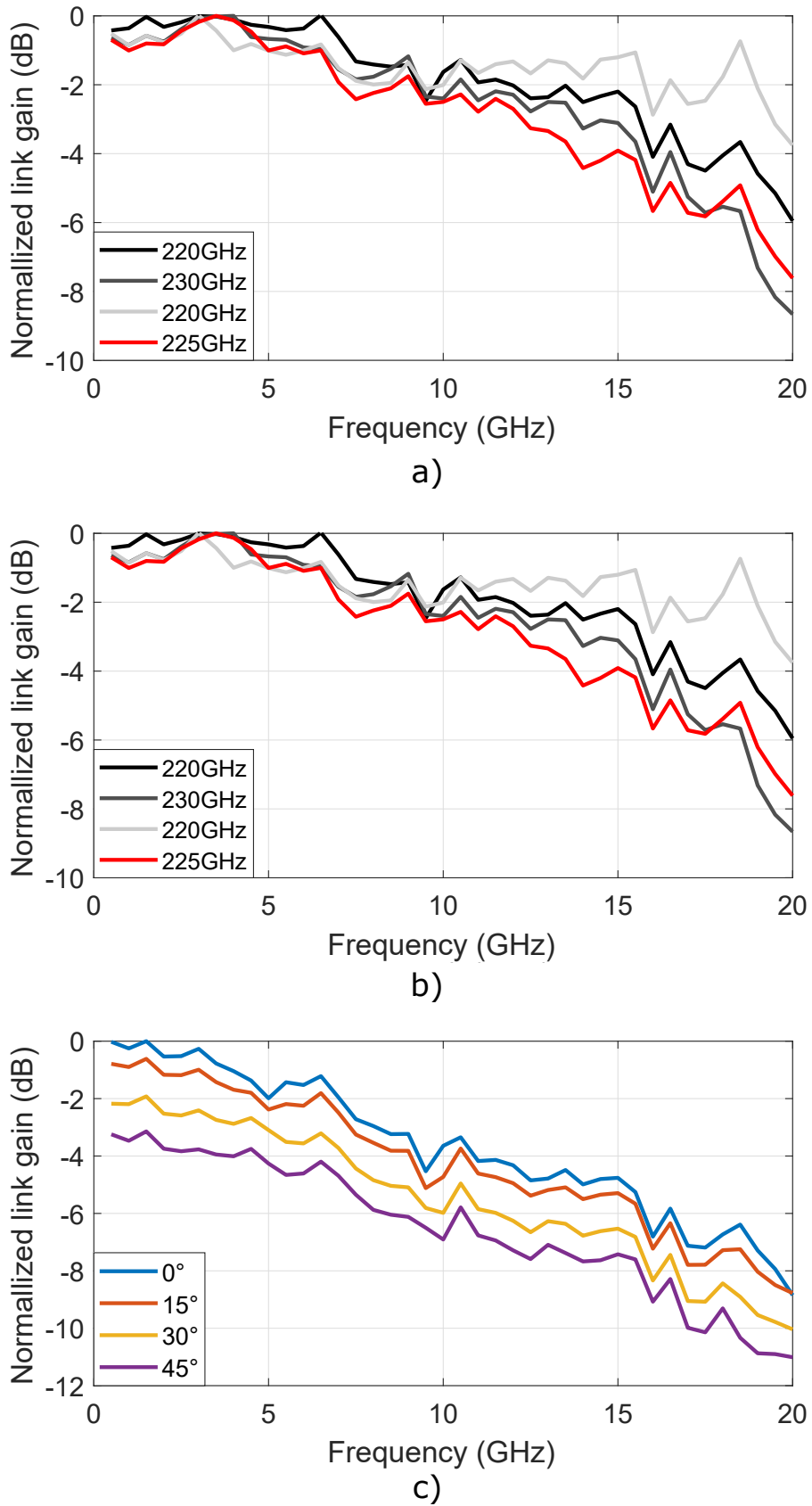


Figure 5.11.: Measured channel BW for a Tx BB input power of a) -5 dB and b) -10 dBm. In c), the effect of changing the relative orientation between the Tx and the Rx is illustrated for a LO frequency of 220 GHz.

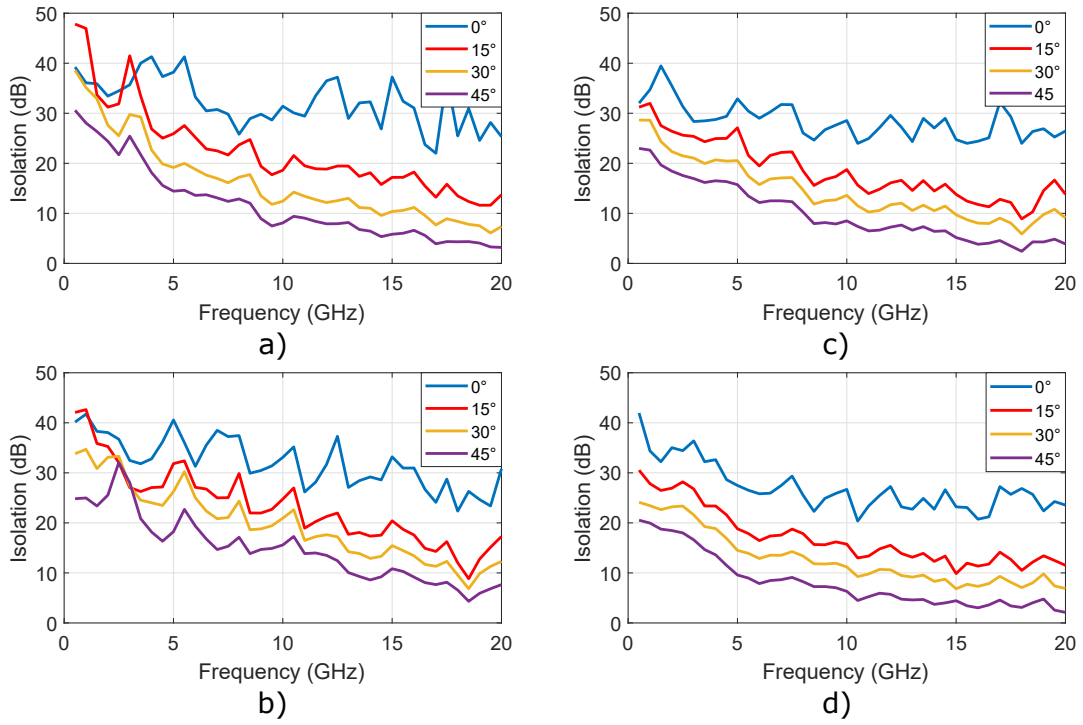


Figure 5.12.: Measured IQ isolation level for a Tx BB input power of -10 dBm using a LO frequency of a) 220 GHz, b) 225 GHz, c) 230 GHz and c) 240 GHz.

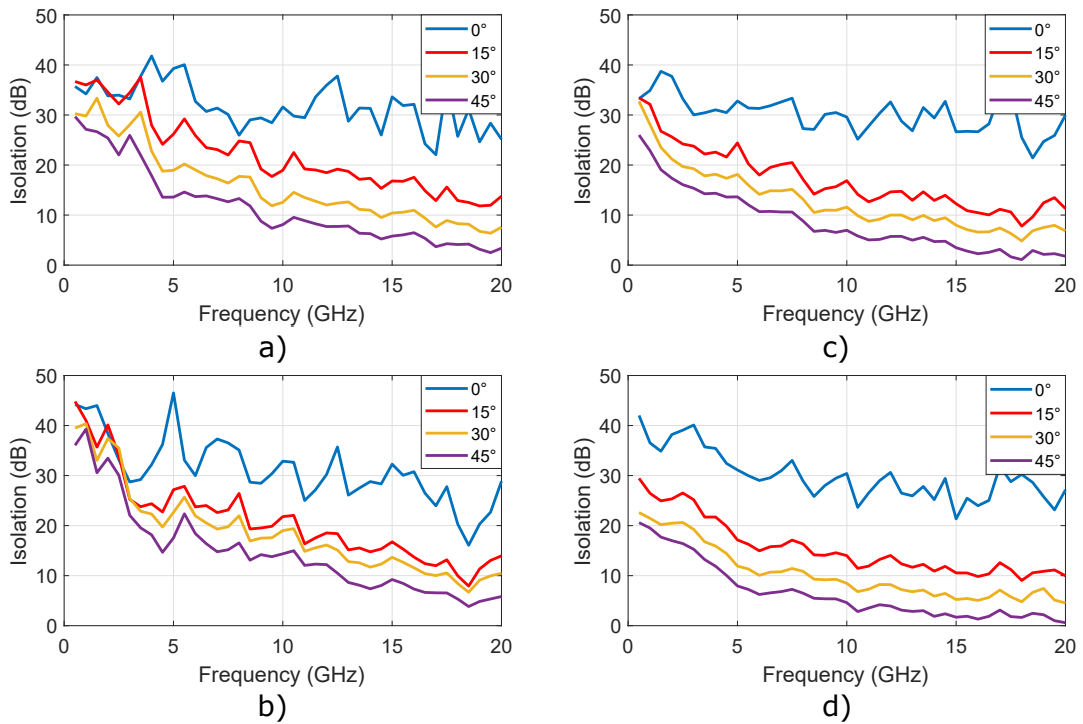


Figure 5.13.: Measured IQ isolation level for a Tx BB input power of -5 dBm using a LO frequency of a) 220 GHz, b) 225 GHz, c) 230 GHz, and d) 240 GHz.

5.4. Wireless Link Results

The Tx and the Rx were mounted in a 60 cm LOS set-up. The set-up is similar to the one described in Chapter 3, please refer to this chapter for more details on the set-up and the EVM analysis. Two sets of measurements were done. In the first, the relative alignment between the Tx and the Rx was initially set to minimize the IQ isolation. An EVM analysis was applied to evaluate the aggregated EVM excess remaining in the wireless link. In the second measurement, the wireless link was tested for relative azimuthal orientations between the Tx and the Rx up to 45° in steps of 15° . This test allowed the investigation of the IQ cross-talk's influence in the wireless communication link. The only error that changes in the wireless link for different orientations is the IQ cross-talk. The influence of the IQ cross-talk in the final EVM can be evaluated by calculating the aggregated EVM excess for each of the different relative orientations after removing the SNR, the measurement set-up, and the phase noise.

5.4.1. Measured link results

The link was tested for LO frequencies from 215 GHz to 240 GHz for QPSK and 16-QAM. A set of 5-dB attenuators was mounted between the AWG and the Tx BB input to ensure the Tx linear operation under 16-QAM. For each of these LO frequencies and modulation formats, the data-rate was gradually increased, starting from 20 Gb/s. The results of these measurements are presented in Fig. 5.14 and Fig. 5.15 for QPSK and 16-QAM, respectively. Thanks to its improved channel BW, reduced IQ cross-talk, and the absence of LO external drive to BB leakage, the QPSK wireless link achieved a maximum data-rate of 85 Gb/s for all LO frequencies except 240 GHz. Using a 16-QAM modulation format, the wireless communication link achieved a similar performance independently of the chosen LO frequency for data-rates up to 100 Gb/s. However, the results for the highest data-rate differ significantly from the expectations set by the RF measurements. For LO frequencies where the Tx shows the most symmetric behavior between the USB and the LSB (220 and 225 GHz), the maximum data-rate is limited to 100 Gb/s, while at the edges of the LO tuning range (215 GHz and 230-240 GHz), the data-rate grows to 120 Gb/s. Moreover, at a carrier frequency of 235 GHz, the maximum achieved data-rate was 140 Gb/s with an EVM of 16.7%. Under the normal operating conditions of a direct-conversion IQ system, the maximum data-rate should have been achieved at the LO frequency that shows the best LSB/USB symmetry. However, due to the IQ channel separation by polarization, this system can operate in single side-band mode, employing only the USB for 215 GHz and the LSB for 230-240 GHz.

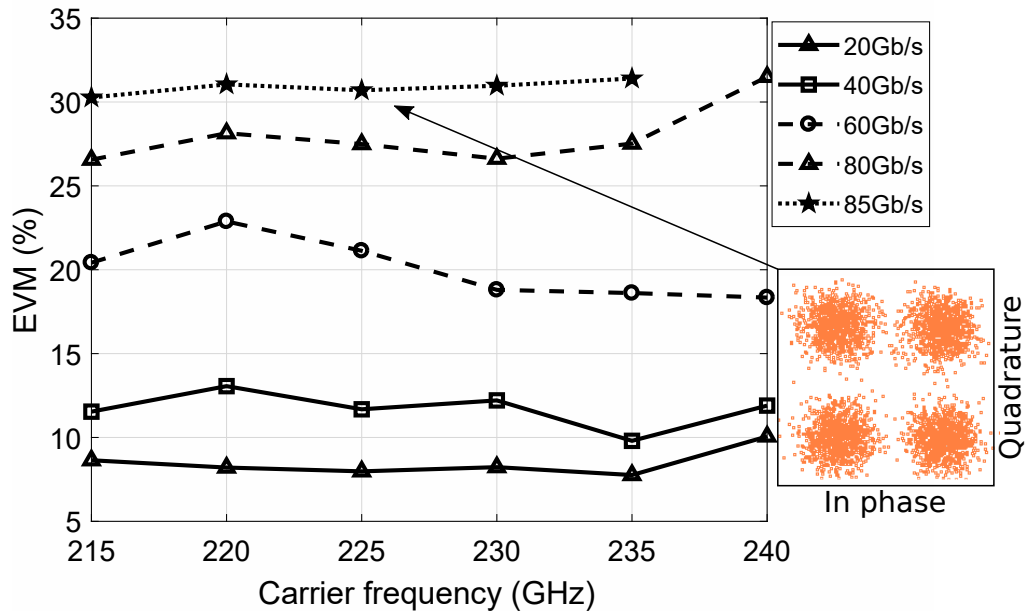


Figure 5.14.: EVM vs. LO frequency and data-rate for a 60-cm link using a QPSK modulation technique. The alignment between the Tx and the Rx is set to 0° , minimizing the IQ cross-talk.

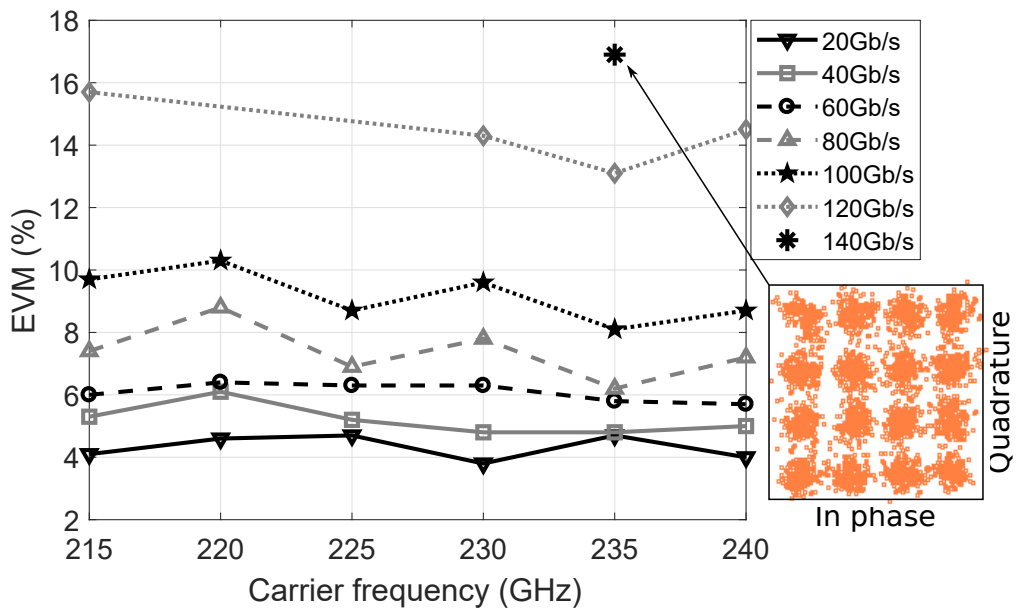


Figure 5.15.: EVM vs. LO frequency and data-rate for a 60-cm link using a 16-QAM modulation technique. The alignment between the Tx and the Rx is set to 0° , minimizing the IQ cross-talk.

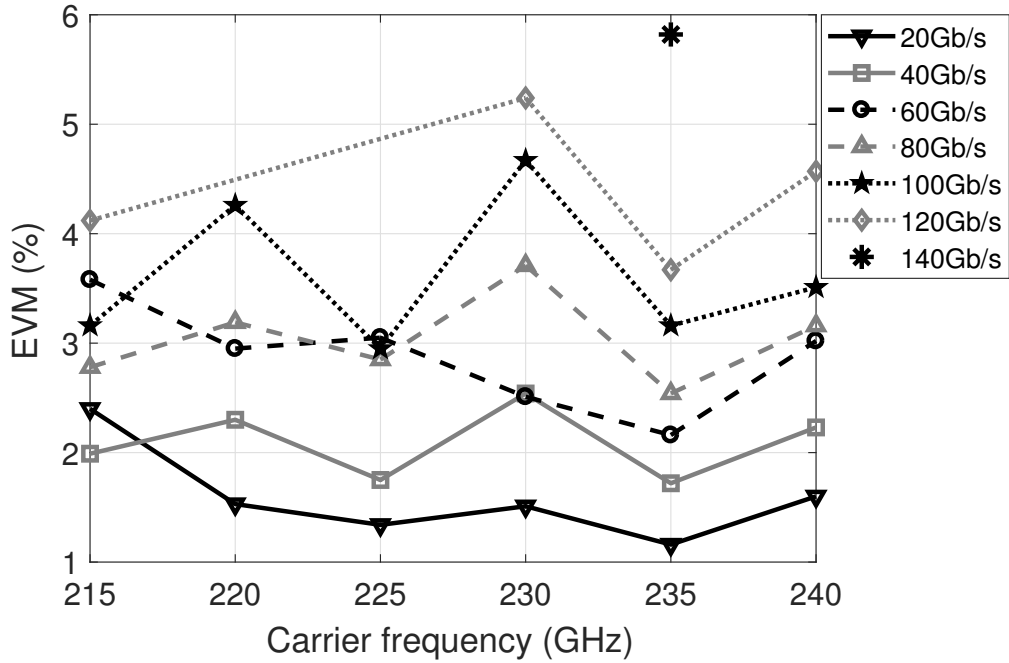


Figure 5.16.: Contribution of the SNR to the EVM in a 60-cm distance link using 16-QAM.

5.4.2. EVM analysis

This section evaluates the EVM contribution of the different impairments (SNR, measurement set-up, and phase noise). First of all, the SNR-related EVM was calculated after digitizing the signal and the noise level at the Rx BB outputs. The results are gathered in Fig. 5.16. As it can be seen, the SNR contribution to the final EVM is minor.

This link's phase noise influence is distinct from the one presented in the previous wireless communication link due to the different LO generation paths. Although the reduced multiplication factor reduced the LO generation path phase noise by 6 dB, the synthesizer's higher noise floor (-145 dBm/Hz) canceled this improvement. Fig. 5.17 displays the relation between phase noise and BB signal BW for this wireless link. The EVM contribution by the phase noise drops only from 9% to 7% when the system operated with a BB signal BW of 15 GHz.

Due to the high harmonic spur rejection level measured at the output of the $\times 8$ breakout, the harmonic contribution to the EVM stays below 1%. Therefore, its contribution to the measured EVM can be ignored. The remaining $EVM_{aggregated}$ excess in the system can be then expressed as

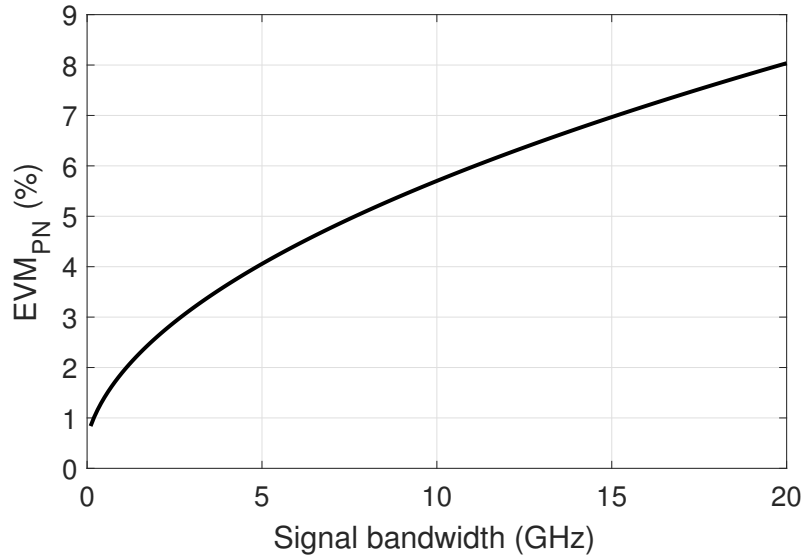


Figure 5.17.: EVM generated by the phase noise vs. BB signal BW.

$$EVM_{aggregated} = \sqrt{(EVM_{meas})^2 - (EVM_{SNR})^2 - (EVM_{AWG})^2 - (EVM_{PN})^2}. \quad (5.10)$$

Fig. 5.18 presents the results of evaluating this equation. For data-rates of 100 Gb/s and below, the remaining aggregated EVM excess stays under 3%, showing a major improvement from the EVM excess of 8.8% for the link established with the mixer-first Rx. For the maximum data-rates of 120 Gb/s and 140 Gb/s, the EVM excess is slightly higher, indicating that the Tx RF BW is not broad enough to support these data-rates.

5.4.3. Wireless link performance for different Tx/Rx azimuthal rotations

To further confirm the hypothesis that the IQ cross-talk is the major contributor to the EVM, the wireless communication link was tested for three different relative orientations between the Tx and the Rx (15°, 30°, and 45°). This test allowed for a steady increase in the level of IQ cross-talk while keeping the other error sources either constant (phase noise and measurement set-up) or easily measurable (SNR). The results of this test are gathered in Fig. 5.19. The maximum data-rate drops from 140 Gb/s to 100 Gb/s by changing the relative Tx/Rx rotation from 0° to 45°. The optimum LO frequency also changes with the relative Tx/Rx rotation. For maximum IQ isolation (0°), the optimum system performance was achieved when the Tx was operated under single side-band conditions at 235 GHz. Contrary, when the IQ isolation by polarization is canceled (45°), the system achieves

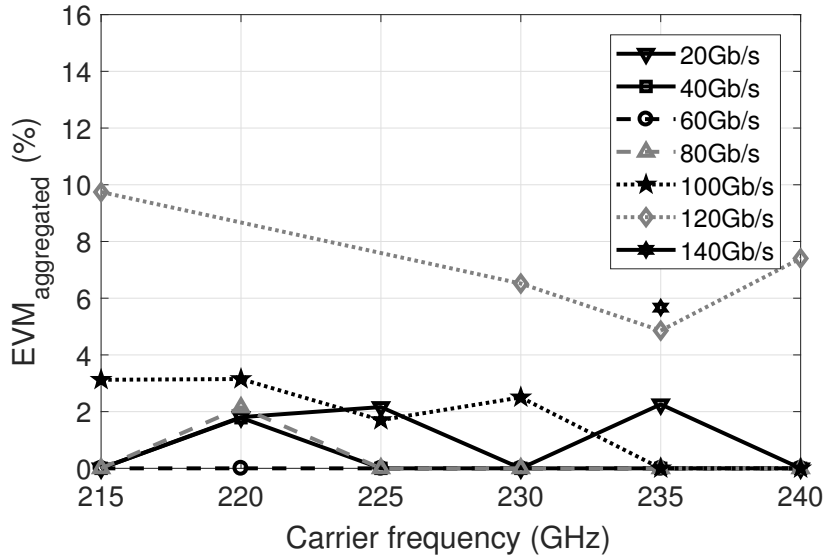


Figure 5.18.: EVM excess after subtracting the influence of the measurement set-up, SNR and phase noise for a 60-cm distance 16-QAM link.

the maximum data-rate at 225 GHz, where the Tx shows the best symmetry between the USB and the LSB. When the Tx/Rx alignment is 45° , the radiated I and Q channels are not separable at the Rx antenna. Under this condition, the wireless link operates as a standard direct-conversion IQ system. The results achieved with a 45° relative azimuthal rotation allow for a fair comparison with the link established in Chapter 4. Although the achieved data-rate remained constant, the maximum link distance drops from 1 m to 60 cm, indicating that the link established with the mixer-first Rx is better suited for real application scenarios.

The EVM generated by the SNR, phase noise, and measurement set-up was subtracted from all previously measured EVM to evaluate the dependence between the remaining EVM excess and the IQ cross-talk. These results are gathered in Fig. 5.20. A clear relation between EVM and IQ cross-talk can be drawn here. At 225 GHz, where the USB/LSB symmetry is maximized, the EVM excess for a data-rate of 100 Gb/s grows from 2.5% to 12% when the Tx rotates from the 0° to the 45° position. With no other relevant error source present in the wireless communication link, this test demonstrates that the main contribution to the EVM is the IQ cross-talk generated by the USB/LSB asymmetry.

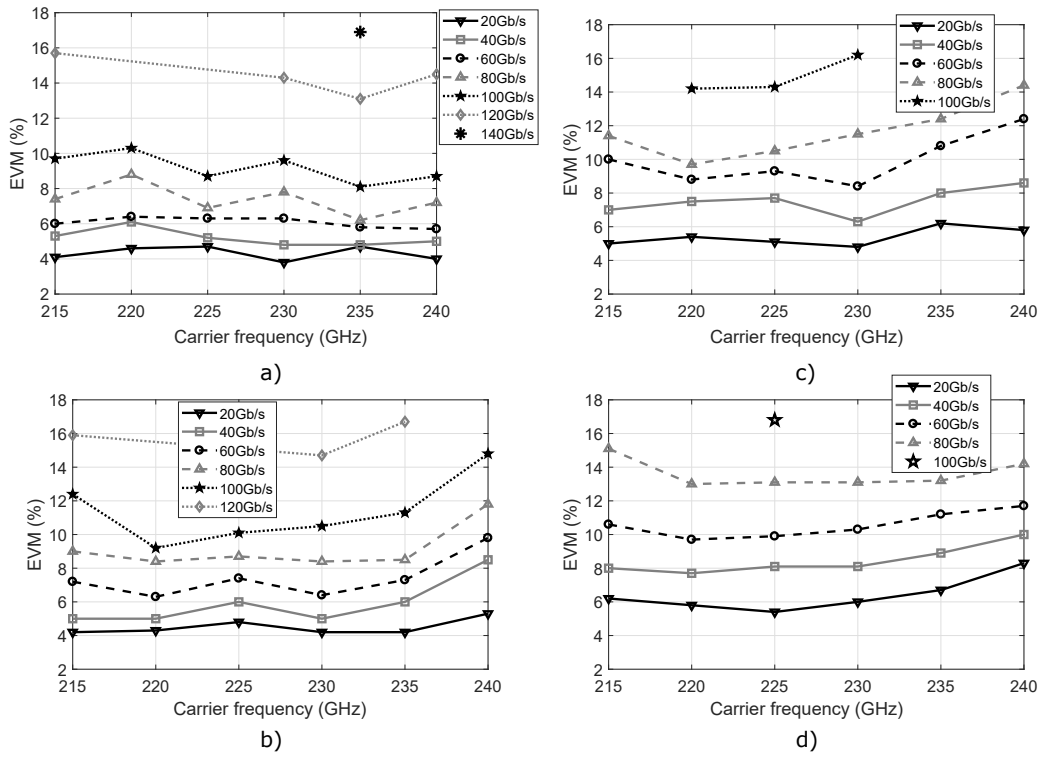


Figure 5.19.: EVM vs. LO frequency and data-rate for a 60-cm link using a 16-QAM modulation technique. The alignment between the Tx and the Rx was set to a) 0°, b) 15°, c) 30°, and d) 45°.

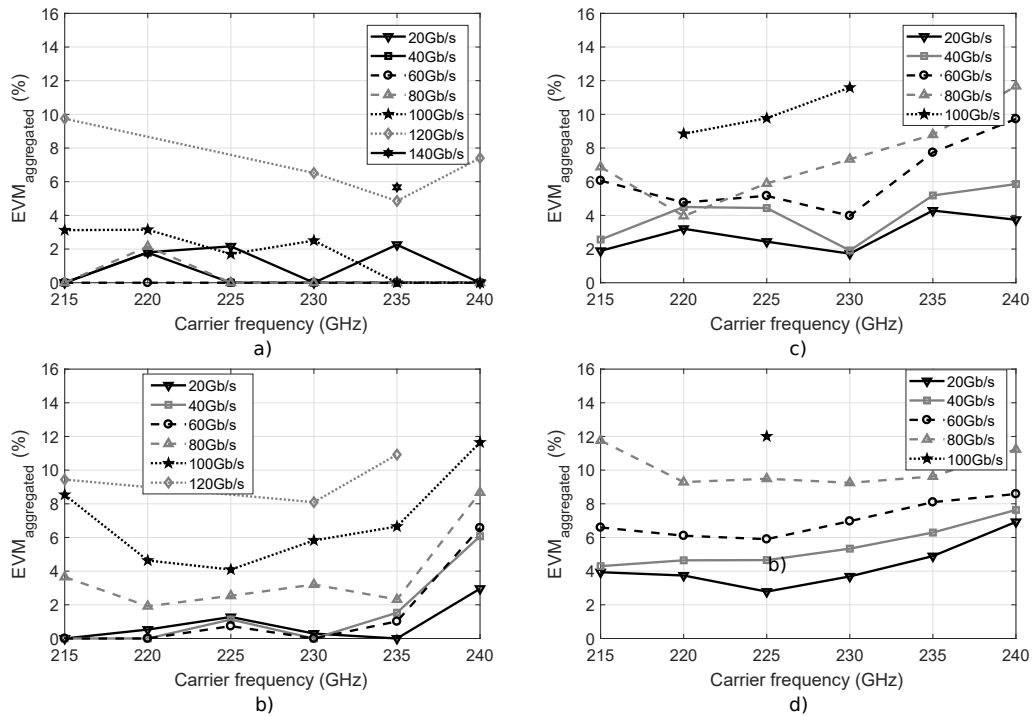


Figure 5.20.: EVM excess after subtracting the influence of the measurement set-up, SNR and phase noise for a 60-cm distance 16-QAM link. The alignment between the Tx and the Rx was set to a) 0°, b) 15°, c) 30°, and d) 45°.

5.5. Conclusions

This chapter demonstrated that the primary EVM source in a broadband wireless communication link operating beyond 200 GHz is the IQ cross-talk. For proper evaluation of this hypothesis, a new controllable orthogonality level between the Tx and the Rx was introduced. In this wireless link, the I and the Q channel are radiated each in an orthogonal linear polarization. The IQ isolation can be controlled by changing the azimuthal orientation between the Tx and the Rx. For the maximum polarization isolation, the IQ isolation was measured to be better than 20 dB for the whole operating BW regardless of the LO frequency. Under this operation condition, a maximum data-rate of 140 Gb/s was measured over a 60-cm distance for an LO of 235 GHz. At this LO frequency, the wireless communication link was operated in single side-band mode. This operating mode was only possible because the Tx and the Rx LO external drive were locked to the same external source, ensuring perfect phase alignment between Tx and Rx LO frequency. With the received signal power dependent on the relative phase difference between the Tx and the Rx LO frequencies, operation under real conditions (Tx/Rx operated with independent LO frequencies) would be not feasible.

For maximum IQ cross-talk (Tx/Rx relative azimuthal rotation at 45°), the maximum data-rate dropped to 100 Gb/s, and the optimum LO frequency moved to 225 GHz, where the USB/LSB symmetry holds best. At 225 GHz, the contribution of the IQ cross-talk to the measured EVM for a data-rate of 100 Gb/s grows from 2.5% to 12% when the Tx rotates from the 0° to the 45° position.

To ensure IQ isolation comparable to the 20 dB achieved by the polarization orthogonality in a standard direct-conversion IQ system, the USB and the LSB should present a variation under 0.1 dB. It is almost impossible to achieve a 3-dB RF BW with such in-band flatness. Moreover, the EVM generated by the measurement equipment grows to 18.4% for a symbol-rate of 42.5 Gbauds, preventing any test for data-rates beyond 160 Gb/s using 16-QAM. The current state-of-the-art of semiconductor technology and lab equipment sets a limit of around 150 Gb/s for the maximum data-rate that can be achieved or tested in a single wireless link operating at frequencies beyond 200 GHz.

If neither the modulation order nor the channel BW can be further enhanced, other implementation strategies must be followed to enhance the data-rates.

Chapter 6

MIMO RF front-end

6.1. Introduction

From the previous chapter, it can be concluded that it is impossible to increase the link data-rate neither by increasing the modulation order nor by enhancing the BW. The phase noise error introduced by the noise floor of the external LO signal drive is the main limitation for achieving higher modulation order. The current semiconductor technology limits the gain-BW product that the amplification stages can reach, setting a limit effectively to the achievable 3-dB RF BW of the Tx.

Considering that both methods of approaching higher data-rates are not feasible, two additional techniques can be further investigated to increase the total aggregate modulation speed by increasing the number of IQ channels operating in parallel. These are spatial/polarization orthogonality and channel bonding. Both, although commonly applied at lower operation frequencies [92]–[96], have not been extensively exploited in prior work on broadband communication beyond 200 GHz. Channel bonding was demonstrated at 240 GHz, achieving an aggregated data-rate of 15.6 Gb/s over a 15-cm distance [39]. Polarization diversity with two linearly-polarized on-chip antennas was demonstrated for a 220 GHz ASK (amplitude shift keying) Tx, achieving a total data rate of 24.4 Gb/s over a 10-cm distance [97]. The use of linear polarization antennas, however, requires accurate relative polarization alignment between Tx and Rx for sufficient leakage suppression between two transmission paths. Such a set-up becomes impractical in real application scenarios and requires the use of depolarizer circuit in the BB [95]. The implementation of these depolarizers at 100+Gb/s data-rates may become challenging, if not impossible. Contrary to that, simultaneous transmission of two circularly-polarized orthogonal waves

can potentially be applied to increase the link spectral efficiency for any relative orientation between Tx and Rx and without the use of a high-speed BB depolarizer under the provision that sufficient isolation between two adjacent transmission paths in the entire modulation BW can be achieved.

This chapter presents the first polarization diversity MIMO system operating at frequencies beyond 200 GHz. It demonstrates the feasibility of doubling the spectral efficiency of a line-of-sight QPSK wireless link by applying polarization orthogonality to a pair of highly-integrated fundamentally-operated direct-conversion IQ modules with a tunable carrier of 220–255 GHz. Both Tx and Rx modules are implemented as single-chip solutions in 0.13- μm SiGe HBT technology with $f_t/f_{\text{max}}=350/550$ GHz in combination with a wire-bonded chip-on-board packaging for high-speed BB signaling and an on-chip radiator interface to free-space. Each of the Tx and Rx chips accommodates two independent up-/down-conversion channels connected to a single silicon lens-coupled on-chip antenna supporting two orthogonal circular polarizations, right-handed circular polarization (RHCP) and left-handed circular polarization (LHCP), with sufficient isolation to implement a polarization-diversity MIMO over large modulation BW. The chipset in combination with a 9-mm diameter hyper-hemispherical Si-lens, providing a directivity of 23.5–27 dBi at 210–270 GHz for each of the modules, demonstrates the simultaneous transmission of 2 independent QPSK data streams, 55 Gb/s each, over a 1-meter line-of-sight distance with an EVM of 31.9% under a board-level limited channel BB BW of 13.5 GHz.

This chapter is organized as follows. Section 6.2 presents a top-level system description and an analysis of the influence of the polarization leakage on the link quality, measured as EVM. It also describes the implementation details for all relevant functional blocks in the transmit and receive path. In Section 6.3, the relevant RF measurements for the dual-polarization (DP) Tx and Rx front-end modules operating individually and in a back-to-back configuration are presented. Section 6.4 demonstrates the MIMO operation of the wireless link and analyzes the EVM measured in the wireless communication link. Finally, Section 6.5 concludes this. The here presented results and figures were previously published in [own9] and the copyright was transferred to IEEE.

6.2. DP Tx and Rx RF Front-end Architecture

A top-level block diagram of the dual-polarization Tx and Rx modules in a back-to-back link configuration is shown in Fig. 6.1. Both Tx and Rx chips consist of two independent

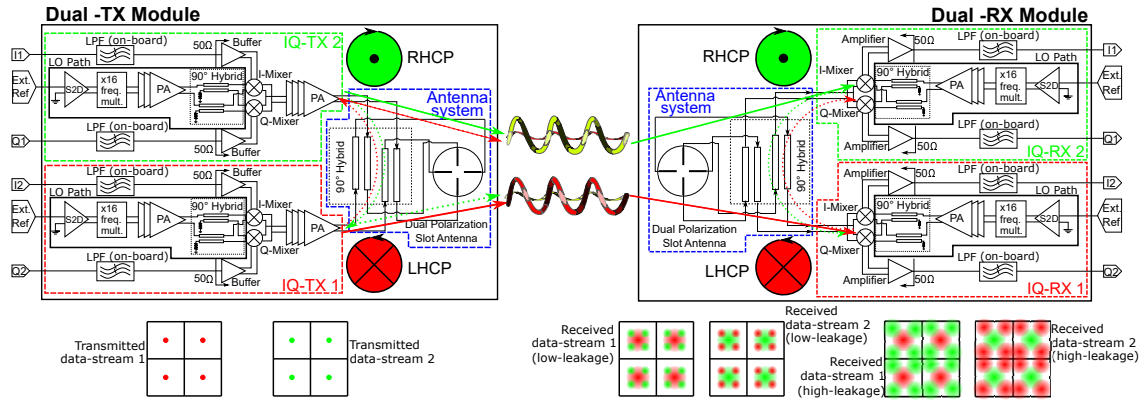


Figure 6.1.: Top-level architecture of the dual-polarization Tx and Rx modules in a back-to-back wireless configuration with the indicated two orthogonal transmission paths (RHCP and LHCP). Two major sources of a finite isolation between both paths are also sketched. These are: the antenna cross-polarization level and a direct leakage between the antenna RHCP and LHCP driving ports on each of the Tx and Rx modules. After [own9] © 2020 IEEE.

transmit/receive paths, respectively, placed side-by-side, as shown in Fig. 6.2. A circularly-polarized on-chip antenna system combines modulated data from both paths on each chip with two input ports supporting the two orthogonal channels in parallel (RHCP and LHCP). Each of the Tx/Rx channels represents a circuit architecture topologically similar to the Tx presented in Chapter 3 and Rx in Chapter 4, featuring an externally-driven $\times 16$ multiplier-chain in the LO generation path and a mixer-first arrangement on the Rx side for improved symmetry between the USB and the LSB. In the current chip implementation, both channels possess separate LO paths, which allows investigation of the on-chip leakage mechanisms between them, as will be explained in the following sections (see Sec 6.3.2). The primary radiator is the annular slot with two pairs of orthogonal feeds providing polarization diversity presented in Chapter 5 [29], [70], [88], [98], which in combination with a quadrature hybrid driving those feeds supports two orthogonal circularly-polarized waves (see Fig. 6.1). The antenna is coupled to a silicon hyper-hemispherical lens to minimize the influence of substrate modes in a silicon chip and to increase the antenna directivity.

For maximum data-rate in the overall polarization-diversity MIMO system, the influence of insufficient isolation between the two channels needs to be carefully considered. The coupling between two orthogonal data streams takes place predominantly on the antenna level. Here, the aggregate isolation is determined by two main factors on each side of the link. These are 1) direct leakage between two antenna driving ports and 2) antenna cross-polarization level (XPD), as indicated with dotted lines in Fig. 6.1. For the circularly-polarized waves, the cross-polarization level in dB can be expressed in terms of axial ratio (AR) [76], [99] as

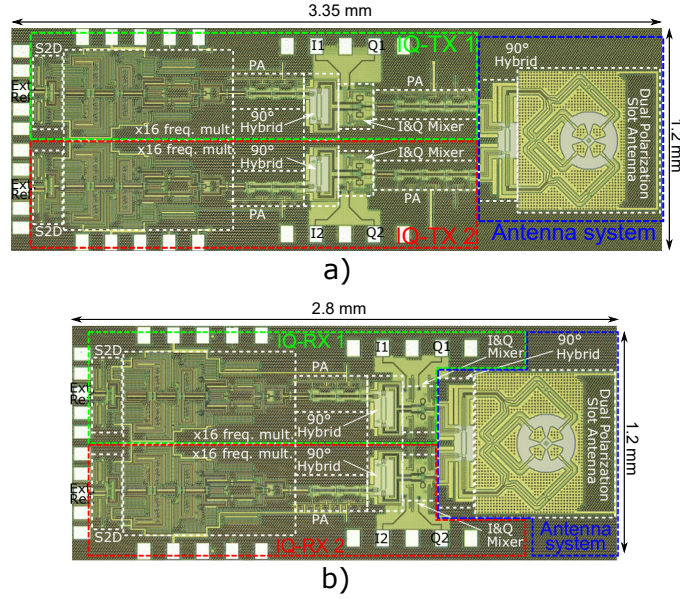


Figure 6.2.: Chip micrographs of a) transmitter, and b) receiver. After [own9] © 2020 IEEE.

$$XPD \text{ (dB)} = 20 \log_{10} \left(\frac{AR + 1}{AR - 1} \right). \quad (6.1)$$

In a back-to-back wireless link, the cross-polarization isolation is a function of the RF frequency and the relative alignment between the major and the minor polarization axis on both sides. In the worst-case scenario, it is a twofold value of XPD under the assumption of equal polarization purity for both RHCP and LHCP on both ends of the link. A direct leakage between the RHCP and LHCP driving ports of the antenna system may further lead to parasitic transmission/reception at the complementary polarization. The overall isolation is the primary design requirement and needs to be provided over the entire RF BW and for any relative orientation between Tx and Rx modules.

The EVM will be used as a standard and a modulation format-independent metric of the link quality [56], [57]. The contribution of all system-level impairments will be added in an aggregate EVM [48], as explained in Chapter 3. Under the assumption of the XPD with a white frequency distribution in the operation BW [58], the influence of the cross-polarization leakage in the link can be described as non-correlated interference as

$$EVM_{SNR} = \sqrt{\frac{1}{XPD}}. \quad (6.2)$$

The deterioration of the link EVM when both polarization channels are operated simultaneously and under the influence of the cross-polar interference is given by the following relation

$$EVM_{total} = \sqrt{(EVM_{single\ path})^2 + (EVM_{XPD})^2}, \quad (6.3)$$

where $EVM_{single\ path}$ is the measured EVM when only one of the polarization channels is active.

6.2.1. Tx and Rx circuit building blocks

This section presents the implementation details for all relevant functional blocks in the Tx and Rx path. As this chapter's primary topic is on the MIMO operation, the design details related to each separate transmission path will not be explained here in detail, referring to the chapters where they are described with more details.

The $\times 16$ LO generation path is topologically similar to the one presented in Chapter 3. It consists of four cascaded Gilbert-cell doublers followed by a 3-stage PA to ensure enough signal drive at the mixer inputs and a broadband hybrid coupler to provide the IQ functionality. The Tx up-conversion path consists of an up-conversion mixer followed by a 4-stage PA, similar to the up-conversion path presented in Chapter 3. The Rx down-conversion implements a mixer first architecture, similar to the one presented in Chapter 4. However, due to the limitations in the number of available lab equipment quantities to simultaneously drive and analyze four high-speed differential BB signals on the Tx and the Rx, respectively, the Rx BB output and the Tx BB inputs had to be operated single-ended. The schematic for the on-chip implementation of this terminations are shown in Fig. 6.3 and Fig. 6.4 for the Tx and the Rx, respectively. The transistors Q10-Q11 and Q14-Q15 have been terminated with an on-chip resistor in the Rx and Tx, which degrades the balance in the output/input amplification stage resulting in a degraded SNR as well as an increased frequency dispersion in the operation bandwidth. This effect will be discussed in more detail in Section 6.4.

6.2.2. Packaging

A low-cost COB packaging solution is used to provide all dc, LO external driving signals, and high-speed modulated BB signals on the board level. Here, each of the Tx and Rx chips is mounted on the backside of a 9-mm diameter hyper-hemispherical lens made of high-resistivity silicon with the primary on-chip radiator aligned with the lens center.

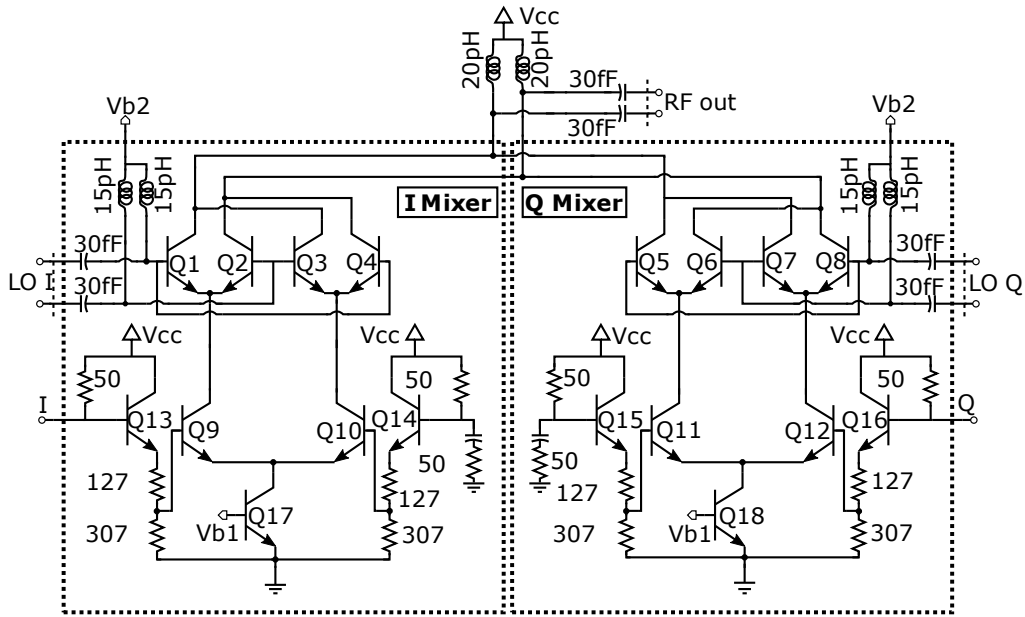


Figure 6.3.: Circuit-level schematic of the double-balanced IQ Gilbert-cell up-conversion mixer. The emitter areas for Q1-Q8, Q9-Q12, and Q13-Q18 are $1 \times (1 \times 0.1) \mu\text{m}^2$, $2 \times (1 \times 0.1) \mu\text{m}^2$, and $4 \times (1 \times 0.1) \mu\text{m}^2$, respectively. One side of the differential BB inputs is terminated to facilitate a single-ended operation with the limited measurement equipment. After [own9] © 2020 IEEE.

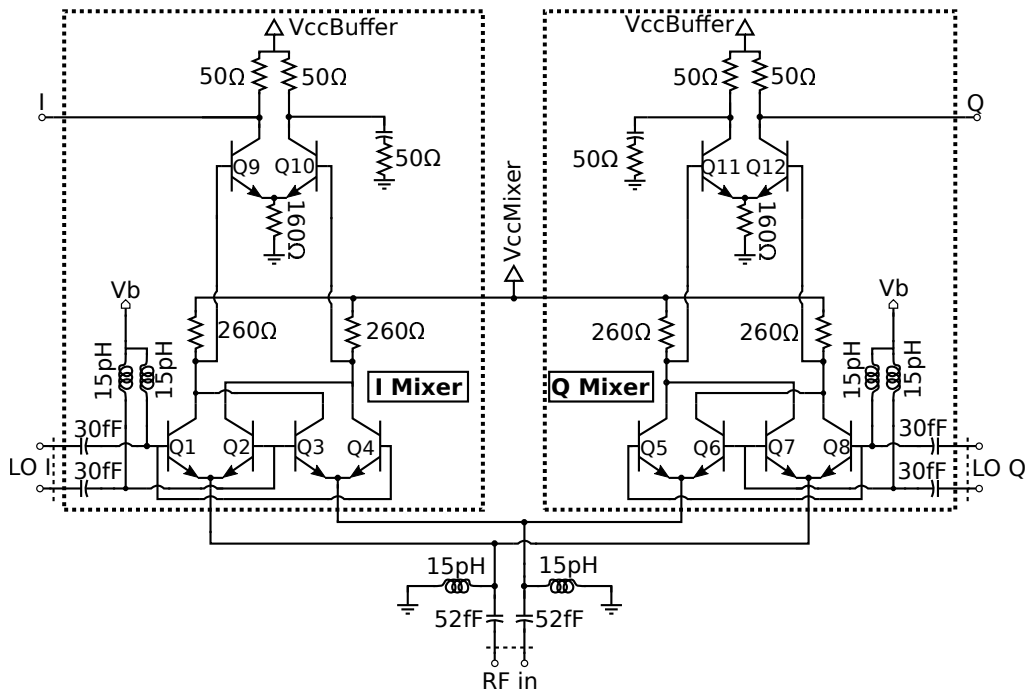


Figure 6.4.: Circuit-level schematic of the double-balanced IQ switching-quad down-conversion mixer, including the BB amplifier. The emitter area for each of Q1-Q12 is $2 \times (1 \times 0.1) \mu\text{m}^2$. One side of the differential outputs is terminated to facilitate a single-ended operation with the limited measurement equipment. After [own9] © 2020 IEEE.

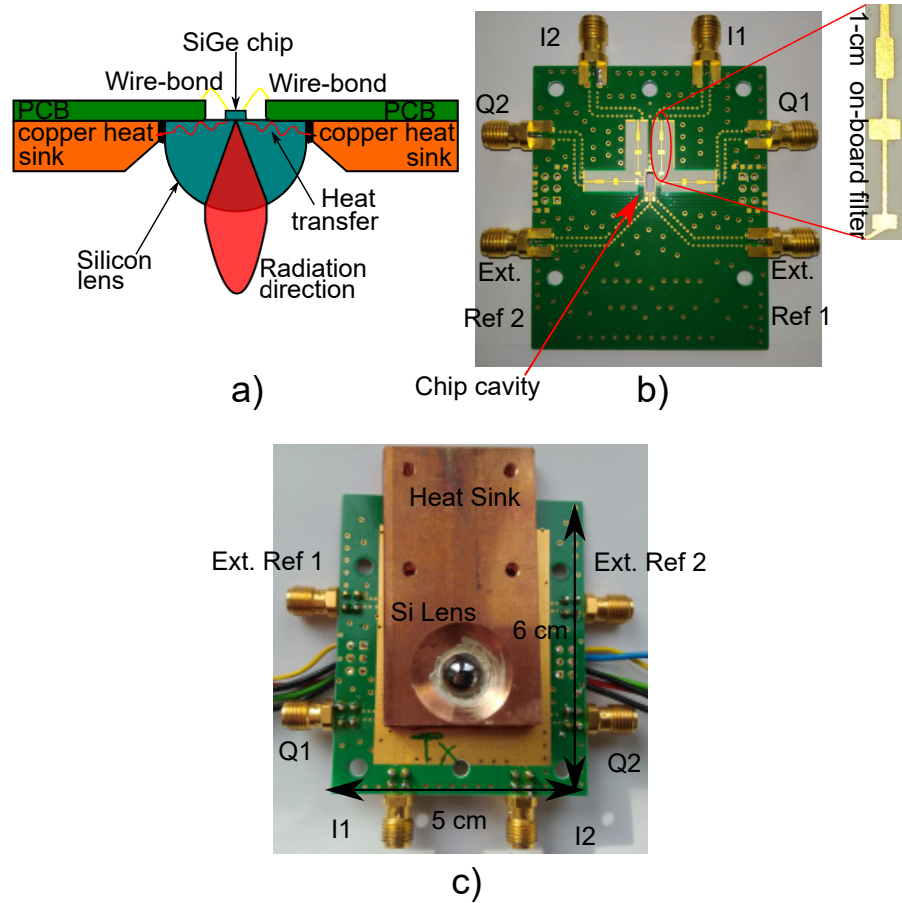


Figure 6.5.: a) Cross-sectional view of the chip-on-lens assembly in the PCB recess, b) photograph of the PCB with the LO and BB signal distribution, including the low-pass filter for wire-bond compensation, and c) photograph of the completely assembled Tx front-end module. After [own9] © 2020 IEEE.

The on-chip heat is transported through the lens to a heat-sink attached to the PCB bottom side. The overall chip-on-lens assembly is placed in a recess of a regular two-layer 0.5-mm thick Rogers 4350B board surrounded by a metal plane, as shown in Fig. 6.5. No anti-reflection coating on the lens aperture is currently provided, which influence the operation of both Tx and Rx modules and is discussed in more detail in Section 6.2.3. The overall antenna directivity can be adjusted simply by changing the lens dimensions to accommodate different link budget constraints.

A manual mm-length wire-bonding process was applied to all on-chip connections. With the limited dimensional control of the wire-bonding process, the bonding process, altogether with the RF connector assembly tolerance, is not only a non-negligible source of mismatch between all 4 I and Q BB paths but also leads to asymmetry in each of the differentially-driven BB input/output signals. To minimize the influence of mm-long wire bonds on the package-level BW, an 8-section step-impedance microstrip-line low-pass filter, similar to the filter presented in Chapter 3, is implemented on-board for each of the

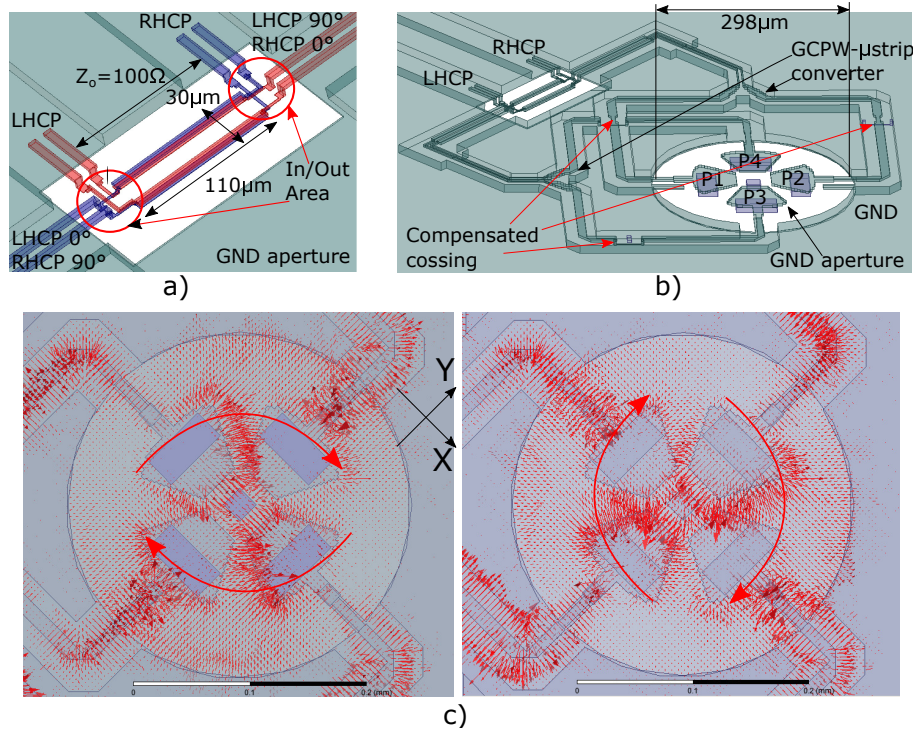


Figure 6.6.: 3-D simulation models of a) the quadrature coupler with the RHCP and LHCP driving ports, b) the complete antenna system, and c) E-field distribution in the BEOL stack around the slot radiator at 240 GHz for two chosen excitation phases of the RHCP polarization advancing each other by 90°. After [own9] © 2020 IEEE.

high-speed BB signals, as indicated in Fig. 6.5.

6.2.3. Circular Dual-Polarization antenna

The complete antenna system, as shown in Figs. 6.6 and 6.7, comprises a cascaded connection of the wideband differential 100- Ω quadrature coupler and the main radiating annular slot illuminating a hyper-hemispherical silicon lens through the backside of a 150 μm thick silicon die with a bulk resistivity of 50 $\Omega\cdot\text{cm}$ [29], [88]. The main radiator is similar to the radiator presented in Chapter 5. The antenna supports 2 orthogonal linear polarizations excited by 2 pairs of patch probes, P1-P2 and P3-P4, located 90° apart along the slot circumference [70], [98] driven in quadrature from two input ports, LHCP and RHCP, of the coupler. The antenna is embedded in a 7-layer 12 μm thick BEOL stack of a silicon chip. The quadrature hybrid coupler is similar to the one used for IQ generation in the LO path; however, here, the 50 Ω resistors placed at the terminated port have been removed, and this port is used as an additional input required for the second polarization channel to operate. The coupler outputs feed directly a dual-polarization antenna.

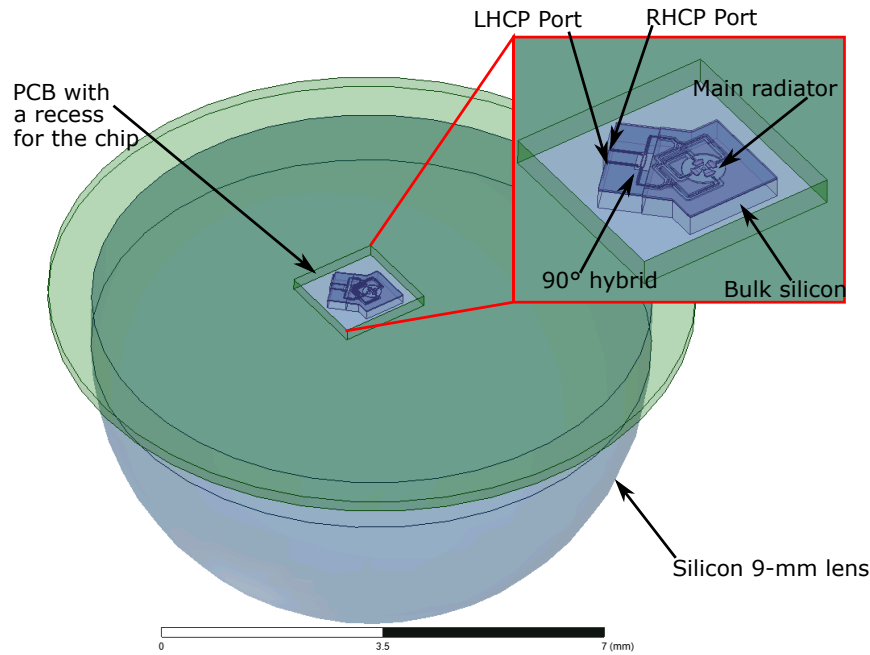


Figure 6.7.: 3-D simulation model of the packaged RF module with a silicon chip on the backside of a 9-mm silicon lens. The lens is attached to the metallized PCB, whereas the front-end chip sits inside a rectangular recess. A magnified view of the on-chip antenna system is shown in the inset. After [own9] © 2020 IEEE.

The major simulation results of the complete circularly-polarized antenna (slot radiator with coupler) on a silicon half-space for 210-310 GHz indicate a broadband match better than -26 dB for both LHCP and RHCP input driving ports with a RHCP-to-LHCP port isolation below -22 dB. The axial ratio at boresight for both circular polarizations stays below 1.3. The E-field distribution in the BEOL stack around the slot radiator excited in RHCP polarization at 240 GHz for one arbitrary chosen excitation phase and another one advancing the previous by 90° is plotted in Fig. 6.6 for completeness, indicating the E-field vector rotation characteristic for circular polarization. The simulated radiation efficiency into a silicon half-space decreases from 51% to 43% and is largely defined by the coupler and feed line losses. The inherent radiation efficiency of the slot radiator is around 90% [70], [98]. The simulations were conducted assuming 2.0×10^7 S/m, 0.02, and $50 \Omega \cdot \text{cm}$ for metal conductivity, the dielectric loss tangent of the BEOL stack, and the silicon bulk resistivity, respectively.

The packaging scheme followed in this implementation is similar to the one presented in Chapter. 3. In the current implementation, no anti-reflection coating layer is applied to the lens aperture. For the Rx module, the main consequence is limited to an increase in its NF. However, the influence of a missing anti-reflection coating layer may become more complicated for the Tx module. In particular, the rays reflected an odd number of times

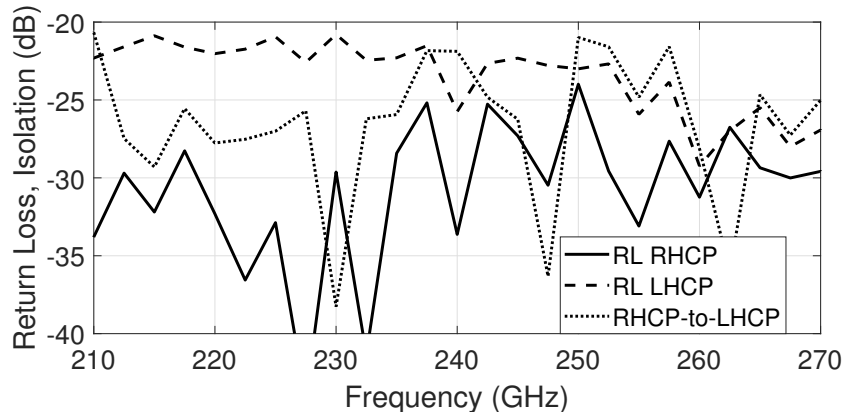


Figure 6.8.: Full-wave simulated return loss at both RHCP and LHCP driving ports and the isolation between them for the complete chip-on-lens packaged assembly in the transmit mode of operation. After [own9] © 2020 IEEE.

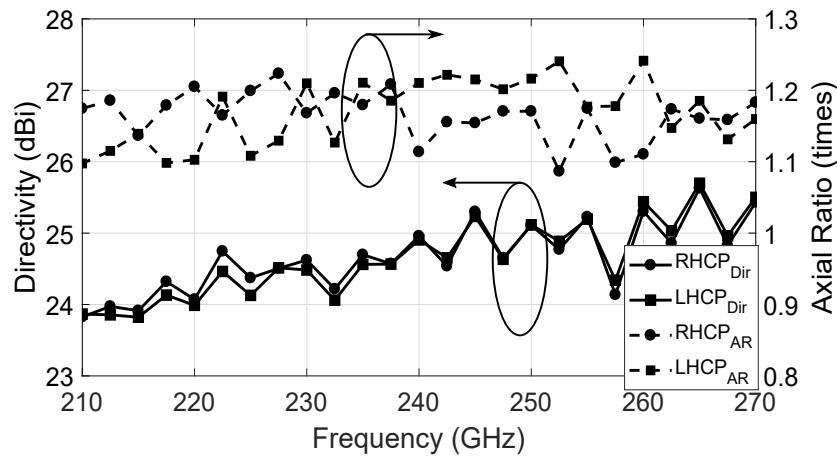


Figure 6.9.: Full-wave simulated frequency-dependent directivity and axial ratio at bore-sight for the complete chip-on-lens packaged assembly operated in transmit mode from the RHCP and LHCP driving ports. After [own9] © 2020 IEEE.

at the lens-air aperture are prone to polarization change between LHCP and the RHCP, and therefore, can be coupled back to the antenna feed port of the adjacent polarization and be finally re-transmitted. The rays undergo an even number of reflections preserve their original polarization, but may lead to group delay distortion if they contribute to the main radiation lobe. Both phenomena are a complex function of wave propagation through the primary-feed on-chip antenna, its illumination pattern of the lens aperture, and ray propagation within the lens volume [100], [101], and were considered in the design process.

A complete chip-on-lens assembly mimicking the packaging scheme from Sec. 6.2.2 was modeled and simulated (Ansoft HFSS) to investigate the influence of internal reflections at the lens-air interface in the transmit mode of operation on key parameters relevant for

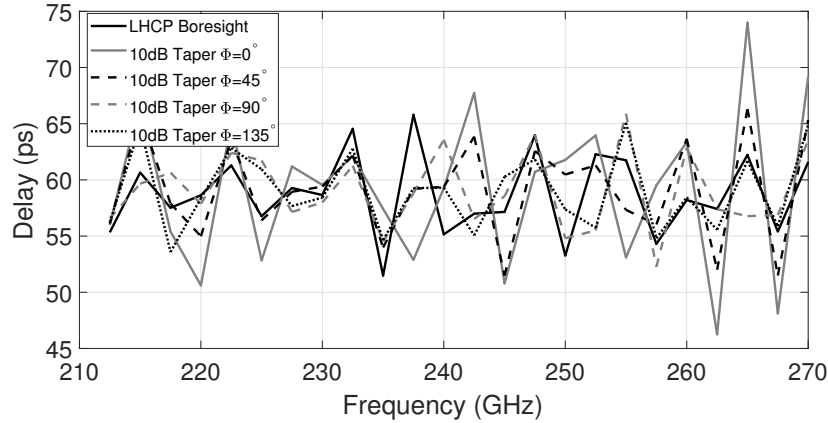


Figure 6.10.: Full-wave simulated group delay between the LHCP driving port and free-space for the complete chip-on-lens assembly. A group delay for different locations in the main beam, including boresight and beam edges defined by a 10 dB taper, is indicated. Four characteristic beam cross-section defined with respect to the coordinate system from Fig. 6.6 are plotted. After [own9] © 2020 IEEE.

the implemented polarization-diversity MIMO system. As shown in Fig. 6.8, both the simulated input match for RHCP and LHCP driving ports, as well as isolation between them, are superior to -21 dB in the entire 210–270 GHz operation frequency range. The simulated directivity, shown in Fig. 6.9, ranges between 23.8 dB and 25.4 dB, and is similar for both LHCP and RHCP polarizations. The frequency-dependent axial ratio at boresight (see Fig. 6.9) for both polarizations stays in the range of 1.08-1.24 and according to Eq. (6.2) should be sufficient to support a 16-QAM modulation format in the absence of other system impairments. The axial ratio was additionally verified to stay largely below 2 within the entire main beam defined by a 10-dB taper from boresight.

The frequency dependence of a group delay incurred between the RHCP/LHCP driving ports and free-space was further simulated for different locations in the main beam. Some selected results for LHCP polarization at boresight and around the beam edges ('10 dB taper') across 4 characteristic beam cross-sections defined with respect to the coordinate system from Fig. 6.6 are presented in Fig. 6.10. An average delay of around 60 ps with a typical deviation below 6 ps at boresight and slightly higher at the beam edges is preserved for 210–270 GHz, correlating well with the time of flight through the lens. The periodic-like changes in the de-embedded delay should be attributed to the internal lens reflections but may also be partly accounted for by finite accuracy of the meshed volume and of the absorbing boundary conditions.

6.3. RF characterization

Two different groups of RF measurements have been performed. The first encompasses a set of single-tone measurements allowing separate investigation of the frequency-dependent lower- and upper-sideband characteristics for key Tx/Rx performance metrics. In the second, the measurements involve a combined operation of the Tx and Rx modules configured into a free-space back-to-back line-of-sight set-up. Here, both double-sideband quadrature up-conversion and down-conversion are performed between the BB Tx inputs and the Rx outputs, which supports a study of the influence of different hardware imperfections acting simultaneously in the set-up mimicking a real wireless link. All measurements have been taken in free-space and at the board level, including the influence of all on-board and on-chip components cascaded between the on-board high-speed connector and the lens-coupled on-chip antenna. An absorbing material was applied to cover the major reflecting surfaces to minimize the influence of parasitic reflections in the measurement set-up.

6.3.1. Single-tone RF measurements of the Tx and Rx

For these measurements, the set-up presented in Chapter 3 was employed; please refer to this chapter for more details about the set-up. However, the linearly-polarized horn antenna of the OML module captures only a linear projection of the circularly-polarized electrical fields generated by the on-chip antennas. Therefore, the complete Tx/Rx RF characteristics were found by the superposition of two constitutive series of measurements for two relative azimuthal orientations around boresight between Tx/Rx and OML modules, which correspond to the major and the minor axis of a general polarization ellipse [76].

Antenna measurements. To use the Friis-formula, a set of antenna measurements, including axial ratio at boresight and co-polarization radiation patterns with the corresponding antenna directivity, was performed for both Tx and Rx modules and each polarization path. Each of the modules was mounted on a motorized 2-D rotational stage with an additional rotational alignment in the azimuthal plane around the boresight. Here, by continuous rotation around the boresight, the minor and the major axis of the polarization ellipse with respect to the OML module orientation corresponding to the minimum and maximum measured power levels can be found. From the square-root ratio of these power levels, the AR can be calculated [76], [99]. As presented in Fig. 6.11, an AR of 1.05–1.31 for RHCP polarization was measured for both Tx and Rx modules in the frequency range of 210–270 GHz. Some differences between both curves can be partly accounted for by a

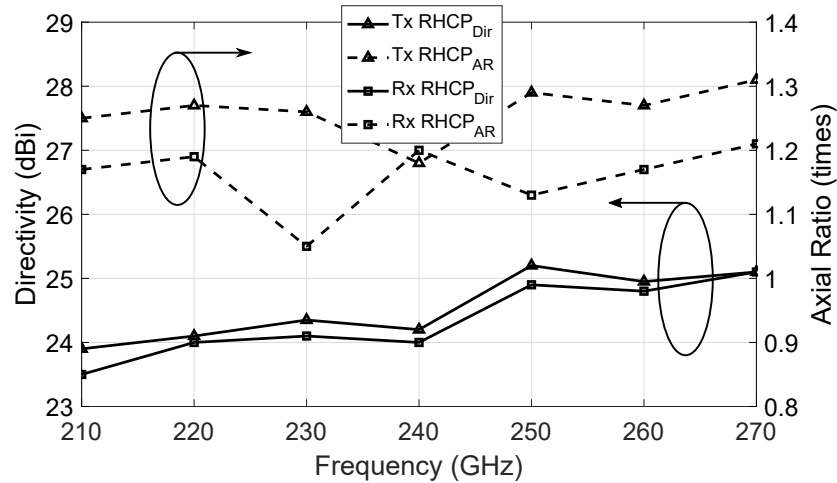


Figure 6.11.: Measured frequency-dependent axial ratio at boresight and directivity for the Tx and Rx modules operating with RHCP polarization. After [own9] © 2020 IEEE.

finite alignment accuracy in the measurement set-up and insufficient precision of the chip-on-lens assembly. Similar values were acquired for orthogonal LHCP polarization with a maximum deviation between each other below 0.1 and an upper bound of 1.4, correlating well with the simulation results from Fig. 6.9.

Next, the antenna radiation pattern measurements for both polarization states (RHCP and LHCP) of the Tx/Rx modules were performed for the previously-defined orthogonal orientations corresponding to the major and minor axis of the polarization ellipse in each case, and each total co-polar radiation pattern was found by superposition of two constitutive partial measurements. The directivity was finally calculated by integrating the measured values of the 2-D power density co-polar patterns acquired over a $\pm 40^\circ \times \pm 40^\circ$ -sector of the hemisphere because of the mechanical limitations. The measured frequency-dependent antenna directivity for RHCP polarization, as shown in Fig. 6.11, increases monotonically from 23.5 dBi to 25.2 dBi in the frequency range of 210-270 GHz for both Tx and Rx modules, well correlating to the simulation results from Fig. 6.9. The corresponding LHCP antenna directivity, although not shown, deviates by no more than 0.5 dB from the plotted RHCP values. An azimuthal view of the exemplary chosen RHCP radiation pattern measured at 240 GHz in the transmit mode is shown in Fig. 6.12, indicating a good beam rotational symmetry.

Up-conversion path of Tx module. Two up-conversion paths of the Tx chip were measured with a tunable 220–255 GHz LO frequency, and for BB signals up to 20 GHz provided from the board level. As explained in Sec. 6.2.1, the BB input ports were operated single-ended. For characterization of the IQ amplitude imbalance, the I and Q ports were driven separately, whereas for the total radiated power measurement in the upper and

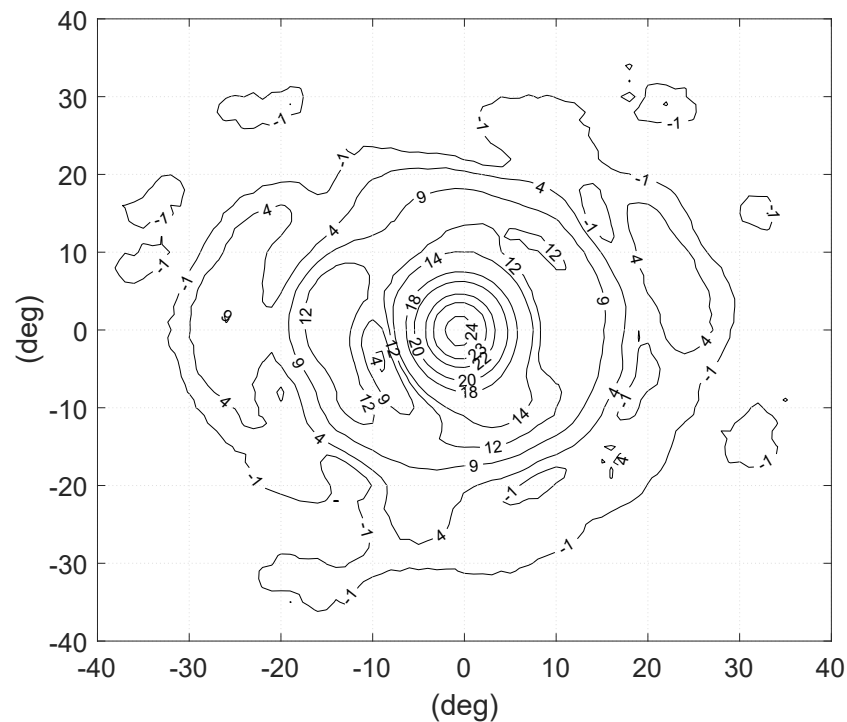


Figure 6.12.: Measured 2-D contour plot of the co-polar RHCP radiation pattern at 240 GHz for the Tx module. After [own9] © 2020 IEEE.

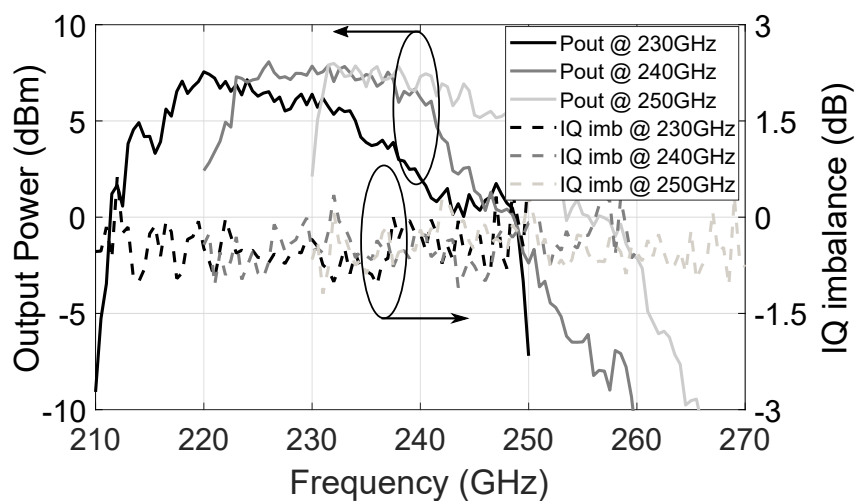


Figure 6.13.: Measured total radiated power and IQ amplitude imbalance in the RHCP Tx path for different LO frequencies and an input power level of -5 dBm at each of the BB driving ports. After [own9] © 2020 IEEE.

the lower sideband, a broadband (0.5–20 GHz) 90° hybrid (QH0226 Marki) was used to combine the I and Q signals at the mixer BB ports. The Tx RF characteristics for an input power level of -5 dBm at each of the BB driving ports are gathered in Fig. 6.13. This power level allows the Tx to operate close to saturation and maximizes the link performance for QPSK modulation (see Section 6.4). The key Tx parameters do not only depend on LO frequency but also vary as a function of the frequency difference between RF and LO; with the LSB typically outperforming USB. The peak radiated power is around 7.5 dBm per polarization channel. The LHCP transmission path exhibits very similar characteristics with a maximum deviation in the radiated power between LHCP and RHCP below 0.5 dB across the measured operation frequency range. The IQ amplitude imbalance was measured below 1 dB in the entire BB BW, and is partly defined by the board-level mismatch between I and Q paths incurred by the finite assembly tolerances.

Down-conversion path of Rx module. Similarly to the Tx chip, the Rx BB outputs were operated single-ended, immediately degrading the measured Rx CG by 3 dB. The Rx BB outputs in the wireless communication link set-up require to be cascaded with the broadband amplifiers PSPL5882 from Tektronix to raise the output noise spectral density above the noise floor of the consecutive high-speed oscilloscope. This complete cascaded configuration of the Rx was further applied in the measurement set-up to facilitate a direct comparison of the Tx/Rx chipset operating in a wireless back-to-back loop with the single-tone RF characterization results. The measured cascaded CG, SSB NF, and IQ amplitude imbalance for the RHCP receive path operated at 3 different LO frequencies are gathered in Fig. 6.14. The Rx shows a peak CG of around 18 dB and a board-level limited 3-dB RF BW of 28 GHz with a very weak dependence on LO frequency. The IQ amplitude imbalance stays below 1 dB, similarly to the Tx module. The cascaded in-band SSB NF is around 18 dB and was estimated by employing an indirect measurement method from [77], due to the lack of a noise source at these frequencies in our lab.

LO generation path The direct leakage between the external LO signal drive to the Rx BB output was measured at -50 to -55 dB below the power of the external driving signal for the multiplier chain. The distance between the desired $\times 16$ harmonics and the unwanted spurs generated by the multiplier chain ($\times 14$, $\times 15$, $\times 17$, and $\times 18$) was measured to be better than 30 dB in the 225–245 GHz band, dropping to a level of 15–20 dB for the other LO frequencies. The close-carrier phase noise of the Tx LO path driven from the reference synthesizer (Keysight E8257D) was measured to scale as expected according to $10 \cdot \log_{10}(16) = 24.1$ dB.

On-chip isolation between two polarization paths. As discussed in Sec. 6.2, the direct leakage between the driving ports of the antenna system (hybrid coupler inputs)

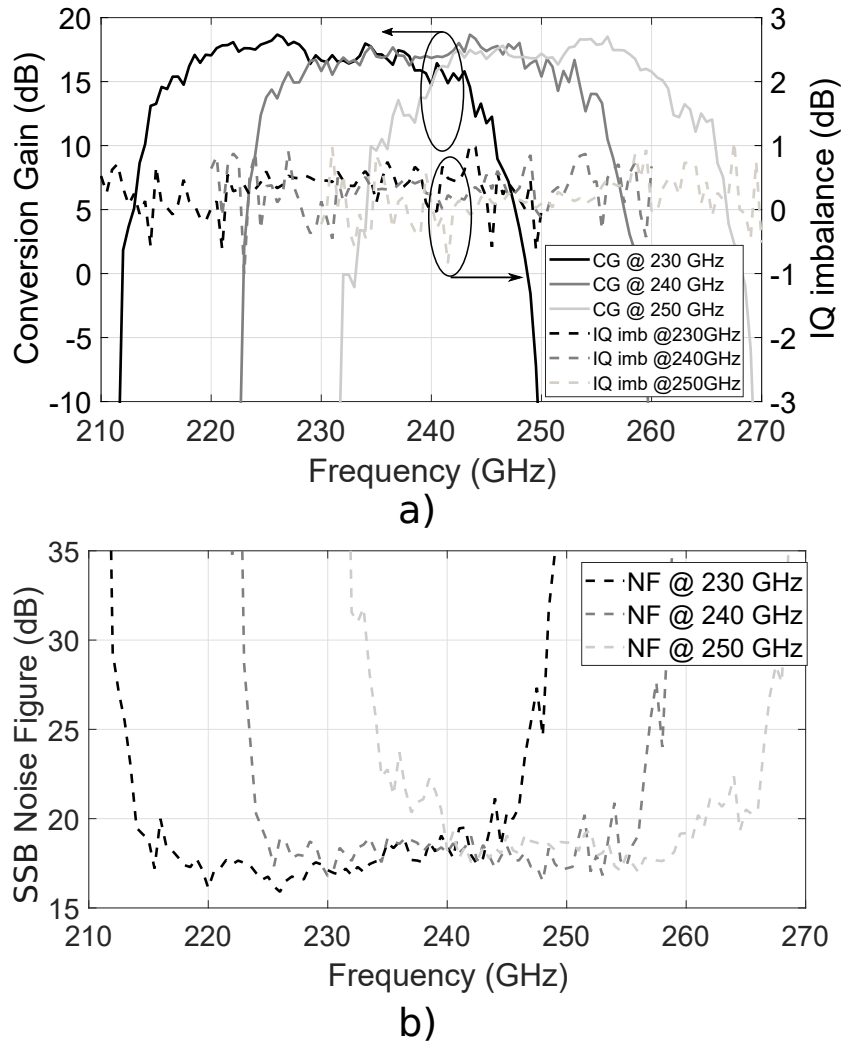


Figure 6.14.: Measured frequency-dependent a) conversion gain, b) IQ amplitude imbalance, and c) SSB NF in the RHCP Rx path, for different LO frequencies. After [own9] © 2020 IEEE.

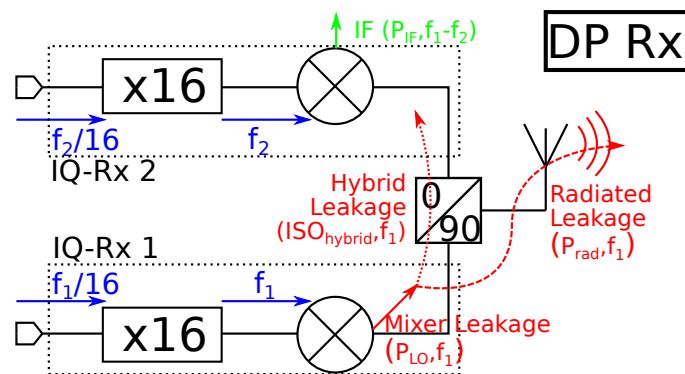


Figure 6.15.: A simplified block diagram of the Rx chip in a test configuration applied to measure isolation between two driving ports of the antenna system. After [own9] © 2020 IEEE.

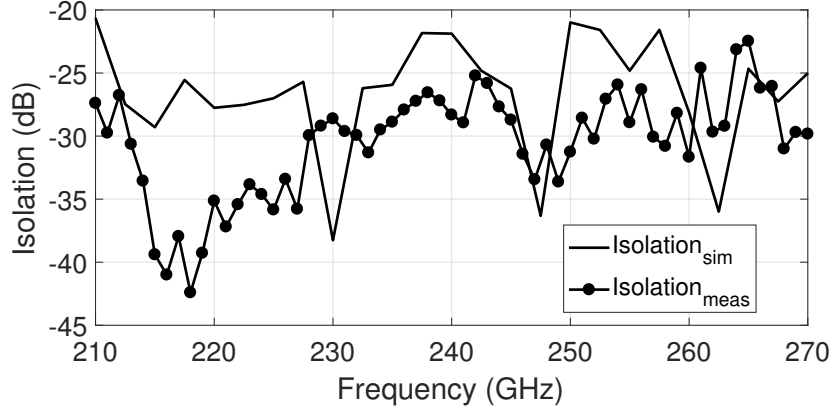


Figure 6.16.: Measured and simulated isolation between two driving ports (RHCP and LHCP) of the antenna system. After [own9] © 2020 IEEE.

is one of the potential major sources of coupling between the two polarization-orthogonal channels. To characterize this leakage, a dedicated test procedure was developed. An outline of the procedure is illustrated in Fig. 6.15. This set-up exploits the two independent LO paths, $IQ - Rx1$ and $IQ - Rx2$, operating at two different LO frequencies f_1 and f_2 with a frequency offset of $f_1 - f_2$. Here, the LO power P_{LO} leaking through the down-conversion mixer, $IQ-Rx1$, is down-converted to P_{IF} due to the finite isolation between the two ports of the antenna system ISO_{Hybrid} . The isolation of the hybrid ISO_{Hybrid} can be calculated as

$$ISO_{Hybrid}(dB) = P_{IF} - P_{rad} - CG_{IQ-Rx2} - 2 \cdot Ant_{Loss}, \quad (6.4)$$

where CG_{IQ-Rx2} denotes the previously measured conversion gain of the $IQ-Rx2$ Rx path and Ant_{Loss} refers to the simulated loss of the complete antenna system from Sec. 6.2.3. P_{rad} is the LO power leaking through the mixer $IQ-Rx1$ corrected by the insertion loss incurred by the antenna system, as $P_{rad} = P_{LO} - Ant_{Loss}$, and was characterized directly with the free-space single-tone measurement set-up. The isolation was measured in the 210–270 GHz frequency range by simultaneous tuning in both LO paths with a constant frequency offset of 500 MHz and is presented in Fig. 6.16 altogether with the previous simulation results from Fig. 6.8; both correlating well with each other. The isolation is superior to -22 dB for the entire 210–270 GHz range and is, therefore, expected to be less critical than that incurred by the axial ratio.

A similar set-up cannot be applied to the Tx chip because of the reverse isolation of the PA block inserted between the up-conversion mixer and the antenna system. It is assumed that both Rx and Tx chips show similar on-chip isolation between RHCP and LHCP paths due to identical antenna layouts.

6.3.2. Tx and Rx back-to-back results

The effective channel BW of each complete transmission path (LHCP or RHCP) in a back-to-back configuration is set by RF bandpass and BB low-pass characteristics of both Tx and Rx modules acting together by performing the combined double-sideband up-conversion and down-conversion between the corresponding BB Tx and Rx ports. In particular, double side-band operation involves the asymmetry between LSB and USB of both modules in the transmission process and, therefore, the frequency-dependent characteristics, both amplitude and group delay, of the complete path, are not simple replicas of the Tx and Rx RF properties found from single-tone measurements. The aggregated isolation between both transmission paths is related to a direct leakage between the RHCP and LHCP antenna driving ports on each chip, the antenna axial-ratio on both sides of the link, and a relative azimuthal orientation around boresight between the transmit and the receive block. The highest cross-polarization incurred coupling appears when the major axes of the polarization ellipse on both Tx and Rx side are rotated by around 90° and corresponds to the sum of the antenna cross-polarization level, XPD, on both sides.

In order to measure the Tx/Rx performance in a back-to-back configuration, the set-up presented in Fig. 6.17 was used. Here, the Tx and Rx modules were placed in the line-of-sight at a 1-m distance and all on-chip LO generation paths were driven from a single frequency synthesizer. The LO frequency was tuned between 210 GHz and 270 GHz with the corresponding BB sweep of 15 GHz for each LO frequency setting. Although the isolation between RHCP and LHCP paths does not depend on a relative phase difference between the Tx and Rx LO chains to the first-order extend, a phase shifter, as shown in Fig. 6.17, was used to facilitate the channel measurements for both of them by ensuring the maximum power transfer for each of the consecutive I and Q paths in each orthogonal polarization.

An exemplary chosen measured isolation between the Tx RHCP path and the Rx LHCP path as a BB frequency function for different relative azimuthal orientations between Tx and Rx operating at 230 GHz is shown in Fig. 6.18. The measurement results for the opposite combination (Tx-LHCP-to-Rx-RHCP), although not shown, are very similar. Please note that the measured aggregated isolation includes not only the influence of the expected antenna cross-polarization level and direct leakage between two antenna driving ports on each chip, but it is also affected by the finite alignment accuracy and the presence of standing waves between both modules. For the worst-case alignment corresponding to angle $\Delta\Phi$ of around $80\text{--}100^\circ$, the isolation varies between -17 dB to -18 dB across the entire BB BW, thus, correlating well with the previous single-tone measurements and simulation results from Sec. 6.2.3 which predict the antenna cross-polarization level

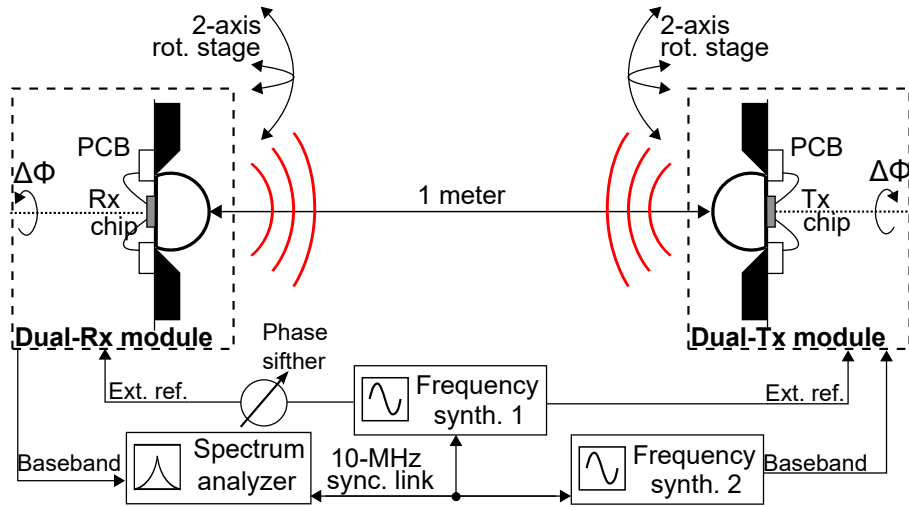


Figure 6.17.: Measurement set-up for characterization of the TX/RX in a back-to-back configuration. After [own9] © 2020 IEEE.

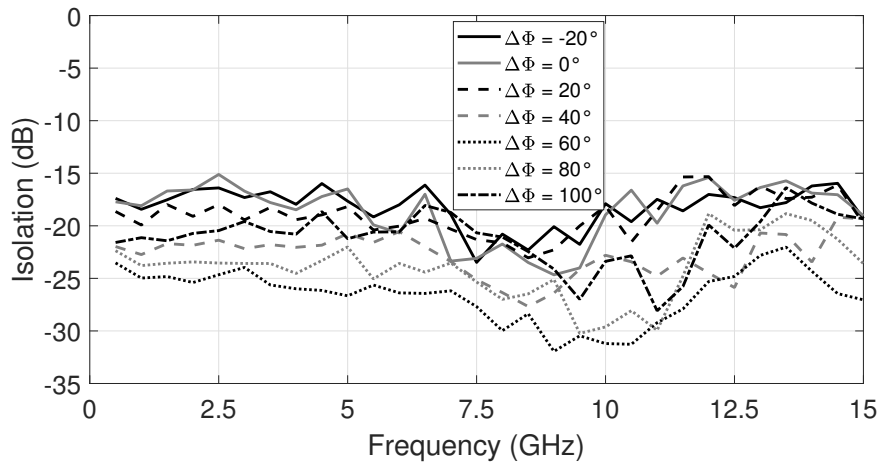


Figure 6.18.: Measured isolation between the Tx RHCP path and the Rx LHCP path at a 1-m distance as a function of the BB frequency for different relative azimuthal orientations between the Tx and the Rx operating at 230 GHz. After [own9] © 2020 IEEE.

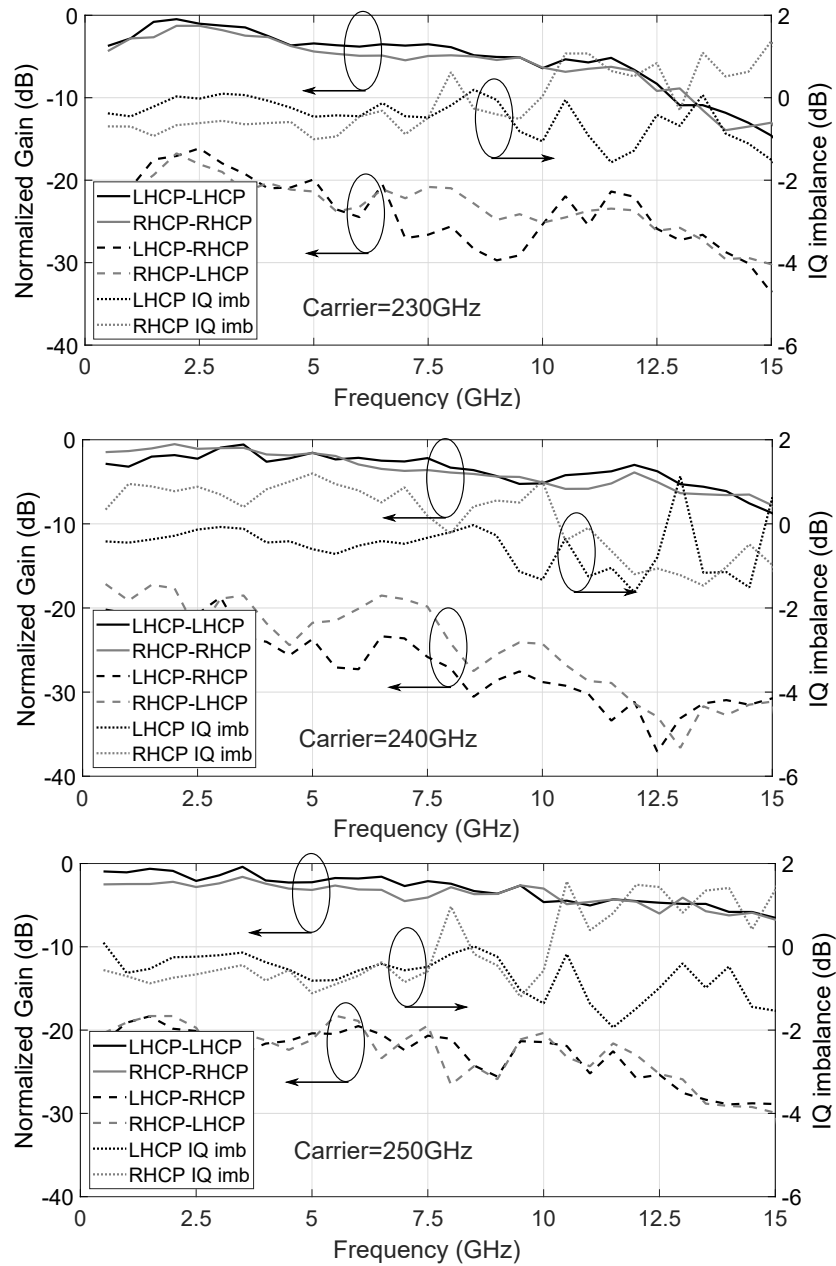


Figure 6.19.: Channel BW, IQ amplitude imbalance, and isolation between the RHCP and LHCP transmission paths for different carrier frequencies and the worst-case azimuthal alignment between the Tx and Rx modules at a 1-m distance. Each of the plots is normalized to its corresponding maximum signal level at the Rx output. After [own9] © 2020 IEEE.

(XPD) of 18–32 dB and the antenna on-chip isolation between the RHCP and LHCP driving ports of -40 dB to -22 dB across 210–270 GHz. According to [58], such isolation should be sufficient for 16-QAM simultaneous operation of both polarization paths in the absence of other link impairments. The next set of plots in Fig. 6.19 presents the isolation measured for 3 different LO frequencies under the worst-case alignment scenario, indicating very consistent values with low dependence on the LO frequency. The 6-dB defined BB channel BW is above 13.5 GHz for all LO frequencies with a typical in-band IQ amplitude imbalance below 1 dB. The amplitude imbalance grows up to 2 dB for some frequency points in the higher-end of the BB BW and is largely attributed to a finite control of the board-level low-pass filter characteristics.

The IQ cross-talk behavior is similar to the one presented in Chapter 4. The IQ cross-talk stays at a level of -10 dB for the whole operating BW at 230 GHz. The IQ cross-talk level increase for other LO frequencies.

The group delay of the entire 1-m distance wireless set-up in a back-to-back configuration was measured by connecting a 2-port VNA (Vector Network Analyzer) to the IQ BB ports of the Tx and Rx modules for each separate polarization. An arbitrarily chosen group delay plot across the entire 15 GHz BB BW for the I channel of the RHCP transmission path operating at 230 GHz is shown in Fig. 6.20. The measured delay of 3.55 ns with a typical in-band variation below ± 50 ps in the entire operating BW corresponds well to a total propagation time through the air path, on-board filters, and lens-coupled antennas on both sides of the link. Although the group delay measurements involving a very large number of periods in the transmission path challenge the measurement accuracy (800 for a carrier frequency of 240 GHz at a 1-meter distance), the LO frequency-independent location and shape of the ripples in the plot correlate with the ones of the on-board filter, as shown in Fig. 3.8, indicating that the group delay dispersion is largely dominated by the packaging and not by RF bandpass response of the on-chip circuitry.

6.4. Wireless Communication link

A diagram of the used measurement set-up is presented in Fig. 6.21. For simultaneous wireless measurements of RHCP and LHCP transmission paths in a line-of-sight 1-m distance configuration, two 2-channel 100 Gs/s Tektronix DPS77004SX real-time oscilloscopes with single-ended input ports and four 50 Gs/s Tektronix AWG, synchronized in pairs, were used. A set of phase-matched cables was applied to connect the Tx and Rx on-board BB connectors to the corresponding ports of the generators and oscilloscopes. Due to the low noise level at the Rx outputs, a set of broadband amplifiers PSPL5882 from Tektronix

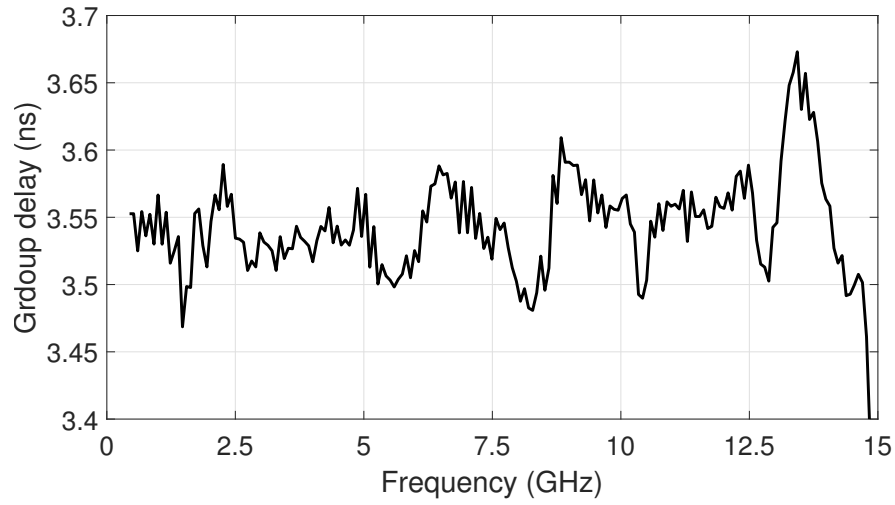


Figure 6.20.: Measured group delay through a 1-m distance line-of-sight link across the entire 15 GHz BB BW for the I channel of the RHCP transmission path operating at 230 GHz. After [own9] © 2020 IEEE.

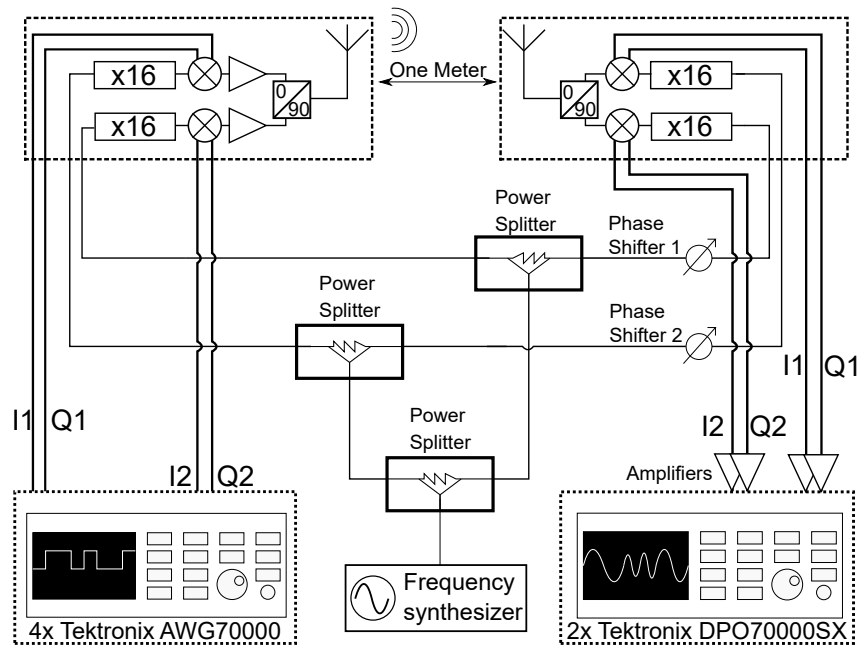


Figure 6.21.: Block diagram of the wireless link set-up. After [own9] © 2020 IEEE.

was placed between the Rx output and the oscilloscope inputs. This was done to amplify the signal power and the noise power spectral density at the output of the Rx above the oscilloscope noise floor to shield the effect of the latter from the wireless communication link results. As explained before in Secs. 6.2.1 and 6.3.1, the differential input and output BB stages of the Rx and Tx needed to be operated as single-ended, resulting not only in an SNR decrease but more important in a degraded drive balance leading to a more pronounced frequency dispersion in the operation BW. For more details about the AWG and the oscilloscope configuration and quality, please refer to Chapter 3.

The relative azimuthal orientation between the Tx and Rx modules was chosen to correspond to the highest leakage between the RHCP and LHCP paths, as found from the previous single-tone measurements in a back-to-back configuration (Sec. 6.3.2). Both transmission channels were operated simultaneously at the same carrier frequency to double the spectral efficiency of the MIMO link. Therefore, the external LO driving frequency was provided from the same synthesizer after the power split. A set of phase shifters was also inserted to expedite the carrier synchronization for each independent transmission path, particularly in the presence of low SNR at the Rx outputs for the highest modulation speeds. An adaptive decision-directed FIR feed-forward equalizer with a varying number of taps of up to 61 was applied to the received signals [64].

6.4.1. EVM results and analysis

To separate the EVM contributions resulting from a finite isolation between the RHCP and LHCP transmission paths from those related to the hardware impairments in each individual MIMO path, the link was first characterized under the single-path operation conditions and for multiple carrier frequencies between 220 GHz and 255 GHz.

The measured EVM for the arbitrary chosen QPSK-modulated RHCP path as a function of the modulation speed and the carrier frequency is shown in Fig. 6.22. A maximum data-rate of 55 Gb/s with an EVM of 30% (BER better than 10^{-3}) was achieved at 230 GHz, where the entire available BB BW was fully exploited and the aggregate influence of all the system impairments, such harmonic interference, was minimized. For 225–245 GHz, the measured EVM dependence on LO frequency and modulation speed shows a similar trend up to 50 Gb/s with relatively minor variation between all curves. This variation is determined mainly by the Tx asymmetry between LSB and USB, and by the suppression level of the externally provided LO driving tone at the Rx BB outputs with respect to the down-converted power density of the modulated spectrum, as it was discussed in Chapter 4. For sufficiently low modulation speeds, the leaking LO/16 tone can be practically

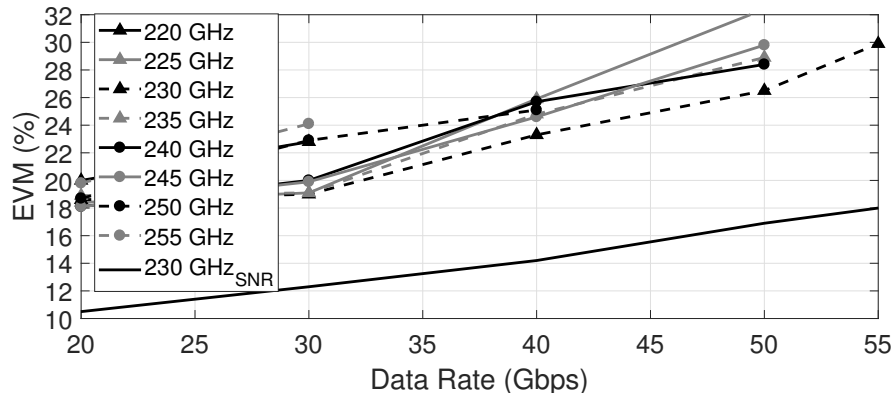


Figure 6.22.: Measured EVM for the QPSK-modulated RHCP transmission path as a function of modulation speed and carrier frequency. The EVM associated to the measured SNR at 230 GHz is given for comparison. After [own9] © 2020 IEEE.

eliminated with a digital filter at the Rx output, but this filtering can no longer be applied without affecting the modulated spectrum for the higher modulation BW reaching the spectral location of the LO/16 tone. For LO frequencies outside of the 225-245 GHz range, the EVM grows faster, and it is mainly a direct consequence of the increased IQ cross-talk generated by the USB and LSB asymmetry.

For a better understanding of the minimum achieved EVM at low data rates, a signal-to-noise ratio at the Rx outputs before demodulation was measured directly and the resulting minimum AWGN-limited EVM bound ($EVM = 1/\sqrt{SNR}$) for 230 GHz is additionally plotted in Fig. 6.22. A non-negligible discrepancy between the measured EVM and the calculated minimum bound can be noticed. This minimum value of around 18% does not improve for lower wireless distances neither for lower data-rates, indicating that neither SNR neither the phase noise limit the link in its current state. According to the EVM introduced by the SNR, the link could operate with a data-rate of 55 Gb/s up to 2-meters for a single channel. By comparison with previous wireless experiments which operated the Tx/Rx BB ports fully differentially and reported an EVM as low as 7% for the same baud rates (see Chapter 4), the main source of EVM deterioration was found to be an imbalanced single-ended drive of the high-speed ports through the wire-bonded interconnects; as previously mentioned in Sec. 6.2.1. A minimum EVM of 18% in each single-polarization path currently prevents the MIMO operation with higher-order modulation formats, such as 16-QAM, even though the measured RHCP-to-LHCP isolation may potentially allow it. This error dominates the link performance. Therefore the EVM analysis presented in this chapter will focus only on analyzing the influence of the XPD.

Similar plots to those from Fig. 6.22 were acquired for two transmission paths (RHCP and LHCP) operating simultaneously, as shown in Fig. 6.24. It can be noticed that both

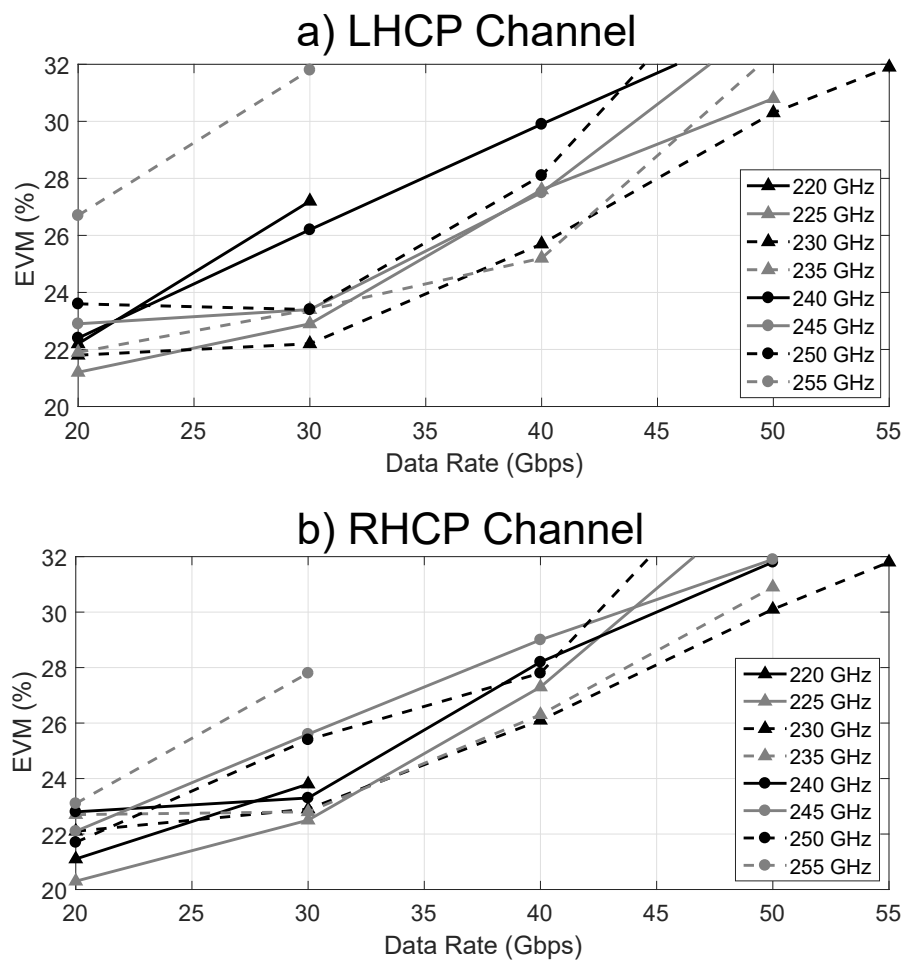


Figure 6.23.: Measured EVM for the QPSK-modulated a) LHCP and b) RHCP transmission paths under simultaneous operation as a function of modulation speed and carrier frequency. After [own9] © 2020 IEEE.

paths show some EVM differences for the same combination of LO frequency and modulation speed, but the general EVM trends for both plots are well preserved. Some differences between the RHCP and LHCP links are attributed mainly to: 1) the limited package-level assembly tolerances and 2) the differences in cross-polarization levels for RHCP-to-RHCP and LHCP-to-LHCP polarizations. The EVM contributions related to the single-channel operation (see Fig. 6.22) can be combined with the channel-to-channel isolation (see Fig. 6.19) into an aggregate EVM [58], modeling the polarization leakage as Gaussian noise, contributing to the EVM with a 12.6% to the total EVM of the wireless communication link. The result of adding this EVM caused by the polarization interference with the EVM of the link when only one of the channels is operating is additionally plotted in Fig. 6.24 for the carrier frequency of 230 GHz to allow direct comparison with the directly measured total EVM. As can be noticed, both the calculated (denoted as $EVM_{\text{calculated}}$) and the measured values correspond well to each other, indicating the absence of further potential link impairments affecting the MIMO operation. The maximum aggregate data-rate of 110 Gb/s with an EVM of 31.9% was achieved at 230 GHz, similarly to the single-polarization operation. At 255 GHz, which is in the operation range of the IEEE 802.15.3d-2017 standard (channels 1, 2, 33, and 49) [9], a maximum data rate of 60 Gb/s was achieved. For a 2-m distance link, the maximum link speed measured was reduced to 80 Gb/s and was achieved at 230 GHz with an EVM of 32%. A set of the measured constellation diagrams with one arbitrary chosen spectrum of the down-converted 55 Gb/s QPSK waveform at the Rx BB ports before demodulation is presented in Fig. 6.25. Here, the presence of the external LO/16 driving signal is evident.

The measured EVM does not scale according to the link-budget calculation defined by the Friss formula, but also not by the other impairments defined previously in this thesis. The link performance is dominated by the asymmetric operation of the differential pairs. In fact, with an EVM of 12.6% associated with the polarization interference, the system could tolerate an aggregated additional EVM of 12%. If the error associated with the single-ended error would not be present, the EVM that a single polarization channel shows would be very similar to the link presented in Chapter 4. That is to say that a 16-QAM wireless link operating simultaneously two data-streams of 70 Gb/s would be possible to established, achieving an aggregated data-rate of 140 Gb/s over a distance of 1-meter.

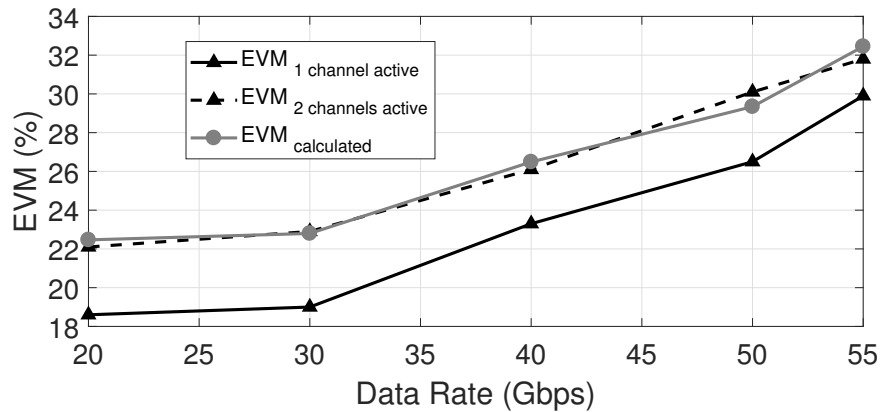


Figure 6.24.: Measured and calculated EVM for the QPSK-modulated RHCP and LHCP transmission paths under simultaneous operation as a function of modulation speed and carrier frequency. After [own9] © 2020 IEEE.

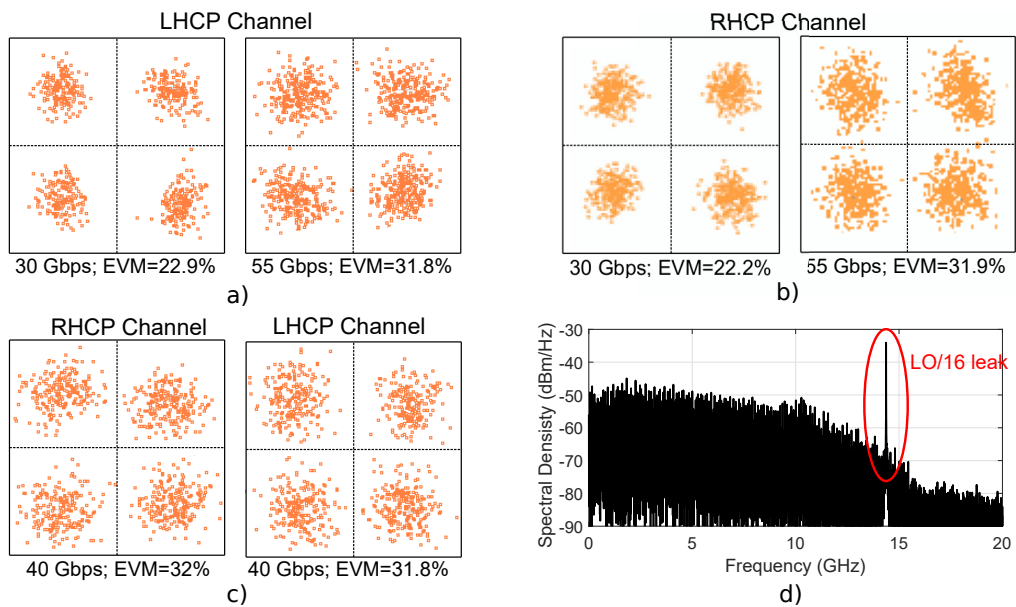


Figure 6.25.: A set of the measured constellation diagrams with one arbitrary chosen down-converted spectrum before demodulation: a) 30 Gb/s and 55 Gb/s LHCP path at 230 GHz and 1-m distance, b) 30 Gb/s and 55 Gb/s RHCP path at 230 GHz and 1-m distance, c) 40 Gb/s LHCP and RHCP paths at 230 GHz and 2-m distance, d) spectral density of the down-converted 55 Gb/s QPSK waveform at the RX RHCP BB ports before demodulation. After [own9] © 2020 IEEE.

6.5. Conclusions

In this chapter, the feasibility of doubling the spectral efficiency of a line-of-sight wireless transmission by applying the polarization-diversity MIMO to a set of highly-integrated and fully packaged fundamentally-operated direct-conversion IQ Tx and Rx modules has been demonstrated. Each of the modules is implemented in 0.13- μm SiGe HBT technology as a single-chip solution in combination with a low-cost COB packaging for the high-speed BB signaling and the silicon lens-coupled on-chip antenna interface to free-space. The chipset can simultaneously transmit two orthogonal circular polarizations (RHCP and LHCP) without the need of a high-speed depolarizer in the BB for any relative azimuthal orientation between the Tx and Rx modules, solving the problem of the relative orientation between the Tx and the Rx. This, in addition to the used QPSK modulation scheme, relaxes the complexity of the future BB circuitry attached to this system. These two points are particularly important steps towards the realization of future 6G mobile applications at this frequency range.

On the link level, a channel-to-channel isolation of at least 18 dB for the entire measured 210-270 GHz band was achieved, which is sufficient for simultaneous operation of two high data-rate 16-QAM modulated waveform, as long as the EVM contribution of the other impairments present in the link stays below 12%, including the SNR contribution. In view of a minimum EVM of around 18% achieved for each of the channels operating separately, caused by the single-ended operation of the up- and down-conversion mixers, the MIMO operation with a 16-QAM modulation format was not possible. For QPSK modulation, a maximum aggregate data-rate of 110 Gb/s and 80 Gb/s was achieved at 230 GHz for 1-m and 2-m distance, respectively. For the highest LO frequency of 255 GHz, which is in the operation range of the new IEEE 802.15.3d-2017 standard, 60 Gb/s was demonstrated. By correcting the error that the single-ended operation of the Tx and the Rx BB port introduces, an aggregated data-rate of 140 Gb/s for a 1-meter link distance is anticipated.

Part III.

Conclusion and future outlook

Chapter 7

Thesis Summary

7.1. Thesis Summary

This work enhances the SoA for communications beyond 200 GHz for 6G wireless links in two different ways. First, this thesis presented the fastest wireless communication links based on silicon technologies. Chapter 4 presented the first silicon-based 16-QAM 1-meter 100 Gb/s wireless link with an EVM of 17% operating beyond 200 GHz. The first silicon-based MIMO wireless communication system beyond 200 GHz was presented in Chapter 6. Combining two QPSK channels, the link achieved a data-rate of 110 Gb/s and 80 Gb/s with an EVM below 32% for distances of 1 and 2 meters, respectively. The use of two circular polarizations (RHCP and LHCP) permits the link to operate without a high-speed depolarizer in the BB for any relative orientation between the TX and RX modules, solving the problem of the relative orientation between the Tx and the Rx. Both systems operate up to a LO frequency of 255 GHz, which is the operating range of the new IEEE 802.15.3d-2017 standard [9]. Table 7.1 shows a comparison of the wireless communication links presented in this thesis with the current SoA. The work presented in this thesis achieved the highest data-rate and the longest link distance among all implementations in silicon technology. Only the link published in [35] showed better data-rates and longer distances. However, this system was implemented in III-V technology, which is not a well-suited technology for the mass-market application due to its high cost and low fabrication yield. Furthermore, the 4-meters link distance was achieved using external horn antennas and optical lenses. With a packaging scheme based on a bulky wave-guide assembly, this system is not mechanically suited for the requirements of the future 6G mobile systems. The second contribution of this thesis is an analysis of the impairment that affects the

wireless link. Five different impairments were analyzed in this thesis: the error generated by the measurement set-up, the phase noise, the harmonic spurs, the IQ cross-talk, and the SNR.

1. The EVM generated by the measurement set-up stays below 2.5% for a symbol rate under 25 Gbauds, playing a minor role in the link EVM. However, its influence grows exponentially for higher symbol rates. For a symbol rate of 42.5 Gbauds, the EVM introduced by the measurement set-up is 18.4%, preventing the link from operating for any modulation order higher than QPSK. The performance of the measurement equipment, particularly the AWG, must be improved to test data-rates beyond 150 Gb/s in a single link.
2. The phase noise error introduced by the noise floor of the frequency synthesizer prevents high modulation orders from operating in wireless communication links beyond 200 GHz. Even for 64-QAM, the system can only operate a fraction of the available BW. For BB signals with a BW below 2.5 GHz, the influence of the phase noise in the link EVM is at least 3%. This EVM prevents the link from operating with 256-QAM. Any phase noise reduction achieved in the LO generation path's multiplication factor is almost entirely compensated by a rise in the noise floor of the frequency synthesizer for higher frequencies.
3. The harmonics spurs' influence in the link performance was found to be minor. Ensuring a suppression of at least 20 dB in the Tx and the Rx, the self-harmonic products' influence on the link EVM stays under 1%. The adjacent harmonic products' influence is stronger, but it can be easily eliminated with an appropriate frequency planning on the system, as demonstrated in Chapter 5.
4. For data-rates beyond 50 Gb/s, the main contributor to the final EVM is the IQ cross-talk. This error is generated by the USB/LSB asymmetry in the RF band-pass characteristic of both Tx and Rx. As demonstrated in Chapter 5, an IQ isolation level of at least 20 dB is required to keep the contribution of this impairment to the total EVM below 3%. To achieve this goal in a typical direct-conversion IQ system, the difference between the USB and the LSB must be better than 0.1 dB.
5. The effect of the SNR on the presented wireless links is minor compared to the error set by the IQ cross-talk at a 1-meter distance for the highest data-rates. However, it plays a major role in the lower data-rates together with the phase noise. Its contribution will grow for higher distances due to the lower link budget available. However, for the RF front-end presented in this thesis, this problem could be par-

tially compensated using a bigger silicon lens, increasing the antenna directivity and compensating for additional propagation losses.

7.2. Future Directions

With the modulation order limited by the phase noise error and the usable channel BW limited by the IQ cross-talk, the only possible option to increase the data-rate is to operate multiple parallel channels. Another approach would be to increase the functionality that the wireless link supports. Several options can be considered here.

Improving the MIMO system. If the error introduced by the single-ended operation is corrected, the MIMO system presented in Chapter 6 could operate under 16-QAM with expected data-rates in the range of 150 Gb/s. Besides, any improvement in the antenna axial-ratio will increase the channel isolation, reducing the EVM error generated by the channel coupling and potentially increasing the potential data-rates towards 200 Gb/s.

Channel Bonding. The idea behind this technique would be to divide the available RF BW into narrower sub-bands, minimizing the effect of the phase noise in the overall link. Each of these sub-bands should be designed to be narrow enough to keep the EVM generated by the phase below 2%. This reduced EVM would allow for the use of 64-QAM and 256 QAM techniques in the link, increasing its spectral efficiency and its potential aggregated data-rate. A set of intermediate frequency mixers will up- and down-convert the multiple BB signals at the Tx and Rx side, respectively. Keeping a high isolation level between the multiple BB channels would be the most significant implementation challenge of such systems. This technique has already been demonstrated for frequencies beyond 200 GHz [39]. However, only a modulation format of 16-QAM was achieved. The demonstrated data-rate stayed below 15.6 Gb/s for a link distance of 15 cm.

Beam-steering. The main problem that the wireless links presented in this thesis will face in a mobile application scenario is the high antenna directivity. This high directivity is required to overcome the high free-space path loss at frequencies beyond 200 GHz. However, this limits the Tx/Rx relative positioning to a fixed LOS link. Adding beam-steering capabilities to the Tx or the Rx will allow for dynamic operation. The first phase-shifters [83], [106], [107] and the first beam-steering sources [108], [109] at frequencies beyond 200 GHz have already been demonstrated. However, no wireless link with beam-steering capabilities has been published. Keeping a constant phase offset over tens of GHz between the

Table 7.1.: State-of-the-art of electronic-based wireless links above 200 GHz

Technology	Frequency (GHz)	Modulation	On-chip LO generation	Packaging	Data-rate (Gb/s)	Distance (cm)	P _{DC} (W)	# of channels	Ref.
35nm InP HEMT	240	8-PSK	yes	waveguide	96	40m	-	1 IQ channel	[36]
80nm InP HEMT	270	16-QAM	no	waveguide+lens	120	400	-	1 channel	[35]
130nm SiGe	190	BPSK	no	no packaging	50	0.6	0.154	1 channel	[37]
65nm CMOS	240	QPSK	yes	Chip-on-board	16	1	0.48	1 IQ channel	[102], [103]
40nm CMOS	300	16-QAM	no	no packaging	32	1	2.05	1 channel	[46]
40nm CMOS	265	16-QAM	no	no packaging	80	3	1.79	1 channel	[45]
32nm CMOS	210	OOK	yes	Chip-on-board	10	4	-	1 channel	[104]
65nm CMOS	254	OOK	yes	no packaging	10	2	0.23	1 channel	[105]
130nm SiGe	240	BPSK	yes	Chip-on-board	25	100	1.41	1 channel	[38]
130nm SiGe	240	16-QAM	yes	Chip-on-board	15.6	15	-	3 IQ channels	[39]
130nm SiGe	240	16-QAM	yes	Chip-on-board	60 ³	80	-	1 IQ channel	[40]
130nm SiGe	225-255	QPSK/16-/64-QAM	yes	Chip-on-board	65/90/81	100	1.96	1 IQ channel	Chapter 3
130nm SiGe	225-255	QPSK/16-QAM	yes	Chip-on-board	60/100	20	0.95	1 IQ channel	Chapter 4
130nm SiGe	215-240	QPSK/16-/64-QAM	yes	Chip-on-board	85/140/90 ¹	60cm	2.6	1 IQ channel ²	Chapter 5
130nm SiGe	225-255	QPSK	yes	Chip-on-board	110/80	100/200	2.85	2 IQ channels	Chapter 6

¹ Only when the polarization separation between IQ channels is maximum, ² IQ channels separated by polarization, ³ 100 Gb/s were reported for 16-QAM with an EVM of 18.6%

multiple radiator elements seems to be the major design challenge. This functionality will allow for the creation of mobile wireless networks beyond 200 GHz.

Bibliography

Own Publications

- [own1] M. Giordani, M. Polese, M. Mezzavilla, S. Rangan, and M. Zorzi, "Toward 6G Networks: Use Cases and Technologies," *IEEE Communications Magazine*, vol. 58, no. 3, pp. 55–61, 2020.
- [own2] P. Rodríguez-Vázquez, J. Grzyb, N. Sarmah, B. Heinemann, and U. R. Pfeiffer, "A 219–266 GHz LO-tunable direct-conversion IQ receiver module in a SiGe HBT technology," *International Journal of Microwave and Wireless Technologies*, vol. 10, no. 5-6, pp. 587–595, 2018.
- [own3] N. Sarmah, J. Grzyb, K. Statnikov, S. Malz, P. Rodriguez Vazquez, W. Föerster, B. Heinemann, and U. R. Pfeiffer, "A Fully Integrated 240-GHz Direct-Conversion Quadrature Transmitter and Receiver Chipset in SiGe Technology," *IEEE Transactions on Microwave Theory and Techniques*, vol. 64, no. 2, pp. 562–574, Feb. 2016.
- [own4] P. Rodríguez-Vázquez, J. Grzyb, N. Sarmah, B. Heinemann, and U. R. Pfeiffer, "A 65 Gbps QPSK one meter wireless link operating at a 225–255 GHz tunable carrier in a SiGe HBT technology," in *2018 IEEE Radio and Wireless Symposium (RWS)*, 2018, pp. 146–149.
- [own5] P. Rodríguez-Vázquez, J. Grzyb, N. Sarmah, B. Heinemann, and U. R. Pfeiffer, "Towards 100 Gbps: A Fully Electronic 90 Gbps One Meter Wireless Link at 230 GHz," in *2018 48th European Microwave Conference (EuMC)*, 2018, pp. 1389–1392.
- [own6] P. Rodríguez-Vázquez, J. Grzyb, B. Heinemann, and U. R. Pfeiffer, "Performance Evaluation of a 32-QAM 1-Meter Wireless Link Operating at 220–260 GHz with a Data-Rate of 90 Gbps," in *2018 Asia-Pacific Microwave Conference (APMC)*, 2018, pp. 723–725.
- [own7] P. Rodríguez-Vázquez, J. Grzyb, B. Heinemann, and U. R. Pfeiffer, "Optimization and Performance Limits of a 64-QAM Wireless Communication Link at 220-260 GHz in a SiGe HBT Technology," in *2019 IEEE Radio and Wireless Symposium (RWS)*, 2019, pp. 1–3.
- [own8] P. Rodríguez-Vázquez, J. Grzyb, N. Sarmah, B. Heinemann, and U. R. Pfeiffer, "A 16-QAM 100-Gb/s 1-M Wireless Link With an EVM of 17% at 230 GHz in an SiGe Technology," *IEEE Microwave and Wireless Components Letters*, vol. 29, no. 4, pp. 297–299, 2019.
- [own9] P. Rodríguez-Vázquez, J. Grzyb, B. Heinemann, and U. R. Pfeiffer, "A QPSK 110-Gb/s Polarization-Diversity MIMO Wireless Link With a 220–255 GHz Tunable LO in a SiGe HBT Technology," *IEEE Transactions on Microwave Theory and Techniques*, vol. 68, no. 9, pp. 3834–3851, 2020.
- [own10] J. Grzyb, P. R. Vazquez, N. Sarmah, B. Heinemann, and U. R. Pfeiffer, "Performance evaluation of a 220–260 ghz lo tunable bpsk/qpsk wireless link in sige hbt technology," in *2018 48th European Microwave Conference (EuMC)*, 2018, pp. 1397–1400.

- [own11] P. R. Vazquez, J. Grzyb, N. Sarmah, B. Heinemann, and U. R. Pfeiffer, "A 219–266 GHz fully-integrated direct-conversion IQ receiver module in a SiGe HBT technology," in *2017 12th European Microwave Integrated Circuits Conference (EuMIC)*, 2017, pp. 261–264.
- [own12] P. R. Vazquez, J. Grzyb, N. Sarmah, B. Heinemann, and U. R. Pfeiffer, "A 219–266 GHz fully-integrated direct-conversion IQ receiver module in a SiGe HBT technology," in *2017 12th European Microwave Integrated Circuits Conference (EuMIC)*, 2017, pp. 261–264.
- [own13] P. Rodríguez-Vázquez, M. E. Leinonen, J. Grzyb, N. Tervo, A. Parssinen, and U. R. Pfeiffer, "Signal-processing Challenges in Leveraging 100 Gb/s Wireless THz," in *2020 2nd 6G Wireless Summit (6G SUMMIT)*, 2020, pp. 1–5.

Cited References

- [1] Cisco Visual Networking Index, "Forecast and Trends 2017-2022," in *White Paper*, Feb. 2019.
- [2] Yole Développement, "5G Impact on RF Front-End Module and Connectivity for Cell phones 2019," Aug. 2019.
- [3] Arraycomm. (2011). "Graph of Cooper's Law," [Online]. Available: <http://www.arraycomm.com/cooperslaw>.
- [4] B. Aazhang, P. Ahokangas, H. Alves, *et al.*, *Key drivers and research challenges for 6G ubiquitous wireless intelligence (white paper)*. Sep. 2019.
- [5] Intel Corporation, "New SID: Study on supporting NR from 52.6 GHz to 71 GHz," in *RP-193259, 3GPP TSG RAN Meeting # 86*, Dec. 2019.
- [6] O. Tervo, T. Levanen, K. Pajukoski, J. Hulkkonen, P. Wainio, and M. Valkama, "5G New Radio Evolution Towards Sub-THz Communications," in *2020 2nd 6G Wireless Summit (6G SUMMIT)*, 2020, pp. 1–6.
- [7] IEEE. (2020). "6G Wireless Summit," [Online]. Available: <https://www.6gsummit.com/>.
- [8] DARPA. (2018). "U.S. Electronics Innovation Leaps Forward Via Joint University Microelectronics Program," [Online]. Available: <https://www.darpa.mil/news-events/2018-01-17>.
- [9] "IEEE standard for high data rate wireless multi-media networks—amendment 2: 100 Gb/s wireless switched point-to-point physical layer," *IEEE Std 802.15.3d-2017 (Amendment to IEEE Std 802.15.3-2016 as amended by IEEE Std 802.15.3e-2017)*, pp. 1–55, Oct. 2017.
- [10] F. Tariq, M. R. A. Khandaker, K. -K. Wong, M. A. Imran, M. Bennis, and M. Debbah, "A Speculative Study on 6G," *IEEE Wireless Communications*, vol. 27, no. 4, pp. 118–125, 2020.
- [11] S. Mumtaz, "Terahertz Communication for Vehicular Networks," *IEEE Transactions on Vehicular Technology*, vol. 66, no. 7, pp. 5617–5625, 2017.
- [12] W. Saad, M. Bennis, and M. Chen, "A Vision of 6G Wireless Systems: Applications, Trends, Technologies, and Open Research Problems," *IEEE Network*, vol. 34, no. 3, pp. 134–142, 2020.
- [13] B. Li, Z. Fei, and Y. Zhang, "UAV Communications for 5G and Beyond: Recent Advances and Future Trends," *IEEE Internet of Things Journal*, vol. 6, no. 2, pp. 2241–2263, 2019.
- [14] S. R. A. Jafri, T. Hamid, and T. Mahmood, "Wireless Brain Computer Interface for Smart Home and Medical System," *Wireless Personal Communications*, vol. 106, no. 4, pp. 2163–2177, Jun. 2019.

- [15] A. Tripathy, S. Chinara, and M. Sarkar, "An application of wireless brain-computer interface for drowsiness detection," *Biocybernetics and Biomedical Engineering*, vol. 36, no. 1, pp. 276–284, 2016.
- [16] Neuralink. (2021). "Neuralink," [Online]. Available: <https://neuralink.com>.
- [17] Cisco. (2021). "The internet of everything," [Online]. Available: https://www.cisco.com/c/dam/en_us/about/business-insights/docs/ioe-value-at-stake-public-sector-analysis-faq.pdf.
- [18] IoE. (2021). "Internet of everything," [Online]. Available: <https://ioe.org>.
- [19] H. Song and T. Nagatsuma, "Present and Future of Terahertz Communications," *IEEE Transactions on Terahertz Science and Technology*, vol. 1, no. 1, pp. 256–263, 2011.
- [20] P. H. Siegel, "Terahertz technology," *IEEE Transactions on Microwave Theory and Techniques*, vol. 50, no. 3, pp. 910–928, 2002.
- [21] D. L. Woolar, J. O. Jensen, R. Hwu, and M. Shur, *Terahertz Science and Technology for Military and Security Applications*. World Scientific, 2007.
- [22] S. L. Dexheimer, J. O. Jensen, R. Hwu, and M. Shur, *Terahertz Spectroscopy: Principles and Applications*. CRC Press, 2007.
- [23] T. Globus, D. Woolard, T. Crowe, T. Khromova, B. Gelmont, and J. Hesler, "Terahertz Fourier transform characterization of biological materials in a liquid phase," *Journal of Physics D: Applied Physics*, vol. 39, p. 3405, Jul. 2006.
- [24] K. Ajito and Y. Ueno, "THz Chemical Imaging for Biological Applications," *IEEE Transactions on Terahertz Science and Technology*, vol. 1, no. 1, pp. 293–300, 2011.
- [25] Z. D. Taylor, R. S. Singh, D. B. Bennett, *et al.*, "THz Medical Imaging: in vivo Hydration Sensing," *IEEE Transactions on Terahertz Science and Technology*, vol. 1, no. 1, pp. 201–219, 2011.
- [26] Y. Shen and P. F. Taday, "Development and Application of Terahertz Pulsed Imaging for Nondestructive Inspection of Pharmaceutical Tablet," *IEEE Journal of Selected Topics in Quantum Electronics*, vol. 14, no. 2, pp. 407–415, 2008.
- [27] D. Banerjee, W. Spiegel, M. Thomson, S. Schabel, and H. Roskos, "Diagnosing water content in paper by terahertz radiation," *Optics express*, vol. 16, pp. 9060–6, Jul. 2008.
- [28] D. Mittleman, *Sensing with Terahertz Radiation*. Jan. 2003.
- [29] J. Grzyb, K. Statnikov, N. Sarmah, B. Heinemann, and U. R. Pfeiffer, "A 210-270-GHz circularly polarized FMCW radar with a single-lens-coupled SiGe HBT chip," vol. 6, no. 6, pp. 771–783, Nov. 2016.
- [30] L. Zhang, Y. Wei, M. Zhang, *et al.*, "A novel sine ridge waveguide for 0.65 THz backward wave oscillator," Sep. 2014, pp. 1–2.
- [31] M. Brandstetter, C. Deutsch, A. Benz, *et al.*, "THz quantum cascade lasers with wafer bonded active regions," *Optics express*, vol. 20, pp. 23832–7, Oct. 2012.
- [32] X. Mei, W. Yoshida, M. Lange, *et al.*, "First Demonstration of Amplification at 1 THz Using 25-nm InP High Electron Mobility Transistor Process," vol. 36, no. 4, pp. 327–329, 2015.
- [33] Qualcomm. (2021). "Snapdragon X50 5G Modem-RF System," [Online]. Available: <https://www.qualcomm.com/products/snapdragon-x50-5g-modem>.
- [34] B. Heinemann, H. Rücker, R. Barth, *et al.*, "SiGe HBT with f_t/f_{max} of 505 GHz/720 GHz," in *2016 IEEE International Electron Devices Meeting (IEDM)*, Dec. 2016, pp. 3.1.1–3.1.4.
- [35] H. Hamada, T. Tsutsumi, H. Matsuzaki, *et al.*, "300-GHz-Band 120-Gb/s Wireless Front-End Based on InP-HEMT PAs and Mixers," vol. 55, no. 9, pp. 2316–2335, 2020.

- [36] F. Boes, T. Messinger, J. Antes, D. Meier, A. Tessmann, A. Inam, and I. Kallfass, "Ultra-broadband MMIC-based wireless link at 240 GHz enabled by 64GS/s DAC," in *2014 39th International Conference on Infrared, Millimeter, and Terahertz waves (IRMMW-THz)*, 2014, pp. 1–2.
- [37] D. Fritsche, P. Stärke, C. Carta, and F. Ellinger, "A Low-Power SiGe BiCMOS 190-GHz Transceiver Chipset With Demonstrated Data Rates up to 50 Gbit/s Using On-Chip Antennas," vol. 65, no. 9, pp. 3312–3323, Sep. 2017.
- [38] M. H. Eissa, A. Malignaggi, R. Wang, M. Elkhoully, K. Schmalz, A. C. Ulusoy, and D. Kissinger, "Wideband 240-GHz Transmitter and Receiver in BiCMOS Technology With 25-Gbit/s Data Rate," *IEEE Journal of Solid-State Circuits*, vol. 53, no. 9, pp. 2532–2542, 2018.
- [39] M. H. Eissa, N. Maletic, L. Lopacinski, A. Malignaggi, G. Panic, R. Kraemer, G. Fischer, and D. Kissinger, "Frequency Interleaving IF Transmitter and Receiver for 240-GHz Communication in SiGe:C BiCMOS," *IEEE Transactions on Microwave Theory and Techniques*, vol. 68, no. 1, pp. 239–251, 2020.
- [40] M. H. Eissa, N. Maletic, E. Grass, R. Kraemer, D. Kissinger, and A. Malignaggi, "100 Gbps 0.8-m Wireless Link based on Fully Integrated 240 GHz IQ Transmitter and Receiver," in *2020 IEEE/MTT-S International Microwave Symposium (IMS)*, 2020, pp. 627–630.
- [41] P. Hillger, J. Grzyb, R. Jain, and U. R. Pfeiffer, "Terahertz Imaging and Sensing Applications With Silicon-Based Technologies," *IEEE Transactions on Terahertz Science and Technology*, vol. 9, no. 1, pp. 1–19, 2019.
- [42] S. Lee, B. Jagannathan, S. Narasimha, *et al.*, "Record RF performance of 45-nm SOI CMOS Technology," in *2007 IEEE International Electron Devices Meeting*, 2007, pp. 255–258.
- [43] H. Li, B. Jagannathan, J. Wang, *et al.*, "Technology Scaling and Device Design for 350 GHz RF Performance in a 45nm Bulk CMOS Process," in *2007 IEEE Symposium on VLSI Technology*, 2007, pp. 56–57.
- [44] J. Park, S. Kang, S. V. Thyagarajan, E. Alon, and A. M. Niknejad, "A 260 GHz fully integrated CMOS transceiver for wireless chip-to-chip communication," in *2012 Symposium on VLSI Circuits (VLSIC)*, 2012, pp. 48–49.
- [45] S. Lee, R. Dong, T. Yoshida, S. Amakawa, S. Hara, A. Kasamatsu, J. Sato, and M. Fujishima, "9.5 An 80Gb/s 300GHz-Band Single-Chip CMOS Transceiver," 2019, pp. 170–172.
- [46] S. Hara, K. Katayama, K. Takano, *et al.*, "A 32Gbit/s 16QAM CMOS receiver in 300GHz band," in *2017 IEEE MTT-S International Microwave Symposium (IMS)*, Jun. 2017, pp. 1703–1706.
- [47] C. E. Shannon, "Communication in the Presence of Noise," *Proceedings of the IRE*, vol. 37, no. 1, pp. 10–21, 1949.
- [48] A. Georgiadis, "Gain, phase imbalance, and phase noise effects on error vector magnitude," *IEEE TVT*, vol. 53, no. 2, pp. 443–449, Mar. 2004.
- [49] N. Sarmah, "Wideband Circuit Design Techniques for Ultra-High Data-Rate Wireless Communication in Silicon Technologies," Ph.D. dissertation, University of Wuppertal, 2016.
- [50] S. Malz, "Silicon Integrated Radio Front-End Design for 100 Gbit/s and Beyond," Ph.D. dissertation, University of Wuppertal, 2020.
- [51] R. Gallager, *Principles of Digital Communications*. MA, USA: MIT OpenCourseWare, 2006.
- [52] J. S. Belrose, "Fessenden and Marconi: their differing technologies and transatlantic experiments during the first decade of this century," in *Proceedings of the 1995 International Conference on 100 Years of Radio*, 1995, pp. 32–43.

- [53] A. Grami, *Introduction to Digital Communications*. London Wall, London, UK: Academic Press, 2015.
- [54] M. Freimer, B. Gold, and A. Tritter, "The Morse distribution," *IRE Transactions on Information Theory*, vol. 5, no. 1, pp. 25–31, 1959.
- [55] F. Chang, K. Onohara, and T. Mizuochi, "Forward error correction for 100 G transport networks," *IEEE Communications Magazine*, vol. 48, no. 3, S48–S55, 2010.
- [56] R. Schmogrow, B. Nebendahl, M. Winter, *et al.*, "Error Vector Magnitude as a Performance Measure for Advanced Modulation Formats," *IEEE Photonics Technology Letters*, vol. 24, no. 1, pp. 61–63, 2012.
- [57] R. Schmogrow, B. Nebendahl, M. Winter, *et al.*, "Corrections to "Error Vector Magnitude as a Performance Measure for Advanced Modulation Formats" [Jan 1, 2012 61-63]," *IEEE Photonics Technology Letters*, vol. 24, no. 23, pp. 2198–2198, 2012.
- [58] R. A. Shafik, M. S. Rahman, and A. R. Islam, "On the Extended Relationships Among EVM, BER and SNR as Performance Metrics," in *2006 International Conference on Electrical and Computer Engineering*, 2006, pp. 408–411.
- [59] H. T. Friis, "A Note on a Simple Transmission Formula," *Proceedings of the IRE*, vol. 34, no. 5, pp. 254–256, 1946.
- [60] J. B. Johnson, "Thermal Agitation of Electricity in Conductors," *Nature*, vol. 119, no. 50, 1927.
- [61] L. Pilato, G. Meoni, and L. Fanucci, "Design and quantization limits of root raised cosine digital filter," in *2017 3rd International Conference on Frontiers of Signal Processing (ICFSP)*, 2017, pp. 59–62.
- [62] Chia-Yu Yao and Chiang-Ju Chien, "Design of a square-root-raised-cosine FIR filter by a recursive method," in *2005 IEEE International Symposium on Circuits and Systems*, 2005, 512–515 Vol. 1.
- [63] Hangcheng Han, Chen Zheng, and Jihua Lu, "Square-root raised-cosine filter and its software-realization in DSP," in *2011 International Conference on Computer Science and Service System (CSSS)*, 2011, pp. 3574–3576.
- [64] M. Wickert, S. Samad, and B. Butler, "An Adaptive Baseband Equalizer for High Data Rate Bandlimited Channels," *International Telemetering Conference Proceedings*, Oct. 2006.
- [65] I. Glover, *Digital Communications (2nd ed.)* One Lake, NJ, USA: Prentice Hall, 2003.
- [66] H. Rucker, B. Heinemann, and A. Fox, "Half-Terahertz SiGe BiCMOS technology," in *2012 IEEE 12th Topical Meeting on Silicon Monolithic Integrated Circuits in RF Systems*, Jan. 2012, pp. 133–136.
- [67] B. Razavi, "Design considerations for direct-conversion receivers," *IEEE Transactions on Circuits and Systems II: Analog and Digital Signal Processing*, vol. 44, no. 6, pp. 428–435, 1997.
- [68] B. Liebowitz, "The theory of heterodyne receivers," *Proceedings of the Institute of Radio Engineers*, vol. 3, no. 2, pp. 185–194, 1915.
- [69] N. Sarmah, B. Heinemann, and U. R. Pfeiffer, "235–275 GHz (x16) frequency multiplier chains with up to 0 dBm peak output power and low DC power consumption," in *2014 IEEE Radio Frequency Integrated Circuits Symposium*, 2014, pp. 181–184.
- [70] J. Grzyb, K. Statnikov, N. Sarmah, and U. R. Pfeiffer, "A wideband 240 GHz lens-integrated circularly polarized on-chip annular slot antenna for a fmcw radar transceiver module in SiGe technology," in *2015 SBMO/IEEE MTT-S International Microwave and Optoelectronics Conference (IMOC)*, 2015, pp. 1–4.
- [71] S. Malz, B. Heinemann, R. Lachner, and U. R. Pfeiffer, "J-band Amplifier Design Using Gain-Enhanced Cascodes in 0.13 μm SiGe," *International Journal of Microwave and Wireless Technologies*, vol. 7, no. 3-4, pp. 339–347, 2015.

- [72] J. Grzyb, H. Sherry, A. Cathelin, A. Kaiser, and U. R. Pfeiffer, "On the co-design between on-chip antennas and thz mosfet direct detectors in cmos technology," in *2012 37th International Conference on Infrared, Millimeter, and Terahertz Waves*, 2012, pp. 1–3.
- [73] J. Grzyb, Y. Zhao, and U. R. Pfeiffer, "A 288-GHz Lens-Integrated Balanced Triple-Push Source in a 65-nm CMOS Technology," *IEEE Journal of Solid-State Circuits*, vol. 48, no. 7, pp. 1751–1761, 2013.
- [74] J. Grzyb, R. Al Hadi, Y. Zhao, and U. Pfeiffer, "Toward room-temperature all-silicon integrated thz active imaging," in *2013 7th European Conference on Antennas and Propagation (EuCAP)*, 2013, pp. 1740–1744.
- [75] D. Pozar, *Microwave engineering, 4th edition*. Wiley, 2011.
- [76] C. A. Balanis, *Antenna theory: analysis and design*. New York, NY, USA: Wiley, 2005.
- [77] E. Ojefors, B. Heinemann, and U. R. Pfeiffer, "Subharmonic 220- and 320-GHz SiGe HBT Receiver Front-Ends," *IEEE Transactions on Microwave Theory and Techniques*, vol. 60, no. 5, pp. 1397–1404, 2012.
- [78] T. Nakagawa and K. Araki, "Effect of phase noise on rf communication signals," in *Vehicular Technology Conference Fall 2000. IEEE VTS Fall VTC2000. 52nd Vehicular Technology Conference (Cat. No.00CH37152)*, vol. 2, 2000, 588–591 vol.2.
- [79] T. Shao, F. Paresys, G. Maury, Y. L. Guennec, and B. Cabon, "Investigation on the Phase Noise and EVM of Digitally Modulated Millimeter Wave Signal in WDM Optical Heterodyning System," *Journal of Lightwave Technology*, vol. 30, no. 6, pp. 876–885, 2012.
- [80] J. Antes and I. Kallfass, "Performance estimation for broadband multi-gigabit millimeter- and sub-millimeter-wave wireless communication links," *IEEE Transactions on Microwave Theory and Techniques*, vol. 63, no. 10, pp. 3288–3299, 2015.
- [81] M. R. Khanzadi, D. Kuylenstierna, A. Panahi, T. Eriksson, and H. Zirath, "Calculation of the performance of communication systems from measured oscillator phase noise," *IEEE Transactions on Circuits and Systems I: Regular Papers*, vol. 61, no. 5, pp. 1553–1565, 2014.
- [82] A. V. Oppenheim, *Signal and Systems*. Englewood Cliffs, NJ, USA: Prentice-Hall, 1983.
- [83] M. Elkhoully, Y. Mao, S. Glisic, C. Meliani, F. Ellinger, and J. C. Scheytt, "A 240 GHz direct conversion IQ receiver in 0.13 um SiGe BiCMOS technology," in *2013 IEEE Radio Frequency Integrated Circuits Symposium (RFIC)*, Jun. 2013, pp. 305–308.
- [84] Y. Mao, K. Schmalz, J. Borngraber, and J. C. Scheytt, "245-GHz LNA, Mixer, and Subharmonic Receiver in SiGe Technology," *IEEE Transactions on Microwave Theory and Techniques*, vol. 60, no. 12, pp. 3823–3833, Dec. 2012.
- [85] M. H. Eissa, A. Awny, M. Ko, K. Schmalz, M. Elkhoully, A. Malignaggi, A. C. Ulusoy, and D. Kissinger, "A 220–275 GHz Direct-Conversion Receiver in 130-nm SiGe:C BiCMOS Technology," *IEEE Microwave and Wireless Components Letters*, vol. 27, no. 7, pp. 675–677, 2017.
- [86] A. Pawlak, M. Schröter, A. Mukherjee, S. Lehmann, S. Shou, and D. Céli, "Automated model complexity reduction using the hicum hierarchy," in *2011 Semiconductor Conference Dresden*, 2011, pp. 1–4.
- [87] B. Heinemann, R. Barth, D. Bolze, *et al.*, "SiGe HBT technology with f_T/f_{max} of 300GHz/500GHz and 2.0 ps CML gate delay," in *2010 International Electron Devices Meeting*, 2010, pp. 30.5.1–30.5.4.
- [88] J. Grzyb, K. Statnikov, N. Sarmah, and U. Pfeiffer, "A lens-integrated on-chip circular slot antenna for a 240 GHz power source in SiGe technology," in *2015 IEEE International Symposium on Antennas and Propagation & USNC/URSI National Radio Science Meeting*, Jul. 2015, pp. 2055–2056.

- [89] J. Wan, Z. Chen, Q. An, and X. Wang, "A Truly Balanced Q-Band CMOS Frequency Doubler Based on Hybrid Quadrature Coupler," vol. 27, no. 2, pp. 165–167, 2017.
- [90] B. Gilbert, "The MICROMIXER: a highly linear variant of the Gilbert mixer using a bisymmetric Class-AB input stage," vol. 32, no. 9, pp. 1412–1423, 1997.
- [91] B. Gilbert, "The multi-tanh principle: a tutorial overview," vol. 33, no. 1, pp. 2–17, 1998.
- [92] C. Ahn, S. Oh, and K. Chang, "A dual-frequency omnidirectional antenna for polarization diversity of MIMO and wireless communication applications," vol. 8, pp. 966–969, 2009.
- [93] K. Pedram, M. Karamirad, and S. M. H. Ranjbaran, "A novel circular polarization MIMO antenna in 60 GHz technology," in *2017 IEEE 4th International Conference on Knowledge-Based Engineering and Innovation (KBEI)*, Dec. 2017, pp. 0335–0338.
- [94] S. V. Nesteruk and P. I. Travkin, "Double-polarization antenna for MIMO system of wireless communication," in *2011 VIII International Conference on Antenna Theory and Techniques*, Sep. 2011, pp. 214–216.
- [95] K. Dasgupta, S. Daneshgar, C. Thakkar, *et al.*, "A 60-GHz transceiver and baseband with polarization MIMO in 28-nm CMOS," vol. 53, no. 12, pp. 3613–3627, Dec. 2018.
- [96] K. K. Tokgoz, S. Maki, J. Pang, *et al.*, "A 120Gb/s 16QAM CMOS millimeter-wave wireless transceiver," in *2018 IEEE International Solid - State Circuits Conference - (ISSCC)*, Feb. 2018, pp. 168–170.
- [97] C. Jiang, A. Cathelin, and E. Afshari, "A High-Speed Efficient 220-GHz Spatial-Orthogonal ASK Transmitter in 130-nm SiGe BiCMOs," vol. 52, no. 9, pp. 2321–2334, 2017.
- [98] J. Grzyb, K. Statnikov, N. Sarmah, and U. R. Pfeiffer, "A broadband 240 GHz lens-integrated polarization-diversity on-chip circular slot antenna for a power source module in SiGe technology," in *2015 European Microwave Conference (EuMC)*, Sep. 2015, pp. 570–573.
- [99] S. M. Bowers and A. Hajimiri, "Multi-port driven radiators," vol. 61, no. 12, pp. 4428–4441, Dec. 2013.
- [100] M. J. M. van der Vorst, P. J. I. de Maagt, and M. H. A. J. Herben, "Effect of internal reflections on the radiation properties and input admittance of integrated lens antennas," vol. 47, no. 9, pp. 1696–1704, Sep. 1999.
- [101] M. J. M. van der Vorst, P. J. I. de Maagt, A. Neto, A. L. Reynolds, R. M. Heeres, W. Luinge, and M. H. A. J. Herben, "Effect of internal reflections on the radiation properties and input impedance of integrated lens antennas-comparison between theory and measurements," vol. 49, no. 6, pp. 1118–1125, Jun. 2001.
- [102] S. Kang, S. V. Thyagarajan, and A. M. Niknejad, "A 240 GHz Fully Integrated Wideband QPSK Transmitter in 65 nm CMOS," vol. 50, no. 10, pp. 2256–2267, 2015.
- [103] S. V. Thyagarajan, S. Kang, and A. M. Niknejad, "A 240 GHz Fully Integrated Wideband QPSK Receiver in 65 nm CMOS," vol. 50, no. 10, pp. 2268–2280, 2015.
- [104] Z. Wang, P. Chiang, P. Nazari, C. Wang, Z. Chen, and P. Heydari, "A cmos 210-ghz fundamental transceiver with ook modulation," *IEEE Journal of Solid-State Circuits*, vol. 49, no. 3, pp. 564–580, 2014.
- [105] H. Koo, C. Kim, and S. Hong, "A 254 GHz CMOS Transmitter With VCO-Q Modulation," *IEEE Microwave and Wireless Components Letters*, vol. 26, no. 6, pp. 458–460, 2016.
- [106] P. V. Testa, C. Carta, and F. Ellinger, "A 160–190-GHz Vector-Modulator Phase Shifter for Low-Power Applications," *IEEE Microwave and Wireless Components Letters*, vol. 30, no. 1, pp. 86–89, 2020.
- [107] Y. Kim, S. Kim, I. Lee, M. Urteaga, and S. Jeon, "A 220–320-GHz Vector-Sum Phase Shifter Using Single Gilbert-Cell Structure With Lossy Output Matching," *IEEE Transactions on Microwave Theory and Techniques*, vol. 63, no. 1, pp. 256–265, 2015.

-
- [108] Y. Tousi and E. Afshari, "A High-Power and Scalable 2-D Phased Array for Terahertz CMOS Integrated Systems," *IEEE Journal of Solid-State Circuits*, vol. 50, no. 2, pp. 597–609, 2015.
 - [109] K. Guo and P. Reynaert, "29.2 A 0.59THz Beam-Steerable Coherent Radiator Array with 1mW Radiated Power and 24.1dBm EIRP in 40nm CMOS," in *2020 IEEE International Solid-State Circuits Conference - (ISSCC)*, 2020, pp. 442–444.